

Atmospheric Inputs of Iron and Other Key Nutrients to the Tropical North Atlantic

Claire Powell

A thesis presented to the School of Environmental Sciences, University of East
Anglia, in candidature for the degree of Doctor of Philosophy
·September 2010·

*This copy of the thesis has been supplied on condition that anyone who consults it is
understood to recognise that its copyright rests with the author and that no quotation
from the thesis, nor any information derived therefrom, may be published without the
author's prior, written consent. ©2010*

Abstract

Atmospheric deposition represents as much as 70% of the average global input of iron to the open ocean (*Jickells et al.*, 2005), and is also a significant transport vector for phosphate and nitrogen, particularly to the Eastern Tropical North Atlantic (ETNA). However, the overall effect on phytoplankton ecosystems is uncertain. It is difficult to assess the relative supply of these key nutrients because the atmospheric deposition varies in composition, and over seasons.

Data from three research cruises conducted during winter 2006, summer 2006 and winter 2008, at periods of high dust deposition were used to characterise the typical sources of iron, nitrogen, and phosphate to the region. Further data from ship based measurements gathered on over 20 cruises between 2000 and 2009 were then used to examine the solubility of the iron input, as a proxy for the bioavailability. Finally, the data was used in conjunction with air mass back trajectories to derive a seasonal flux climatology for all three nutrients.

Iron inputs to the region are dominated by Saharan dust and it is unlikely that anthropogenic sources of iron are significant. Iron solubility is probably controlled, at least in part, by particle size. The concentration of phosphate contains a strong component from both mineral dust and African biomass burning. Reactive nitrogen also contains a strong biomass burning signal, but there are also many other, mainly anthropogenic sources.

The climatology shows a strong seasonal change in the deposition of iron, with over 70% of the annual flux being deposited in the winter and summer months. As the majority of aerosol samples collected in this region have been in spring and autumn (during AMT cruises), this means previous observations may significantly underestimated the annual iron flux. The deposition flux of nitrogen is dominated (at 65% of the inorganic nitrogen flux) by nitrate, which is due to the slower dry deposition velocity of the predominantly fine mode ammonium, although there is not a seasonal signal in either nitrate or ammonium deposition. The deposition of phosphate is relatively high, compared to other remote regions, and there is a seasonal signal, with higher deposition during winter, coincident with high dust input to the region.

Acknowledgements

First up, many thanks to my supervisors Alex Baker and Tim Jickells, who have both been brilliant especially when I was writing up. I'm afraid I still don't really understand cricket though.

Secondly, thanks to my examiners, Malcolm Nimmo and Carol Robinson, who helped me realise that this thesis was worth doing after all. The lab support at UEA has also been very good, and Liz Rix and Kim Wright have both made my being in the lab a lot easier. They also managed to refrain from laughing on the occasions when I have been unable to add up, for which I am grateful.

Thanks also go to Dad, who didn't say too much about my not having a real job, and Mum, who didn't ask me too often if I'd finished yet, also Elé and Alex, who did. I am also grateful to Will for putting up with me over the last six months and also to Nem for putting me up.

Thanks (and apologies) also go, in no particular order, to Liz, Pete, Steve, Tom, Gareth, Laura, Sally, Rich, Alba, Janina, Johanna, Anne, Martin, Claire, Ross, Katie, Helen, Simon and Chris. You all know who you are...

Contents

Abstract	ii
Acknowledgements	iii
Glossary	xx
1 Introduction	1
1.1 Background	3
1.2 Phytoplankton requirements	3
1.2.1 The bioavailability of iron	4
1.3 Phytoplankton requirements in the ETNA	5
1.4 The relative importance of atmospheric supply of nutrients	5
1.5 Saharan dust deposition to the ETNA	7
1.5.1 African biomass burning	8
1.6 Aims and Objectives	9
2 Methods	11
2.1 Sample Collection	13
2.1.1 Sampling Location	13
2.1.2 Wet Deposition	14
2.1.3 Aerosol deposition	16

2.1.3.1	Calibration	17
2.1.3.2	Size Segregation	19
2.1.3.3	Sampling Protocol	21
2.1.3.4	Filter Preparation	21
2.1.3.5	Extraction	23
2.2	Sample Analysis	24
2.2.1	Ion Chromatography	24
2.2.2	Total Soluble Nitrogen	26
2.2.3	Soluble Trace Metal analysis using ICP OES	26
2.2.4	Molybdenum Blue Phosphate Analysis	27
2.2.5	Total Trace Metal analysis using Neutron Activation	28
2.3	Data Processing	28
2.4	Conversion of aerosol atmospheric concentration to flux	30
2.5	Air mass back trajectories and source region	32
3	The aerosol concentration of iron and other nutrients on D326, M68 and P332	37
3.1	Background	39
3.2	Seasalt Aerosol	40
3.3	Saharan Dust	45
3.4	Anthropogenically influenced aerosol	51
3.4.1	Nitrogen Aerosol	51
3.4.2	Non-seasalt sulphate	57
3.4.3	Biomass Burning	59
3.5	Trace metal solubility	60
3.6	Summary	66

4	Gradients in Iron Soluble Fraction	67
4.1	Background	69
4.2	Aerosol concentration data set for the ETNA	70
4.3	Anthropogenically produced iron aerosol	71
4.4	Changes in iron solubility across the Sahara	73
4.5	Atmospheric Processing	78
4.6	Solubility as a function of particle size	81
4.7	Iron soluble fraction in the tropical North Atlantic	84
5	Climatology	87
5.1	Background	89
5.2	Defining the ETNA region	93
5.3	The ETNA data set	93
5.4	Constructing the aerosol climatology	94
5.4.1	Seasonal back trajectory probabilities	95
5.4.2	Seasonal average aerosol composition	101
5.4.3	The seasonally averaged aerosol flux	107
5.5	Constructing the rainfall climatology	108
5.5.1	Average precipitation rates	109
5.5.2	Average rain composition	110
5.5.3	The average rain flux	111
5.6	The ETNA aerosol and rainfall climatology	112
5.6.1	Soluble and total iron	112
5.6.2	Inorganic nitrogen species, and total nitrogen estimate	116
5.6.3	Soluble reactive phosphate	120
5.6.4	The annual atmospheric flux and its impacts	122

5.7 Summary	125
6 Conclusions	129
Appendices	137
A Appendix to Chapter 2	139
B Appendix to Chapter 3	147
C Appendix to Chapter 5	155
D Papers published using data from this thesis	173
E Appendix - Matlab Code	187
E.1 Cal.m	189
E.2 Conc.m	194
E.3 Driftconc.m	195
E.4 Molar.m	196
E.5 Dblanks.m	197
E.6 Atmospheric.m	199
E.7 Climatology.m	199
Bibliography	201

List of Figures

1.1	Global iron input to the world ocean	6
1.2	Airflow patterns and dust-transport directions in northwest Africa	8
1.3	Global peak vegetation fire month	9
2.1	Cruise tracks for three different cruises between 2006 and 2008	13
2.2	Rain collecting equipment	14
2.3	Washing procedures for rain sampling equipment	15
2.4	High volume aerosol sampler	16
2.5	Calibration	18
2.6	Diagram showing how the cascade impactor works	20
2.7	Protocols for the preparation of Whatman-41 filters prior to sampling	22
2.8	Methods used for the extraction of the chemical constituents from aerosol samples	23
2.9	General protocol used for the analysis of all samples	25
2.10	Dry deposition velocity as a function of wind speed for fine particles, mineral dust and seasalt	31
2.11	Examples of HYP SLIT back trajectory plots	33
2.12	Source regions for the Tropical North Atlantic	35
3.1	Relative concentrations of Na^+ , Cl^- , Mg^{2+} and total Al	43
3.2	Atmospheric concentration of sodium for the three cruises	44

3.3	Dust mass loading for the three cruises	45
3.4	Atmospheric concentration of crustal materials for the three cruises	47
3.5	Ratio of total aluminium to (a) total iron, (b) total manganese, (c) non-seasalt calcium, and (d) SRP	48
3.6	Atmospheric concentration of nitrogen aerosol for the three cruises	54
3.7	Correlation of nitrate and ammonium and non-seasalt sulphate and ammonium	55
3.8	Atmospheric concentration of non-seasalt sulphate for the three cruises . . .	57
3.9	Atmospheric concentration of nitrate and non-seasalt sulphate plotted against the ratio of sodium to chloride	58
3.10	Atmospheric concentration of non-seasalt potassium for the three cruises . .	59
3.11	Atmospheric concentration of soluble trace metals for the three cruises . . .	62
3.12	Atmospheric trace metal solubility for the three cruises	64
3.13	Iron solubility plotted against dust mass loading: this data compared to <i>Baker and Jickells</i> (2006)	65
4.1	Iron solubility plotted against dust mass loading: this data compared to <i>Baker and Jickells</i> (2006)	71
4.2	(a) Box and whisker plots for the iron solubility for each air mass type; (b) Iron solubility against dust loading showing air mass type	72
4.3	Aerosol iron solubility plotted against the ratio of total iron to total aluminium	73
4.4	Different source regions in the Sahara from <i>Chiapello et al.</i> (1997)	74
4.5	(a) Box and whisker plots for the iron solubility for each Saharan Region; (b) Iron solubility against dust loading showing Saharan region	75
4.6	The variation of non-seasalt calcium to aluminium ratio in Saharan region samples	76
4.7	(a) Box and whisker plots for the iron solubility during Winter and Summer; (b) Iron solubility against dust loading showing Winter and Summer; (c) Box and whisker plots for the iron solubilities collected at different latitude bands; (d) Iron solubility against dust loading for different latitude bands	77

4.8	Variation of iron solubility with (a) nitrate; (b) sulphate; and (c) aerosol acidity, as defined in equation 4.1	79
4.9	Variation of iron solubility with (a) aluminium solubility and (b) the solubility change between iron and aluminium	81
4.10	Variation of dust mass loading with (a) surface area to volume ratio; (b) iron % solubility for this data	83
4.11	Soluble iron fine fraction divided by coarse fraction, plotted against iron solubility, values less than 1 indicate larger particles, greater than 1 smaller particles	84
5.1	The sampling locations of all wet and dry deposition data used	94
5.2	Flow chart for assigning air mass back trajectories to air mass types	96
5.3	Annual source region percentages for each climatology point	98
5.4	The seasonal variation of source region percentages for each climatology point	100
5.5	The distribution of data over the year between different regions	101
5.6	The seasonal distribution of samples from each climatology point for each source region	102
5.7	The seasonal variation of air mass type probabilities for each climatology point	103
5.8	The distribution of data over the year for the northern and southern part of the ETNA	103
5.9	Unweighted dry deposition concentration and flux for SAH air mass types for total iron, total soluble inorganic nitrogen, and total soluble reactive phosphate	105
5.10	The seasonal dry deposition flux climatology for total iron	108
5.11	Seasonal mean rainfall in mm day ⁻¹ between March 1999 and March 2009 for each climatology point	109
5.12	The distribution of rain samples collected sorted by season, climatology point and climatology half	110
5.13	The annual wet deposition flux climatology for total iron	112

5.14	The climatologies for deposition of total iron to the ETNA shown as (a) total iron aerosol deposition and (b) total iron in rain	113
5.15	The climatologies for deposition of soluble iron to the ETNA shown as (a) soluble iron aerosol deposition and (b) soluble iron in rain N.B. the difference in colour scales between these plots and figure 5.14	114
5.16	The climatologies for deposition of nitrogen to the ETNA shown as (a) nitrogen aerosol deposition and (b) nitrogen in rain	117
5.17	The climatologies for deposition of ammonium to the ETNA shown as (a) ammonium aerosol deposition and (b) ammonium in rain	118
5.18	The climatology for the aerosol deposition of soluble reactive phosphate to the ETNA	121
5.19	The seasonal variation in the ratio of SRP flux / total aluminium flux for each climatology box	122
A.1	Calibration curves for six stage cascade impactor	142
B.1	Air mass back trajectory plots for each sampling date on D326. Dates are shown above each plot	149
B.2	Air mass back trajectory plots for each sampling date on M68. Dates are shown above each plot	151
B.3	Air mass back trajectory plots for each sampling date on P332. Dates are shown above each plot	153
E.1	Screen shot of the cal GUI	189

List of Tables

1.1	Annual atmospheric deposition of nitrogen to the oceans	7
2.1	Details of the three cruises	14
2.2	Blanks used to ensure quality control of samples	21
2.3	Typical extract sample and blank concentrations in $\mu\text{mol dm}^{-3}$	30
2.4	Details of the mass-median diameters (MMD) used in calculating flux	31
2.5	Typical characteristics of each source region defined in this study	34
3.1	Average aerosol atmospheric concentrations	39
3.2	Major ions of seawater	40
3.3	Crustal ratios of Al, Fe, Ca, P, Na, Mn, Cl and V from <i>Wedepohl</i> (1995)	49
3.4	The ratio of different species to total aluminium, calculated by performing a linear regression on the plots in figure 3.5	49
3.5	Correlation of nitrate and non-seasalt sulphate to ammonium	56
3.6	The approximate ratio of nutrient elements in biomass burning aerosol from <i>Crutzen and Andreae</i> (1990)	59
4.1	Literature values for iron solubility	69
5.1	Atmospheric deposition flux estimates	92
5.2	Details of each climatology region	93
5.3	Number of trajectories assigned to each air mass and percent for each climatology point	99

5.4	Seasonal distribution of data according to source region (numbers are number of samples)	102
5.5	Uncertainty values assigned to the average values according to the number of data points averaged (after <i>Baker et al.</i> , 2010)	104
5.6	Average wind speeds for the climatology region (all in ms^{-1})	106
5.7	Seasonally averaged rainfall for each climatology box (all in mm d^{-1})	110
5.8	Regional distribution of rain samples according to season (numbers are number of samples)	111
5.9	Total iron deposition flux in aerosol and rain, units in $\mu\text{mol m}^{-2} \text{day}^{-1}$ and soluble iron deposition flux, units in $\text{nmol m}^{-2} \text{day}^{-1}$; R/A is the rain flux divided by aerosol flux	115
5.10	Nitrate and ammonium deposition flux in aerosol and rain, units in $\mu\text{mol m}^{-2} \text{day}^{-1}$; TIN is the sum of ammonium and nitrate fluxes and TSN has been calculated from the TIN flux by assuming that soluble organic nitrogen represents 30% of the total soluble nitrogen flux (<i>Duce et al.</i> , 2008). R/A is the rain flux divided by aerosol flux	119
5.11	Soluble reactive phosphate deposition flux in aerosol, units in $\text{nmol m}^{-2} \text{day}^{-1}$, N.B. rain samples were not analysed for SRP	121
5.12	Annual deposition fluxes to the ETNA calculated from this work	123
5.13	N:P, Fe:N and N:C ratios for primary producers and the calculated aerosol fluxes ^a - from <i>Sunda</i> (1997) ^b - from <i>Berman-Frank et al.</i> (2001)	124
A.1	Ideal standard concentrations used in ion chromatography analysis	143
A.2	Ideal standard concentrations used in TN analysis	144
A.3	Ideal standard concentrations used in soluble trace metal analysis by ICP OES	144
A.4	Ideal standard concentrations used in SRP analysis	145
B.1	Air mass assignments and descriptions of the collected filters for each sampling date on D326	150
B.2	Air mass assignments and descriptions of the collected filters for each sampling date on M68	152

B.3	Air mass assignments and descriptions of the collected filters for each sampling date on P332	154
C.1	Details of the cruises crossing the ETNA between 2000 and 2009	157
C.2	Distribution of dry deposition data throughout the climatology region (numbers are number of samples)	158
C.7	Volume weighted mean rainwater concentrations (conc), with % uncertainties (%u), for northern (ABCD) and southern (EFGH) climatology regions . . .	171
C.8	The calculated rain flux for each climatology region and % uncertainty (%u), based on the volume weighted mean and the average annual rainfall to each climatology region	171

Glossary

NH_4^+	Ammonium, 25
NO_3^-	Nitrate, 25
PO_4^{3-}	Phosphate, 26
Average Composition Field	average values for aerosol composition used in the climatology and derived from aerosol concentration data, 90
dust loading	The total amount (mass) of mineral dust collected by a sample. It can be calculated by assuming that the dust is 8.1% by mass aluminium, 43
ETNA	Eastern Tropical North Atlantic, 3
ETNA(A-H)	Labels given to the 8 different boxes within the climatology region, as shown in table 5.2, 89
ITCZ	Intertropical Convergence Zone, 7
MBL	Marine Boundary Layer - the part of the lower troposphere adjacent to the open ocean, 9
MMD	Mass Median Diameter. The median particle diameter of a population sorted by mass, rather than number density, 30
NO_x	Nitrogen oxides, or the sum of nitric oxide, NO, and nitrogen dioxide, NO ₂ , 50

SAL	Saharan Air Layer, a wind system that transports Saharan dust at mid tropospheric levels across the Atlantic, 7
SON	Soluble Organic Nitrogen, 25
TIN	Total Inorganic Nitrogen, the sum of nitrate and ammonium, 112
TIN	Total Inorganic Nitrogen, 88
trace metal solubility	The fraction of a trace metal that will dissolve from an aerosol sample, also called its fractional solubility, 59
TSN	Total Soluble Nitrogen, 25

Chapter 1

Introduction

Each of the main chapters in this thesis is meant to stand alone, so they all include an introduction, however a short background is also necessary here to establish the global context of the main theme: whether atmospheric deposition of iron, nitrogen and phosphate to the open ocean is important globally and for the eastern Tropical North Atlantic (ETNA); how aerosol deposited in the ETNA region is produced and transported; and what the prevailing meteorological and oceanographic conditions are.

1.1 Background

While aerosols have a direct effect on climate via cloud formation (*Twohy et al.*, 2009; *DeMott et al.*, 2003) and radiative forcing (*Maher et al.*, 2010; *McConnell et al.*, 2008; *Osborne et al.*, 2008) they are also of considerable importance as a source of nutrients to marine phytoplankton, which affect climate via carbon drawdown and other feedback mechanisms (*Ridgwell*, 2009; *Duce et al.*, 2008; *Jickells et al.*, 2005). Saharan dust, in particular, is a significant transport vector for the nutrients phosphorus and iron to the nutrient depleted waters of the Tropical North Atlantic with fixed nitrogen often transported with it (*Baker et al.*, 2006c,a). However, the overall effect of atmospheric deposition on phytoplankton ecosystems is uncertain and assessment of the relative supply of iron, phosphate and reactive nitrogen compared to phytoplankton requirements is an important part of evaluating the ecological impact of atmospheric deposition.

1.2 Phytoplankton requirements

In general, the nutrient requirements of phytoplankton are considered to be close to the Redfield ratios for these nutrients. Redfield ratios describe the average composition of marine organic matter, and for the P:N ratio is approximately 1:16 (*Lenton and Watson*, 2000). On a global scale, it is broadly considered that nitrate is more depleted than phosphate in the surface ocean, thus nitrate is the proximal limiting nutrient for primary productivity (*Broecker and Peng*, 1982). However, the conversion of dissolved dinitrogen to nitrate by nitrogen fixing organisms (diazotrophs), provides a feedback mechanism which maintains nitrate close to the Redfield ratio with phosphate, and thus external phosphate inputs control longer-term primary production in the global ocean, i.e. it is the ultimate limiting nutrient (*Tyrrell*, 1999).

In addition to the macronutrients nitrate and phosphate, iron has also been shown to be an important micronutrient, playing a role in photosynthesis, respiration, and nitrogen fixation (*Falkowski et al.*, 1998). Although iron does not occur in stoichiometric amounts in the major structural and information containing components of cells like nitrate and phosphate, but rather in catalytic centres of enzymes (*Sunda*, 1997), it has been shown

to limit primary productivity in as much as a third of the world ocean (*Boyd et al.*, 2007; *Martin and Fitzwater*, 1988). Additionally, in the case of nitrogen fixation, the distribution of diazotrophs is intrinsically linked to the presence of the mineral dust (*Mahaffey et al.*, 2005), as nitrogenase, the enzyme responsible for nitrogen fixation, has the lowest catalytic activity of any iron-containing enzyme involved in nitrogen metabolism (*Falkowski*, 1997), and thus the iron requirement for nitrogen fixers approximately 100-fold higher than for primary producers (*Deutsch et al.*, 2007).

1.2.1 The bioavailability of iron

An additional feature of determining the supply of iron to the surface ocean with respect to phytoplankton requirements is whether or not the iron is bioavailable, i.e. whether organisms are able to utilize the iron supplied.

The major source of iron to the ocean is mineral dust, where iron is often bound in the low solubility aluminosilicates (*Jickells et al.*, 2005). Thus, most of the iron potentially supplied to the ocean by atmospheric deposition occurs as Fe(III) (*Siefert et al.*, 1999), which has a very low solubility in seawater (*Liu and Millero*, 2002) and as a result, it rapidly forms colloids or is scavenged onto larger particles, thus iron has a short residence time in the water column (*Croot et al.*, 2004). Dissolved Fe(II) and the dissolved forms of Fe(III) are known to be bioavailable and can be taken up directly by the phytoplankton (*Baker and Croot*, 2010). However, iron complexed by organic ligands dominates the dissolved forms of iron (*Rue and Bruland*, 1995) although the bioavailability of such complexes is not clear and appears to change for a given phytoplankton taxon depending on the specific ligand in question (*Tagliabue and Arrigo*, 2006). Additionally, colloidal or nano-particulate iron which can be transformed, via post-depositional processes, into soluble iron (*Baker and Croot*, 2010). Nevertheless bioavailable iron is dominated by soluble iron, and thus iron solubility is used as a proxy for bioavailability.

The solubility of iron in aerosol can be affected by a number of processes, including the source of aerosol, e.g. iron aerosol deriving from aluminosilicate Saharan dust has a much lower fractional solubility (in the order of 0.01 – 0.3 %) than iron aerosol derived from heavy fuel oil burning (*Sedwick et al.*, 2007). A gradient may also exist in iron solubility for aerosols coming from across the Saharan region, consistent with a change in minerals from North Africa to the Sahel (*Journet et al.*, 2008). Other reasons for changes in the solubility of iron aerosol include the acid processing in clouds (*Raes et al.*, 2000), the photoreduction of insoluble iron III in the aerosol to soluble iron II by sunlight (*Siefert et al.*, 1999), and size fractionation of aerosol due to the lower deposition velocity of smaller (and more soluble) sized particles *Baker and Jickells* (2006).

1.3 Phytoplankton requirements in the ETNA

The eastern Tropical North Atlantic is the region of the Atlantic to the west of Africa, including the Cape Verde and Canary Islands. The Mauritanian upwelling zone, which is within the ETNA, is an area where nutrient rich water is upwelled from depth, is located close to the African coast and tends to be stronger in the springtime, although it is confined closer to the coast in the summer (*Schlosser and Croot, 2009*). Outside of the upwelling region, wind driven mixing in the water column tends to be inhibited by strong temperature and density gradients (*Kump et al., 2004*), so the waters are generally described as oligotrophic, or depleted in nutrients (*Mills et al., 2004; Wu et al., 2001*). However, despite the low concentration of nutrients and thus low rates of primary productivity of $10\text{-}30 \text{ mmol C m}^{-2} \text{ d}^{-1}$ (*Poulton et al., 2006*), in the oligotrophic North Atlantic (*Longhurst et al., 1995*), the fact that this oligotrophic region covers a large area and the absence of strong seasonality in this region is believed to make even low production rates important for carbon export from the upper ocean in a global sense (*Painter et al., 2008*).

In this context, the supply of nutrients to the ETNA by aeolian deposition can promote productivity in this region, although the mechanism by which this happens depends crucially on the relative amounts of nutrients supplied (*Mahaffey et al., 2005*). *Mills et al.* (2004) show that primary productivity in the oligotrophic north Atlantic is limited by nitrogen. However, the ETNA has been shown to be rich in diazotrophs and nitrogen fixation in this region has been shown to be co-limited by iron and phosphate (*Mills et al., 2004*).

1.4 The relative importance of atmospheric supply of nutrients

Atmospheric deposition is a major source of nutrients to the open ocean, in the absence of wind induced mixing and upwelling of nutrients from depth. *Jickells et al.* (2005) estimate that at approximately 16 Tg yr^{-1} , the atmospheric flux of iron is around just 2% of the total global flux of all iron to the ocean (as summarised in figure 1.1), however, due to the low solubility of iron in oxic seawater and the efficient trapping of iron in near-coastal areas, this figure rises to 70% of the annual input to the open ocean.

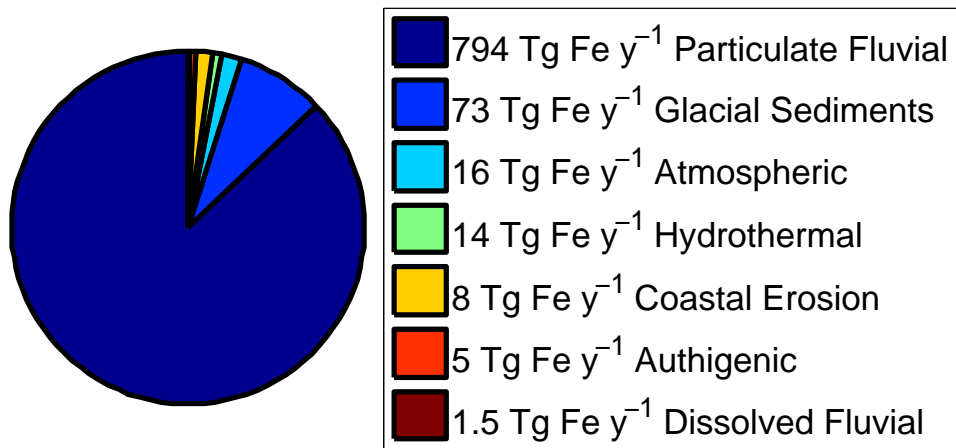
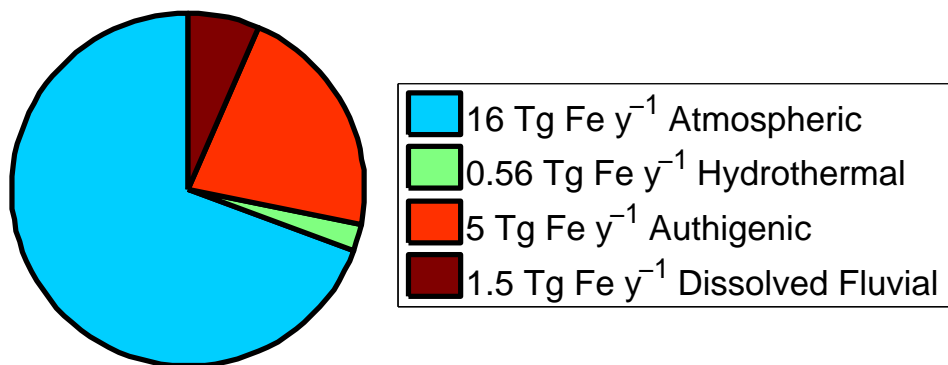
(a) *Iron Flux to the Global Ocean from Jickells et al. (2005)*(b) *Iron Flux to the Open Ocean*

Figure 1.1: *Global iron input to the ocean, (a) taking the fluxes from Jickells et al. (2005) (b) modifying these inputs to take into account the processes which trap particulate iron in near-coastal areas, and the stabilization of 4% of the iron from hydrothermal vents by organic ligands (Bennett et al., 2008)*

In the same vein *Galloway et al. (2008)* show that rivers are important inputs of fixed nitrogen to coastal areas. However, due to efficient denitrification in estuarine systems, only a small proportion of the fixed nitrogen from rivers reaches the open ocean, thus atmospheric deposition becomes more important in the supply of fixed nitrogen to the ocean. *Duce et al. (2008)* estimate that the atmospheric supply of fixed nitrogen to the oceans is around 67 Tg yr^{-1} , of which 54 Tg yr^{-1} is from anthropogenic sources, these results are summarised in table 1.1.

The lack of data on phosphorus and phosphate make global inputs to the ocean difficult to constrain, but *Graham and Duce (1979)* estimate that atmospheric inputs of phosphorus amount to around 10% of the fluvial flux of phosphorus to the oceans. However, as much of the phosphorus is in the particulate phase, most of it is removed by sedimentation

Nitrogen Species	Input	
	Tg yr ⁻¹	% of total
NO _y	23 (17)	34%
NH _x	24 (21)	36%
Organic N _r	20 (16)	30%
Total N _r	67 (54)	–

Table 1.1: *Estimated annual atmospheric deposition of reactive nitrogen (N_r) to the global ocean from Duce et al. (2008); numbers in brackets show the anthropogenic contribution to each species*

in near-shore areas and it is thought that the flux of dissolved phosphorus to the open ocean is around 0.9-4.5 Tg yr⁻¹ (Benitez-Nelson, 2000). This compares to an estimated global atmospheric input of 0.56 Tg yr⁻¹ total phosphorus and 0.10 Tg yr⁻¹ phosphate to the global ocean, of which an estimated 15% and 5% respectively is directly due to anthropogenic activities (Mahowald et al., 2008).

1.5 Saharan dust deposition to the ETNA

The atmospheric deposition of nutrients to the ETNA is dominated by the transport of dust from the Saharan region (Chiapello et al., 1997; Mills et al., 2004; Duce and Tindale, 1991), in fact the transport of Saharan dust into the North Atlantic accounts for about 43% of the annual dust input to the global ocean (Jickells et al., 2005), so this is an area of potentially high annual dust input. Biomass burning aerosols also make a significant contribution to the input of soluble iron, phosphate and reactive nitrogen at up to 10% (Guieu et al., 2005), 5% (Mahowald et al., 2008), and 12–40% (Crutzen and Andreae, 1990; Duce et al., 2008) of the respective estimated annual global inputs. However, the deposition and transport of Saharan dust is episodic (Chiapello et al., 2005) with several different atmospheric transport pathways (Middleton and Goudie, 2001).

The major atmospheric feature over the ETNA is the seasonal shift of the Intertropical Convergence Zone, ITCZ, which is characterised by extensive cloud cover and heavy precipitation. The ITCZ moves from around 19°N during summer (June, July and August) to around 5°S during winter (December, January and February) (Stuut et al., 2005). This seasonal variation of the position of the ITCZ has large effects on both the source region and transport pathways for Saharan dust aerosol (Middleton and Goudie, 2001). For example, Prospero and Lamb (2003) show from observations made in Barbados, that the dust uplift from the Sahel region is low in seasons following high amounts of rainfall. It is interesting to note that although the deep convection associated with the ITCZ should bring a large amount of rainfall, one effect of high atmospheric aerosol loading could act to diminish precipitation, either by dust aerosol acting as cloud condensation nuclei, thus decreasing mean droplet size (Twohy et al., 2009) or perhaps by suppressing deep

convection (*Huang et al.*, 2009b), although the magnitude of these effects is unclear.

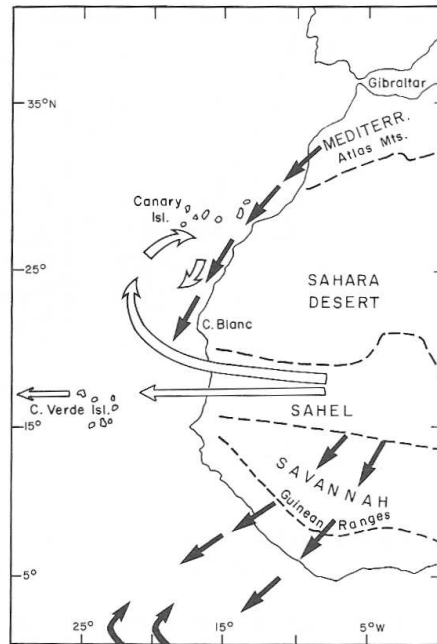


Figure 1.2: *Airflow patterns and dust-transport directions in northwest Africa, from Pye (1987). solid arrows: meridional surface winds; open arrows: mid-tropospheric zonal winds of the Saharan Air Layer (SAL)*

There are generally three wind systems which transport dust to the ETNA (*Pye*, 1987), and these are represented in figure 1.2. First, there is the low level north east trade winds coming from the Atlas Mountains, which run parallel to the coast and are active throughout most of the year (*Stuut et al.*, 2009). Secondly there are the central Saharan expression of NE trade winds, the Harmattan, which transport dust all year round, but are at their most intense during winter (December, January and February) (*Chiapello et al.*, 1997), when the ITCZ is located to the south. Finally, as the ITCZ travels north during summer, uplifted dust is pushed up to mid-tropospheric levels into the Saharan Air Layer (SAL), which transports dust across the Atlantic and is the system responsible for the Saharan Dust that has been collected as far afield as the Caribbean and Bermuda (*Prospero and Lamb*, 2003).

1.5.1 African biomass burning

Another feature of the ETNA region is that as it is adjacent to Africa, some of the aerosol collected in the region is due to biomass burning, a catchall term that is applied to the burning of vegetation and peat set either by humans or by naturally occurring phenomena including lightning, in addition to the use of wood and peat as biofuels for domestic purposes (*Langmann et al.*, 2009). The global emissions of biomass burning are dominated

by Africa, due to the large savannah in both hemispheres. The seasonal distribution of biomass burning in Africa is dominated by fires in this savannah region (*Cooke et al.*, 1996) and is part of a long established agricultural pattern, with peak biomass burning occurring during the dry season in each hemisphere as shown in figure 1.3. Observations have shown that biomass burning aerosol is often transported with mineral dust from the Saharan region, for example, the observation by *Real et al.* (2010) of the observed uplift of aerosol from the central African biomass burning plumes, which are at their peak during June, July and August, into the SAL during summer dust events.

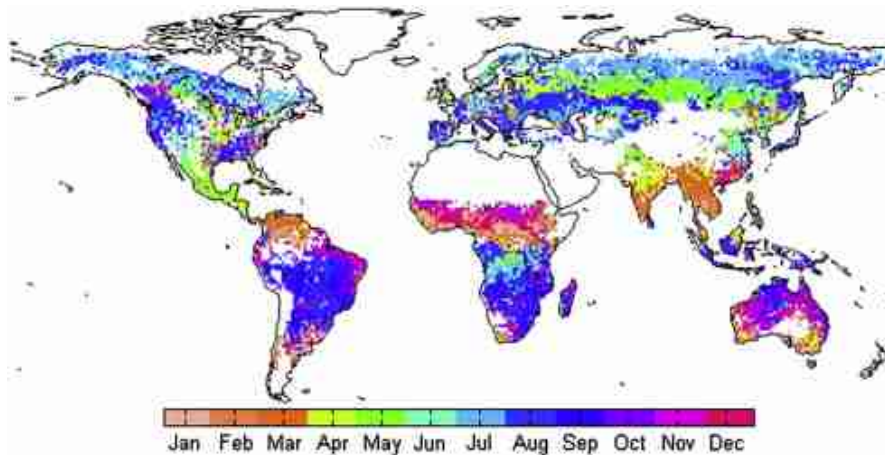


Figure 1.3: *Global peak vegetation fire month determined from satellite measurements between 1997–2006, from Langmann et al. (2009)*

Biomass burning releases as much as 1800–4700 Tg C year⁻¹ into the atmosphere, although less than 5% of this will be in particulate form (*Andreae*, 1983). In addition to soot, other trace elements are emitted in particle form, including nitrogen, potassium, phosphate, magnesium and sulphate, in varying proportions, depending on the substance being burned (*Crutzen and Andreae*, 1990). Thus these elements, particularly particulate potassium with a particle size of less than 1.7 μm , but greater than 1.0 μm in diameter, can be used to indicate the presence of a biomass burning signal in aerosol samples (*Andreae and Crutzen*, 1997).

1.6 Aims and Objectives

The atmospheric deposition of iron and nutrients could make an important contribution to the primary productivity, and therefore particle (and thus carbon) export, in the oligotrophic North Atlantic. However, due to the episodic nature of the deposition, seasonal fluxes and therefore the impact on the marine biota are far from certain.

The aim of this thesis is to quantify and characterise the input of iron, reactive nitrogen and phosphate to the ETNA.

In order to address this problem it has been broken down into three main objectives, which are presented in this thesis as chapters:

Characterisation of aerosols collected during dust storms in the ETNA – Chapter 3

examines the elemental concentration data for aerosol samples gathered in the region on three separate cruises - attention has been focused on how much aerosol there was present, with an emphasis on iron, nitrogen and phosphate; where it derives from; and which chemical components were being co-transported.

Investigation into the solubility of iron aerosol transported to the region – Chapter 4

considers how soluble the iron aerosol in the region is, what factors might control this solubility, and how these effects might change the nature of the aerosol iron deposition to the area and uses a much larger data set, from aerosol samples gathered in the ETNA over the last 10 years.

Quantification of the atmospheric fluxes of iron, nitrogen and phosphate to the ETNA

– Chapter 5 quantifies the aerosol and rainfall deposition to the ETNA using a novel approach, which uses air mass back trajectories to take into account where the aerosol in each sample has come from and whether there is any seasonal cycle to the patterns of atmospheric deposition for the area. These flux estimates are used to consider the wider implications of the atmospheric deposition for the area.

Chapter 2

Methods

2.1 Sample Collection

This chapter describes the methods used to quantify the atmospheric flux, and determine the chemical composition of the flux, to the ETNA.

This section details how measurements from three different cruises were collected; section 2.2 then outlines how samples were analysed and processed; and section 2.4 goes on to discuss how the resulting data were then used to calculate the atmospheric concentration of each chemical species and its corresponding flux to the ocean.

2.1.1 Sampling Location

Samples were collected on three different scientific research cruises, all within the Eastern Tropical North Atlantic region. Figure 2.1 shows each cruise track, along with the start point for each aerosol sample taken.

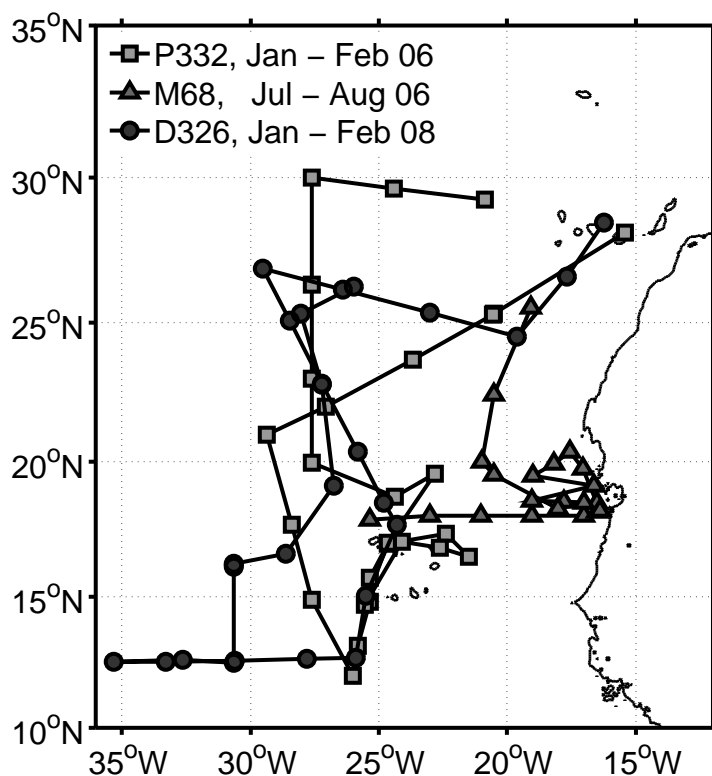


Figure 2.1: *Cruise tracks for three different cruises between 2006 and 2008 with the start locations of each sample collected shown*

Aerosol samples were collected using a high volume aerosol sampler with a cascade impactor, as described in section 2.1.3, so were size segregated, except for a few major-ion samples collected during D326 that were collected in bulk sampling mode. In order to

minimise trace metal contamination on the filters, those used for the trace metal (TM) analysis on P332 and M68 were acid washed using trace metal analysis grade (aristar) HCl. Those used for D326 were HCl/HNO₃ washed (c.f. section 2.1.3.4). Table 2.1 details the cruise dates; the start and end ports; and the sampling methods employed.

Cruise	Dates	From / To	Sampling Details
P332	Jan-Feb 06	Las Palmas, Gran Canaria	1 x hivol (TM/MI) 2 x Rain Funnels (TM+MI)
M68	Jul-Aug 06	Mindelo, Cape Verde to Tenerife	1 x hivol (TM/MI)
D326	Jan-Feb 08	Tenerife	2 x hivol (TM+MI) 2 x Rain Funnels (TM+MI)

Table 2.1: *Details of the three cruises: TM/MI indicates filters were prepared for Trace Metal and Major Ion analysis, TM+MI indicates that trace metal and major ion samples were collected separately*

2.1.2 Wet Deposition

Equipment was set up on all three cruises to collect wet deposition (rainfall). This involves attaching a holder to a railing on the ship, preferably close to where the high volume aerosol sampler is located (section 2.1.3.3). When it is raining a 60cm diameter low density polyethylene (LDPE) rain funnel attached to a poly-tetrafluoroethylene (PTFE) screw-top sampling bottle is secured to the holder (figure 2.2).



Figure 2.2: *Rain collecting equipment*

It is important that the equipment is kept covered until it is raining, otherwise samples will be contaminated with dry aerosol that has deposited on the funnel.

Samples collected for trace metal analysis are easily contaminated and care must be taken

to minimise this and reduce blank concentrations to an acceptable level (*Jickells and Spokes, 2001*). As metals tend to adsorb to the surface of the rain funnel and collecting bottles (*Witt, 2003*), the equipment is acid washed before each cruise, as summarized in figure 2.3. This desorbs metals from the PTFE/LDPE surfaces that may otherwise contaminate samples. In addition, prior to use, TM sampling bottles are stored filled with a 0.1 % solution of trace metal analysis grade HNO_3 , which has the dual purpose of preventing any metals adsorbing to the inside surfaces during storage and it can be used to rinse the rain funnel just before sampling, to ensure that it is as clean as possible.

Unfortunately acid washing can also leave a residue of NO_3^- , so a second set of equipment is required for major ion sampling. The rain funnel and sample bottles are washed in Decon and milli-q (as detailed in figure 2.3) avoiding the use of acid. MQ sample bottles are stored prior to use filled with milli-q, for the same reasons as for the TM samples.

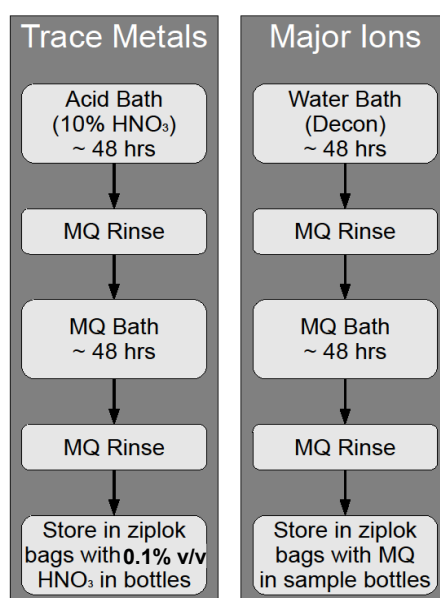


Figure 2.3: *Washing procedures for rain sampling equipment in preparation for sampling*

Rainfall blanks were taken periodically by setting up the equipment, rinsing the contents of another sample bottle into the funnel and storing it at -20°C for analysis with any samples collected.

Once a sample was collected it was stored at -20°C to be taken back to the laboratory for analysis. Samples can be stored this way for several months without appreciably deteriorating (*Baker et al., 2007*). Rain samples have been stored until enough samples were accrued to make analysis cost effective. Rain water samples collected for trace metal analysis were acidified using 0.1 % trace metal analysis grade HNO_3 prior to analysis, although this step is not necessary for the analysis of samples collected for major ions and phosphate analysis. The analyses were carried out in the same manner as for the extracted dry aerosol sample extracts (see section 2.2).

Unfortunately the tropical North Atlantic is an area of particularly low precipitation, and although there were occasional squally showers during the cruises they were either too light to collect any appreciable amount in the sample bottles, or seemed to avoid the ship altogether. Out of all three cruises only two usable rain samples were collected. As a result the rain samples from D326 and P332 have not been included in the discussion in chapter 3 as there is not enough detail in two data points for any meaningful discussion, however, the samples were considered as part of a whole data set for the region in chapter 5.

2.1.3 Aerosol deposition

Aerosol samples was collected on filters using high volume Graseby Anderson-type aerosol samplers (hivols) of the type pictured in figure 2.4. These act in a manner similar to a vacuum cleaner: air is sucked by a motor through a filter or set of filters. Aerosol suspended in the air is deposited onto these filter(s).

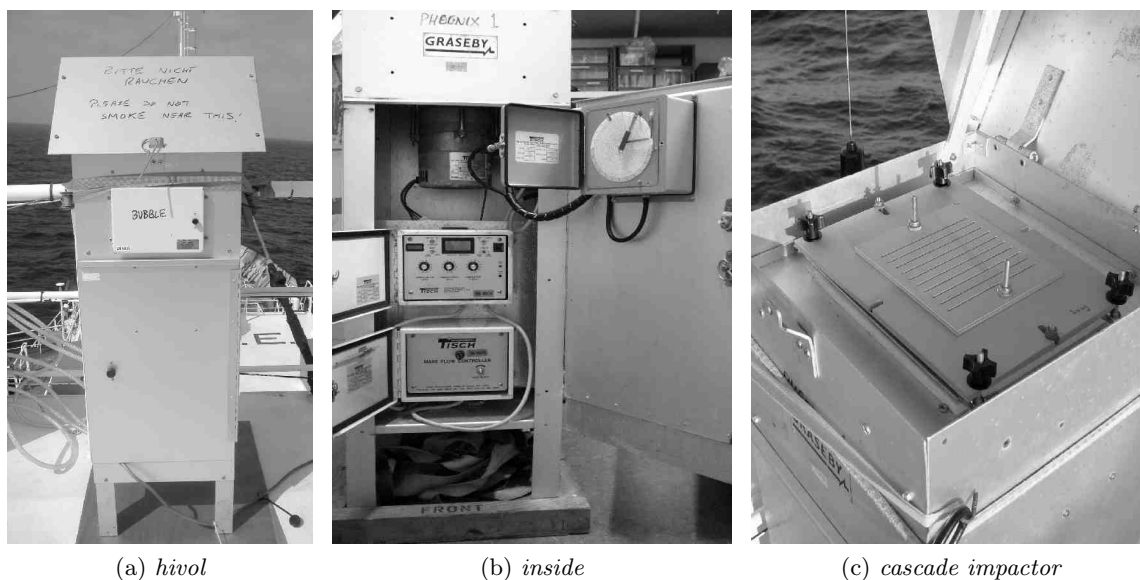


Figure 2.4: (a) High volume aerosol sampler (b) inside: the motor; power control unit; and mass flow control (MFC) unit. The continuous flow recorder is on the door (c) with cascade impactor. N.B. the hivol in (b) has the MFC unit inside whereas it is located just above the door in (a)

Samples were collected using the guidelines set out in section 2.1.3.3 and could be collected either as bulk or size segregated samples (see section 2.1.3.2) using a cascade impactor (figure 2.4c).

After collection samples were stored at -20°C to prevent samples deteriorating (Baker *et al.*, 2006c) and taken back to the laboratory for analysis in order to determine the amount and nature of material captured on them. Several different chemical analyses were carried out; each different analysis required the filters to be prepared in a different

way before sampling (as discussed in section 2.1.3.4) and the material on the samples then had to be extracted differently afterwards (section 2.1.3.5).

Once extracted using the correct method, samples were analysed for trace metals (iron, aluminium, manganese and vanadium) using Inductively Coupled Plasma Optical Emission Spectroscopy (ICP-OES); major ions - i.e. sodium, chloride, magnesium, potassium, calcium, ammonium, nitrate and sulphate - were analysed using dual channel ion chromatography; and phosphate levels were determined using a spectrophotometric method (see section 2.2 for a complete description).

In order to calculate the atmospheric concentration and flux of aerosol from each filter, not only does one need to know the amount of material captured upon it, but one also needs to know how much air was processed through it, i.e. the volume of air that was sampled. As the length of sampling time can be calculated from the sample start and end times, which can be corroborated by the start and end reading given by the counter (figure 2.4b), it is then possible to calculate the volume of air sampled if the flow rate of air through the filter is also known.

This rate is set by the user (see section 2.1.3.1) to $1\text{m}^3\text{min}^{-1} \pm 5\%$ although several factors can alter it including heavy filter loadings, changes in atmospheric pressure and temperature and wind speed.

Deviations from the set flow rate can be quantified using the plenum pressure (the pressure differential across the port at the exit of the motor housing) measured in CFM (cubic feet per minute) and recorded by the continuous flow recorder (figure 2.4b). Calibration of the hivol means that the plenum pressure can be related to the flow rate of the air through the filters in $\text{m}^3\text{min}^{-1}$ (as discussed in section 2.1.3.1).

2.1.3.1 Calibration

Calibrations are done using the calibration plate and slack tube manometer pictured in figure 2.5c. Briefly, the calibration plate consists of a base plate with a cylinder attached. The cylinder has holes at the bottom and top. The holes at the bottom have a variable aperture and can be opened and shut using the knob at the top of the cylinder, thus varying the flow rate through the hivol sampler. As the calibration plate itself is calibrated by the manufacturer, the difference between atmospheric pressure and the pressure in the calibration cylinder which is measured using the slack tube manometer, corresponds to an exact flow rate (as discussed below).

The aerosol collectors used are mass flow controlled (MFC), which means they have a sensor located in the throat of the collector (the narrowest part between the filters and the motor) that detects changes in the flow past it and adjusts the motor speed accordingly

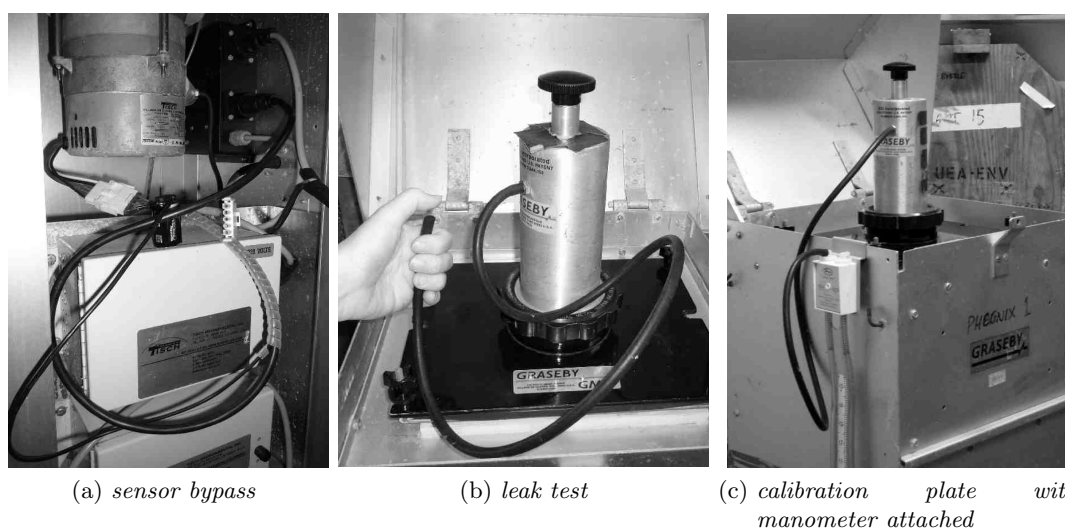


Figure 2.5: Calibration. (a) disconnection of the sensor with a 9V battery, (b) leak test, (c) manometer connected, calibration is done by turning the knob on top

so that the flow rate is kept to within 5% of the set flow rate.

Before calibration can take place this sensor must be disabled, so it cannot interfere with the calibration. In older models this is done by adjusting the mass flow control potentiometer (figure 2.4b) until the motor is running at full speed and its pitch no longer changes. In newer models the sensor is simply disconnected and replaced with a 9V battery as shown in figure 2.5a, which again causes the motor to run at full speed.

Once the calibration plate is secured in place a leak test should be performed. This is done by blocking the holes at the top of the calibrator with tape and placing a thumb over the connecting tube for a few seconds as shown in figure 2.5b. The pitch of the motor should increase and any leaks should be audible as air is sucked through and can usually be eliminated by tightening the wingnuts fixing the plate to the sampler or adjusting the foam seal.

After the leak test is finished the tape should be taken off the holes at the top of the calibrator and the connecting tubing can be connected to the slack tube manometer (figure 2.5c): it is expedient to check that both the manometer inlets are properly open and that there is adequate fluid inside before it is connected - the fluid levels should be level before connection and higher on one side after, reflecting the pressure differential caused by the motor sucking air through the calibrator plate.

The flow rate is related to the pressure difference (ΔH , in inches H_2O) measured by the slack tube manometer at a given atmospheric temperature (T_a , in K) and atmospheric pressure (p_a , in Torr) by an equation 2.1, where b and m are calibration constants specific to the individual calibration plate, determined by the manufacturer.

$$FlowRate = \frac{1}{m} \sqrt{\Delta H \frac{T_a}{p_a}} - b \quad (2.1)$$

The plenum pressure (P, in CFM) can be adjusted for atmospheric temperature and pressure using equation 2.2.

$$P_{T,p} = P \sqrt{\frac{T_a}{p_a}} \quad (2.2)$$

As the flow rate varies linearly with the corrected plenum pressure ($P_{T,p}$) calibration is then a matter of recording P for several different ΔH and then performing a linear regression on flow rate vs $P_{T,p}$.

The coefficients produced should be used to find the set-point plenum pressure at which the flow rate is equal to $1\text{m}^3\text{min}^{-1}$.

The calibration plate should be removed and replaced with an ordinary filter holder or cascade impactor and the MFC sensor reconnected. The flow should be adjusted using the mass flow controller (figure 2.4b) so that the set-point plenum pressure is reached. The flow rate is now set to $1\text{m}^3\text{min}^{-1}$.

As mentioned before, the plenum pressure is continuously measured by the continuous chart recorder, using a new chart for each sample, and any deviations from the set point are recorded and can be converted to flow rate using the calibration above. In general, chart records show that the plenum pressure fluctuates around the set point and deviations tend to be small (within 1–2 % of the set flow rate, with larger deviations if the wind is gusting), however, deviations of greater than 5 % of the set flow rate indicate problems with the sampling equipment, most likely resulting from the neoprene seal between the sample holder and the hivol sampler being incorrectly aligned.

2.1.3.2 Size Segregation

The aerosol samples are generally collected using a cascade impactor (figure 2.4c) to size segregate the samples into coarse and fine modes by aerodynamic diameter. Although technically the size distributions for the coarse and fine modes do overlap slightly, in terms of mass concentration this crossover is very small.

The cascade impactor works by separating suspended particles in the air by momentum (figure 2.6). The air is pulled through the parallel slots on the topmost stage and then accelerates as it is forced through the narrower slots in the stage below, which are offset from the slots in the top stage. A slotted filter paper is positioned in alignment on top of

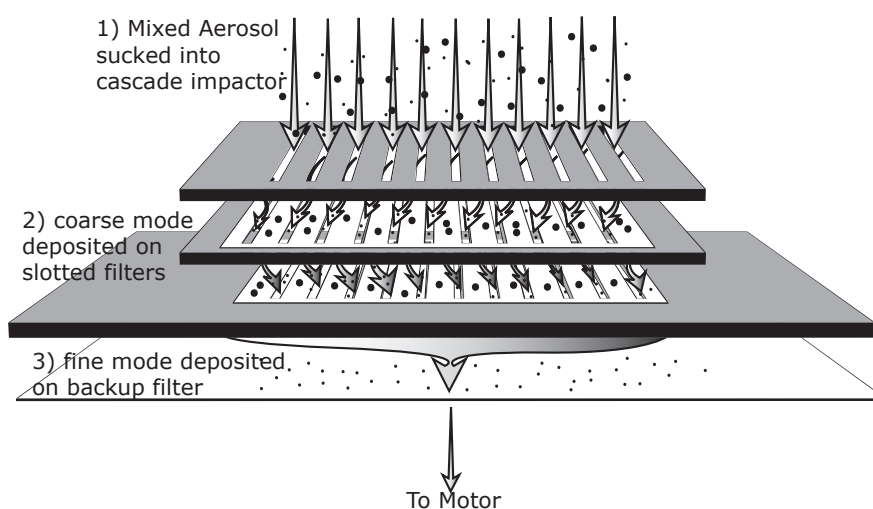


Figure 2.6: *Diagram showing how the cascade impactor works*

this lower stage so that the larger, heavier particles suspended in the air, which have too much inertia to be accelerated round, are deposited on the filter paper. In the same way the airflow accelerates past the (narrower still) slots in the next stages and the baseplate, leaving progressively smaller particles deposited on the filter paper aligned on top of them (figure 2.6 only depicts two stages being used for simplicity). Lastly the air flows through the backup filter, where the remaining, smaller, particles are deposited.

Only stages three and four of the six stage cascade impactor were used, and as the hivol was calibrated to a flow of $1\text{m}^3\text{min}^{-1}$, this gives slotted filter/backup filter particle diameter cut off at $1\mu\text{m}$, i.e. coarse mode particles should be deposited on the slotted filters and the fine mode particles on the backup filter. The cascade impactor has been calibrated by the manufacturer and particle sizes measured for each plate at varying flow rates, figure A.1 on page 142 shows these calibrations, as plotted by *Yeatman* (2000).

As the cascade impactor uses momentum to sort the particles, the effectiveness of the size segregation does depend on the flow rate, i.e. if the flow rate deviates from the set point of $1\text{m}^3\text{min}^{-1}$, the size distribution of particles deposited at each stage will deviate slightly and the slotted filter/ backup filter cut off will deviate from $1\mu\text{m}$. Hence size segregation depends on the hivol being calibrated properly and running smoothly, i.e. with no sudden changes in flow rate. This can be checked by looking at the continuous flow recorder chart.

2.1.3.3 Sampling Protocol

Finding the optimal place to position aerosol collectors on a research ship is difficult: it should be positioned to receive clean air from the front of the ship; away from the smoke of the ship's stack; unlikely to be wetted by waves washing over the bow; and easily accessible (even in bad weather). On each of the cruises the best position was found to be on the wheelhouse roof. Once fixed in place the hivol(s) were calibrated, and then a series of three blanks would be taken (see table 2.2). The purpose of these blanks is to allow correction for any contamination caused by filter papers or the sampling process. The calibration and blanks were also repeated at the end of each cruise.

Blank	Description	Duration	Testing For
Cassette	cassette (cascade impactor) loaded only	24h	background due to cassette loading process (including laminar flow hood)
Motor	hivol fitted with loaded cassette and turned on	10min	background due to hivol motor
Exposure	hivol fitted with cassette, but NOT turned on	24h	passive deposition

Table 2.2: *Blanks used to ensure quality control of samples*

After calibration and taking a set of blanks, samples were generally run for 24 hour periods, except in periods of very low anticipated aerosol concentration in cruise P332 and in periods of high anticipated aerosol concentration in cruises P332 and D326 where sampling periods were changed to 48 hours and 12 hours respectively.

Hivol samplers were turned off manually whenever the wind was coming from behind the ship and blowing smoke from the ship's stack towards them. They were also turned off whenever any other activities on board the ship were likely to contaminate aerosol samples e.g. barbeques or testing of safety flares. Smoking was banned anywhere forward of the wheelhouse roof.

The cassette was loaded and unloaded in an ISO14644 class 6 (US class 100) laminar flow hood, and carried between the flow hood and the hivol in a large, clean plastic bag. Used filters were placed in separate plastic Ziploc bags, and placed in an additional second Ziploc bag for each sample. These were then stored at -20°C until they could be sent back to the laboratory for analysis by courier.

2.1.3.4 Filter Preparation

Whatman-41 cellulose filters, which are cost-effective and used in the collection of a wide range of aerosols under hivol conditions (for example *Prospero*, 1989; *Savoie et al.*, 2002;

Baker et al., 2006c,a,b), were used in the analysis of trace metals and major ions. It has been shown that under high volume sampling conditions the efficiency of these filters over the radii range 0.01-2 μ m is greater than 80% (*Watts et al.*, 1987).

Although Whatman-41 filters are known to collect gas phase nitric acid (*Baker et al.*, 2003) and perhaps ammonium (*Pszenny et al.*, 1993), the concentrations for both these gasses in the marine boundary layer are low and in the case of nitric acid, it is suppressed by the presence of seasalt aerosol (*Pryor and Sørensen*, 2002) so that the effect of these artefacts is unlikely to be large.

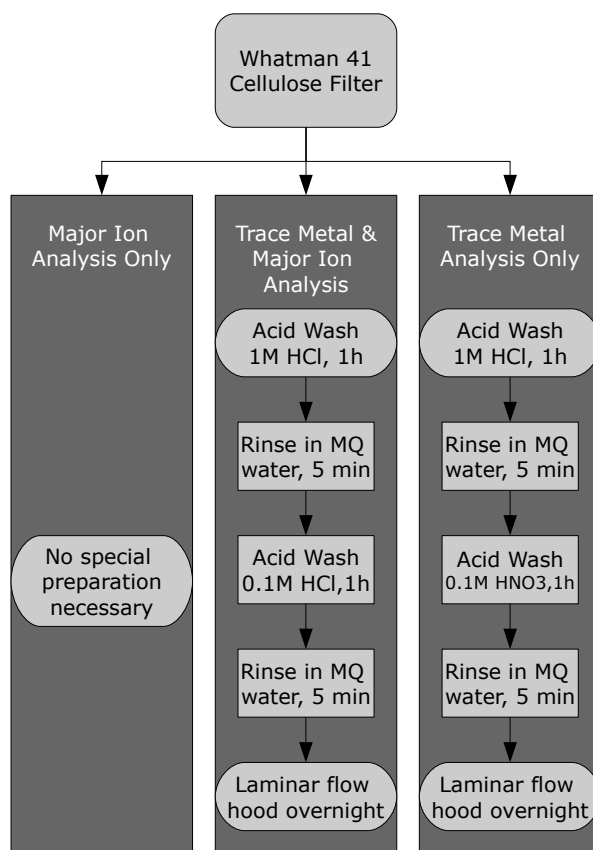


Figure 2.7: *Protocols for the preparation of Whatman-41 filters prior to sampling*

Each set of analyses (trace metals, major ions, phosphate) required a slightly different filter preparation. The exact processes used are summarized in figure 2.7

For trace metal analysis all the filters used needed to be washed in trace metal analysis grade (aristar) acid and then dried overnight in a clean, dust and trace metal free environment.

Major ion analysis includes the analysis of nitrate and ammonium and the presence of acid on the filter, particularly nitric acid (*Baker et al., 2006c*), can skew the concentrations measured. For this reason, when trace metal and major ion concentrations were to be measured from the same filter hydrochloric acid was used in place of nitric acid and care was taken to ensure filters were thoroughly washed in ultra-pure water afterwards. However, aristar grade acids are expensive and it is not necessary to acid wash filters for major ion analysis, so the acid washing step was omitted for samples which were collected only major ion analysis.

It should be noted that phosphate analysis neither requires that filters are acid washed, nor does acid washing introduce any artefacts into the analysis. Therefore samples for phosphate analysis were extracted from filters collected for either trace metal or major ion analysis, depending on the availability of samples.

2.1.3.5 Extraction

In general only a quarter of a filter is needed for each analysis (or an eighth in the case of trace metal analysis by neutron activation). This means that provided the filters were prepared correctly, several different analyses can be performed on just one sample. However, each analysis requires the filter subsample to be treated in a different manner, as summarized in figure 2.8.

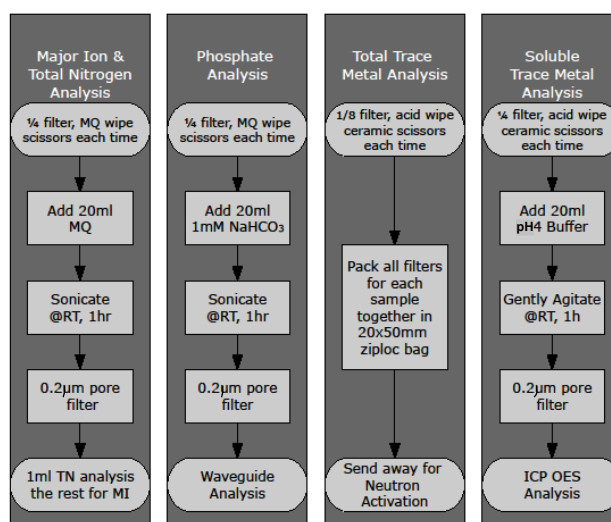


Figure 2.8: *Methods used for the extraction of the chemical constituents from aerosol samples*

In order to ensure an even distribution of aerosol in each subsample, filters are sliced across the length of the filter, i.e. the cuts should go across slots in the slotted filter, rather than

against them. Filters should be cut in an aerosol free environment to avoid contamination: in the case of trace metal analysis this requires the use of a trace metal clean room (in this case, ISO14644 class 6 clean room and an ISO14644 class 2 laminar flow hood) and the use of clean, ceramic scissors, which should be wiped with a 0.1% nitric acid solution between each filter.

After each subsample is taken it is then cut into small pieces of $\approx 1\text{cm}^2$ and placed into a 50cm centrifuge tube, or in the case of analysis by neutron activation a 20x40mm Ziploc bag.

Samples for soluble trace metal, major ion and phosphate analysis were leached for an hour in 25ml 1.1M ammonium acetate (pH 4.7) buffer (*Sarthou et al.*, 2003), ultra pure water (*Spokes et al.*, 2000) and 1M sodium bicarbonate (*Baker et al.*, 2006c) respectively (see figure 2.8) and then filtered using $0.2\mu\text{m}$ cartridge filters into 15ml centrifuge tubes. It should be noted that centrifuge tubes used for trace metal samples were first cleaned in a 10% HNO_3 bath overnight and then rinsed in ultra-pure water. The extracts were then either analysed straight away (c.f. section 2.2) or frozen at -20°C for later analysis.

2.2 Sample Analysis

All the analysis methods used here are well established for the analysis of aerosol, and so are only briefly described here.

In all cases the analysis would follow the same basic protocol as outlined in figure 2.9. In each case several different runs would be made with a separate run for three different categories: coarse mode, fine mode and blanks. This made it easier to anticipate the likely concentrations so that appropriate calibrations could be made. A run would consist of a calibration (6 points including a blank) 10-15 samples (depending on the accuracy of the instrument) and then another full calibration, repeating until all samples were finished and ending on a calibration. This ensured any instrumental drift was picked up and taken into account. Immediately after analysis samples were checked to see if they were within the range of the calibration. Samples above the calibration range were diluted and re-analysed, and if possible samples below the calibration range were re-analysed with less concentrated standards.

2.2.1 Ion Chromatography

Ion chromatography (IC) is an efficient method for separating and determining concentrations of ions based upon ion-exchange resins (*Kebbekus and Mitra*, 1997). The resin on the column can be damaged if acidified samples are introduced - therefore IC is unsuitable for

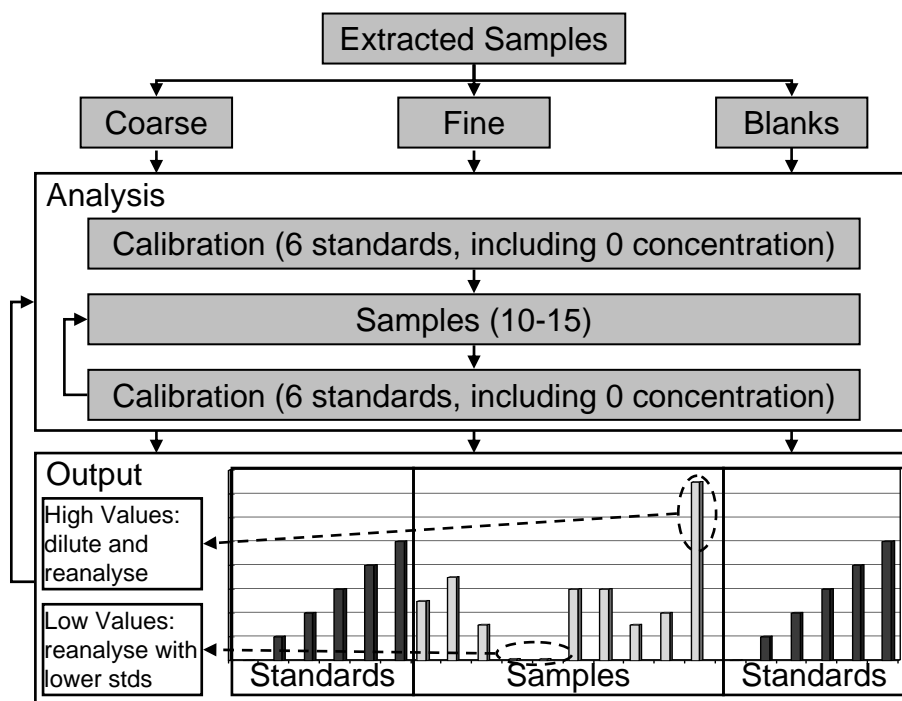


Figure 2.9: General protocol used for the analysis of all samples, where 0 concentration refers to a 'blank' standard

trace metal analysis, although it is perfectly suitable for the analysis of major ions.

IC is widely used to analyse aerosol major ions (see, for example, *Savoie and Prospero, 1982; Spokes et al., 2000*) because used properly it is a precise, relatively inexpensive, multi-element technique. The ion chromatograph used here (model Dionex DX600) has the added advantage that it is a dual channel instrument, so both cations and anions can be analysed from a single injection.

The Dionex DX600 was used to take $1000\mu\text{l}$ from each sample with the AS18 column, eluted with potassium hydroxide (KOH), for the analysis of cations (Na^+ , Mg^{2+} , K^+ , Ca^{2+} , NH_4^+) on a $25\mu\text{l}$ injection loop, and the CS12 column, eluted with methanesulfonic acid (MSA), for the analysis of anions (Cl^- , NO_3^- , SO_4^{2-}) also on a $25\mu\text{l}$ injection loop. A conductivity sensor was used for detection (*Wright, 2009*).

Care must be taken that sample concentrations of an ion do not exceed 10 mg l^{-1} , otherwise the column(s) become overloaded and the resin on the column can become damaged. For this reason samples with an expected high concentration, i.e. all coarse mode samples, were diluted 1:3 with ultrapure water before analysis. Samples were divided into 3 different analysis sets: coarse, fine and blanks, for which three different sets of standards were made up (see table A.1 on page 143).

2.2.2 Total Soluble Nitrogen

The total nitrogen was measured by high temperature catalytic combustion (HTCC) using a Thermalox TOC/TN analyser coupled to a chemiluminescence detector (CLD) as described by *Suratman et al.* (2008). All nitrogen species are oxidised at high temperature ($680 \pm 5^\circ\text{C}$) using a Pt/Al₂O₃ catalyst to NO_x gases, which are then detected by the CLD.

Although the analysis of total soluble nitrogen (TSN), and subsequent calculation of soluble organic nitrogen (SON), has previously been done using persulphate oxidation (*Spokes et al.*, 2000) and/or UV oxidation (*Cape et al.*, 2001) a recent review by *Worsfold et al.* (2008) has shown that there is no significant difference between these approaches and HTCC. Analysis by HTCC was chosen here as it is easier, faster and requires less sample handling (*Rogora et al.*, 2006). Additionally this method has been shown to efficiently combust all species of nitrogen, so the use of additional organic standards, like guanine, has been shown to be unnecessary (*Suratman*, 2007). The inorganic standard used was potassium nitrate (KNO₃), in line with recommendations (*Hopkinson et al.*, 1993) and the concentrations of standards used are listed in table A.2 on page 144.

In order to avoid problems with the detection of any N₂ that may be produced as part of the oxidation process O₂ was used as a carrier gas. A sample injection volume of 30 μl was generally used, although it was found that an injection volume of 15 μl made no difference to the result.

2.2.3 Soluble Trace Metal analysis using ICP OES

Inductively coupled plasma optical emission spectrometry (ICP OES) makes use of a high temperature ($\approx 7000\text{K}$) argon plasma to efficiently atomize a sample and promote its constituent atoms to an electronically excited state. The optical emissions produced can be simultaneously detected, making ICP OES a fast, efficient multi-element technique (*Kebbekus and Mitra*, 1997).

Due to the nature of the argon plasma, atoms are easily electronically excited and there is very little chemical interference by oxygen or other active species. This produces clean spectra with clear lines, low backgrounds and little interference and stable calibrations that are linear over wide concentration ranges. This makes ICP OES a multi-element technique which is well suited to the analysis of iron (Fe), aluminium (Al), zinc (Zn), vanadium (V) and manganese (Mn) (*Baker et al.*, 2006c; *Alastuey et al.*, 2005).

The instrument used here was a Varian-Vista Pro CCD simultaneous ICP OES, Sample injections of 3ml are nebulised into the argon carrier gas, with typically $\approx 10\%$ of this being taken up into the plasma. The CCD simultaneous detector was set up to measure

emissions from Al, Fe, Mn, and V.

Standards were made up from certified ICP standards, and the concentrations used are listed in table A.3 on page 144.

2.2.4 Molybdenum Blue Phosphate Analysis

The molybdenum blue method from *Parsons et al.* (1984) (originally in *Murphy and Riley*, 1962) involves reaction of orthophosphate (PO_4^{3-}) with ammonium molybdate under acidic conditions form a complex, which is then reduced by ascorbic acid in the presence of antimony to give a blue complex. This complex has an absorption band which obeys the Beer-Lambert law over a good working range and can be determined at 660 – 880nm on a spectrophotometer.

The molybdenum blue method is widely used to analyse soluble reactive phosphate (SRP) primarily because it is a simple method and is easily adapted to automation for routine analysis of large numbers of samples (*Patey et al.*, 2008).

The method has a limit of detection of around $0.03\mu\text{M}$, which has, in the past meant that it is very difficult to measure the SRP content of aerosol. However, the limit of detection can be greatly reduced by the use of a liquid waveguide capillary cell (LWCC) with the spectrophotometer. The longer path length does attenuate the signal at wavelengths above 700nm, so the signal is measured at 690nm. The loss in sensitivity of the signal at this wavelength is more than compensated by the increase in signal created by using the waveguide. In addition the illumination from the light source is better at this frequency.

Samples were prepared by adding 3ml to 0.3ml of a mixed reagent. This is made by the combination of 100ml 25mM ammonium molybdate; 250ml 3M sulphuric acid; 100ml 300mM ascorbic acid; and 50ml 4mM potassium antimonyl-tartrate. This reagent is not stable and was mixed fresh each day. Samples were then left to develop for a few minutes for the phospho-molybdenum blue complex to form and then analysed within 2 hours.

Measurements were taken using a FO-6000 light source connected to a Tidas detector via a 50cm path length LWCC. The detector was set to single scan absorbance, integrated over 5s and the peak height measured. Samples were allowed to run through the waveguide for 4 minutes (using ≈ 2.5 ml sample); measured; then rinsed through with $\approx 10\text{ml}$ ultrapure water. Standards were prepared using dihydrogen phosphate (KH_2PO_4) and it was found that the method had an upper limit of detection of $0.8\mu\text{M}$ KH_2PO_4 . As each sample was introduced manually, only one set of standards was made (concentrations used are listed in table A.4 on page 145) and samples over this limit were diluted and re-analysed.

2.2.5 Total Trace Metal analysis using Neutron Activation

Although in the past total trace metal analysis has been carried out by the total digestion of whatman-41 filters by hydrofluoric acid (HF) and subsequent ICP-OES analysis, the use of HF in the laboratory has been strongly discouraged and alternative methods of analysis have been encouraged wherever possible.

Neutron activation analysis (NAA), is a technique whereby samples are bombarded with neutrons from a nuclear reactor. A proportion of the atoms within each sample will be converted to a radioactive isotope of the original element. These radioactive atoms subsequently emit gamma-rays, which have a characteristic frequency that can be detected. The exact amount of each element in a sample can then be calculated by comparing with standard solutions. Analysis has shown that relative error in NAA analysis is less than 1% for Mn and between 1–8% for Al and Fe (*Paiva et al.*, 1993).

Samples were prepared by carefully packing them in small (20mmx50mm) ziplok bags and sending them for analysis at the NAA facility at Ecole Polytechnique, Montreal, Quebec. Samples were bombarded at a neutron flux of $5 \times 10^{11} \text{ cm}^{-2} \text{ s}^{-1}$ and the radioactive decay of isotopes of Al, Fe and Mn were measured at 1779, 1099, and 847 keV respectively. The system was calibrated with standard solutions prepared from certified standards (Caledon Inc. USA and Alfa Aesar USA, Specpure Plasma Standards, 1000 ppm solutions certified to be accurate to 0.3%) *Chilian, Personal Communication*.

Most importantly the data from the NAA analysis of several samples were compared with data for the same samples from the total digestion of the whatman-41 filters and subsequent ICP-OES analysis (*Baker et al.*, 2006c). Correlations were found to be very strong, with correlation coefficients exceeding 0.997 *Baker, Personal Communication*.

2.3 Data Processing

After data collection and analysis, all data was treated in the same way, regardless of method used. Matlab™ was used to process all the data, so the routines written and used (.m files) are all attached in appendix E.

Raw data from each of the chemical analyses was calibrated by a linear least squares fit (*Miller and Miller*, 2005) using a graphical user interface (GUI) in Matlab called cal.m, rather than using any of the inbuilt functions of the analysis instruments themselves. This gives a better control over calibrations, and a better feel for when the range of a calibration is too high or too low for the range of measurements.

As calibrations were performed every 10-15 samples, concentrations were found from each

calibration (using Matlab script `conc.m`) and then linearly interpolated to adjust values for any instrumental drift (using Matlab script `driftcorrection.m`). The limit of detection (lim) is worked out from the intercept and slope of each of the calibration curves using equation 2.3. Any concentrations below the limit of detection were set to a value of $0.75 * lim$ and flagged as 'd' (Helsel and Hirsch, 2005). If a concentration fell below the limit of detection for one calibration but not for another the value was kept but it was flagged as 'c' for no drift correction.

The standard error for each sample was calculated using equation 2.4 (from Miller and Miller, 2005). The error was then propagated through all calculations. For concentrations below detection limit, the standard error was changed to 'NaN' (not a number) as there is no standard error for the detection limit (Helsel and Hirsch, 2005).

After the extract concentration was found, the amount of material on each filter was calculated using equation 2.5 using Matlab script `molar.m`.

$$lim = \frac{3 * S_{\frac{y}{x}} - intercept}{slope} \quad (2.3)$$

$$Std.Err. = \frac{s_{\frac{y}{x}}}{slope} * \sqrt{1 + \frac{1}{n} + \frac{(y - \bar{y})^2}{slope^2 * (\sum x^2)^2}} \quad (2.4)$$

$$Amount = Concentration * 4 * ExtractVolume \quad (2.5)$$

$$Atmospheric Concentration = \frac{Amount}{AirVolume} \quad (2.6)$$

Once in molar concentrations, filter and instrumental blanks were compared, averaged and subtracted (using Matlab script `dblanks.m`). In the case of a high-value blank with low-concentration samples, this may have meant that some values were now negative, so any values now found to be below the detection limit were again set to $0.75 * lim$ (detection limit) and flagged as 'b' for below blanks. Table 2.3 lists the typical (i.e. median) fine and coarse mode concentrations and interquartile ranges (IQR) for each aerosol component analysed, excluding total trace metals, along with median values for the filter blanks and the typical sample to blank ratio.

Data was then converted to atmospheric concentrations using equation 2.6 where air volume is the volume of air that passed through the sample during the sampling period.

At this stage bulk atmospheric concentration was calculated for size segregated samples by adding the concentrations for coarse and fine modes together.

The Matlab routines used for data processing `cal.m`; `conc.m`; `driftcorrection.m`; `dblanks.m`; and `atmconc.m` are in appendix E. All other Matlab scripts and data files that were used in this thesis are included in the DVD-ROM attached to the back page of the thesis.

Component	Fine Mode				Coarse Mode			
	Conc	IQR	Blank	B/M	Conc	IQR	Blank	B/M
Soluble Trace Metals								
Al	3.75	7.42	0.68	0.18	6.35	11.59	0.51	0.08
Fe	0.67	1.31	0.12	0.17	0.83	1.30	0.14	0.17
Mn	0.13	0.51	0.01	0.09	0.50	1.36	0.02	0.03
V	0.21	0.33	0.03	0.16	0.62	0.67	0.04	0.06
Total Soluble Nitrogen								
TSN	346.87	531.54	50.40	0.15	476.47	620.21	36.93	0.08
Major Ions								
Na	129.18	99.13	49.87	0.39	2024.55	1688.65	51.49	0.03
NH ₄	63.59	365.73	25.11	0.39	66.88	80.28	23.60	0.35
K	9.80	8.83	5.32	0.54	40.92	27.90	2.56	0.06
Mg	11.72	13.85	3.87	0.33	199.31	159.65	4.22	0.02
Ca	36.59	78.94	5.55	0.15	101.35	176.29	3.91	0.04
Cl	173.95	76.98	85.73	0.49	2149.87	1755.23	67.87	0.03
NO ₃	36.03	30.59	3.23	0.09	217.48	248.55	14.10	0.06
SO ₄	154.58	303.10	4.18	0.03	180.42	161.33	3.54	0.02
Soluble Reactive Phosphate								
SRP	0.26	0.52	0.06	0.23	0.34	0.61	0.05	0.16

Table 2.3: Typical extract sample and blank concentrations in $\mu\text{mol dm}^{-3}$ for all chemical components analysed. Values are median values and IQR is the interquartile range of the measurements

2.4 Conversion of aerosol atmospheric concentration to flux

To convert the atmospheric concentrations to flux equation 2.7 is used:

$$F_d = C_d * \nu_d \quad (2.7)$$

Where F_d is the dry aerosol flux in $\mu\text{mol m}^{-2} \text{d}^{-1}$, C_d is the atmospheric concentration of the aerosol in $\mu\text{mol m}^{-3}$ and ν_d is the deposition velocity in m d^{-1} . Although, in the past, constant ν_d have been used for coarse mode and fine mode aerosol (*Baker et al.*, 2006b; *Duce and Tindale*, 1991), deposition velocity depends on many variables, including wind speed and particle size (*Slinn and Slinn*, 1980; *Seinfeld and Pandis*, 2006)). The deposition velocities used here have been derived using the *Ganzeveld et al.* (1998) model, which modifies the *Hummelshøj et al.* (1992) model to include whitecapping, and is used in *Baker et al.* (2010). The variation of deposition velocity with wind speed for three different particle sizes are shown in figure 2.10.

One important limitation to the modelling of deposition velocity is that it is very difficult to measure the particle size distributions for different particle types, e.g. seasalt, mineral dust and anthropogenically produced particles. For this reason mass median diameters (MMD),

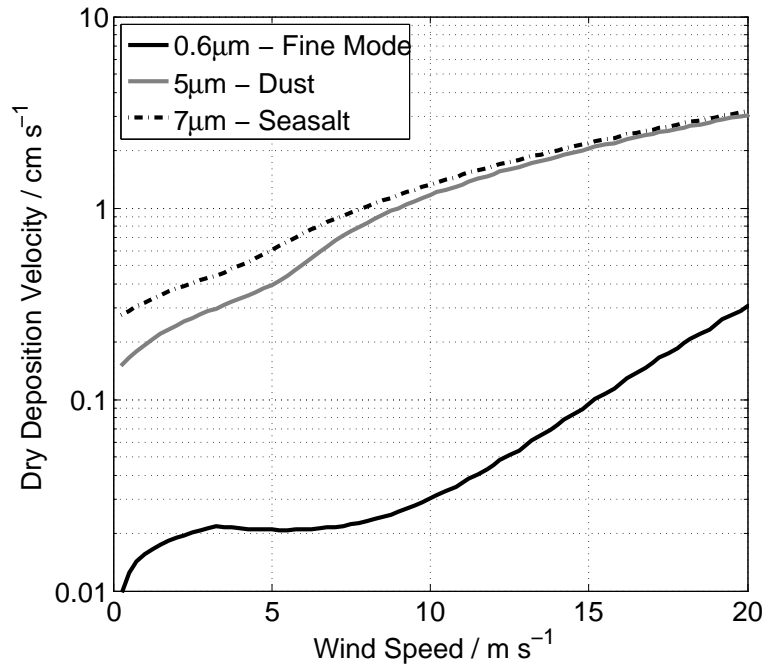


Figure 2.10: *Dry deposition velocity as a function of wind speed for fine particles, mineral dust and seasalt (mass median diameter 0.6, 5 and 7 μm respectively)*

i.e. the median particle diameter when sorting particles by mass, rather than number density, have been assumed from data and reported values (*Baker et al.*, 2010; *Arimoto and Duce*, 1986). The MMD used for mineral dust, seasalt and anthropogenically derived aerosols are listed in table 2.4, along with other values used elsewhere for comparison.

Aerosol type	MMD μm	Source
Values used here		
Seasalt	7 \pm 5	<i>Baker et al.</i> (2010)
Mineral dust	5 \pm 1.5	Calculated from size segregated data from cruise ANT18-1 (see table C.1) using the method in (<i>Arimoto and Duce</i> , 1986)
Fine mode	0.6 \pm 0.1	
Values used elsewhere		
Sea-salt	8.6 \pm 6.8	<i>Arimoto and Duce</i> (1986)
Mineral dust	2.0 \pm 5.2	
Pb (fine mode)	0.52 \pm 7.4	
Sea-salt	8.6 \pm 6.8	<i>Rädlein and Heumann</i> (1995)
Mineral dust	2.0 \pm 5.2	
Pb (fine mode)	0.52 \pm 7.4	
Coarse NO_3^-	7.6	Averages from <i>Keene et al.</i> (2009) as used in <i>Baker et al.</i> (2010)
Fine NO_3^-	0.6	
SO_4^{2-}	0.9	

Table 2.4: *Details of the mass-median diameters (MMD) used in calculating flux*

2.5 Air mass back trajectories and source region

Although the amount and composition of aerosol varies greatly from sample to sample, aerosol types can be characterised by the region from which the aerosol has come from, i.e. its source region, and the time it has been suspended in the air (*Baker et al.*, 2006b).

Air mass back trajectories are widely used in aerosol studies (*Buck et al.*, 2010; *Baker et al.*, 2006b; *Wagener et al.*, 2008) in order to have an idea of the source region of a sample. These use archived meteorological data to model the movement of a parcel of air to its arrival at a given location, i.e. you input a location and time and the back trajectory models where the air parcel has been previously.

For the initial classification of aerosol samples, air mass back trajectories from the NOAA HYSPLIT (HYbrid Single Particle Lagrangian Integrated Trajectory) model were used (*Draxler and Rolph*, 2003) and examples of the output from this model are shown in figure 2.11. There are many advantages of this model: it is available to everybody; the input interface is web based and very easy to use; and additionally it can give an idea of whether any precipitation may have occurred along the trajectory.

Five day back trajectories were requested for the mid-point date, time, longitude and latitude for each sample at 10m, 500m and 1000m above ground level. The mid-point values were chosen as these were thought to be the most representative of each sample and the three different heights were chosen to represent movement of air masses along the surface (10m) and also higher in the marine boundary layer (500m and 1000m), as samples may contain particles that were originally transported at these heights and which subsequently settled by gravitation, as is the case with Saharan dust transport during the summer months (*Stuut et al.*, 2005).

2.5 Air mass back trajectories and source region

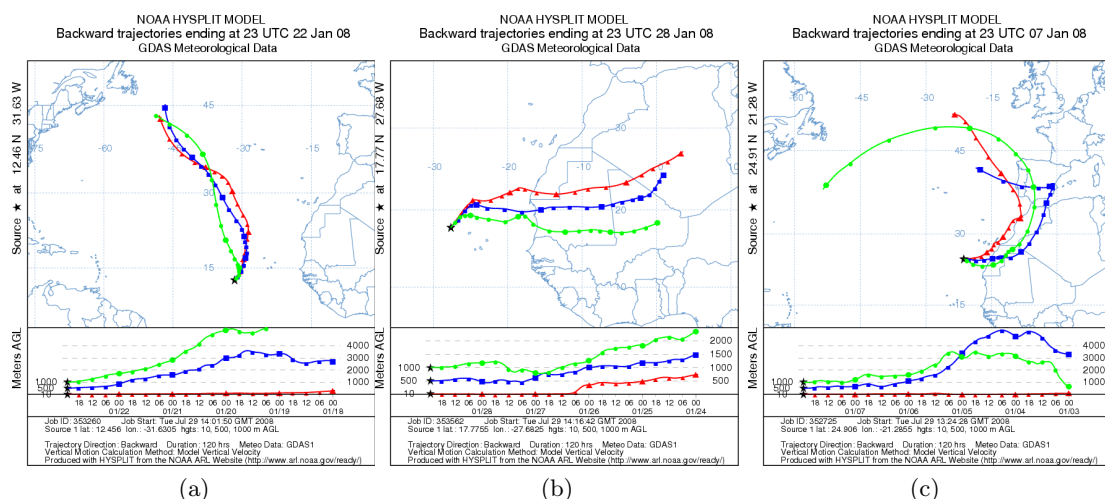


Figure 2.11: *Examples of HYPPLIT back trajectory plots (a) all three trajectories are from a remote North Atlantic origin (b) all three trajectories come from the Sahara (c) mixed air masses come down through Europe and then over the Sahara.*

When constructing the climatology (chapter 5), the British Atmospheric Data Centre (BADC) trajectory service was used because it is possible to request many back trajectories for the same location automatically. This database makes use of ECMWF data (ECMWF, 2006) and five day back trajectories were requested for each climatology point at 995, 950 and 900 hPa (roughly equivalent to 100m, 500m and 1000m above ground level in the ETNA region), for every 12 hours between 14th March 1999 and 14th March 2009. The choice of 995 hPa (100m) was made as it was found that trajectories lower than this would sometimes run into ground level and then stop before the endpoint of the 5 day backwards run requested (this also happens when using the HYSPLIT model), and although it is relatively easy to account for this on a sample-by-sample basis, it becomes very inconvenient with much larger numbers of trajectories. Given that samples which have similar air mass back trajectories, and therefore have the same source region, should have signature chemical properties it is possible to categorise each sample by source region, or air mass type. Figure 2.12 shows the eight air mass types used in this study (from Baker *et al.*, 2006c), with a brief description of each given in table 2.5. For example, an aerosol coming from the Sahara should be rich in mineral dust, with relatively high concentrations of iron and aluminium in the coarse mode, however a sample where the aerosol came mostly from the European continent should have a low content of mineral dust, but high amounts of nitrate and other species associated with pollution.

For the purposes of this thesis, i.e. approximating air mass source region, the choice of either HYSPLIT or BADC trajectory model appears to make little difference. For example, the air mass assignments for samples collected on cruise D326 remained the same whether the trajectories were produced from either model.

Code	Identifier	Region	Description
0	NAM	North America	polluted aerosol, mostly fine mode associated with gas to particle conversions
1	NRM	Remote North Atlantic	sea salt and low concentrations of well-mixed fine mode aerosol
2	EUR	Europe	polluted aerosol, mostly fine mode associated with gas to particle conversions
3	SAH	Sahara & Sahel	coarse mode mineral dust with some anthropogenic aerosol
4	SAF	Southern Africa	some mineral dust and other aerosols associated with industry and agriculture
5	SAB	Southern Africa (Biomass Burning Season)	as SAF, but with biomass burning aerosol from southern africa
6	SRM	Remote South Atlantic	sea salt and <i>very</i> low concentrations of well-mixed fine mode aerosol

Table 2.5: *Typical characteristics of each source region defined in this study*

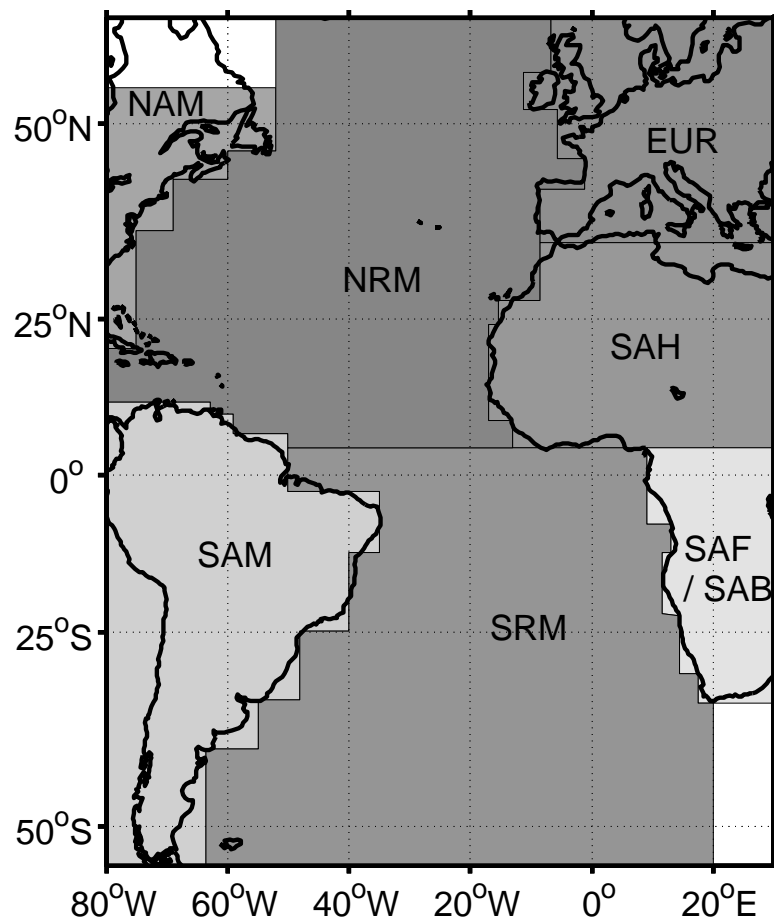


Figure 2.12: Source regions for the Tropical North Atlantic (identifiers are defined in table 2.5)

Chapter 3

The aerosol concentration of iron and other nutrients on D326, M68 and P332

3.1 Background

The purpose of this chapter is to use the data from the analyses of samples as discussed in chapter 2 to describe the nature of the aerosol collected on cruises D326, M68, and P332.

The three cruises (D326, M68 and P332) all took place between January 2006 and February 2008, and were based in the ETNA region. Details of the sampling locations; cruise tracks; starting and finishing ports for each cruise can be found in section 2.1.1. Aerosol samples from several cruises going through the region on long Meridional transects (*Baker et al.*, 2006c) show increased iron and aluminium on the filters, consistent with dust events, but there was little information about the variability of the aerosol concentration within the region.

Because these three cruises concentrated specifically in the ETNA, we can consider the aerosols transported to the region and how they might vary from sample to sample.

The HYSPLIT back trajectories calculated for each aerosol sample have been analysed, and the resulting trajectories are shown in appendix B, along with a table showing the assignment of air mass type for each sample. The assignment of air mass type using air mass back trajectories is described in detail in the climatology chapter, section 5.4.1 on page 95 (see also section 2.5 on page 32). For consistency, the samples collected on D326, M68 and P332 have been assigned air mass types in the same way.

In order to put the atmospheric concentrations reported in this chapter into context, table 3.1 summarises the average atmospheric concentrations for iron, nitrogen and phosphate.

Chemical	Region	Airmass Type	Values (nmol m^{-3})	Source / Comment
Iron	ETNA	SAH	0.1–0.6	<i>Baker et al.</i> (2006b)
	ETNA	NRM	0.0–0.1	
Total Nitrogen	ETNA	SAH	0–140	
	ETNA	NRM	10–40	
Phosphate	ETNA	SAH	0.01–0.06	
	ETNA	NRM	0.01–0.04	

Table 3.1: *Average atmospheric concentrations of aerosol components reported elsewhere for comparison to the results reported here*

By far the largest contribution to aerosol mass in the MBL is seasalt (*Raes et al.*, 2000). Seasalt aerosol particles are formed primarily during whitecapping, of which some are subsequently entrained upwards by turbulent eddies (*Lewis and Schwartz*, 2004). The particle number concentration therefore increases nonlinearly with increasing wind speed (*Mahowald et al.*, 2006). In order to examine the deposition of iron and other nutrients from terrestrial regions to the open ocean, the seasalt concentration of each aerosol species should first be taken into account, as discussed in section 3.2.

The most important source region for aerosol containing iron and nutrients to the ETNA is the directly adjacent Saharan Desert. More information about Saharan dust is given in the chapter 1, but here we can look in detail at how much of the dust is composed of iron, and start looking at how bioavailable this iron may be. Considering the other species in addition to the iron: aluminium, non sea-salt calcium, phosphate, manganese all give clues as to what kind of minerals the iron might be contained in therefore what kind of bonding environment it might be present as. Other factors that may affect the nature of the aerosol iron in the aerosol include how well mixed the Saharan dust is with other aerosols; and whether these other aerosols will react with the iron to make it more labile. One example of this is acid processing: *Spokes and Jickells (1995)* show how atmospheric acid processing could affect the solubility of iron in Saharan dust. Two species that are responsible for the acid processing are sulphuric acid and nitric acid, the concentrations of which are reflected in their salts: sulphate and nitrate. Hence the inclusion of concentration data of these and other major ion species in section 3.4.

Other aerosols which contain very soluble forms of iron might also be present - iron aerosol is also released from heavy industry and biomass burning (*Luo et al., 2005*): if this anthropogenically produced aerosol is also transported to the ETNA, it may affect the supply of bioavailable iron in addition to that associated with Saharan Dust.

3.2 Seasalt Aerosol

Seasalt is composed of several major ions in addition to Na^+ and Cl^- : those of interest to this thesis are listed in table 3.2. Because it is assumed that these ions are conservative in seawater, i.e. they remain in the same ratio relative to each other, regardless of salinity or absolute concentration and these ratios are constant throughout the world ocean (*Libes, 1992*), if we can show that the aerosol concentration of one of these ions is solely due to seasalt, we can therefore derive the seasalt contribution and hence the non-seasalt contribution to aerosol concentrations of all the other ions in table 3.2 from their seasalt ratios.

Major Ion		Concentration g / kg	Sodium Ratio	
			by mass	by molar amount
Chloride	Cl^-	19.344	1.796	1.164
Sodium	Na^+	10.733	–	–
Sulphate	SO_4^{2-}	2.712	0.252	0.060
Magnesium	Mg^{2+}	1.294	0.120	0.114
Calcium	Ca^{2+}	0.412	0.038	0.022
Potassium	K^+	0.399	0.037	0.022

Table 3.2: Major ions of seawater: concentrations, in g/kg of seawater with salinity 35, are from *Libes (1992)*

In selecting a particular major ion as a tracer for seasalt aerosol *Keene et al.* (1986) point out that aside from analytical uncertainties and those arising from assuming that major ions are conservative, errors in seasalt concentrations arise from the reference species not coming from a purely marine source and fractionation occurring during or after the production of the seasalt aerosol. They emphasise the importance of evaluating individual data sets for the most appropriate ion, although they suggest the use of either Mg^{2+} or Na^+ as the reference species.

The possibility of using Mg^{2+} as a reference species for seasalt aerosol was considered as it is present in seawater at a lower concentration than sodium, meaning that analytical error is not compounded by having to dilute the extracted samples (*Farhana, 2005*). However, experiments by *Keene et al.* (1990) showed that whilst most major seawater species, including Na^+ , are 100% recovered from Whatman-41 filters, the recovery of Mg^{2+} varied from only 80–90%. It is thought that the Mg^{2+} adsorbs to the cellulose filter in some way, and in practice, although the amount of Mg^{2+} recovered seems to vary randomly from one batch of samples to the next, the amount of recover within a batch seems highly reproducible (*Baker, personal communication*). This result is reflected in the results shown in figure 3.1b where $\text{Mg}^{2+}:\text{Cl}^-$ ratios are depleted relative to the seawater ratio, consistent with incomplete recovery of Mg^{2+} from the filters. Therefore the use of Mg^{2+} as a reference species for seasalt would result in an underestimation of seasalt concentrations and consequently an overestimation of non-seasalt species. This retention of Mg^{2+} on the filters was considered to be a far greater source of error than any resulting from the dilution of samples. Figure 3.1b appears to show this effect is slightly enhanced for samples collected on P332, however, a Kruskal-Wallis test shows that there is no significant difference between the P332 samples and those collected on the other cruises.

Although a major ion in seawater, the use of Cl^- as a reference species was ruled out due to the acid displacement reaction of seasalt aerosol Cl^- with nitric acid, HNO_3 , and to a much lesser extent, sulphuric acid, H_2SO_4 , gasses (*Raes et al., 2000*) as shown in equations 3.1 and 3.2 respectively. The effect of these displacement reactions is that HCl gas is liberated, thus depleting Cl^- in the seasalt aerosol relative to seawater ratios.

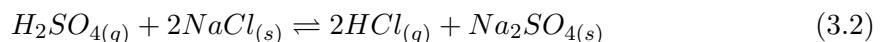
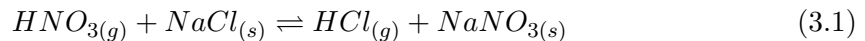


Figure 3.1a shows that chloride is more depleted with respect to sodium and magnesium on cruise M68, perhaps indicative of a slightly more acidic aerosol than the other two cruises, and although the corresponding air mass back trajectories do not indicate that the source regions for these samples are particularly acidic, perhaps acidic aerosol is mixed

in from elsewhere.

In the case of the data for D326, M68 and P332, Na^+ was concluded to be the best tracer for seasalt as Na^+ is relatively inert and, like other major inorganic cations in seawater, there is no major evidence that it is fractionated more than a few percent relative to other cations (*Keene et al.*, 1986). Theoretically, a major source of error in using it as a reference species could arise from the fact that although it is the major cation in seawater; it is also a significant ion in the earth's crust and therefore in Saharan dust (see table 3.3) and the ETNA is a high dust input region. *Chiapello et al.* (1999) correct the sodium concentrations obtained using x-ray fluorescence spectrometry directly on quartz filters, i.e. total sodium concentrations, by using aluminium as a tracer for crustal material. However a plot of Na^+ to total aluminium (figure 3.1d) shows that there is no correlation between the two for D326, M68 or P332.

Additionally, as Cl^- is not such a major component in crustal material (see table 3.3), if the amount of crustal Na^+ in the samples was significant, we would expect an increase in the ratio of $\text{Na}^+:\text{Cl}^-$ relative to that of seawater, at least during periods of high dust deposition. As figure 3.1a shows: this is not the case.

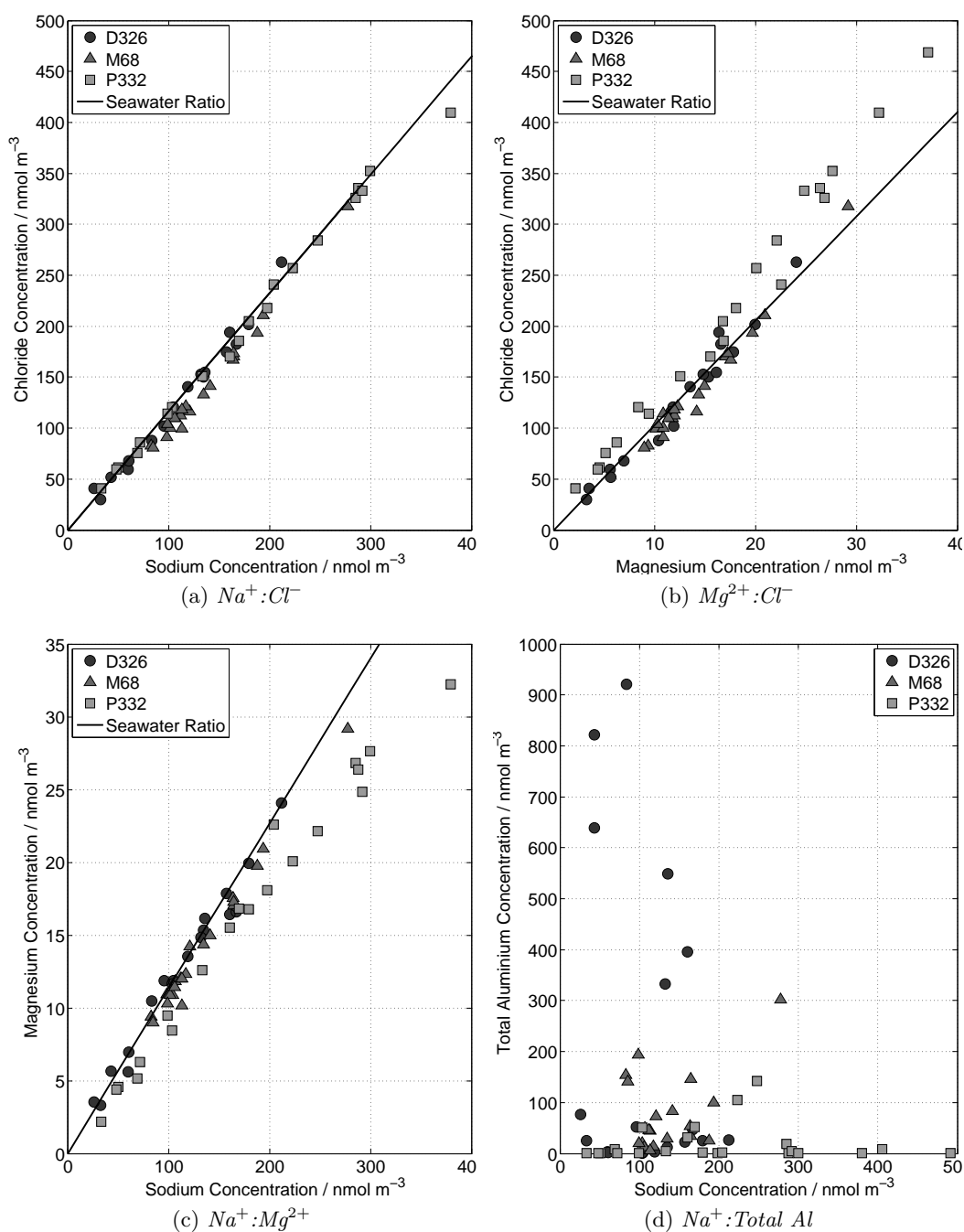


Figure 3.1: *Relative concentrations of sodium, chloride, magnesium and total aluminium*

These results can be explained by taking into account the method by which the major ion samples were extracted and the relative solubility of Na^+ in seasalt and crustal material. Seasalt is very soluble, so the extraction procedure for major ions, as described in section 2.1.3.5, can be assumed to dissolve all seasalt from the filters. In contrast, the Na^+ in crustal material is insoluble (relative to seasalt), and therefore under the conditions described in section 2.1.3.5 it can be assumed that the amount extracted into solution is negligible.

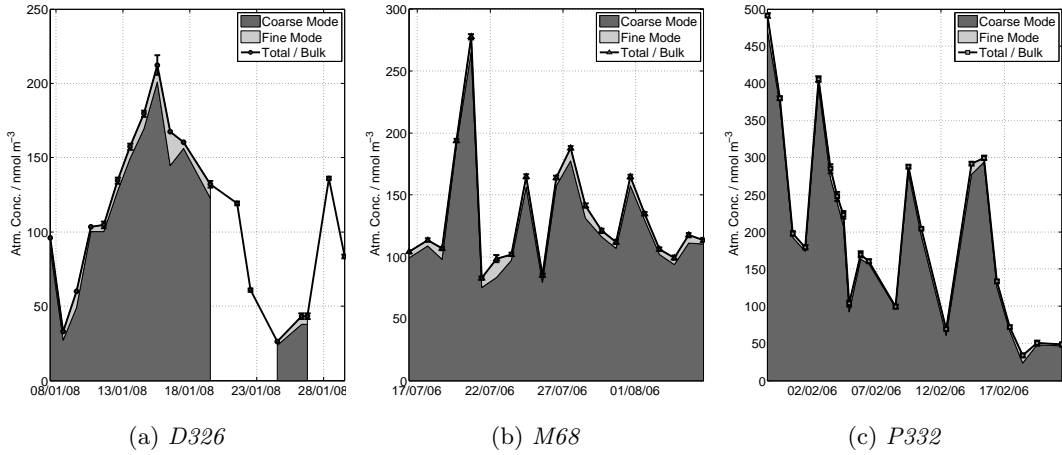


Figure 3.2: Atmospheric concentration of sodium for the three cruises - *N.B.* the y-scales are all different

Figure 3.2 shows that most of the atmospheric of sodium is in the coarse mode for all three cruises, consistent with it originating from seasalt. Factors that control the amount of seasalt aerosol include wind speed, and this may be a reason that the concentration of Na^+ is so much higher for P332 compared with the other two cruises. However, it is not possible to confirm this effect as the wind speed data for M68 and D326 has been difficult to obtain as it was not included in the standard meteorological data that was recorded on these cruises and the meteorological data for P332 has become corrupt.

Having chosen a suitable reference species, the fraction of each major ion species that is due to seasalt, i.e. its seasalt concentration, $[C]_{ss}$, can be found for each sample using equation 3.3, after *Keene et al.* (1986).

$$[C]_{ss} = \frac{[C]_{sw}}{[Na^+]_{sw}} * [Na^+]_{sample} \quad (3.3)$$

Where $[C]_{sw}$ is the concentration of the species C in bulk seawater (see table 3.2), $[Na^+]_{sw}$ is the concentration of sodium in seawater and $[Na^+]_{sample}$ is the concentration of sodium in the sample.

From $[C]_{ss}$ the non-seasalt concentration of the species, $[C]_{nss}$, can be calculated using equation 3.4.

$$[C]_{nss} = [C]_{sample} - [C]_{ss} \quad (3.4)$$

The non-seasalt concentration of several species are used later in this chapter, including non-seasalt calcium, which is a constituent of mineral dust (*Croot et al.*, 2004), non-seasalt

potassium, which is a useful indicator of biomass burning (*Mahowald et al.*, 2005a) and non-seasalt sulphate, which can be used to estimate the strength of anthropogenic and non seasalt marine SO₂ inputs *Keene et al.* (1998).

3.3 Saharan Dust

A first indication of the presence of Saharan dust in aerosol samples is the orange brown colour of the material collected. Dust clouds might be visible on satellite pictures and as a haze around the sun. In fact, during the dust deposition events on D326, large amounts of dust were also visible on the decks of the ship.

Dust aerosol contains a relatively high amount of aluminium, and as it is only present in very small amounts in sea salt aerosol, it can be used as a tracer for the amount of mineral dust present in a sample (*Chiapello et al.*, 1997). On average, crustal material contains about 8.1% by mass aluminium (*Taylor and McLennan*, 1985), and it is generally acceptable (*Duce and Tindale*, 1991; *Arimoto et al.*, 1995) to use of total amount of aluminium in a sample to derive the amount of dust in a sample, or the dust loading (equation 3.5).

$$Dust\ Loading = C_{(Tot.Al)} * A_{r(Al)} * \frac{100}{8.1} \quad (3.5)$$

Where $C_{(Tot.Al)}$ is the atmospheric concentration of aluminium and $A_{r(Al)}$ is the relative atomic mass of aluminium.

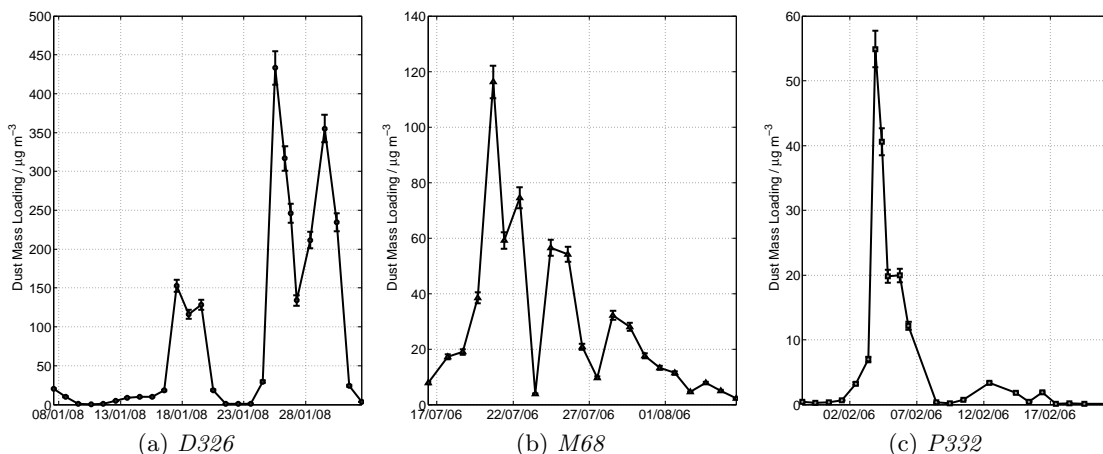


Figure 3.3: *Dust mass loading for the three cruises, calculated from atmospheric total aluminium concentrations, where coarse and fine fractions were measured together, hence measurements are for bulk mode, N.B. the y-scales are all different*

Figure 3.3 shows the atmospheric dust mass loadings on D326, M68 and P332. Typical dust concentrations from samples collected off the coast of West Africa have been 9–104 $\mu\text{g m}^{-3}$ (*Baker and Jickells, 2006*) so the values reported from cruise D326 are particularly high. In contrast to M68, where air mass back trajectories, which are plotted in appendix B on page 147, indicate that the air masses of 20 of 21 samples came from Saharan Africa and dust concentrations are high ($> 20 \mu\text{g m}^{-3}$) most of the time, D326 and P332 show distinct dust events, with high pulses of dust deposition coinciding with air mass back trajectories which indicate Saharan origin, interspersed with low dust deposition ($< 20 \mu\text{g m}^{-3}$), which are associated with remote marine or European air mass types.

The evidence from the air mass back trajectories and the aluminium concentrations is backed up by the appearance of the filters, except during the last part of P332, where air mass back trajectories indicate a Saharan origin, but aluminium concentrations are low and the filters are very pale. This may have been due to precipitation scavenging the dust from the atmosphere during the latter part of this cruise (*Jickells and Spokes, 2001*).

As discussed in section 3.1, other species of interest in Saharan dust are total iron, total manganese, non-seasalt calcium, and phosphate. Plots of these for all three cruises are shown in figure 3.4. For the most part the plots closely resemble the mass loading plots shown in figure 3.3: there are the two distinctive dust events during D326, the smaller dust event in P332 followed by a period of very low dust concentration towards the end of that cruise, and the continuous dust deposition across the whole of M68.

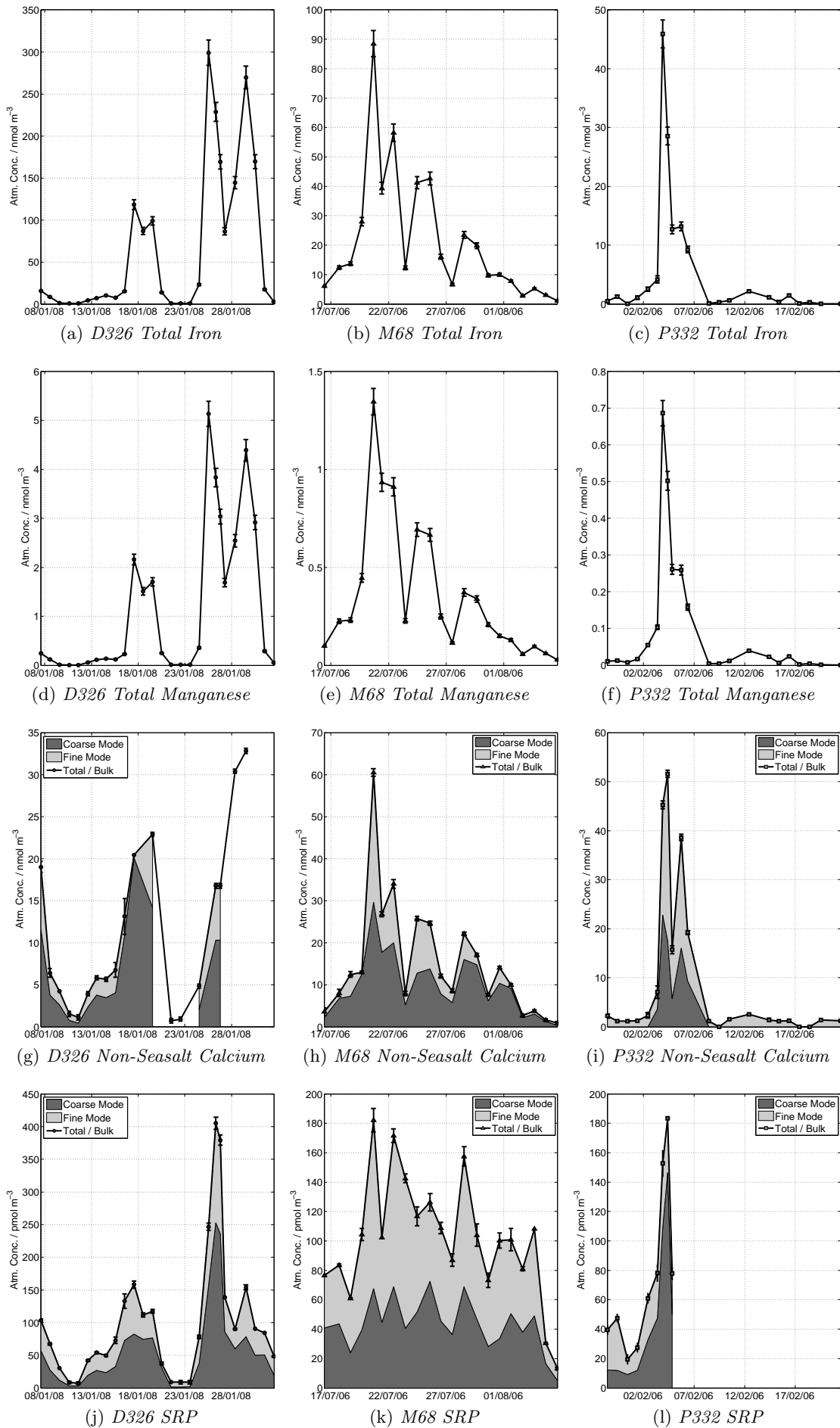


Figure 3.4: Atmospheric concentration of crustal materials for the three cruises: (a-c) total iron, (d-f) total manganese, (g-i) non-seasalt calcium, and (j-l) soluble reactive phosphate. N.B. the change in scale on the y-axes between plots and that total metals were measured as bulk mode, rather than size segregated

The differences in behaviour of these species compared to total aluminium, and hence dust loading as defined in equation 3.5, are shown more clearly by plotting each species against total aluminium in figure 3.5. For the total iron and total manganese plots it was also possible to find a statistically significant relationship to total aluminium (summarised in table 3.4) and the average crustal ratios, calculated from the crustal concentrations of these elements from *Wedepohl (1995)*, are shown in table 3.3 for comparison.

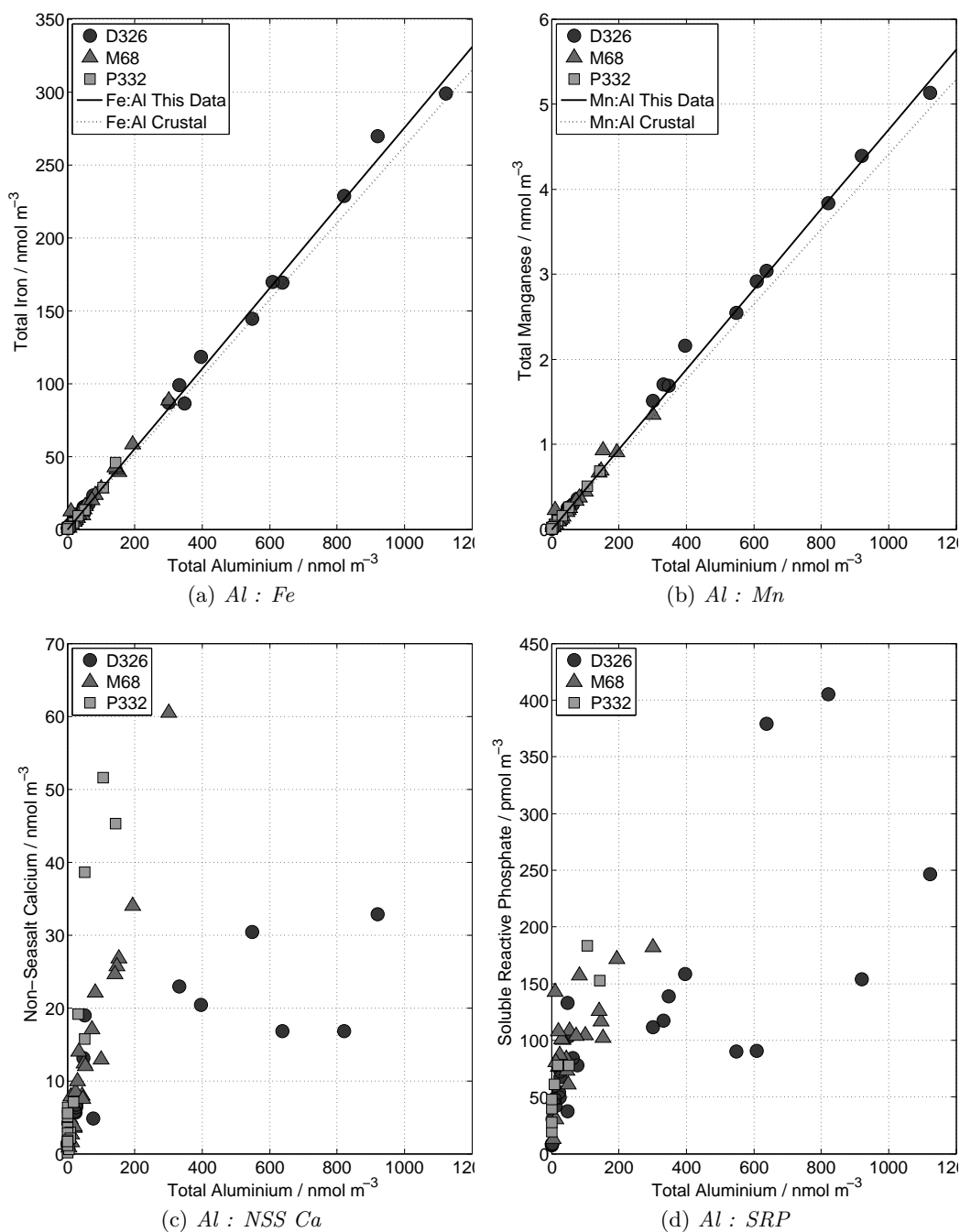


Figure 3.5: Ratio of total aluminium to (a) total iron, (b) total manganese, (c) non-seasalt calcium, and (d) SRP

Element		Concentration %	Aluminium Ratio	
			by mass	by molar amount
Aluminium	Al	7.96	–	–
Iron	Fe	4.32	0.543	0.262
Calcium	Ca	3.85	0.484	0.326
Sodium	Na	2.36	0.296	0.347
Phosphorus	P	0.0757	0.00951	0.00827
Manganese	Mn	0.0716	0.00899	0.00441
Chlorine	Cl	0.0472	0.00593	0.00451
Vanadium	V	0.0098	0.00123	0.000652

Table 3.3: *Crustal ratios of Al, Fe, Ca, P, Na, Mn, Cl and V from Wedepohl (1995)*

It is easy to see from plots a–c and d–f in figure 3.4 that total iron and total manganese, respectively, are very closely related to the mass loading plots in figure 3.3. This is shown more clearly in figures 3.5a and 3.5b where the total iron to total aluminium and total manganese to total aluminium show a statistically significant relationship, which is confirmed by performing a t-test on the linear regressions in table 3.4. Indeed, the ratios calculated from the linear regression of these plots, which are summarised in table 3.4, are close to the crustal ratios shown in table 3.3.

Element	Aluminium Ratio		Correlation Coefficient r^2	Significance? (t-test)
	by mass	by molar amount		
Total Iron	0.5311	0.2756	0.9966	yes
Total Manganese	0.0089	0.0047	0.9972	yes

Table 3.4: *The ratio of different species to total aluminium, calculated by performing a linear regression on the plots in figure 3.5, the significance is the results of a t-test using the 95% confidence interval*

The total iron to total aluminium ratio in table 3.4 is also consistent with other studies: *Chiapello et al.* (1997) report Fe:Al around 0.51-0.54 from aerosol samples originating across the Sahara and Sahel region, which is similar to the ratios observed in sieved soils collected across the Sahara by *Castillo et al.* (2008). Both these authors and *Bergametti et al.* (1989) also report a small gradient in the Fe:Al ratio between the Sahel and the Atlas Mountains, however, given the strong correlation coefficient of total iron to total aluminium (table 3.4) and the absence of scatter in plot 3.5a it is difficult to make a case for a significant Fe:Al gradient using the data in this study, although this is discussed further in section 4.4.

The ratio of total aluminium to total manganese of 0.0096 (table 3.4) is also close to the crustal ratio in table 3.3. This suggests that although manganese aerosol can be produced anthropogenically, it is produced during nonferrous metal production; iron and steel manufacturing; and possibly by cars (*Arimoto et al.*, 1995), there is very little anthropogenic Mn transported in the aerosol on the three cruises relative to the amount

of crustal Mn in the samples.

The close relationship between total aluminium and total manganese is reflected in the correlation coefficient (table 3.4), which suggests that the Mn:Al ratio does not vary much with distinct Saharan dust sources, an observation which is consistent with *Mendez et al.* (2010).

Although the main features of the dust mass loading plots (figure 3.3) are reproduced in the non-seasalt calcium plots (figure 3.4 g–i), there are some differences. Most notably on D326 the non-seasalt calcium concentration increases just before the first dust event shown in the dust mass loading and there are also extra peaks in NSS Ca during M68 and P332.

The extent of the Sahara and the variety of crustal material types that it covers is discussed in chapter 1, so perhaps it is surprising that the total iron and total manganese are so similar to the total aluminium (or dust mass loading). In the case of NSS Ca, a large proportion of which is in soil in the form of calcium carbonate, CaCO_3 (*Andrews et al.*, 2003), is not uniformly present in Saharan soil, several studies have shown that there is a gradient in the total calcium to total aluminium ratio across the Sahara (*Chiapello et al.*, 1997; *McConnell et al.*, 2010), which may account for the differences seen in figure 3.4 g–i. Whether or not a possible change can be detected, or any difference seen across the Sahara using air mass back trajectories is discussed in section 4.4.

Another feature of this data, which may compound these differences, is that the dust mass loading is calculated from the total aluminium, whereas the NSS Ca is calculated from the amount of calcium soluble in ultrapure water (see section 2.1.3.5 on page 23). If there is a gradient in the proportion of total aluminium to non-seasalt calcium across the Sahara, due to a change from the minerals in the soils in the Sahel to those of the Atlas Mountains (*Bergametti et al.*, 1989; *Castillo et al.*, 2008), one could also infer that there must also be a change in the solubility of the calcium, as soils are more soluble in water than other clay minerals.

The widest deviation from the dust mass loading plots is shown in plots 3.4 j–l, the concentration of soluble reactive phosphate: the second peak in the second dust event in D326 is not entirely reproduced and the peaks in M68 are not quite so defined. One reason for this is that PO_4^{3-} in mineral dust exists almost exclusively in the sparingly soluble mineral apatite, which is not distributed evenly across the Saharan region, although there are huge sedimentary deposits in Western Africa that are mined for fertilizer (*Albarède*, 2003).

Additionally it is noticeable that the ratio of coarse mode SRP to fine mode SRP changes quite markedly from D326 and P332 to M68. This may be due to the fact that although mineral dust is a major source of PO_4^{3-} , especially in the Saharan region, other sources of

PO_4^{3-} in aerosol include biomass burning (*Mahowald et al.*, 2005a); plant-related emissions (*Artaxo et al.*, 1988) and fuel emissions (*Anderson et al.*, 2010). Cruise M68 took place during biomass burning season for the Central Africa (*Cooke et al.*, 1996), so the increase in the amount of fine mode PO_4^{3-} is probably due to biomass burning (as discussed in section 3.4.3) and the subsequent incorporation of the biomass burning aerosol with Saharan air mass types (*McConnell et al.*, 2010).

In summary, total aluminium has been used to calculate aerosol dust mass loading, and the atmospheric concentrations of total iron and total manganese are very closely related to the dust loading. However, the soluble non-seasalt calcium and phosphate transported in the dust are not so closely related, possibly in part due to a reported gradient in the relative concentrations of phosphate and calcium compared to aluminium across the region (*Anderson et al.*, 2010; *Chiapello et al.*, 1997), and in the case of fine mode phosphate, due the incorporation of biomass burning aerosols into the Saharan dust air masses (*Mahowald et al.*, 2005a).

3.4 Anthropogenically influenced aerosol

In addition to naturally produced Saharan dust and seasalt, anthropogenic emissions also produce aerosols, both directly in the form of primary particles, e.g. the production of soot during biomass burning, and in the form of finer particles from gas to particle conversions, like the conversion of NO_x to nitrate aerosol.

This section looks first at nitrogen aerosols, then at other anthropogenically influenced aerosols such as non-seasalt potassium and non-seasalt sulphate.

3.4.1 Nitrogen Aerosol

One important nutrient input that is strongly affected by anthropogenic activity is the input of nitrogen. Although *Delon et al.* (2010) show that there is a weak source of nitrogen in the Sahel, it is only present in crustal material in small amounts (*Duce et al.*, 2008), so most of the nitrogen aerosol seen on D326, M68 and P332 has been transported with Saharan dust from other sources.

Chapter 2 described the analysis of the total soluble nitrogen, TSN, content of the samples as well as the inorganic nitrogen in the form of nitrate, NO_3^- , and ammonium, NH_4^+ . Soluble organic nitrogen, SON, was then calculated from the difference between TSN and NO_3^- and NH_4^+ as in equation 3.6.

$$C_{SON} = C_{TSN} - C_{NO_3^-} - C_{NH_4^+} \quad (3.6)$$

The uncertainties associated with the TSN, NO_3^- , and NH_4^+ are compounded when considering the precision of the derived SON concentration: the standard error for the SON concentration is calculated using equation 3.7, so the precision and reproducibility of SON measurements tend to be best when the concentration of inorganic nitrogen species is lower, relative to the total nitrogen concentration (*Cornell et al.*, 2003).

$$\sigma_{SON} = \sqrt{(\sigma_{TSN})^2 + (\sigma_{NO_3^-})^2 + (\sigma_{NH_4^+})^2} \quad (3.7)$$

The atmospheric concentrations of TSN are shown in figure 3.6 plots a–c. It is worth noting that although the atmospheric concentration of TSN does appear to increase during dust events (shown in figure 3.3) it is also present at other times, suggesting that TSN is often transported, and well mixed, with dust, but originates from other additional sources.

Inorganic nitrogen in the form of nitrate aerosol is ultimately formed from the gas to particle conversion of nitric oxide, NO, and nitrogen dioxide, NO_2 , which are often denoted NO_x , as the two are known to interconvert rapidly. The NO_2 can then be oxidised in the atmosphere to form nitric acid, HNO_3 . A thorough reaction scheme for the reactions from NO_x to HNO_3 can be found in *Seinfeld and Pandis* (2006) or *Yeatman* (2000). In the terrestrial atmosphere $HNO_3(g)$ then reacts with $NH_3(g)$ to form aerosol particles as shown in equation 3.8.

Globally, the majority (64%) of the annual emissions of NO_x into the troposphere can be accounted for by fossil fuel combustion, particularly from road vehicle combustion engines and high temperature combustion processes used in power production (*NEG-TAP*, 2001), with a further 15% of emissions due to biomass burning, and biological processes in soils and lightning accounting for around 20% (*Seinfeld and Pandis*, 2006). *Delon et al.* (2010) report that in the Sahelian dry savannah, the proportion of NO_x emissions due to biomass burning and biogenic emissions from the soil are much higher, however, these emissions are very low compared with the amount being transported from Europe and other major urban centres. In the Eastern Tropical North Atlantic, NO_3^- aerosol tends to be associated with, and therefore acts to a certain extent as a tracer of, more polluted air mass sources like Europe and North America (*Baker et al.*, 2006b). However, there is some evidence that suggests that biomass burning in parts of Central Africa (*Real et al.*, 2010) and soil emissions from dry savannah in the Sahel region (*Delon et al.*, 2010) are small, but significant sources of NO_3^- aerosol in Saharan dust plumes during summer. The reaction scheme in equation 3.8 is reversible, and as nitric acid and nitrate aerosol are transported over the marine boundary layer, and mixes with seasalt, the acid displacement reaction in equation 3.1 occurs. Additionally, nitrate may be taken up directly by Saharan

dust aerosol, although recent studies have shown this effect may be less important than previously thought (*Tang et al.*, 2010). This means that rather than the fine mode particles expected from gas-to-particle conversions, most of the inorganic nitrate in the MBL is associated with seasalt and therefore in the coarse mode as plots (d) to (f) in figure 3.6 show.

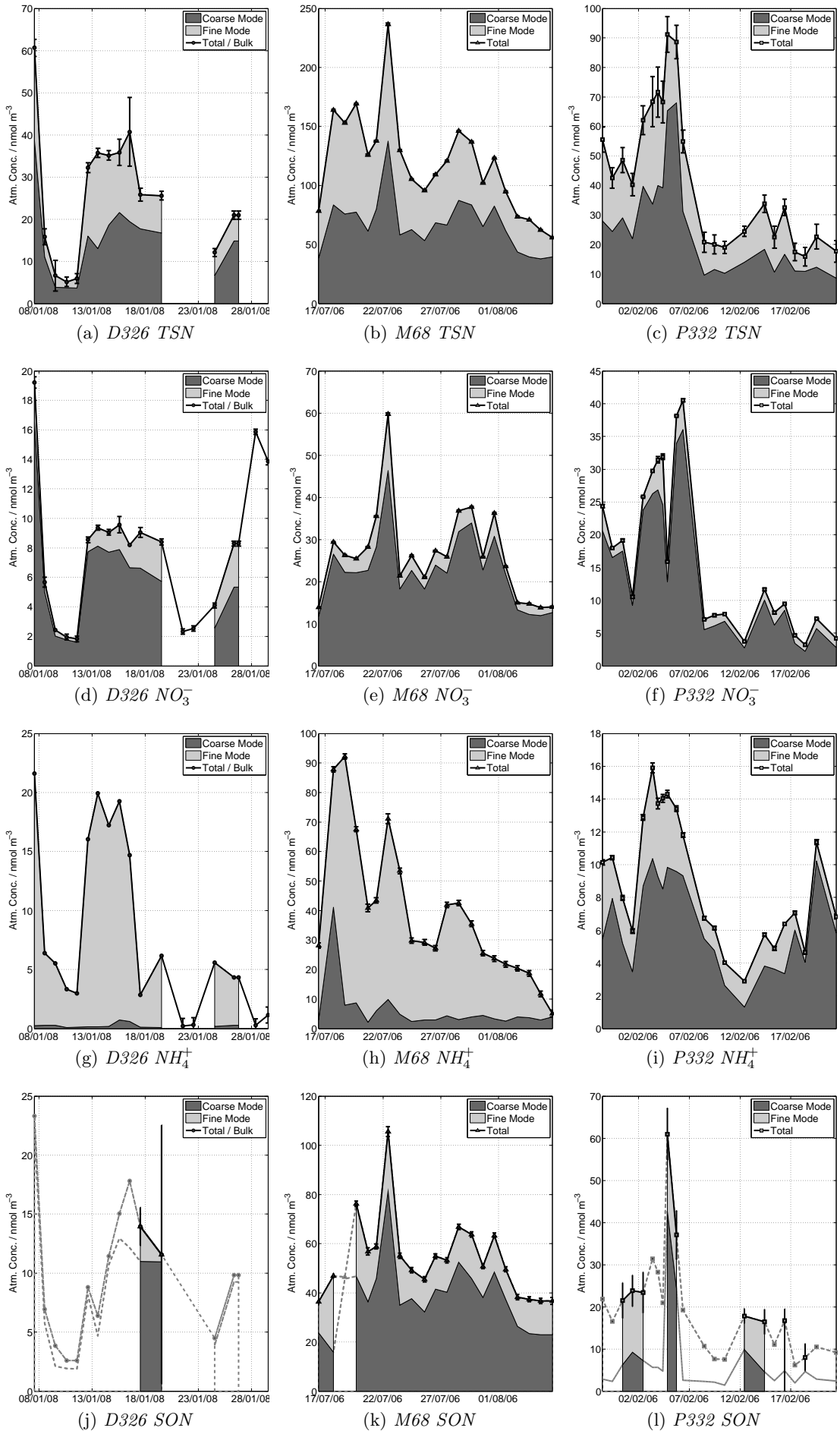
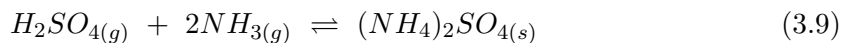


Figure 3.6: Atmospheric concentration of nitrogen aerosol for the three cruises: (a-c) total soluble nitrogen, (d-f) nitrate, (g-i) ammonium, and (j-l) soluble organic nitrogen - dotted lines show where the standard errors exceed the calculated values, N.B. the change in scale on the y-axes between plots

Again, the atmospheric concentration of NO_3^- shown in figure 3.6 d–f is similar to, but not exactly the same as the dust mass loading, suggesting that it is at least transported with, if not on, Saharan dust, but that this is not the exclusive source of NO_3^- aerosol.

The other inorganic form of nitrogen measured was ammonium, NH_4^+ , which is formed via a gas-to-particle conversion of ammonia gas, NH_3 , with acidic species in the atmosphere such as HNO_3 in the terrestrial atmosphere and H_2SO_4 in the marine boundary layer, as outlined in equations 3.8 and 3.9.



The atmospheric concentrations of nitrate and non-seasalt sulphate are plotted against the atmospheric concentrations of ammonium in figures 3.7 a and b respectively. The correlation coefficients (r-values) for linear regressions for nitrogen and non seasalt sulphate are shown in table 3.5, which show that concentrations for these species are significantly correlated, however this does not necessarily imply that the ammonium has chemically reacted with either the nitrate or the sulphate, since nitrate, non-seasalt sulphate and ammonium concentrations are likely to be subject to the same transport processes, thus should be present in lower concentrations further away from source regions.

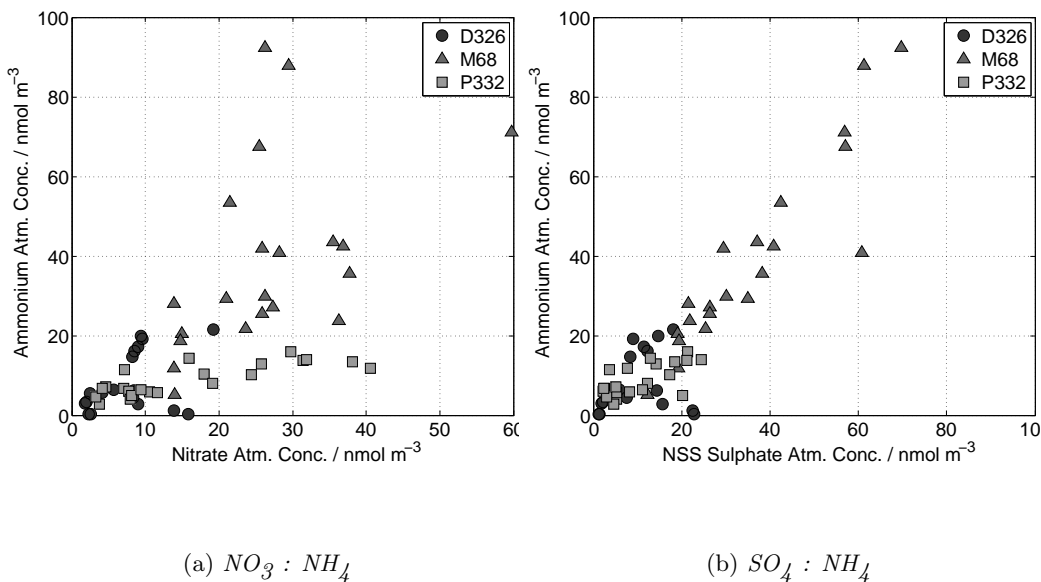


Figure 3.7: Correlation of nitrate and ammonium and non-seasalt sulphate and ammonium

Cruise	r	r ²	Significant Correlation?
Linear Regression of Nitrate on Ammonium			
D326	0.413	0.170	no
M68	0.480	0.231	yes
P332	0.800	0.640	yes
All	0.625	0.391	yes
Linear Regression of Non-Seasalt Sulphate on Ammonium			
D326	0.241	0.058	no
M68	0.919	0.845	yes
P332	0.155	0.024	no
All	0.313	0.098	yes

Table 3.5: Correlation of nitrate and non-seasalt sulphate to ammonium, r is the correlation coefficient and the significance of the correlation was calculated using a t -test with a 95% confidence interval

The most (around 85%) of anthropogenic emissions of ammonia are due to intensive agriculture, primarily from livestock, but also from the use of fertilizers in arable farming. Other sources include combustion, fertilizer production, landfill and sewage sludge (NEG TAP, 2001). Ammonia is also emitted biogenically, but although remote oligotrophic regions at lower latitudes may be a net source of ammonia to the atmosphere (Johnson *et al.*, 2008) the extremely low seawater concentrations in these regions mean that concentrations produced are very small compared to the anthropogenic source in all but the cleanest marine air.

Plots g–i in figure 3.6 show the atmospheric ammonium concentrations measured for all three cruises. The plots show some of the main features as the nitrate plots (d–f in figure 3.6), but there are some marked differences, perhaps reflecting the slightly different sources of the two.

The vast majority of ammonium is in the fine mode (plots 3.6 g–h), as would be expected from a gas to particle conversion (Yeatman, 2000), although the plot for P332 (plot 3.6 i) shows most of the ammonium to be in the coarse mode. After having examined the experimental procedure and subsequent calculations, there is no obvious reason for this anomaly, except perhaps that the conditions on board the ship meant that the motor of the hivol was not working at the same speeds at sea as it was when calibrated whilst in dock. The lower motor speed would mean that the air sucked into it would be travelling more slowly, and particles in it would have less momentum when going through the cascade impactor, therefore the aerodynamic diameter cut-off between slotted filters and backup filter would be smaller, i.e. particles smaller than 1 μ m would be deposited with the coarse mode aerosol. Since calibration of hivol was otherwise correct and that no calibrations were actually carried out whilst at sea, it is not possible to accurately redefine the cut-off diameter for these samples. Either way the proportion of ammonium in the coarse mode for P332 is a result that should be treated with caution.

As mentioned above, the calculation of soluble organic nitrogen is subject to relatively large errors, particularly when the ratio of SON to TSN is very low (*Cornell et al.*, 2003). The soluble organic nitrogen shown in plots j–l of figure 3.6 are therefore shown in solid line where the concentration exceeds the standard error for the sample and a dashed line where the concentration is lower than the standard error. In this case it was felt that, due to the poor reproducibility of the TSN measurements, the uncertainties in the SON data were too high to have any confidence in them.

3.4.2 Non-seasalt sulphate

In addition to the acid HNO_3 , sulphuric acid, H_2SO_4 is also ubiquitous in the free troposphere.

Sulphate aerosol originates from seasalt, but is also formed by the oxidation of sulphur dioxide, SO_2 , which is produced by biomass burning (*Langmann et al.*, 2009); fossil fuel combustion (*NEG TAP*, 2001); volcanic emissions (*Bao et al.*, 2010); and in the MBL as an oxidation product of the biogenically produced trace gas dimethyl sulphide, DMS (*Bell et al.*, 2006). The oxidation of sulphur dioxide can occur via several mechanisms depending on flux and atmospheric conditions (*Seinfeld and Pandis*, 2006), but in the MBL the reaction with ammonia gas (equation 3.9) is significant. However, in the MBL SO_4^{2-} derived from seasalt is important, so it is necessary to correct atmospheric aerosol SO_4^{2-} concentrations for seasalt contribution.

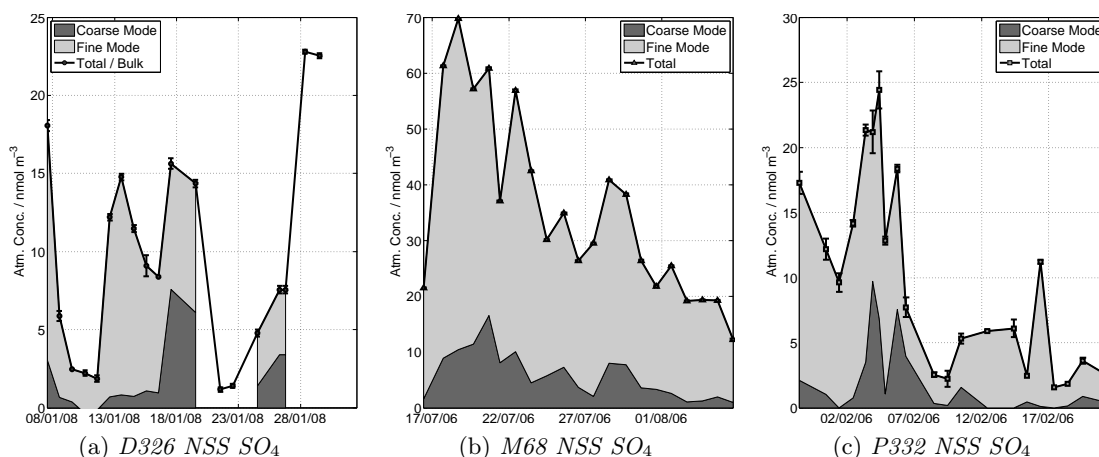


Figure 3.8: Atmospheric concentration of non-seasalt sulphate for the three cruises

As seasalt sulphate is a primary particle, we would expect it to be coarse mode, compared to other sources, which are formed by gas to particle conversions. Although these fine mode sulphate containing particles are theoretically subject to the acid displacement reaction in the presence of seasalt shown in equation 3.2, which works in an analogous way to

the acid displacement reaction of nitrate in the presence of seasalt (equation 3.1), it is unlikely that this reaction is important in the marine boundary layer (*Seinfeld and Pandis, 2006*). However simple comparison of coarse to fine mode is not sufficient to filter out the influence of seasalt, therefore equation 3.4 is used to derive the non-seasalt fraction of sulphate aerosol from the concentration of sodium aerosol. The atmospheric concentration of non-seasalt sulphate, NSS SO_4 , calculated in this way is shown in figure 3.8

The interesting feature of the plots in figure 3.8 is that they are very similar to plots g–i in figure 3.6, especially during M68, where there are large concentrations of NSS SO_4 in the fine mode, consistent with the formation of ammonium sulphate from sulphuric acid and ammonia (equation 3.9), this is confirmed by a t-test, the results of which are shown in table 3.5.

The degree to which the acid displacement reactions 3.1 and 3.2 have occurred can be examined by looking at plots of NSS SO_4 and NO_3^- to the $\text{Na}^+:\text{Cl}^-$ ratio (figure 3.9). In theory if Cl^- is being displaced by NO_3^- or NSS SO_4 , then the $\text{Na}^+:\text{Cl}^-$ ratio should increase (there should be more Na^+ relative to Cl^-) and the concentrations of NO_3^- and NSS SO_4 increase.

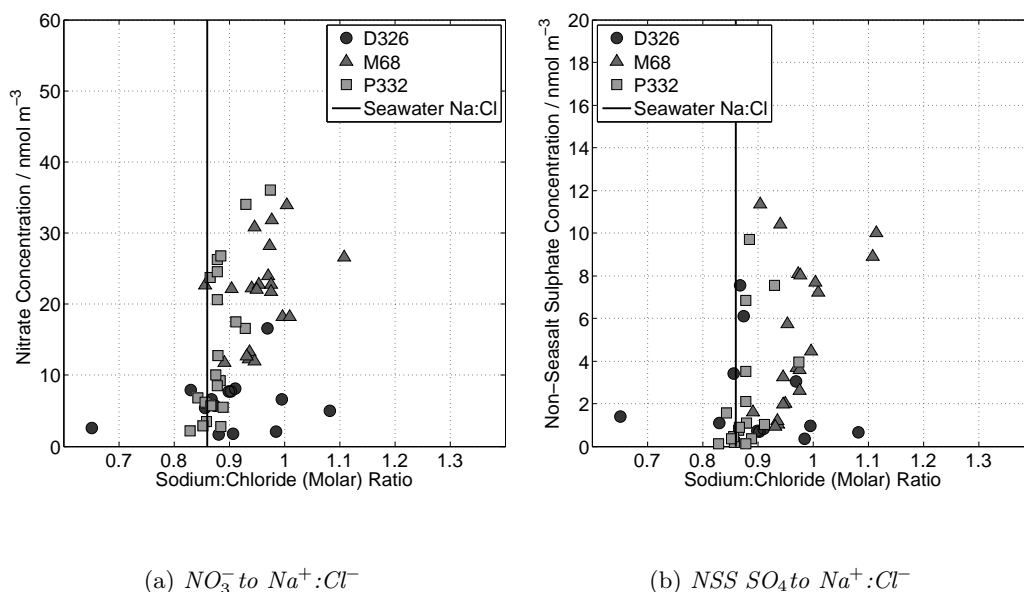


Figure 3.9: Atmospheric concentration of nitrate and non-seasalt sulphate plotted against the ratio of sodium to chloride

For the cruise D326 the $\text{Na}^+:\text{Cl}^-$ ratio doesn't increase significantly with either NO_3^- or NSS SO_4 , indicating that acid displacement of Cl^- doesn't really happen in these samples, perhaps due to the high amount of mineral dust present, which would increase the pH of the aerosols and inhibit the acid displacement reaction. However in M68 and the second

half of P332 there does appear to be some acid displacement of Cl^- occurring, possibly due to the fact that the transport of the dust is at higher altitude during summer months (see section 1.5) with other air mass types becoming entrained. However, it is difficult to establish whether this is due to the NO_3^- or NSS SO_4 , although given that most of the NSS SO_4 seems associated with NH_4^+ , it seems more likely that the species responsible is NO_3^- .

3.4.3 Biomass Burning

A major anthropogenic source of aerosol local to the Saharan region is biomass burning. The nutrient element content of the biomass varies with season, but estimates of the ratios in biomass burning aerosols are shown in table 3.6.

Nutrient element		% content in biomass burning aerosol by mass	
Nitrogen	N	0.3	– 3.8
Sulphur	S	0.1	– 0.9
Phosphorus	P	0.01	– 0.3
Potassium	K	0.5	– 3.4

Table 3.6: *The approximate ratio of nutrient elements in biomass burning aerosol from Crutzen and Andreae (1990)*

Non-seasalt potassium, NSS K, is calculated from potassium and sodium concentrations using equation 3.4 and, although potassium is present in crustal material (*Wedepohl*, 1995), it tends to remain in the coarse mode, so the presence of enhanced levels of fine mode NSS K is usually considered to be a tracer for aerosols produced by biomass burning (*Andreae*, 1983).

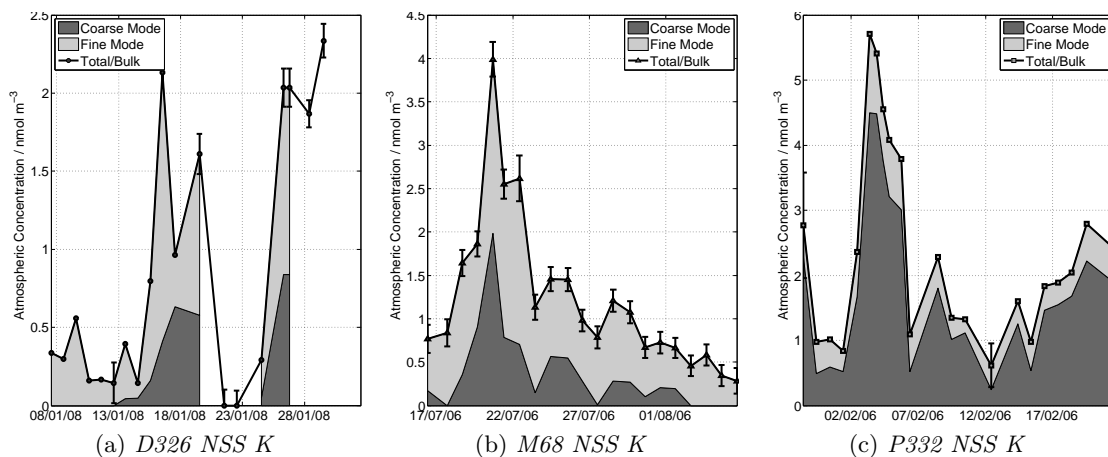


Figure 3.10: *Atmospheric concentration of non-seasalt potassium for the three cruises*

The plots of NSS K in figure 3.10 seem generally to follow the general features of the dust

mass loading in figure 3.3, although there are several similarities to the fine mode NSS SO_4 (figure 3.8) and SRP (figure 3.4 (j-1)), particularly for M68. This indicates that there is a biomass burning signal, and that it is carried with Saharan dust, which is consistent with observations of central African biomass burning plumes being uplifted into the Saharan air layer during the summer dust season by *Real et al.* (2010). The enhanced levels of coarse mode NSS K during P332 are consistent with a change in the cascade impactor cutoff, as seen in the ammonium concentrations in figure 3.6f.

In summary, the deposition of nitrogen species appears to be dominated by inorganic species (NO_3^- and NH_4^+) although it is difficult to quantify the amount of organic nitrogen present in samples due to the uncertainties involved (*Cornell et al.*, 2003). Most of the NO_3^- occurs in the coarse mode, indicating that it has undergone the acid displacement reaction with seawater shown in equation 3.1. On the other hand NSS SO_4 occurs predominantly in the fine mode, indicating that the corresponding acid displacement reaction for sulphuric acid (equation 3.2) is not important in the marine boundary layer. Whilst NSS SO_4 seems to be associated with NH_4^+ , indicating that the reaction in equation 3.9 is important, during periods of biomass burning over central Africa, high concentrations on NSS SO_4 also seem to be associated with fine mode SRP and NSS K, indicating that these together are useful tracers of biomass burning.

3.5 Trace metal solubility

The concentrations of total iron, aluminium and manganese are discussed in section 3.3, and although this reveals a lot about the quantity of these aerosols in the atmosphere, in order to better assess the effect of these trace metals on phytoplankton communities in the ocean, in particular whether they may be bioavailable or not, more detail is needed. The link between trace metal bioavailability and solubility is discussed in more depth in section 1.2.1 on page 4 and comparison of soluble trace metal concentrations and total trace metal concentrations gives a useful picture of solubility.

The atmospheric concentrations of soluble trace metals, defined here as the aerosol that dissolves in a pH4 buffered solution (see section 2.1.3.5), are shown in figure 3.11. This definition is operationally defined and the technique was originally used to mimic the dissolution of dust in rainwater (*Baker et al.*, 2006c), however, it represents perhaps maximum amount of trace metals that may dissolve from aerosol particles throughout the water column.

Vanadium is included in plots 3.11 j-1 for completeness and because although observations of aerosols derived from North African soil dusts have shown that the ratio of vanadium to aluminium is close to the average crustal ratio quoted in (*Taylor and McLennan*, 1985), it is highly enriched in heavy fuel oil used in ships and oil-fuelled power stations, and to

3.5 Trace metal solubility

a lesser extent in coal, so enrichment of V in aerosol relative to Al can be used as an indicator of combustion of these sources (*Arimoto et al.*, 1995).

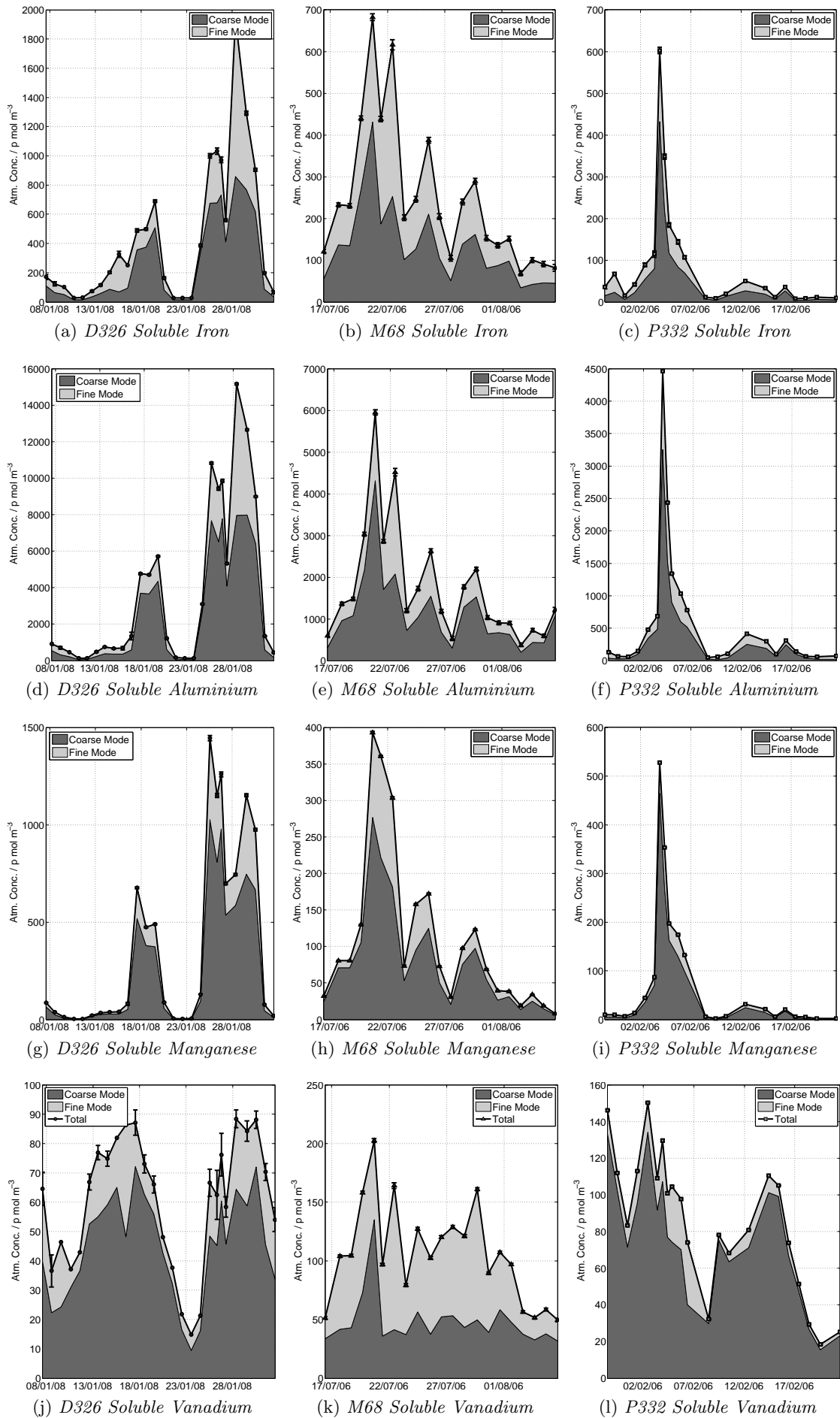


Figure 3.11: Atmospheric concentration of soluble trace metals for the three cruises: (a-c) soluble iron, (d-f) soluble aluminium, (g-i) soluble manganese, (j-l) soluble vanadium N.B. the change in scale on the y-axes between plots

At a first glance, the main features of the dust loading (figure 3.3) are reproduced in the plots in figure 3.11. However, the vanadium plots (figure 3.11 j–l, are quite different, especially for D346 and P332, and more strongly resemble the plots for NSS SO₄ in figure 3.8. This would be consistent with the presence of some sort of combustion signal, as sulphate is also enhanced in heavy fuel oil burning

In order to get a better idea of how the other soluble trace metals change with respect to the total trace metal concentrations, the trace metal solubilities have been plotted in figure 3.12.

To avoid confusion, the term trace metal solubility used in this thesis refers to its fractional solubility, i.e. the fraction of the metal that will dissolve from an aerosol sample, as defined in equation 3.10, and not a concentration solubility which is usually used to refer to aerosol in the water column (*Baker and Croot, 2010*).

$$\%Sol_X = \frac{[X]_{Soluble}}{[X]_{Total}} * 100 \quad (3.10)$$

Where %Sol_X is the fractional solubility of species X and [X]_{Soluble} and [X]_{Total} are the soluble and total atmospheric concentrations of species X, respectively.

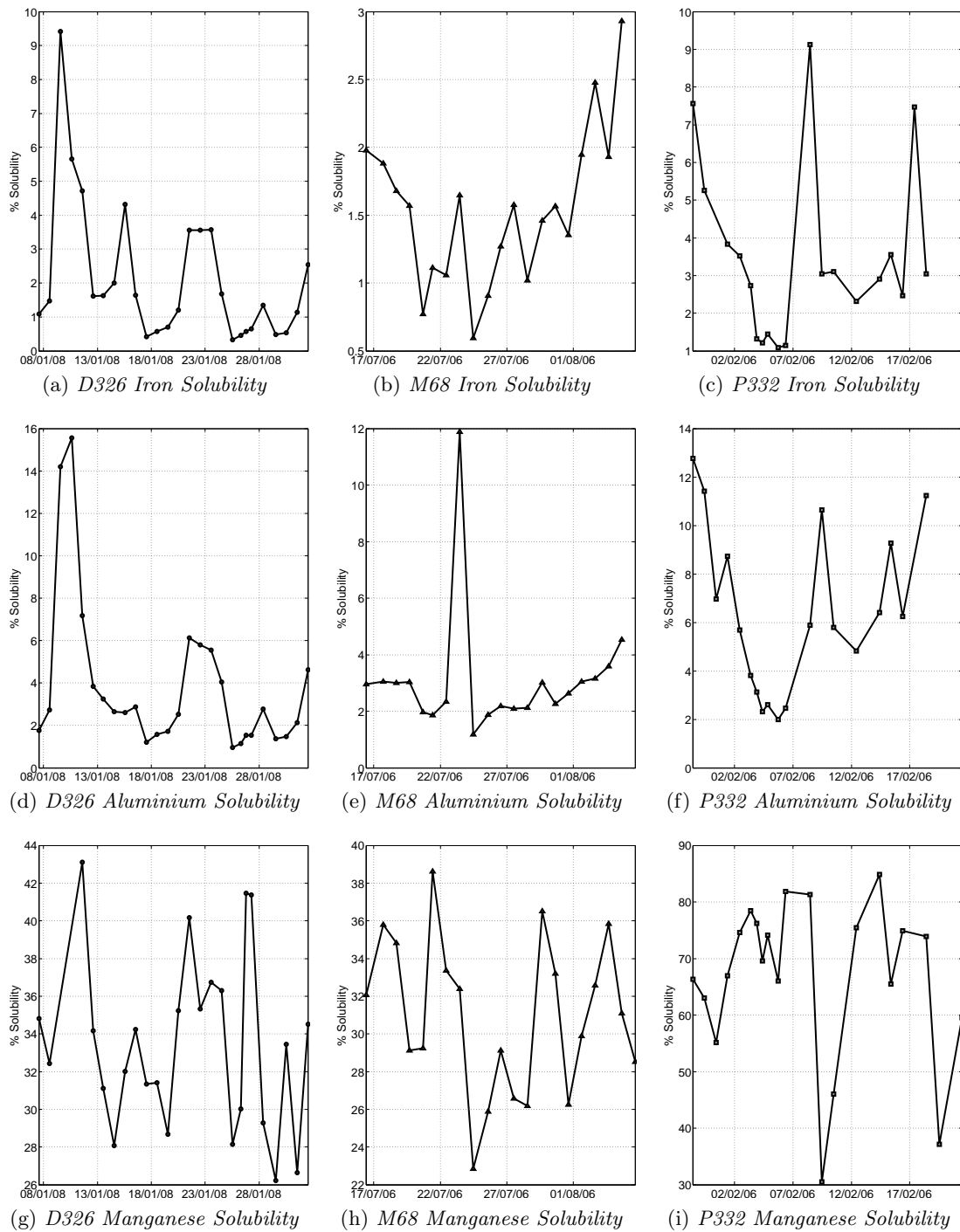


Figure 3.12: Atmospheric trace metal solubility for the three cruises: (a–c) iron, (d–f) aluminium, (g–i) manganese N.B. the change in scale on the y-axes between plots

The most striking thing about the plots in figure 3.12 is that they look almost like a mirror image of the dust loading plots in figure 3.3: in particular, the solubility of both iron (plots a–c) and aluminium (plots d–f) decreases during Saharan dust events.

Typical solubilities for samples for which air mass back trajectories indicate a Saharan origin, i.e. most of M68 and dusty periods during D326 and P332, show solubilities of between 0.1–2% for iron and 1–4% for aluminium, compared to maximum solubilities of 10% for iron and 16% for aluminium at other times. This compares to reported solubilities during dust events of 0.1–2%, and 2–4% for iron and aluminium respectively (*Baker et al.*, 2006c).

Manganese, on the other hand, does not appear to act in quite the same way and solubilities are much higher. Additionally the manganese solubilities for P332 (shown in plot i) are much higher than the other cruises. Comparison with the larger data set used in chapter 4, shows that although typical values for the solubility of manganese tend to be around 25–45%, values in excess of 70–80% are not unknown, and because soluble manganese can be produced from fossil fuel burning (*Mendez et al.*, 2010), enhanced manganese solubilities are possibly indicative of air that has been transported over an urban polluted region at some point.

The variation in iron solubilities, and to a lesser extent aluminium and manganese, is well documented, and *Baker and Jickells* (2006) find an inverse relationship between dust loading, calculated from total aluminium concentrations, and iron solubility (figure 3.13b), which is reproduced by the data from D326, M68 and P332, as shown in figure 3.13a.

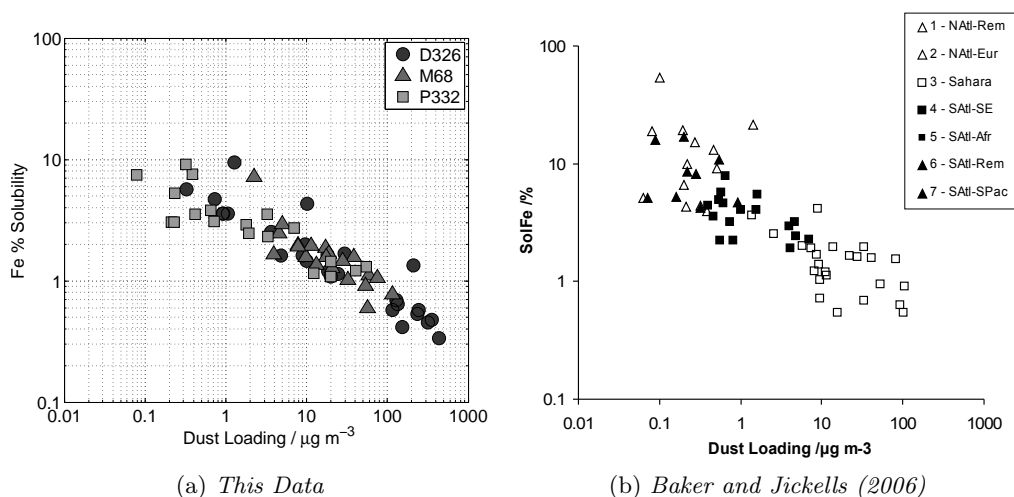


Figure 3.13: *Iron solubility plotted against dust mass loading: this data compared to Baker and Jickells (2006)*

Several other investigators find a similar relationship between aerosol loading and trace metal solubility. Indeed, a recent comparison of several datasets by *Aguilar-Islas et al.* (2010) shows that although the methods used to measure iron solubility varies between different datasets, the observed changes in the solubility are much greater than the offset between different datasets.

As vanadium has been measured for these data, it is relevant to state that *Sedwick et al.* (2007) show that in Bermudan aerosols excess vanadium concentration, i.e. vanadium concentrations greater than the crustal vanadium to aluminium ratio, is related to iron solubility, owing to the fact that when mineral dust transport is low, most of the iron aerosol is derived from anthropogenically produced combustion sources, including heavy fuel oil burning, processes which also produce aerosol enriched in vanadium. However, it is very hard to find a similar relationship for these data, perhaps because periods of low dust deposition are not associated with polluted air mass types in the ETNA, rather they are more associated with remote marine aerosols.

Changes in iron solubility have, amongst many other things, been attributed to particle size sorting during dust transport effects (*Baker and Jickells, 2006*); differences between mineral dust and anthropogenically produced aerosol (*Sedwick et al., 2007*); gradients in the minerals uplifted in the Saharan dust (*Desboeufs et al., 2005*) and atmospheric processing (*Spokes and Jickells, 1995*). The investigation of the influence of all these factors on trace metal solubility requires the analysis of a larger dataset than from three cruises: so the subject of trace metal solubility, and iron solubility in particular, is discussed in more detail, with a much larger data set in chapter 4.

3.6 Summary

In summary the data from D326, M68 and P332 is invaluable in assessing the atmospheric input of iron, phosphate, and nitrogen to the ETNA. Important information can also be derived from solubility data, and whether the aerosol seems affected by anthropogenic aerosol sources. However, these data represent a snapshot of the actual deposition and they need to be considered in the light of other data to assess whether this snapshot is truly representative of the actual deposition to the eastern tropical North Atlantic.

Chapter 4

Gradients in Iron Soluble Fraction

4.1 Background

The aim of this chapter is to establish which factors most affect the fractional solubility of aerosol iron in the ETNA region. There are not enough data from the D326, M68 and P332 (see chapter 3) to tackle this problem, so a much larger dataset has been used, which consists of 273 ship-based aerosol samples taken in the ETNA region between October 2000 and October 2008.

For the purposes of this thesis, iron solubility is defined in equation 3.10 on page 63 as the fractional solubility of iron.

The significance of iron solubility is discussed more fully in section 1.2.1 on page 4, but briefly the dissolution rate of the iron from aerosol into seawater, compared to the sinking rate of that particle generally determines how bioavailable the iron is to phytoplankton. Although the iron solubility here relates to the soluble iron in at pH 4.5, the changes seen in these data should relate to changes seen in the dissolution of aerosol iron in situ.

As the ETNA is directly adjacent to the Sahara - a major source of dust to the worlds ocean (*Jickells et al.*, 2005) - the input of mineral dust should dominate the supply of iron to the region, and therefore have the greatest effect on the iron solubility of aerosols. In addition, since this input from the Sahara accounts for 43% of the world's annual mineral dust flux to the open ocean (*Mahowald et al.*, 2005b), the solubility of the dust flux to the ETNA would affect the global flux of soluble iron to the ocean.

Historically, modelling studies have tended to use a single value for iron solubility however, as figure 3.13 on page 65 shows, the fractional solubility of aerosol iron is not constant and can change by orders of magnitude. This is consistent with several other sets of observations, as shown in table 4.1.

Reference	Method	Region	Solubility / %
(<i>Sholkovitz et al.</i> , 2009)	low volume samplers with rapid leach using DI water	Sargasso Sea	0.44 – 19
(<i>Ooki et al.</i> , 2009)	low volume collectors, continuous artificial seawater leach	Hokkaido, Japan	1.2 – 2.2
(<i>Baker and Jickells</i> , 2006)	hivol samplers, with pH4 leach	North Atlantic	0.5 – 80

Table 4.1: *Values of iron solubility obtained from the literature*

Additionally, the analysis of several datasets together has shown that the variation between iron solubilities is greater than the variation between different methods for calculating iron solubility, i.e. the differences in iron solubility observed in individual data sets are greater than the differences between data sets, suggesting that the same changes can be observed

irrespective of the method used to measure the soluble iron (*Aguilar-Islas et al.*, 2010).

Several hypotheses have been used to explain the observed solubility gradients, including changes in source region, which are often specific to the area the observations are made in, e.g. observations in Bermuda show that the iron solubility is very low during summer months when most of the iron aerosol comes from Saharan dust, but much higher during the winter when most of the soluble iron aerosol is derived from heavy fuel oil burning from North America and shipping in the North Atlantic, thus a change in source region drives a seasonal change in iron solubility (*Sedwick et al.*, 2007). A similar effect has been observed in the eastern Mediterranean, where aerosol iron solubility is at a minimum during periods of high Saharan dust deposition, but increases at other times when iron aerosol flux is lower, but mainly derived from heavy industry in Europe (*Guieu et al.*, 2010). There may also be a gradient in iron solubility for aerosols coming from across the Saharan region, consistent with a change in minerals from North Africa to the Sahel (*Journet et al.*, 2008).

Another mechanism for changing the iron solubility in aerosol is acid processing, where aerosols can be activated by wetting in clouds (*Raes et al.*, 2000) and the cycle of wetting, reaction of aerosol with acid species in the clouds, and subsequent drying can have the effect of increasing iron solubility over time (*Spokes and Jickells*, 1995). The transport of the dust through the atmosphere can also have an effect: *Baker and Jickells* (2006) show that the change in iron solubility can be modelled as particle-size fractionation during transport, and that an empirical relationship can be formed between iron solubility and dust concentration, which can be considered to be a proxy for the distance the material has travelled from its source.

4.2 Aerosol concentration data set for the ETNA

The data used in this chapter has been gathered from 273 samples collected in the ETNA between October 2000 and October 2008. This dataset is the same as the one described in section 5.4.2 on page 101. The sampling location for each of the samples is shown in figure 5.1a, and details of the cruises these samples were collected on are summarised in table C.1 on page 157.

The plot reproduced in figure 3.13 on page 65 has been updated in figure 4.1, to include the whole ETNA dataset. The inverse relationship between iron solubility and dust loading on a log scale noted by *Baker and Jickells* (2006) still appears to hold, and would appear to suggest this is a general relationship and hence is a good place to start investigating gradients in iron solubility.

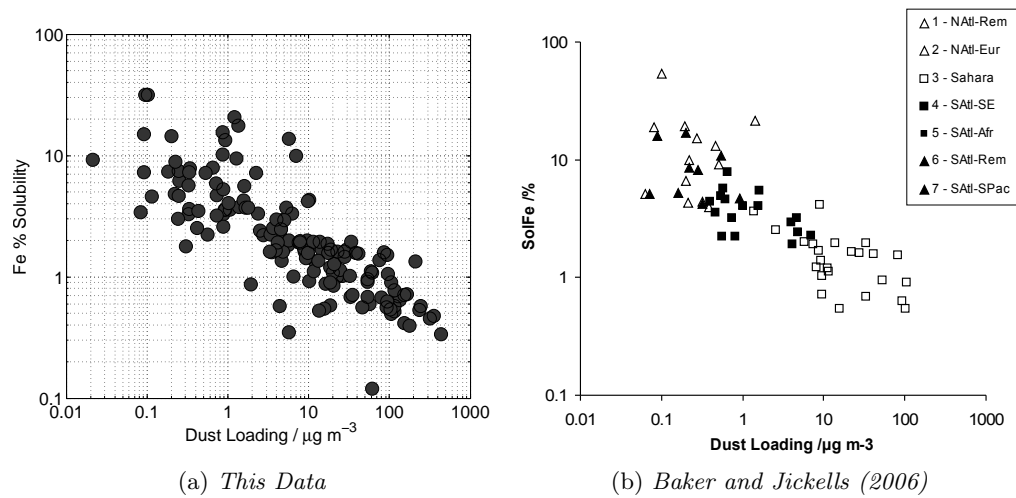


Figure 4.1: Iron solubility plotted against dust mass loading: this data compared to Baker and Jickells (2006)

4.3 Anthropogenically produced iron aerosol

The solubility of iron in aerosols from anthropogenic emissions like coal fly-ash, soot, and other particles produced by the combustion of fossil fuels and biomass or the processing of metal ores, has been shown to be higher than those aerosols originating from arid region soils (*Schroth et al.*, 2009; *Desboeufs et al.*, 2005).

With this in mind it should follow that air masses originating from regions with large amounts of anthropogenic emissions such as Europe and North America, should generally have higher aerosol iron solubilities than those originating from arid regions. Air mass back trajectories (see section 2.5) were used to assign each sample in the dataset an air mass type (as listed in table 2.5 on page 34); figure 4.2 shows the distribution of iron solubilities for each air mass type, and how this changes the plot in figure 4.1a.

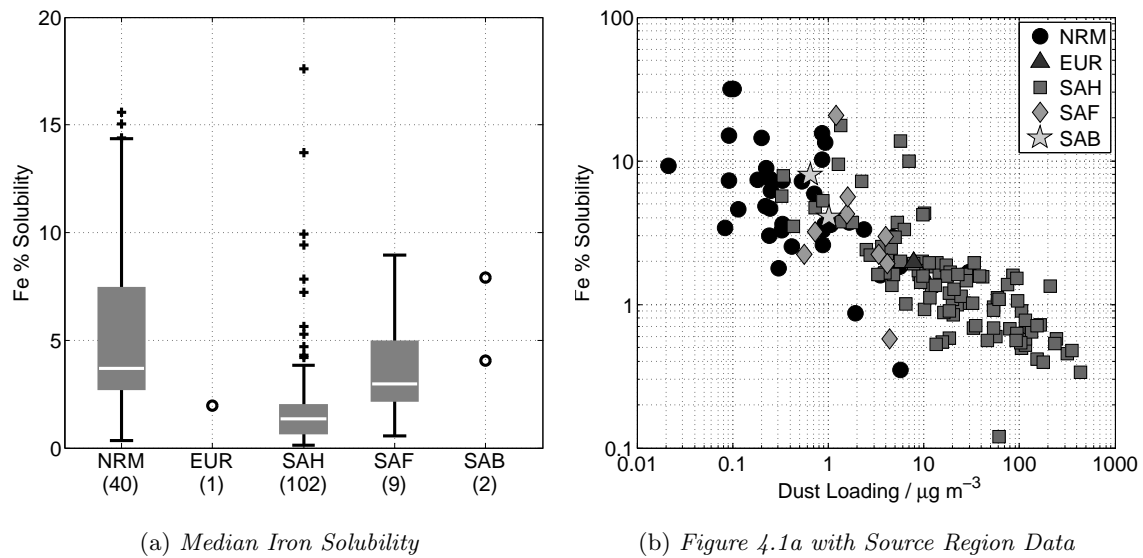


Figure 4.2: (a) Box and whisker plots for the iron solubility for each air mass type (abbreviations are defined in table 2.5), crosses denote outliers and circles show where there were too few data to average, and the number in brackets below each box is the number of observations included in the calculations; (b) Iron solubility against dust loading showing air mass type

Figure 4.2b closely resembles the *Baker and Jickells (2006)* plot, with the lower dust loadings and higher solubilities being attributed to remote regions, in this case the remote North Atlantic, and Saharan-type air masses being associated with lower solubilities and higher dust loadings. Indeed, a Kruskal-Wallis test on the data shown in figure 4.2a confirms that the median values and variance in iron solubility for NRM, SAH and SAF air mass types are different, to a significance value of 0.05.

However, the change in iron solubility between the different air mass types does not necessarily mean that the changes are caused by the presence of more soluble, anthropogenically produced, iron. One way to look for the presence of different sources of iron is to compare the total iron to total aluminium ratio as in figure 4.3. Mineral dust should have the same molar ratio of iron to aluminium as the Earth's crust (a value of 0.262, see table 3.3), although the Fe:Al ratio is much higher in urban particles and types of fly ash (*Desboeufs et al., 2005*). As the proportion of urban particles/fly-ash in the samples increases, so should amount of anthropogenically produced iron and therefore the Fe:Al ratio should also increase along with and the relative aerosol iron solubility. Figure 4.3 shows that this is not the case for this data set, in fact in the few cases where the Fe:Al ratio changes significantly from the crustal ratio, the iron solubility decreases. This implies that for this dataset the aerosol iron solubility is dominated by crustal material and the influence of anthropogenically produced particles transported to this region is minimal.

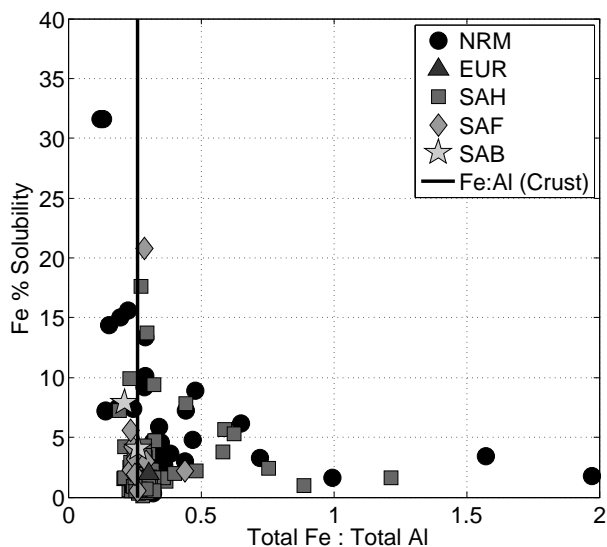


Figure 4.3: Aerosol iron solubility plotted against the ratio of total iron to total aluminium

4.4 Changes in iron solubility across the Sahara

It has been shown that there is a gradient in the relative proportions of calcium, iron and silicates between the Atlas Mountains and the Sahel which is consistent with the change in soil composition (*Chiapello et al.*, 1997). Moreover, *Journet et al.* (2008) show that iron solubility in iron hydroxides such as haematite and goethite is much lower (<1%) than clays (around 4%) and other aluminosilicate materials, hence the point source region within the Sahara could affect solubility.

In order to examine any possible gradient in iron solubility in aerosols derived from different areas from within the Saharan region, a subset of the main dataset was used: those samples assigned to a Saharan air mass type. Air mass back trajectories were then re-examined in order to subdivide the Saharan source region into three sectors, along the same lines as *Chiapello et al.* (1997), who define these sectors as Sahel; south and central Sahara; and north and west Sahara, as shown in figure 4.4.

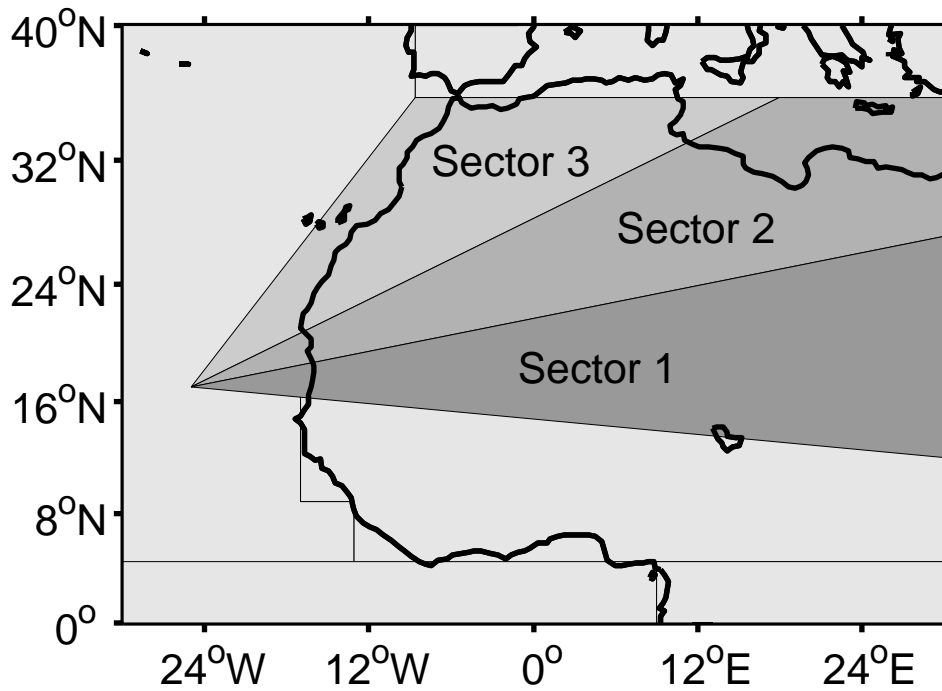


Figure 4.4: Different source regions in the Sahara from Chiapello et al. (1997)

Figure 4.5b shows the mass loading plot, with points shaded according to Saharan region, whilst figure 4.5a shows the median values of iron solubility for each Saharan region, along with inter quartile ranges. A Kruskal-Wallis analysis on these data show that the iron solubilities from each region are not significantly different within the 0.05 confidence interval. It could be argued that the use of air mass back trajectories to define the different regions in the Sahara could be slightly misleading as dust lifted into the atmosphere tend to travel more slowly than the air masses themselves (Pye, 1987) and in any case the back trajectories are subject to errors anywhere between 15 and 30% of the travel distance (Draxler and Rolph, 2003).

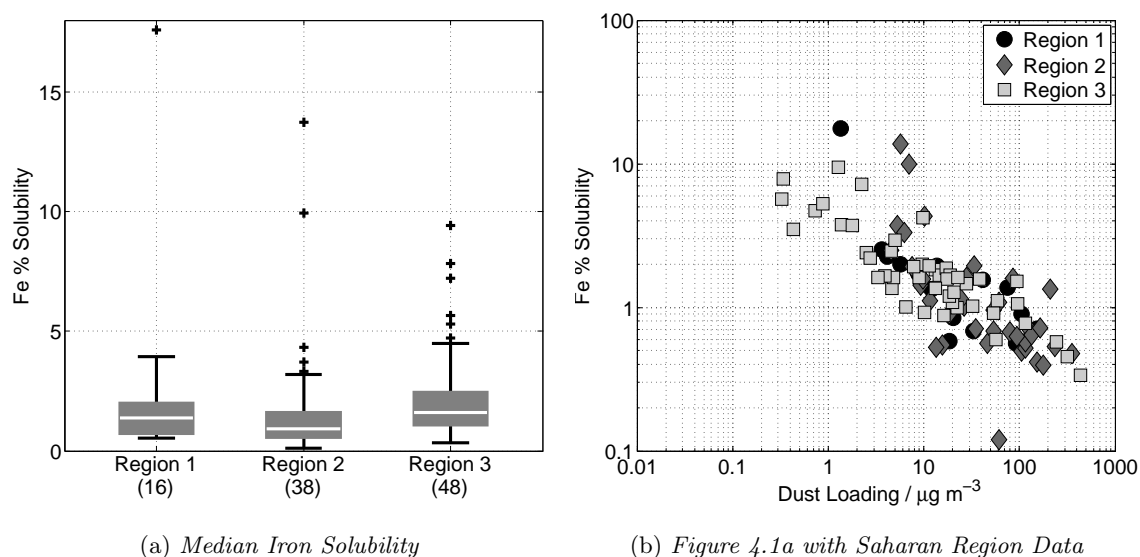


Figure 4.5: (a) Box and whisker plots for the iron solubility for each Saharan Region, as defined in figure 4.4, crosses denote outliers and the number in brackets below each box is the number of observations included in the calculations; (b) Iron solubility against dust loading showing Saharan region

In addition to a variation in iron solubility in aerosols from across the Sahara gradients in the relative amount of non-seasalt calcium has also been reported (*Chiapello et al.*, 1997). (*Formenti et al.*, 2008) show that for samples gathered at ground level in Niger, there is a cut-off in the NSS Ca to total aluminium ratio at 7%, above which dust is advected in from North Africa and the Sahara, and below which the dust is local, Sahelian dust. There is, however a caveat to this cutoff: dust advected from the Bodélé depression also contains a high amount of NSS Ca to aluminium, although this does not affect the general trend very much. Figure 4.6a shows how this cutoff (adjusted for atmospheric molar concentrations) applies to this data set and figures 4.6b and c show the iron solubility against mass loading and the median iron solubilities of the data once it has been divided into groups above and below the cutoff. However, for this data there is obviously little variation in iron solubility with the NSS Ca : total Al ratio. This would appear to suggest that although the relative amount of NSS Ca may change across the Sahara, it is not necessarily coincident with a change in iron solubility, and certainly not one that can be detected in this data.

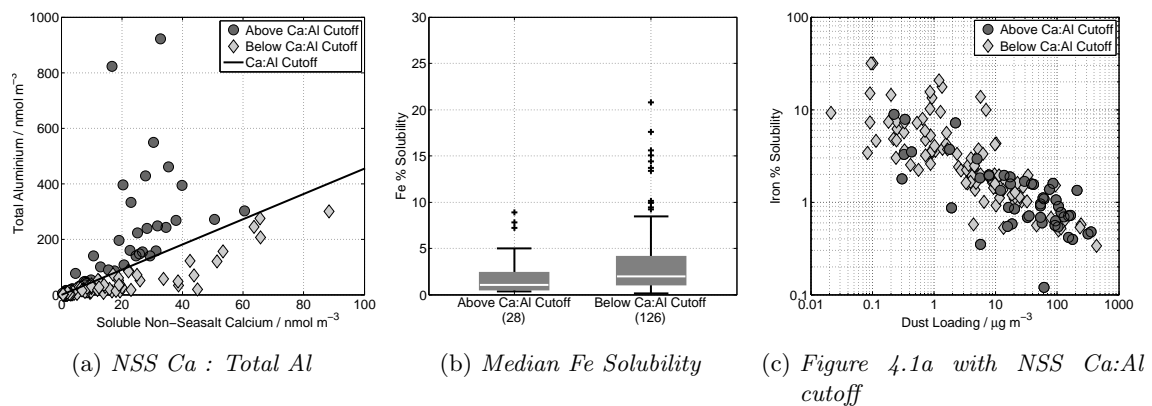


Figure 4.6: The variation of non-seasalt calcium to aluminium ratio in Saharan region samples. (a) shows how the region was divided according to NSS Ca to Al ratio; (b) the median iron solubility for both populations; and (c) the iron solubility to dust loading plot highlighting samples with high and low proportions of NSS Ca to Al

Other methods of differentiating point sources within the Sahara include both the latitude at which the samples were collected and the time of year they were collected in. For example *Stuut et al.* (2009) show that the majority of aerosol deposits from the Cape Verde Islands originate from sandy Saharan regions and are distinct from deposits on the Canary Islands, which are largely Sahelian in origin. Additionally, *Chiapello et al.* (1995) show that although there is some deposition of dust transported to the Cape Verde Islands from the Sahel by the Saharan Air Layer during the summer, the amount of dust aerosol deposited during winter by lower level trade winds is far greater.

In order to examine the idea that point sources in the Sahara can be identified by either season in which the dust is transported (analogous to the change between low level trade wind transport and high altitude SAL transport), or by the latitude band in which it was collected (c.f. the difference in Cape Verde and Canary Island 'loess'), figure /reffig:seasonlat shows the variation in iron solubility for Saharan samples between winter and summer and for samples collected from different latitude bands. However, a Kruskal-Wallis test for both sets of data (figure /reffig:seasonlata & c) show that there is no significant difference in iron solubility for neither seasonally sorted data nor data sorted by the latitude at which it was collected.

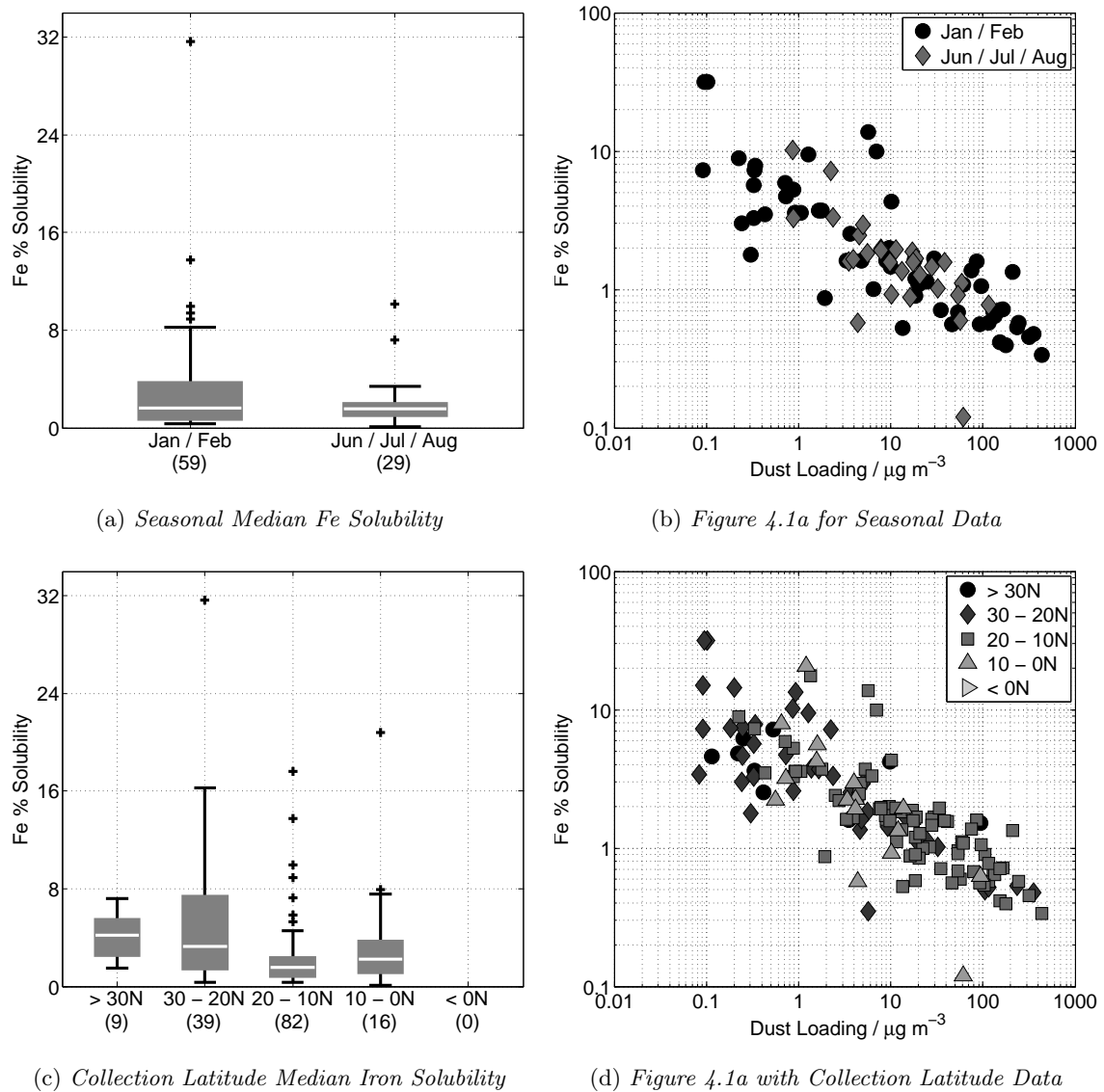


Figure 4.7: (a) Box and whisker plots for the iron solubility during Winter and Summer, crosses denote outliers (b) Iron solubility against dust loading showing Winter and Summer (c) Box and whisker plots for the iron solubilities collected at different latitude bands, crosses denote outliers (d) Iron solubility against dust loading for different latitude bands

In summary, it is not possible to establish that a gradient in iron solubility exists across the Sahara with this data. It is possible that such a gradient does exist, but the reported changes iron solubility in soil samples (*Castillo et al.*, 2008) are less than one or two percent, which would be obscured by the much greater change observed in this data set with respect to dust loading. Additionally, as the samples are collected some distance from the point sources this may mean that different dust particle populations are integrated enough over time to further mask any changes in iron solubility.

4.5 Atmospheric Processing

Laboratory studies have shown how acid species in the atmosphere can increase the solubility of iron in aerosol (*Spokes and Jickells, 1995; Desboeufs et al., 1999*), and several modelling studies include this acid processing effect in their calculations (*Luo et al., 2005*).

Previous observational studies (*Baker and Jickells, 2006*) have looked for a link between species in aerosol normally associated with the acid trace gases in the atmosphere and iron solubility. In a same vein, figure 4.8 shows the variation of aerosol iron solubility with nitrate (plot a) and non-seasalt sulphate (plot b) as proxies for nitric acid and sulphuric acid respectively. However, it could be argued that the extent of acid processing is not only a function of the concentration of acid species within the aerosol, but also the concentration of basic species within the aerosol, i.e. it is the amount of excess acid in the aerosol that should affect the iron solubility (*Jickells et al., 2003*). Aerosol acidity is calculated using equation 4.1 and assumes that all the nitrate and non-seasalt sulphate aerosol are derived from nitric and sulphuric acids respectively; the only basic species in the aerosol are ammonium and calcium carbonate (which is assumed to be the only source of non-seasalt calcium); and that the aerosol is perfectly internally mixed, i.e. the acid species, basic species, and metal species are all present on the all particles. The variation of iron solubility with the aerosol acidity is plotted in figure 4.8c.

$$\text{Aerosol Acidity} = 2 * [NSSSO_4] + [NO_3^-] - [NH_4^+] - 2 * [NSSCa] \quad (4.1)$$

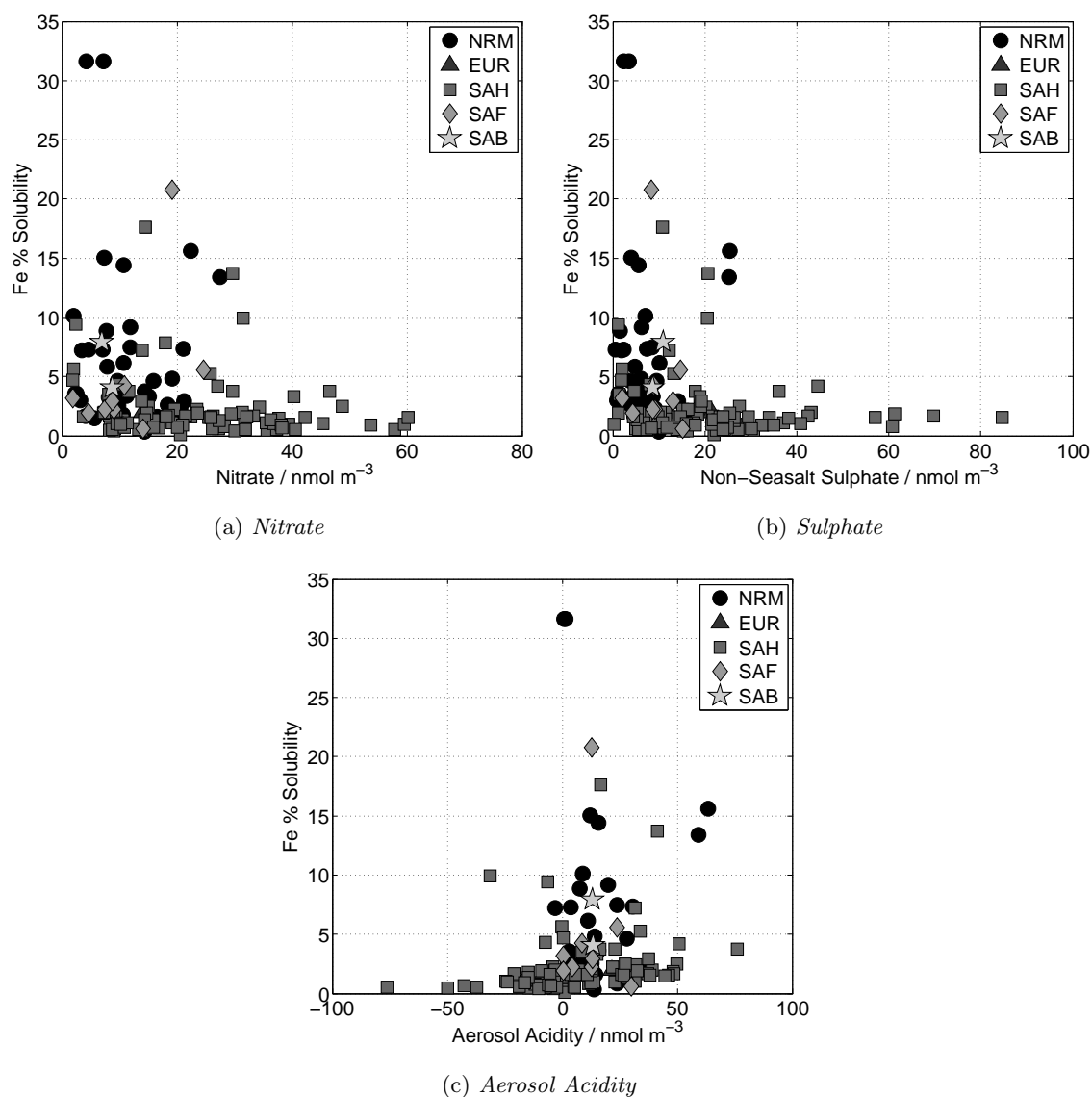


Figure 4.8: Variation of iron solubility with (a) nitrate; (b) sulphate; and (c) aerosol acidity, as defined in equation 4.1

It seems intuitive that if acid processing were occurring, an increase in acidity, sulphate or nitrate concentration would see a corresponding increase in the solubility of iron aerosol, although it would seem from the plots in figure 4.8 that this isn't the case. There are, however, several assumptions that have been made in generating the plots. The main source of uncertainty is the assumption that the aerosol is well mixed and that the acid species are in contact with the iron particles. This may not be the case since although iron aerosol from Saharan dust generally occurs in the coarse mode, sulphate and ammonium aerosols tend to occur in the fine mode (*Baker and Jickells, 2006*), and there is some evidence that aerosol samples originating from the Sahara gathered in the tropical North Atlantic are not well mixed (*Baker and Croot, 2010*, and references therein). Additionally, in the marine boundary layer, sulphate is normally found in the fine mode in the form

of ammonium salts (*Ooki et al.*, 2009), so unable to react with the iron in the coarse mode, although this should be taken into account by calculating aerosol acidity. Nitrate in seasalt is in the coarse mode and will lower pH, but the acid displacement reaction with the seasalt (equation 3.1 on page 41) leads to the release of HCl, which may be lost to the atmosphere before it can react with the iron (*Keene et al.*, 1998). As a result neither nitrate nor sulphate can be used as a reliable tracer of aerosol pH. Finally, if the whole aerosol population were to stay suspended in the airmass, and there was an acid processing effect on the iron containing particles over time, the concentration of acid species might well correlate with iron solubility. However, over time aerosol is deposited to the ocean and larger particles are more subject to gravitational settling than smaller particles. This means that the concentration of acid species within the aerosol diminishes with transport distance thus even if acid processing has occurred, the acid species responsible are unlikely to remain suspended in the air mass for long (*Luo et al.*, 2005).

Another way to look for evidence of atmospheric processing is by looking for changes in the redox state of the iron. *Siefert et al.* (1999) argue that aqueous chemistry occurring in cloudwater in the presence of light and in a complex matrix can lead to the photochemical reduction of ferric iron, Fe(III), species present mineral dust aerosol to more soluble ferrous iron, Fe(II). Labile Fe(II) has not been measured for this data set, however it is possible to test if Fe(III) has been reduced to labile Fe(II) by comparing the iron solubility (which would have increased as a result of this redox chemistry) to the aluminium solubility (which is not affected by redox chemistry) (*Greenwood and Earnshaw*, 1997). For this study the quantity solubility change has been defined in equation 4.2. Both the aluminium and iron solubilities have been normalised by dividing by the median value in order that solubilities can be compared. The major assumption is that aluminium does not undergo any redox chemistry.

$$\text{Solubility Change} = \frac{\%Sol_{Fe}}{\%Sol_{Fe(\text{median})}} - \frac{\%Sol_{Al}}{\%Sol_{Al(\text{median})}} \quad (4.2)$$

Where $\%Sol_{Al}$ and $\%Sol_{Fe}$ are the iron and aluminium solubilities and $\%Sol_{Al \text{ median}}$ and $\%Sol_{Fe \text{ median}}$ are the median iron and aluminium solubility.

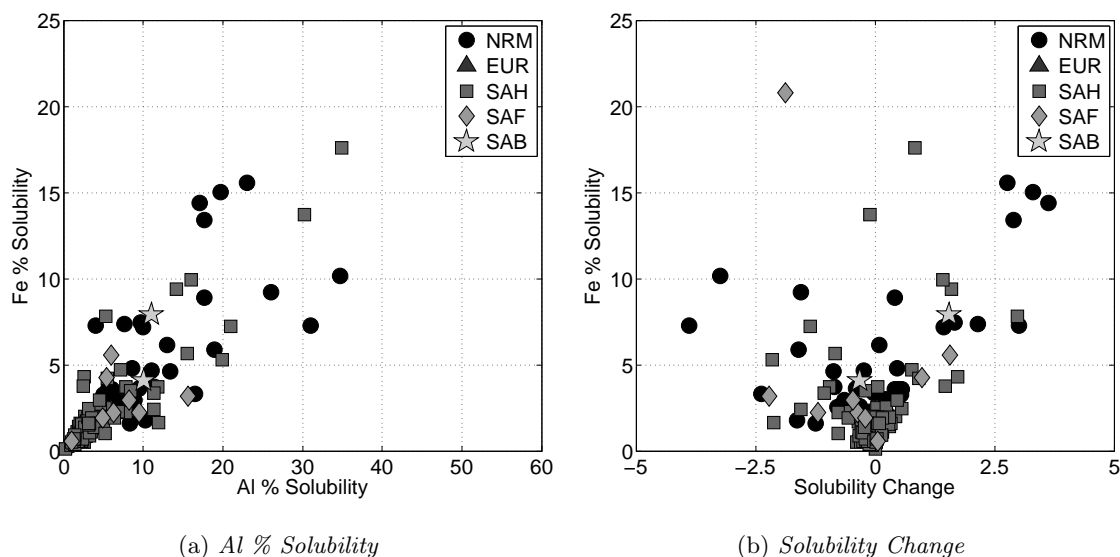


Figure 4.9: Variation of iron solubility with (a) aluminium solubility and (b) the solubility change between iron and aluminium (as calculated from equation 4.2)

As shown in figure 4.9a there is little scatter between the iron and aluminium solubilities, and figure 4.9b shows more clearly that the differences in solubilities are evenly spread about 0, hence either aluminium and iron appear to be behaving in a similar manner, or the iron is undergoing two competing and opposite redox reactions. This would seem to imply that changes in iron and aluminium solubility are brought about by the same mechanism, rather than a photochemical reaction which would be specific to iron alone. This result should be taken with a little caution however, as it is possible that redox chemistry is occurring, but that both the aluminium and iron solubilities are undergoing a greater change due to a different cause, which masks the redox chemistry effect.

In general, although the effect of atmospheric processing on the solubility of aerosol iron cannot be completely ruled out for this data set, it is unlikely that this effect is very large in this data set compared to the observed changes in solubility.

4.6 Solubility as a function of particle size

Particle size can be seen as a physical control on the solubility of iron aerosol, as opposed to the chemical effects of atmospheric processing and mineralogy. If it is assumed that the labile, soluble iron is only present on the surface of the particle, and any iron present inside the crystal lattice of the particle is therefore insoluble on short timescales, it follows that if the aerosol particles have a greater surface area, then proportionally more of the iron will be soluble. Thus smaller particles (with a greater surface area to volume ratio) should have a greater aerosol iron solubility.

Recent data has shown that dust aerosol in the Sahel region is dominated by aluminosilicate material, which occurs both in the coarse and fine mode, but rarely less than $0.4\mu\text{m}$ in diameter (*Osborne et al.*, 2008). As the dust aerosol is transported through the atmosphere a proportion of it will then be deposited back to ground level through gravitational settling and other processes (see section 2.4). Larger particles with greater mass are more susceptible to gravitational settling, as is demonstrated by the deposition velocities shown in figure 2.10 on page 31, which are modelled from the equations in *Ganzeveld et al.* (1998) for different particle diameters. Therefore, ignoring other effects such as the adsorption of seaspray onto mineral dust particles (*Zhang et al.*, 2005), as the dust aerosol is transported coarser particles can be expected to be deposited preferentially, e.g. one would expect the atmospheric concentration of Saharan dust aerosols collected in the Caribbean to be much lower than at their source, but also the average particle size should be smaller.

Linking the expected reduction in dust mass loading with a reduction in average particle size, caused by transporting aerosol over distances, and a corresponding increase in iron solubility, would therefore seem logical. However, it is not easy to find any evidence for this effect: there is a dearth of data that includes both reliable size distribution data and iron solubilities. However *Baker and Jickells* (2006) show from observations that there is an inverse relationship between surface area to volume ratio, A/V , and dust loading (reproduced in figure 4.10a). Given that figure 4.10a reproduces the shape of the mass loading plot (repeated in figure 4.10b for ease of comparison) it is proposed that iron solubility is related to surface area to volume ratio and therefore dust loading. This seems be consistent with observations that fine mode aerosols have higher iron solubilities than fine mode aerosols (*Siefert et al.*, 1999; *Luo et al.*, 2005; *Baker et al.*, 2006c,a). More recently, iron aerosol concentration and solubility data reported by (*Buck et al.*, 2010) for samples size segregated into 9 fractions show that dust particle size distributions are larger (mostly in the coarse mode) for a dust event near the Cape Verde, in contrast to a more even particle size distribution, with proportionally more fine mode particles, for samples collected during a dust event in a remote southern Atlantic region, just south of the main dust transport pathways, which would be consistent with a transport size effect. However, iron solubility is not necessarily greater for the smaller size fractions, and the shape of the iron solubility against dust loading plot 4.10b is not reproduced with their data.

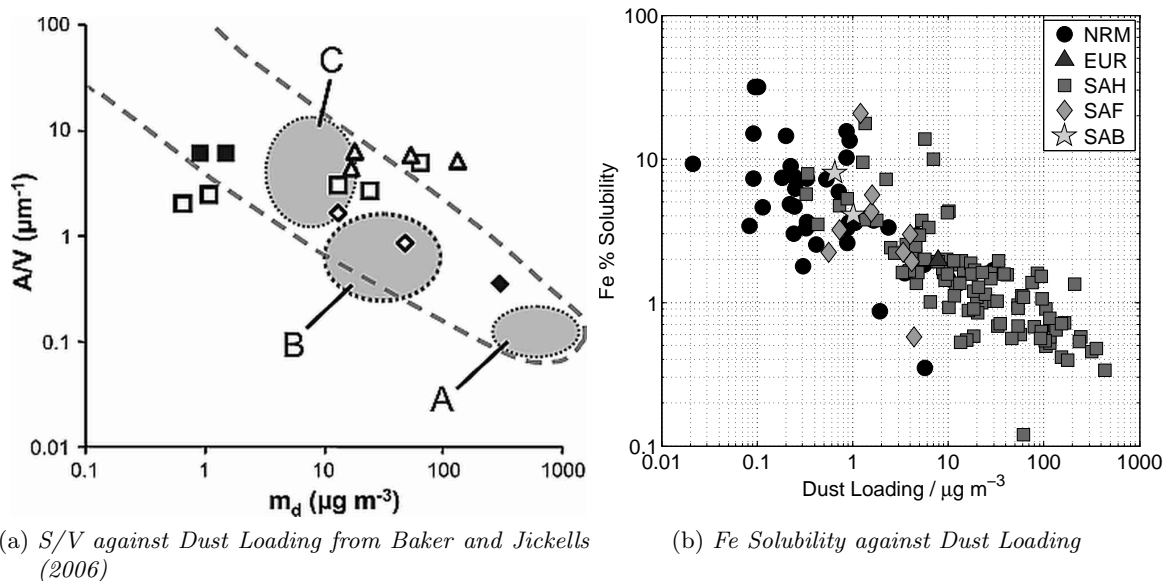


Figure 4.10: Variation of dust mass loading with (a) surface area to volume ratio from Baker and Jickells (2006): A represents near-source dust size distribution and concentration; B, just off the coast of West Africa and C represents data from the Caribbean; (b) iron % solubility for this data for comparison

The data used in this chapter cannot easily be used to investigate this hypothesis: total metal analysis was performed on coarse and fine modes together, and are therefore bulk mode, which means that fractional solubilities are also in bulk mode. However, it is possible to compare coarse and fine fraction of the soluble iron. Figure 4.11 shows the fine to coarse ratio for soluble iron plotted against mass loading. If the particle sizes were distributed symmetrically about a mean value and took the same form, e.g. the normal distribution, for each sample then a lower number would imply more coarse mode aerosol and a greater average particle size. Conversely, a ratio higher than 1 indicates that there is more aerosol in the fine mode, and a smaller average particle size (less than $1\mu\text{m}$). If particle size plays a role in iron solubility and dust mass loading, then we would expect figure 4.11 to show finer aerosols (i.e. the fine to coarse ratio higher) at low dust loading and coarser aerosols (with a lower fine to coarse ratio) at high dust loading. However, it is difficult to see this effect. Greater dust loadings are indeed associated with coarser aerosols, but there is some scatter, and some coarse aerosol is also observed at low dust loadings as well. It is likely that a proportion of the fine dust aerosols increase in size once in the marine boundary layer due to the accumulation of seaspray (Zhang *et al.*, 2005) and this isn't taken into account using simple dust loading as a proxy for dust size.

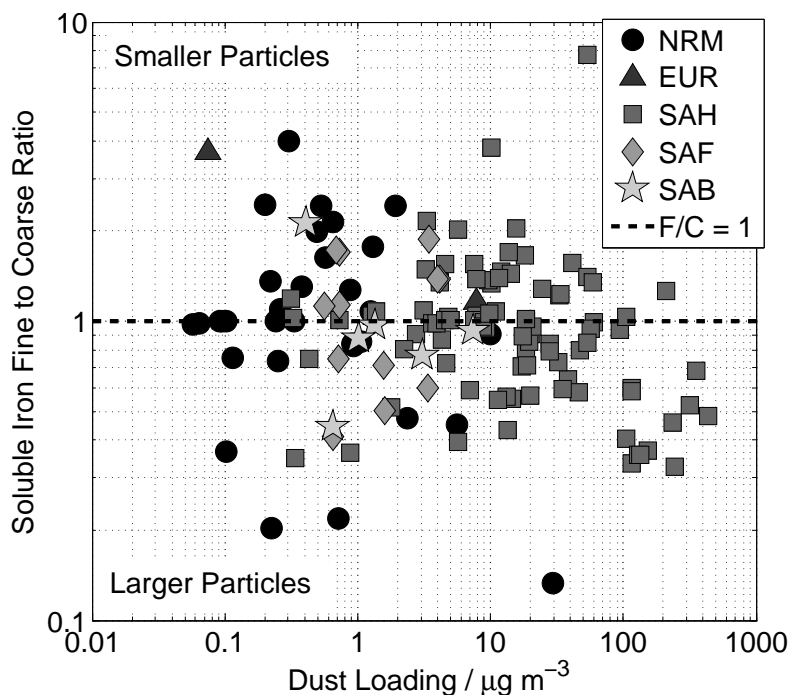


Figure 4.11: *Soluble iron fine fraction divided by coarse fraction, plotted against iron solubility, values less than 1 indicate larger particles, greater than 1 smaller particles*

The observation that dust aerosol occurs predominantly in the coarse mode at high dust loading and both coarse and fine modes at low dust loading in the marine boundary layer, does not prove that there is a relationship between aerosol mass loading and iron solubility due to particle size sorting during atmospheric transport, but neither does it disprove it. The size sorting effect could, in theory, explain the range of solubilities seen in figure 4.10b, but observations of iron solubility with better size resolution are needed to properly test the hypothesis.

4.7 Iron soluble fraction in the tropical North Atlantic

The data set used here is in terms of both spatial coverage and seasonal coverage, quite extensive. This means that the observed increase in iron solubility with the decrease in mass loading is compelling, especially as there is now so much data than in earlier papers (*Baker and Jickells, 2006*).

The atmospheric concentration of total iron aerosol in the eastern tropical North Atlantic is shown by this data set to be dominated by mineral dust from the Saharan and Sahel regions. Because the mineral dusts are so ubiquitous, even during periods of low dust transport, even if iron in a more soluble form is transported to the ocean from anthropogenic sources it is a very small amount in comparison. Therefore, the effect on

iron solubility is very small, and cannot be detected using the data here.

There is evidence that the chemical composition of Saharan/Sahelian dust is remarkably uniform and that in any case dust emitted from different sources quickly converge to a widespread and homogenised atmospheric load, even near-source (*Osborne et al.*, 2008). Any gradients in soil composition are quickly integrated as the dust is transported, so by the time it reaches the ocean any differences may only account for a few fractions of a percent in iron solubility, compared to the orders of magnitude change observed, thus any changes in iron solubility that may be caused by specific source regions across the Sahara are not seen in this data set.

The effect of atmospheric processing on the solubility of iron aerosol cannot be ruled out, but there is little evidence that either acid processing or photochemical reduction has any effect on the iron aerosol solubility in this data set. In any case laboratory experiments (*Spokes and Jickells*, 1995) have shown that iron solubility will change by just a few percent if exposed to acid processing cycles, in comparison to the orders of magnitude difference observed in this data.

The explanation of particle size effects is attractive as it would explain the magnitude of changes in iron solubility seen. However, the data used here cannot be used to prove this hypothesis, although it cannot rule it out either. In the likelihood that aerosol transport does have an effect on dust loading and therefore solubility, it is very difficult to separate the physical effect of particle size fractionation from atmospheric processing effects, particle growth; mixing effects and differences in mineralogy between large and small particles. Aerosol data which includes information on iron solubility and mass particle size distributions, specifically of the mineral dust it contains, would be required to begin looking at this problem in more depth.

In a global context, as 43% of the global dust flux to the world ocean is deposited in the ETNA (*Jickells et al.*, 2005), so it is an important area for global iron biogeochemical cycling, and it is important to quantify not only how much iron this supplies to the ocean, but also whether it is soluble, and therefore likely to be bioavailable for the marine biota. If the increase in iron solubility with decreased mass loading is due to particle size fractionation, it could imply that Saharan dust is more important as a source of iron to the open ocean than originally thought. Although the dust concentrations are lower much further away from the ETNA, the solubility of the iron would be much higher, thus potentially supplying relatively more bioavailable iron to the remote open ocean.

Chapter 5

Climatology

5.1 Background

Given the relative importance of atmospheric deposition of iron, phosphate and, nitrogen, to the open ocean (see section 1.4, figure 1.1) several attempts have been made to estimate the flux of these to the global ocean and the North Atlantic Ocean in particular: table 5.1 lists just a few of these.

Recent estimates of the global atmospheric flux of iron to the open ocean range from 4.5 – 12 Tg yr⁻¹ (*Krishnamurthy et al.*, 2010), although 16 Tg yr⁻¹ is reported elsewhere (*Jickells et al.*, 2005). Modelling studies have estimated that only 2 Tg yr⁻¹ of the global iron flux is due to combustion sources (*Luo et al.*, 2008), and that most of the remainder is derived from mineral dust.

As it is adjacent to West Africa, mineral dust transported from the Saharan region dominates the atmospheric flux of iron the ETNA. The flux of Saharan dust to the North Atlantic alone is estimated at 170 Tg yr⁻¹, which accounts for 43% of the total global flux of mineral dust to the open ocean (*Jickells et al.*, 2005). Thus, the ETNA is an area of high annual mineral dust input and quantifying the dust (and iron) input to this region is important for trying to understand these global fluxes. However, the input of the dust is episodic, for example, the deposition of dust carried to the Caribbean on the SAL is known to pulse every 3–5 days during the summer (*Prospero and Lamb*, 2003). It is this variability which makes dust deposition, and therefore the atmospheric iron flux, difficult to constrain.

In order to quantify dust deposition to the open ocean, several methods have been used to take into account this variability and broadly they can either be described as modelling, satellite observations or measurements. Several global dust aerosol models have been developed to better understand the atmospheric flux of dust. These models usually describe dust as a passive tracer of model-predicted meteorological fields, but with its own set of wet and dry removal processes (*Mahowald et al.*, 2005b). Whilst the modelling of dust transport appears to be good on most models, the source can present a problem, and although recent global models can take into account the influence of different surface conditions like erodible soil elements and soil moisture, the models tend to be limited by the lack of data on these surface conditions. Global models predict dust emissions of between 1000 – 2000 Tg yr⁻¹ for particles with a radius of less than 10 μm (*Mahowald et al.*, 2005b). Smaller-scale regional dust emission models have also been developed for the Saharan region, e.g. *Martcorena et al.* (1997), a model which was parameterized using an established map of surface features for the region coupled with ECMWF surface wind fields. This result was in good agreement with satellite data on dust uplift and production, although there were still difficulties in predicting changes in aerosol size distribution and chemical composition.

In a similar vein, much work has been carried out to quantify global dust fluxes using satellite remote sensing. Sensors used are now capable of distinguishing dust from smoke and marine aerosols, and can be used to derive an atmospheric deposition flux of dust to the ocean ($140 \pm 40 \text{ Tg yr}^{-1}$ (*Kaufman et al.*, 2005)), although information on the chemical composition, and hence the flux of iron or other nutrients is difficult to achieve.

Several flux estimates have been made using long time-series from island sites. *Tian et al.* (2008) use iron measurements from the Bermuda Atlantic Time Series (BATS) site to derive first a seasonal flux for the waters just off the coast of Bermuda, which was then averaged to an annual flux of $171 \mu\text{g m}^{-2} \text{ day}^{-1}$.

Other time series measurements at Barbados by *Prospero et al.* (1996) use observations combined with models to estimate the dust flux to the North Atlantic as 170 Tg yr^{-1} . In general, time-series measurements from island stations and remote sites are invaluable for quantifying the atmospheric flux of iron and dust to the regions they represent. However, they can provide little data for regions further afield, as the spatial coverage is limited. For example the major fraction of this flux collected in Bermuda and Barbados is due to dust pulses recorded during the summer months (June, July and August) (*Prospero and Lamb*, 2003), and low-level dust transport which is particularly intense over the ETNA during winter (*Pye*, 1987) is not transported across the Atlantic.

Other shorter time-series records include the sampling of dust aerosols at the Cape Verde between December 1991 and December 1994 of (*Chiapello et al.*, 1995), who reported a seasonal signal in dust transport to the region and maximum monthly mean dust concentrations of 120, 97, and $70 \mu\text{g m}^{-3}$ for 1992, 1993 and 1994 respectively, although flux to the Cape Verde region was not estimated. Additionally measurements made by *Dulac et al.* (1989) between 1985 and 1986 at the Northwestern coast of Corsica measured the aluminium flux to the western Mediterranean to be $1090 \mu\text{g m}^{-2} \text{ day}^{-1}$, with dust deposition being dominated by particles with a diameter greater than $10 \mu\text{m}$. At the same time *Bergametti et al.* (1992) measured an atmospheric flux of phosphate of $110 \mu\text{g m}^{-2} \text{ day}^{-1}$ for the same region. These shorter time-scale sampling campaigns are very good at providing insights into aerosol composition and dust concentrations under various wind and weather conditions, however deriving average annual fluxes for these regions is difficult as temporal resolution may not be enough.

Although samples taken from on board cruises can provide much better spatial resolution and therefore, in theory, apply to a much wider region, they do provide poorer temporal resolution than time-series observations. Additionally, because the datasets are so small, it cannot be assumed that a mean flux taken from all samples from the area represents a mean value of all deposition to the area (*Miller and Miller*, 2005).

Baker et al. (2010) get round this problem of representation by taking into account the source region of each sample gathered and then weighting each sample by the

probability that aerosol with the same source region would be deposited. This probability can be calculated from air mass back trajectories. The method assumes that aerosol samples originating from the same source region should have the same or similar chemical composition and that any transport effect on the chemical composition of samples taken from the same sampling region will apply equally to all samples. However, the approach taken did not take into account any seasonal deposition patterns, and although this may not be relevant for discussing the deposition of nitrogen aerosol, it is important when considering iron aerosol, due to the fact that the Saharan dust is transported by different wind systems at different times of the year.

The approach adopted here is to expand the *Baker et al.* (2010) method to take into account the seasonal variation of the atmospheric deposition and thus the seasonal cycle of dust deposition. In addition to iron deposition, the atmospheric flux of the nutrients inorganic nitrogen and soluble reactive phosphate is also considered. The robustness of this approach does require a relatively large data set of observed aerosol and rain concentrations within this region, so the dataset used in chapter 4 is used here.

	Region	Deposition Flux		Comments	
		$\mu\text{g m}^{-2}\text{ d}^{-1}$	Tg yr^{-1}		
<i>Krishnamurthy et al. (2010)</i>	Global Ocean	Fe	36 - 98 ‡	4.5-12	Review of modelling and observation
<i>Duce and Tindale (1991)</i>	Global Ocean	Dust		900	extrapolation of observations
		Fe		32	
	North Atlantic	Dust		220	
		Fe		7.7	
<i>Mahowald et al. (2005b)</i>	Global Ocean	Dust		1000 – 2000	modelling and observations
<i>Luo et al. (2008)</i>	Global Ocean	Fe	98 †	12	Model - Fe from dust and combustion sources
<i>Kaufman et al. (2005)</i>	Atlantic Ocean	Dust		100 – 180	Satellite remote sensing
<i>Jickells et al. (2005)</i>	Global Ocean	Dust	3670 †	450	Review of modelling and observation
		Fe	130 †	16	
	North Atlantic	Dust		194 *	
		Fe		3.3 *	
<i>Mahowald et al. (2008)</i>	Global Ocean	P	0.6	4.6	Model data
	Atlantic Ocean	P	0.2	6	
<i>Prospero et al. (1996)</i>	North Atlantic	Dust	3260 * †	170	Observational data and models
		Fe	115 * †	6	
	Bermuda	NO_3^-	145		
	Barbados	NO_3^-	59		
	Mace Head	NO_3^-	190		
<i>Tian et al. (2008)</i>	Bermuda	Al	308.73		dry deposition averaged over sampling period
		Fe	171.97		
<i>Dulac et al. (1989)</i>	Western Mediterranean	Al	870		Observations
		Fe	460 †		
<i>Bergametti et al. (1992)</i>	Northwest Mediterranean	P	110		Observations
<i>Duce et al. (2008)</i>	Global Ocean	TSN	550 †	67	Observations and Models
<i>Baker et al. (2010)</i>	North Atlantic	NO_3^-		4.48	Climatology based on observational data
		NH_4^+		2.28	
		TIN		6.76	
		P		0.004	

Table 5.1: Flux estimates: where values have been converted for easy comparison the following assumptions have been made:

* - assuming that the North Atlantic receives 43% of the global input of dust to the world ocean (*Jickells et al., 2005*)

† - assuming that mineral dust Fe:Al ratio is 0.53 (*Chiapello et al., 1997*)

‡ - assuming surface area of global ocean is $335.3 \cdot 10^6 \text{ km}^2$, North Atlantic (incl. Caribbean) $54.9 \cdot 10^6 \text{ km}^2$, and South Atlantic $51.2 \cdot 10^6 \text{ km}^2$

5.2 Defining the ETNA region

There is currently a large amount of interest in the ETNA, not least because it is an area of such high annual dust input (*Mahowald et al.*, 2005b). Over the last 10 years aerosol concentration data from several cruises in and through the region has been collected (*Baker et al.*, 2006c,b; *Rijkenberg et al.*, 2008) and the climatology described here was developed to look at the aerosol input to this region in more detail. In order to maximise the amount of data available, the climatology area was defined as $-5 - 35$ N; $14 - 38$ W. Table 5.2 shows how this climatology region was then further divided into eight boxes, or climatology points.

Identifier	Latitude ($^{\circ}$ N)	Latitude Bounds ($^{\circ}$ N)	Longitude ($^{\circ}$ W)	Longitude Bound ($^{\circ}$ W)
ETNA A	30	25 - 35	-32	-38 - -26
ETNA B	30	25 - 35	-20	-26 - -14
ETNA C	20	15 - 25	-32	-38 - -26
ETNA D	20	15 - 25	-20	-26 - -14
ETNA E	10	5 - 15	-32	-38 - -26
ETNA F	10	5 - 15	-20	-26 - -14
ETNA G	0	-5 - 5	-32	-38 - -26
ETNA H	0	-5 - 5	-20	-26 - -14

Table 5.2: *Details of each climatology region*

The climatology points ETNAB, ETNAD, ETNAE, and ETNAG (see table 5.2) were chosen to coincide with points in the nitrogen and phosphorus climatology of *Baker et al.* (2010) so comparison between the climatologies could be made. The rest of the points were chosen in order to form a regular grid, so that the expected seasonal changes, especially in the ITCZ, would be shown.

A fuller description of the meteorological conditions of the ETNA is given in section 1.3, but briefly the precipitation falls into 2 regimes: the North Atlantic dry region, where dry deposition dominates, and the inter-tropical convergence zone (ITCZ) where wet deposition dominates, so the northern points in the climatology (ETNAA-D) should be quite different in character to the southern points (ETNAE-H).

5.3 The ETNA data set

The data set used here is the same as the one used in chapter 4 and consists of samples collected on a total of 22 cruises either in or passing through the ETNA between October 2000 and October 2008. The number and type of aerosol and rain samples collected in the ETNA region on each cruise is summarised in table C.1 on page 157. In the case of

aerosol samples, this represents a large dataset of ship collected samples and the sampling location of each of the 273 dry deposition samples used in the climatology is shown in figure 5.1a.

Due to the generally low precipitation rate for the region; the difficulty in sampling wet deposition; and the probability that a cruise will pass directly under a rain cloud at the moment it rains, the number of rainwater samples are fewer (figure 5.1b) with a total of 36 samples, although the small amount of samples is taken into account when the wet deposition fields were calculated.

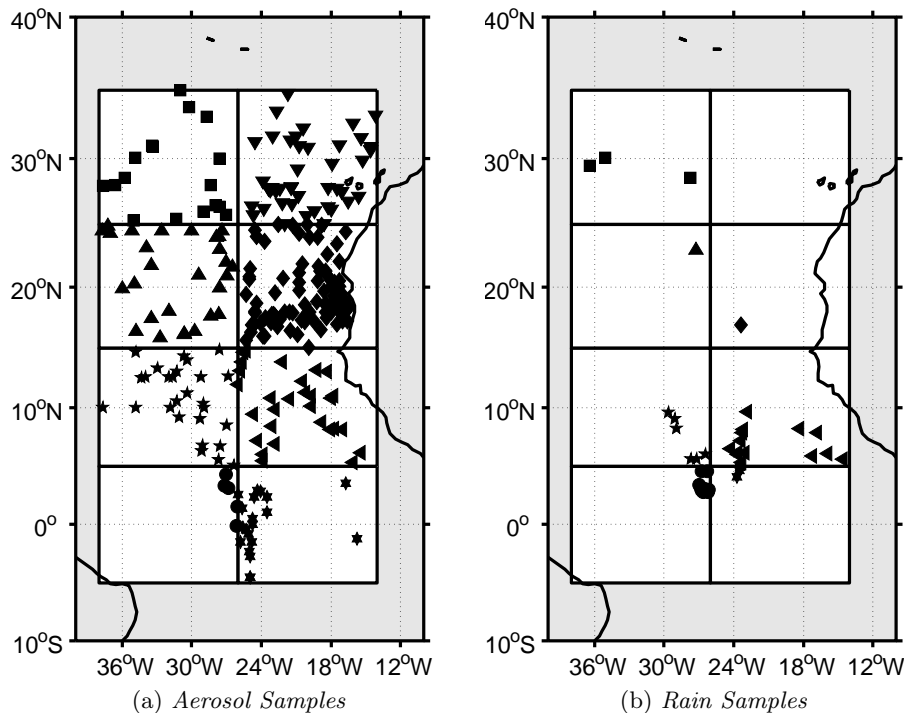


Figure 5.1: *The sampling locations of all wet and dry deposition data used*

5.4 Constructing the aerosol climatology

The seasonal atmospheric deposition climatology for the ETNA region consists of two main elements. First, the probability of the aerosol arriving at each climatology point being derived from any given source region (as defined in figure 2.12 on page 35 was calculated from air mass back trajectories (see section 5.4.1).

Secondly, the ETNA aerosol data set (section 5.3) was used to derive seasonal average values for the aerosol composition (or average composition fields) for the northern and southern half of the climatology region (see section 5.4.2). The average values used here are robust means, as although the much of the atmospheric concentration data are not

exactly normally distributed, they could be regarded as Gaussian with a heavy-tailed error distribution, thus a mean value would be overly affected by any outliers and a median value would overly disregard them (*Miller and Miller, 2005*).

The average composition fields were then weighted by the probabilities to find the flux for each season, which were then added together to find the total flux to the area (section 5.4.3). All the calculations were done using Matlab, and the file containing all the scripts (`climatology.m`) is included in Appendix E

5.4.1 Seasonal back trajectory probabilities

Gathering 5-day air mass back trajectories from BADC for each climatology point at 12 hour resolution over a ten year period has been described earlier in section 2.5 on page 32.

The data was downloaded from BADC in netcdf format. After the files had been read into Matlab, several checks were made to ensure that the data had been read correctly: trajectories for each climatology point must start on 14th March 1999 and finish on 14th March 2009; all trajectories must output at 6 hour intervals; with a total of 120 records for each trajectory; each starting at the correct latitude, longitude and height above ground level; and all trajectories must go backwards in time.

The height and position coordinates were then extracted for each trajectory at each height at the beginning, 3-day back and 5-day back point. In order to facilitate the sorting of back trajectories into source region types a number of other variables were also needed: the month of year, to correctly determine whether the trajectory might be affected by African biomass burning season (see section 1.5.1); and the bearing between the surface and topmost trajectories at 5 days, which was used to identify those trajectories that appear to be SRM in origin, but contain a SAF/SAB signal (see figure 5.2).

Due to the large amount of trajectories involved (7307 requests at 3 different heights for each of the 8 areas giving a total of 175368 trajectories), assigning trajectories to a source region was not trivial: first initial assignments were made according to the location of each trajectory at each height at 3 and 5 days, then these were refined using a rigorous set of rules, using chemical analysis data to check whether or not these rules worked (*Baker et al., 2010*).

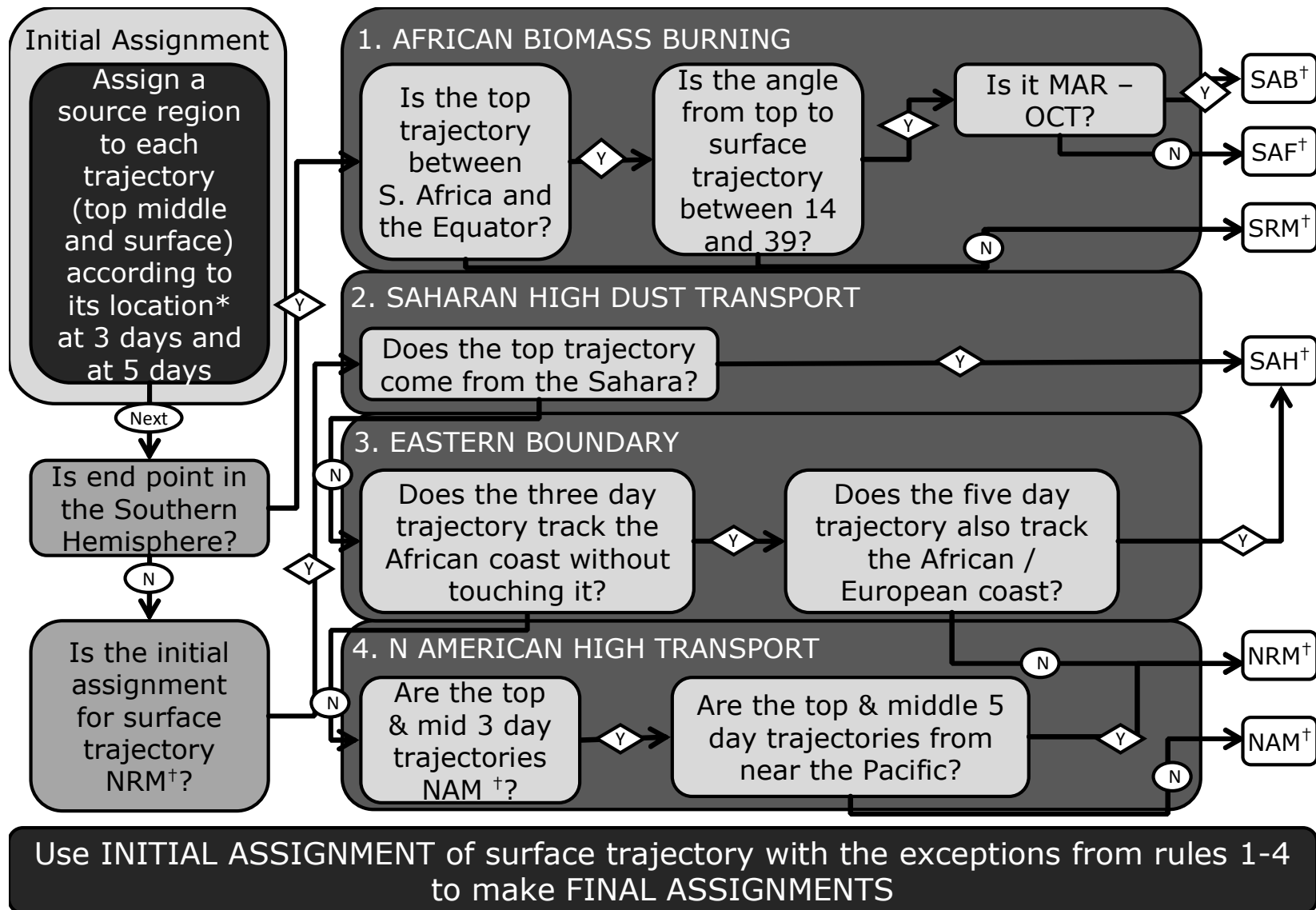


Figure 5.2: Flow chart for assigning air mass back trajectories to air mass types. The air mass types (NAM, EUR, SAH, SAB, SAF) are described in table 2.5 on page 34 and shown on the map in figure 2.12 on page 35

Generally the location of the 3-day surface back trajectory was taken to represent the air mass type, unless this was from a remote region, in which case the 5-day back trajectory position was taken. This is because a continental source region three days back would have a stronger influence than a continental source region 5 days back, however, the concentration of continentally derived aerosol is very low in the marine boundary layer (*Raes et al.*, 2000) so that an air mass that has been over a continent five days back would still have a high aerosol concentration compared to one that had been in a remote area all this time. If the five day surface trajectory was also from a remote region and the upper two trajectories 3-day back trajectories were from the same continental source, these were taken to represent the airmass. This is because the higher air masses can carry large amounts of continental matter at great height, which may then settle gravitationally. Exceptions to this general rule are shown as a flow diagram in figure 5.2.

The first major exception was for trajectories ending in the South Atlantic, i.e. climatology points ETNAG and ETNAH. Previous observations (*Baker et al.*, 2006b) have noted that 5-day back trajectories may track, but not touch, southern Africa, yet the chemical composition is that of a biomass burning (SAB) / continental source (SAF) sample. *Baker et al.* (2010) found that these samples could be differentiated from southern Atlantic remote (SRM) samples by looking at the combination of back trajectories in more detail: first of all the end point would be in the southern hemisphere, below the ITCZ; the top trajectory would come from the direction of Africa, i.e. the bearing between the trajectory end point and the location at 5 days back would have a bearing between that of the endpoint and the equator (0°N) and the endpoint and the coast of South Africa (28°S , 16.5°E); lastly the difference in the bearing between the trajectory endpoint and the location at 5 days for the top trajectory and for the bottom trajectory should be between 14° and 39° .

Secondly, as the majority of the Saharan dust transport during the summer months happens at great height (section 1.3), if the surface trajectory was from a the remote north Atlantic (NRM) and either of the upper two trajectories were from the Sahara (SAH) then the air mass type was designated as SAH.

Likewise, trajectories that track round the coast of Africa and sometimes Europe at all three levels, without actually touching a landmass were also found to have the chemical composition of the Saharan source region, and were assigned as such.

Finally, a few surface trajectories (about 5 or 6 in total) with a North America (NAM) location were found have higher trajectories with a 5-day location in or near the Pacific Ocean. Further analysis showed that although the trajectory location was above North America, they were at a high altitude, and moving much higher and faster than any detectable aerosol pollution, so these trajectories were considered to have a remote origin.

After an air mass type had been assigned to each back trajectory, probability of each

air mass occurring was calculated as the cumulative number of back trajectories assigned to that air mass type, divided by 7307, or the total number of trajectories requested for each climatology point. The annual probabilities for each climatology point are shown graphically in figure 5.3, and the probabilities, both as percentages and absolute numbers of trajectories, can be found in table 5.3.

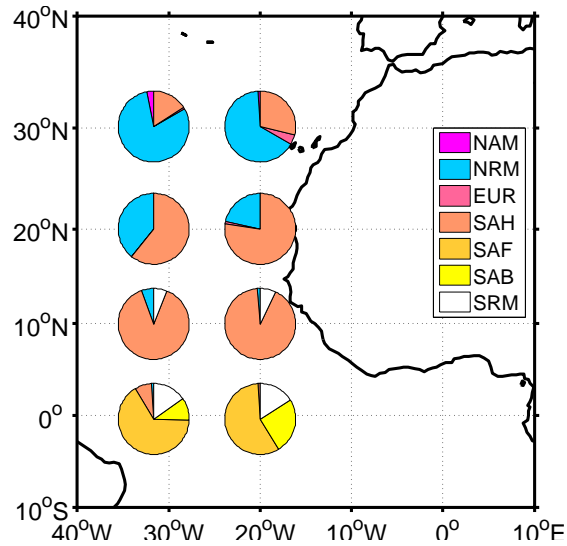


Figure 5.3: Annual source region percentages for each climatology point

Airmass Type		Spring (MAM)		Summer (JJA)		Autumn (SON)		Winter (DJF)		Annual	
		number	%	number	%	number	%	number	%	number	%
ETNAA	NAM	47	3.31	2	0.13	18	1.42	107	7.57	174	3.09
	NRM	1207	85.00	1404	91.88	990	78.08	910	64.40	4511	80.14
	EUR	9	0.63	1	0.07	10	0.79	19	1.34	39	0.69
	SAH	157	11.06	121	7.92	250	19.72	377	26.68	905	16.08
ETNAB	NAM	18	1.24	3	0.20	8	0.64	33	2.32	62	1.10
	NRM	988	68.33	1247	81.99	794	63.07	674	47.33	3703	65.54
	EUR	65	4.50	11	0.72	76	6.04	105	7.37	257	4.55
	SAH	375	25.93	260	17.09	381	30.26	612	42.98	1628	28.81
ETNAC	NAM	1	0.06	0	0.00	0	0.00	3	0.19	4	0.06
	NRM	996	59.04	573	34.39	370	24.73	587	36.80	2526	39.20
	EUR	1	0.06	1	0.06	3	0.20	1	0.06	6	0.09
	SAH	689	40.84	1092	65.55	1123	75.07	1004	62.95	3908	60.65
ETNAD	NAM	1	0.06	0	0.00	0	0.00	2	0.11	3	0.04
	NRM	666	36.69	309	18.66	197	11.28	335	19.00	1507	21.59
	EUR	35	1.93	2	0.12	24	1.37	28	1.59	89	1.27
	SAH	1113	61.32	1345	81.22	1526	87.35	1398	79.30	5382	77.09
ETNAE	NRM	120	6.83	41	4.32	67	5.93	94	5.37	322	5.76
	SAH	1637	93.17	713	75.05	922	81.59	1657	94.63	4929	88.21
	SRM	0	0.00	196	20.63	141	12.48	0	0.00	337	6.03
ETNAF	NRM	32	1.78	13	1.63	14	1.05	13	0.72	72	1.26
	SAH	1762	98.22	482	60.25	1216	91.02	1790	99.28	5250	91.58
	SRM	0	0.00	305	38.13	106	7.93	0	0.00	411	7.17
ETNAG	NRM	65	3.88	0	0.00	0	0.00	13	0.78	78	1.12
	SAH	253	15.11	3	0.17	10	0.55	257	15.35	523	7.49
	SAF	994	59.38	1223	67.31	1186	65.20	1205	71.98	4608	65.98
	SAB	58	3.46	221	12.16	436	23.97	0	0.00	715	10.24
	SRM	304	18.16	370	20.36	187	10.28	199	11.89	1060	15.18
ETNAH	NRM	4	0.23	0	0.00	1	0.05	0	0.00	5	0.07
	SAH	17	0.96	3	0.16	17	0.93	40	2.25	77	1.07
	SAF	1180	66.52	766	41.70	811	44.56	1382	77.73	4139	57.41
	SAB	239	13.47	815	44.37	777	42.69	0	0.00	1831	25.40
	SRM	334	18.83	253	13.77	214	11.76	356	20.02	1157	16.05

Table 5.3: Number of trajectories assigned to each airmass and percent for each climatology point

A seasonal breakdown of these percentages is shown in figure 5.4. This clearly shows higher SAH input to the ETNA in the summer (connected with the high summer transport) and winter (due to the low-level transport across the Sahel). In addition, the marked variation in the source region for the southern boxes as the ITCZ cycles up and down through the year is also shown. Again the percentages and cumulative totals of trajectories are shown in table 5.3. Both these observations are consistent with the known climate of the region (as outlined in section 1.3).

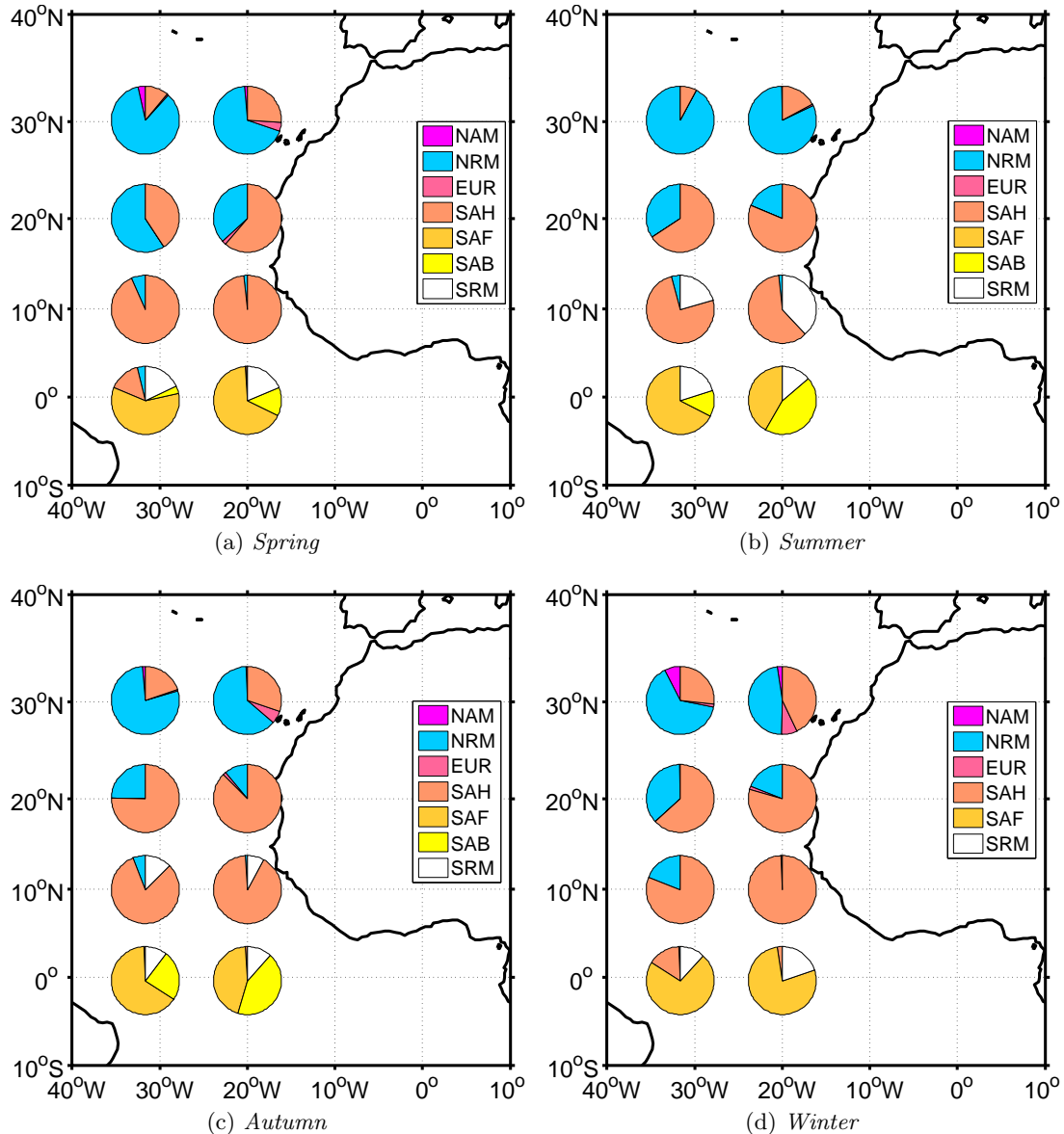


Figure 5.4: The seasonal variation of source region percentages for each climatology point

5.4.2 Seasonal average aerosol composition

Having derived the seasonal probability of an air parcel arriving at each climatology point from each source region in the previous section, seasonal average composition fields are then needed in order to be able to calculate how much iron, aluminium, phosphate and nitrogen would be carried by this air parcel. This is achieved by averaging the available data for the region by season, climatology box and source region type.

When averaging the aerosol data it was important to consider not only the number of samples, but also when and where these samples were collected: ideally, the samples needed to be sorted by air mass type, climatology region and time of year in such a way as to be representative of these conditions once averaged. The month-by-month distribution of dry deposition data between regions is shown in figure 5.5a. This shows how strongly the data is biased to May and October, when most of the Atlantic Meridional Transect (AMT and ANT) cruises took place.

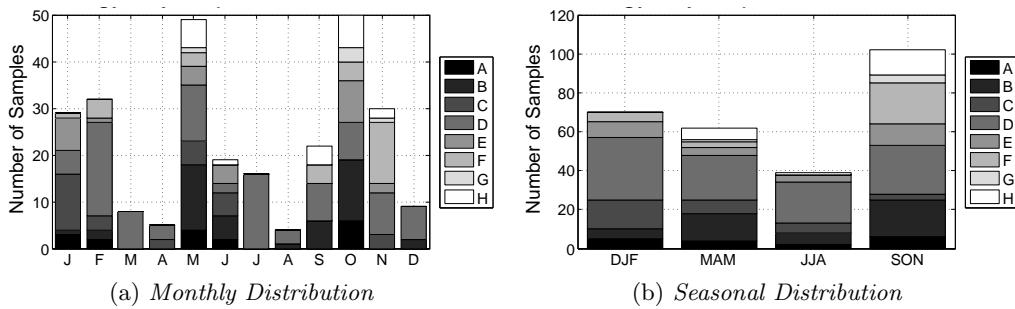


Figure 5.5: *The distribution of data over the year between different regions, for data collected in climatology regions ETNAA–ETNAH (denoted A–H in figures), as defined in table 5.2*

As figure 5.5a shows, there is not quite enough data for averaging on a monthly basis without creating large uncertainties in the averages produced, but the distribution of data on a seasonal basis (figure 5.5b) is a lot more even. The actual number of samples sorted by season and air mass type is listed in table 5.4.

In addition to considering the amount of data for each climatology point, the distribution of data for each climatology point from each source region (figure 5.6) had also to be considered.

Airmass Type	MAM	JJA	SON	DJF	Annual
NAM	0	0	0	0	0
NRM	35	13	28	24	100
EUR	1	1	0	1	3
SAH	21	23	50	45	139
SAF	1	2	14	0	17
SAB	0	0	8	0	8
SRM	4	0	2	0	6
Total	62	39	102	70	273

Table 5.4: Seasonal distribution of data according to source region (numbers are number of samples)

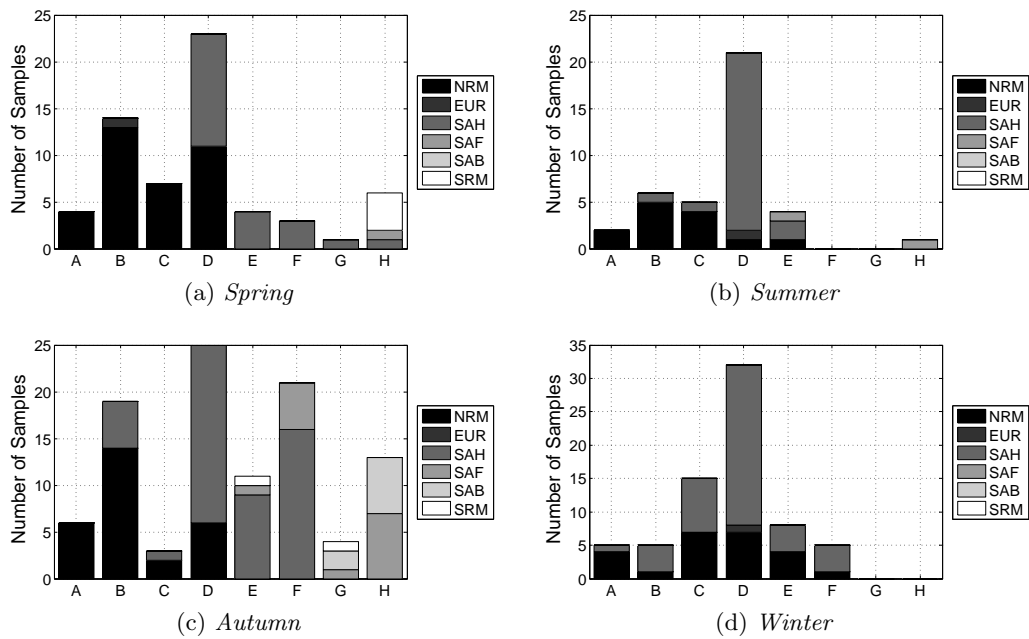


Figure 5.6: The seasonal distribution of samples from each climatology point for each source region

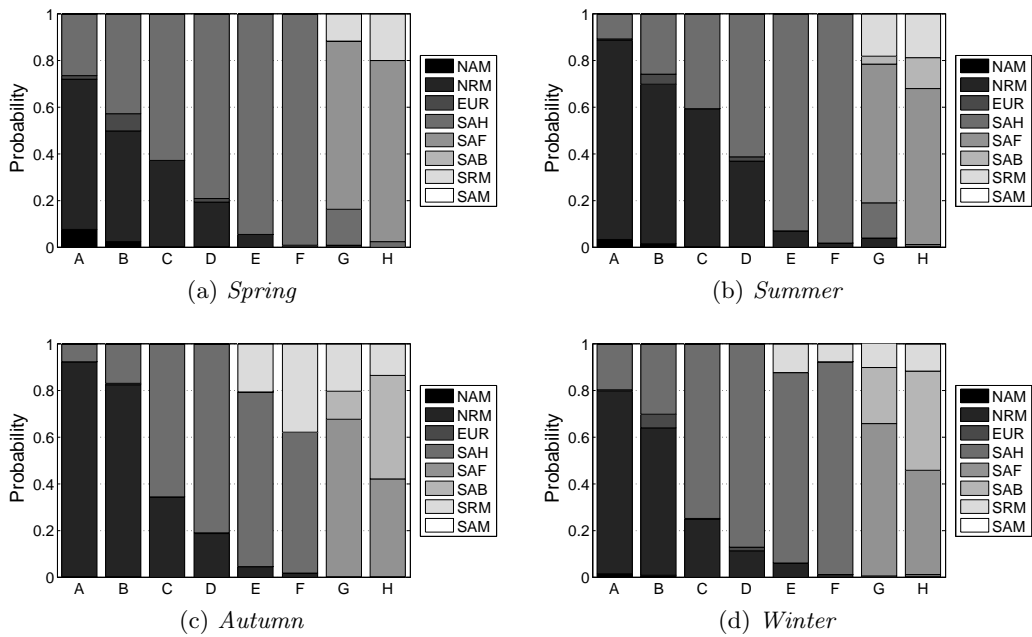


Figure 5.7: The seasonal variation of air mass type probabilities for each climatology point

Due to the limited number of samples, there are not enough samples from each source region for each climatology point to average sensibly. Instead samples would be averaged for the northern half of the climatology (ETNAA - ETNAD) and for the southern half of the climatology (ETNAF - ETNAH). These two distributions are shown in figure 5.8, and the actual numbers of samples are listed in table C.2 on page 158.

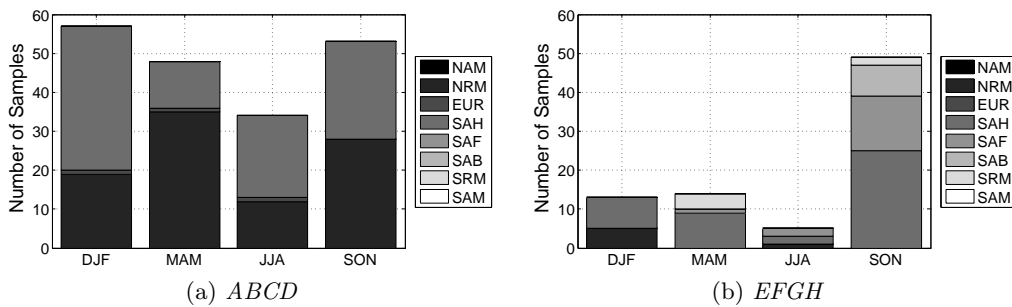


Figure 5.8: The distribution of data over the year for the northern and southern part of the ETNA

Once it was decided that the data would be divided into categories by source region, northern and southern half of the climatology, and then by season, robust mean values, i.e. a mean value that downweights outliers outside of a given range that is calculated from the median value, as defined in *Miller and Miller (2005)*, were found for each category. Calculation of a robust standard deviation was also performed at the same time, in addition to uncertainty values, which depend on the number of data points each category contained and reflect the likelihood that the average value calculated from a small

sample size represents the true value (after *Baker et al.*, 2010). For example, if a category only contains two data points the uncertainty in the average value is much greater than for a category with 30 data points. Table 5.5 lists the uncertainty values assigned for different numbers of data points averaged. Overall the relative uncertainty of each average made was set to the highest out of the robust standard deviation and the uncertainty value.

Number of Data Points in Category (N)	Uncertainty Value	Relative Uncertainty
$N \leq 2$	1.00	100 %
$2 \leq N \leq 5$	0.50	50 %
$5 \leq N \leq 10$	0.30	30 %
$10 \leq N \leq 5$	0.15	15 %

Table 5.5: *Uncertainty values assigned to the average values according to the number of data points averaged (after Baker et al., 2010)*

There were a few categories that didn't contain any data points. In these cases data was interpolated from adjacent categories and assigned a relative uncertainty value of 1. For instance there are no samples for which the air mass type was NAM, so it was assumed that as the ETNA is a great distance away from the North American continent, concentrations of aerosol in air masses originating there must be very low, and in fact very similar to the concentrations of aerosols assigned to the NRM air mass type.

The final average concentration field for each element is summarised in table C.3 on page 159. The number of measurements made make it difficult to show all data in one graph, but the iron, nitrogen and phosphate concentration fields for the SAH air mass type are plotted in figures 5.9a, c and e.

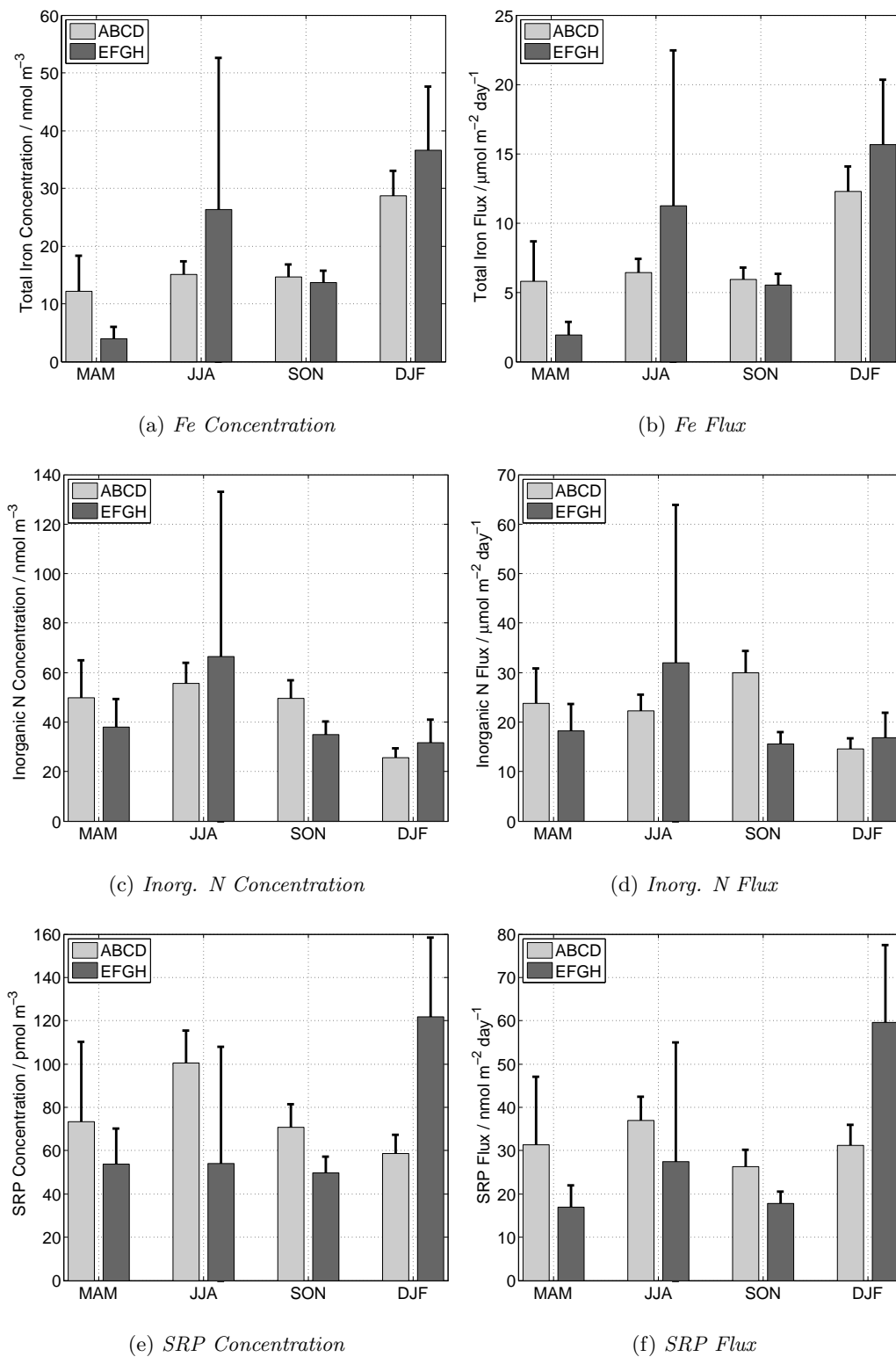


Figure 5.9: Unweighted dry deposition concentration and flux for SAH air mass types for total iron (a and b) total soluble inorganic nitrogen (c and d) and total soluble reactive phosphate (e and f). *N.B.* the difference in units and y-scales between different elements. Concentrations and fluxes for other elements and air mass types are listed in tables C.3 on page 159 and C.4 on page 163 respectively

	Spring	Summer	Autumn	Winter
ETNAA	6.15	5.14	5.73	6.79
ETNAB	6.58	6.61	5.87	6.59
ETNAC	6.91	7.60	6.51	7.44
ETNAD	8.10	7.38	7.22	7.55
ETNAE	7.13	4.86	5.27	7.66
ETNAF	4.69	4.44	3.56	5.41
ETNAG	4.14	6.37	6.77	5.17
ETNAH	4.10	5.84	6.04	4.51

Table 5.6: Average wind speeds for the climatology region (all in ms^{-1})

Having obtained average concentration fields for each element, these were then converted to aerosol deposition fluxes using the equation 2.7 on page 30. However, as mentioned in section 2.4 on page 30 the use of a fixed deposition velocities for coarse and fine mode aerosol is no longer considered appropriate (*Baker et al.*, 2010). The deposition velocities used here are derived using the *Ganzeveld et al.* (1998) model, which requires both wind speed and particle mass median diameter as inputs. As shown in figure 2.10 on page 31, although increasing wind velocity can change the deposition velocities of the larger but a factor of up to 10, coarse mode particles, but changes in wind speed can affect the deposition velocity of smaller, fine mode particles by as much as two orders of magnitude. Each elemental component of the dust was assigned a mass median diameter from table 2.4 on page 31. Fine mode aerosols were assumed to have the same mmd as anthropogenically derived aerosol, and assigned a value of $0.6 \mu m$, whereas coarse mode aerosols were assumed to be either predominantly seasalt or predominantly mineral dust, and assigned values of a 7 and $5 \mu m$ respectively.

The wind speed element of the deposition velocity was more problematic: because not all the samples in the ETNA aerosol data set included wind speed data, average wind speeds for each climatology region for each season were determined by averaging wind speed data from the European Centre for Medium Range Weather Forecasting (ECMWF) Interim Reanalysis Dataset (*ECMWF*, 2010). Simple mean averages were taken for all latitudes and longitudes within each climatology region, and for each data point within each season for the data spanning March 1999 to March 2009. The resultant average wind speeds are shown in table 5.6.

Once the dry deposition velocities were derived for each category using the mass median diameters listed above in conjunction with the wind speeds in table 5.6, the average aerosol flux for each category could then be calculated. Uncertainties in average aerosol atmospheric concentration fields were propagated across to the average aerosol deposition flux fields. Again, the amount of data produced is too great to easily represent in a graph, but the iron, nitrogen and phosphate fluxes for the SAH air mass type is shown in figure 5.9 plots b, d and f respectively and the fluxes calculated are listed in table C.4 on page 163.

5.4.3 The seasonally averaged aerosol flux

Having derived the seasonal probability of each air mass type arriving at each climatology point in section 5.4.1 and the seasonally averaged aerosol composition fields for each air mass type in the northern and southern halves of the climatology in section 5.4.2 the seasonal deposition for each climatology point was derived. This was calculated using equation 5.1.

$$F(x)_{(ETNA[y],x,season)} = \sum^{all\ z} (\rho_{(z,ETNA[y],season)} * F(x)_{(z,ETNA[y],season)}) \quad (5.1)$$

Where $F(x)$ is the flux of element x , $ETNA[y]$ is the climatology region, z is the air mass type, $\rho_{(z,ETNA[y],season)}$ is the probability of the air mass type z reaching region $ETNA[y]$ during that given season and $F(x)_{(z,ETNA[y],season)}$ is the average flux field for element x with air mass type z , in region $ETNA[y]$ during that season. So the Flux of element x to region $ETNA[y]$ during a given season is the sum over all air mass types of the average flux field for element x in region $ETNA[y]$ for the air mass type z weighted by the probability that air mass type z reaches region $ETNA[y]$ during that season.

The seasonal fluxes for each element are listed in table C.6, and as an example, the seasonal total iron aerosol climatology is shown in figures 5.10.

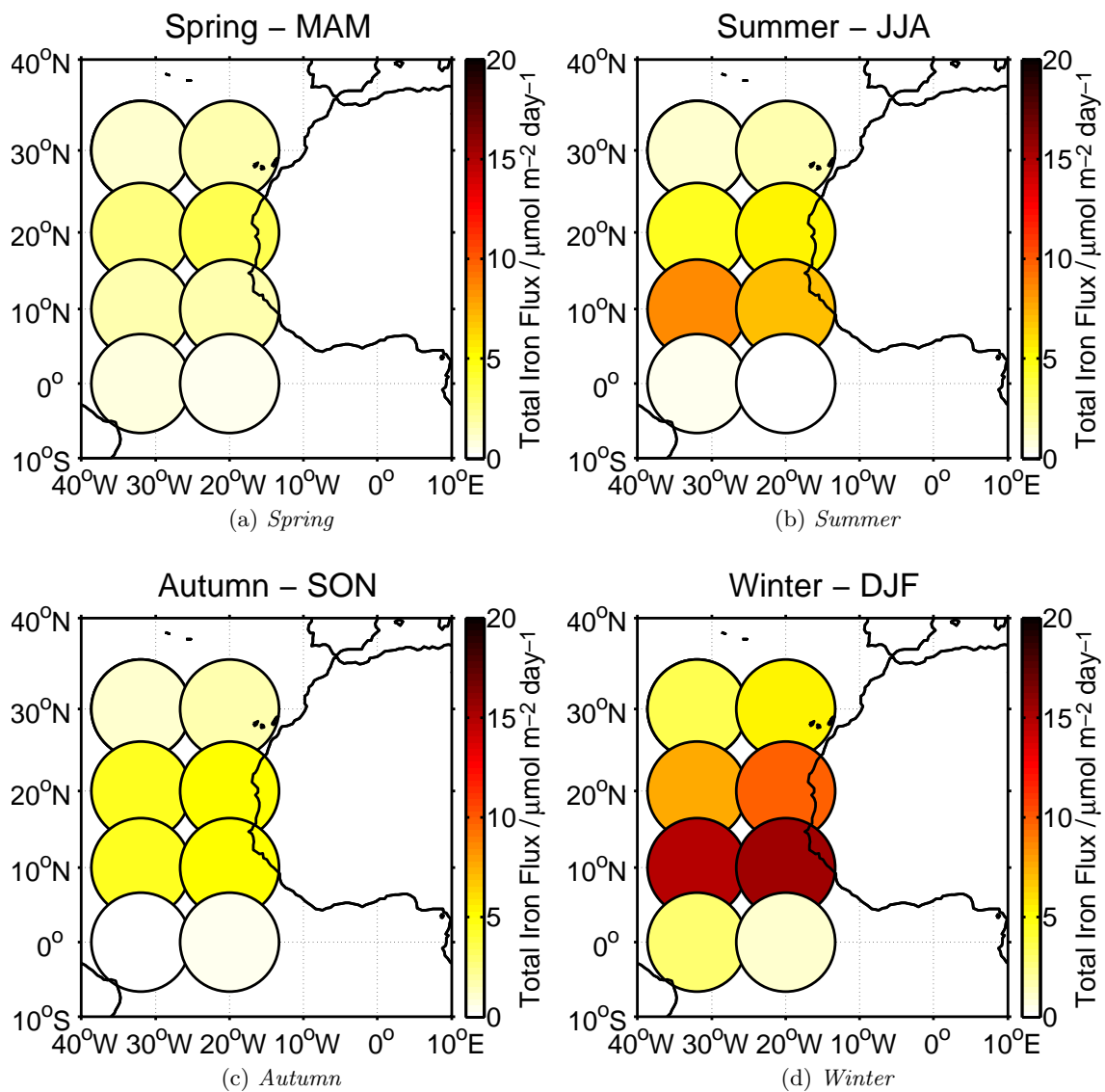


Figure 5.10: The seasonal dry deposition flux climatology for total iron

5.5 Constructing the rainfall climatology

In contrast to the dry deposition climatology, where the averages fluxes were weighted by seasonal air mass type probabilities, the rain climatology used the average rainfall amount for each region and each season (section 5.5.1) to weight concentrations and convert them to fluxes (section 5.5.2).

There are two main reasons that the rain fluxes were not weighted by the air mass type probabilities: firstly the number of samples was so low that there were not enough samples from each air mass type to create a meaningful average; secondly even when air mass back trajectories were analysed for the rain samples collected, allocation to an air mass type

was difficult owing to the fact that back trajectory models cannot easily resolve weather fronts, which are usually associated with rainfall events.

5.5.1 Average precipitation rates

The monthly mean rainfall data from the CPC Merged Analysis of Precipitation data for the ETNA region (*Xie and Arkin, 1997*) was used to derive seasonal and annual average rainfall for each climatology region in the ETNA for the period March 1999 to March 2009. The data is freely available at the CPC website as a netcdf file. Rainfall averages are given on a $2.5^\circ \times 2.5^\circ$ grid between latitudes $88.75^\circ\text{N} - 88.75^\circ\text{S}$ and longitudes $1.25^\circ\text{E} - 358.75^\circ\text{W}$, so all the information outside the climatology region was immediately discarded, as was information before March 1999. In order to calculate the mean rainfall for a particular climatology point for a particular season, a simple average was made of all the rainfall information within that region, for the season, rather than interpolating the rainfall information to a point. The derived mean rainfall values are plotted in figure 5.11 and the actual values (in mm day^{-1} units) are shown in table 5.7.

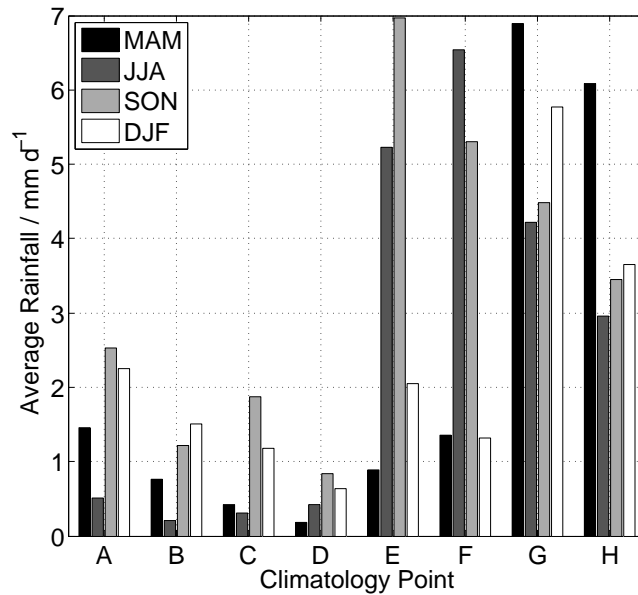


Figure 5.11: *Seasonal mean rainfall in mm day^{-1} between March 1999 and March 2009 for each climatology point*

What is particularly striking about figure 5.11 is the difference between the southern part of the climatology region (ETNAE-H) where there is a large amount of rainfall associated with the ITCZ and the northern part of the climatology region (ETNAA-D) where there is relatively little rainfall.

Climatology Region	MAM	JJA	SON	DJF	Annual
ETNAA	1.5	0.5	2.5	2.3	1.7
ETNAB	0.8	0.2	1.2	1.5	0.9
ETNAC	0.4	0.0	1.9	1.2	0.9
ETNAD	0.2	0.4	0.8	0.6	0.5
ETNAE	0.8	5.2	7.0	2.0	3.8
ETNAF	1.4	6.5	5.3	1.3	3.6
ETNAG	6.9	4.2	4.5	5.8	5.3
ETNAH	6.1	3.0	3.4	3.7	4.0

Table 5.7: *Seasonally averaged rainfall for each climatology box (all in mm d^{-1})*

5.5.2 Average rain composition

The main limitation to the rainfall data is that there is not enough of it: figure 5.12a shows the seasonal distribution of data, and although several samples were collected during spring and autumn (when the AMT cruises took place) less than five samples were collected in either winter or summer, certainly not enough to take a meaningful average.

The distribution of data according to climatology region (figure 5.12b) shows that there are not enough data to for meaningful averages to be made according to this either, although the distribution in figure 5.12c does show that regional averages for the northern (ABCD) and southern (EFGH) halves of the ETNA region would be possible.

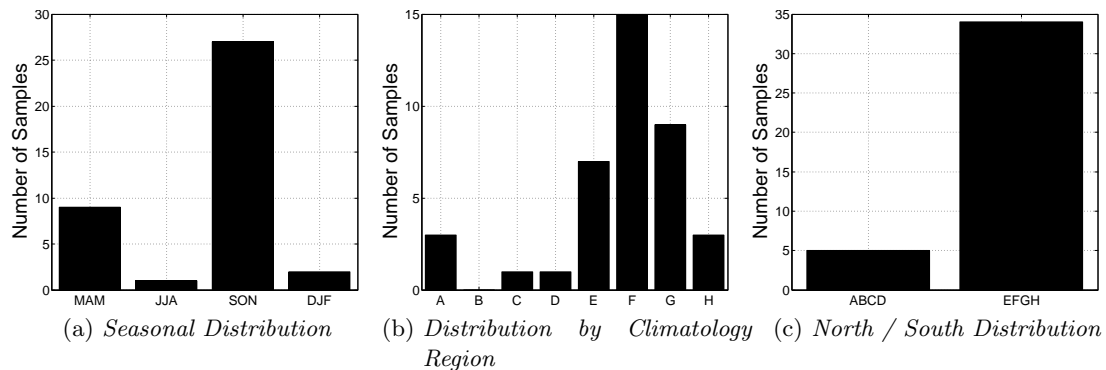


Figure 5.12: *The distribution of rain samples collected sorted by season, climatology point and climatology half*

Table 5.8 shows the number of samples in both northern and southern regions for each season and in total. This clearly shows that whilst samples can be divided between the two regions, there is simply not enough data to make seasonal averages. With this in mind, it was decided that rainfall data should be averaged by area, but annually, rather than seasonally.

In general, the concentration of aerosol components in rainfall decreases with the amount of rainfall. In order to account for this, volume weighted mean concentrations were calculated

Region	MAM	JJA	SON	DJF	Annual
ABCD	2	1	0	2	5
EFGH	7	0	27	0	34
Total	9	1	27	2	39

Table 5.8: *Regional distribution of rain samples according to season (numbers are number of samples)*

from equation 5.2 rather than using the median concentration as used in the dry deposition climatology.

$$C_V = \frac{\sum C_i * V_i}{\sum V_i} \quad (5.2)$$

Where C_V is the volume weighted mean concentration, C_i are the individual sample concentrations, and V_i the individual collected sample volumes. One uncertainty associated with sampling rain from a ship is that it is difficult to sample the whole precipitation event, thus V_i is not necessarily the same as rainfall volume. Table C.7 on page 171 lists the volume weighted mean concentrations calculated, and the errors shown are the percent uncertainty, calculated by considering how many samples were involved in calculating the averages (see table 5.5). In the same way as for the dry deposition climatology concentrations, there were some rain samples for which the concentration of a particular chemical species of a sample had been analysed, but found to be below the detection limit for that species. In each case, a value of 0.75 * that detection limit was substituted as a concentration (*Baker et al.*, 2010; *Helsel and Hirsch*, 2005). This prevents an over-estimation of the volume weighted mean due to high volume rain events with very low concentrations being ignored.

It is interesting to note that the volume weighted mean concentrations listed in table C.7 for region ETNAA-D are different to those for ETNAE-H, with species generally associated with seasalt at much higher concentration in rainfall from the northern half of the ETNA and all other aerosol species measured at higher concentration in precipitation in the southern half of the region. This somewhat justifies the decision to average data by region, rather than season, although the final rain climatology cannot include a seasonal cycle.

5.5.3 The average rain flux

In the case of precipitation, a wet deposition flux can be calculated from volume weighted concentration and the precipitation depth (*Jickells and Spokes*, 2001) using equation 5.3, where F_W is the wet flux, C_V is the volume weighted mean concentration and P is the precipitation.

$$F_w = C_V * P \quad (5.3)$$

The plot in figure 5.13 shows the volume weighted flux for wet deposition of total iron as an example and the fluxes calculated for each element are listed in table C.8 on page 171. It should be borne in mind that the actual data were averaged annually for the ETNAA-D and ETNAE-H regions, so therefore the rain flux climatology can only be an annual average.

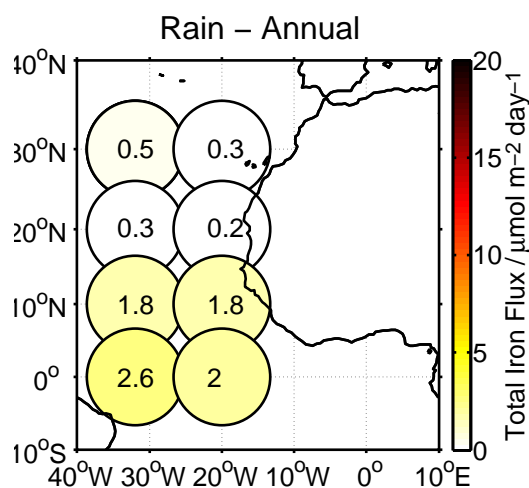


Figure 5.13: *The annual wet deposition flux climatology for total iron*

5.6 The ETNA aerosol and rainfall climatology

5.6.1 Soluble and total iron

The aerosol and rain deposition for soluble iron is shown in figure 5.15 and total iron in figure 5.14. The total wet and dry fluxes are summarised in table 5.9. It should be taken into account that for dry deposition soluble aerosol has been leached at pH4.7, then filtered through a 0.2 μm filter and total iron is the total amount of iron on the filter as determined by INAA. This is in contrast to the rain water, where samples are first acidified, total iron is then measured from an aliquot of samples and dissolved iron is measured from a further aliquot which has first been filtered through a 0.2 μm filter. All samples were determined using ICP OES. Thus although dissolved iron in rainfall should correspond to soluble iron in aerosol, total iron in aerosol and total iron in rainfall are not necessarily the same.

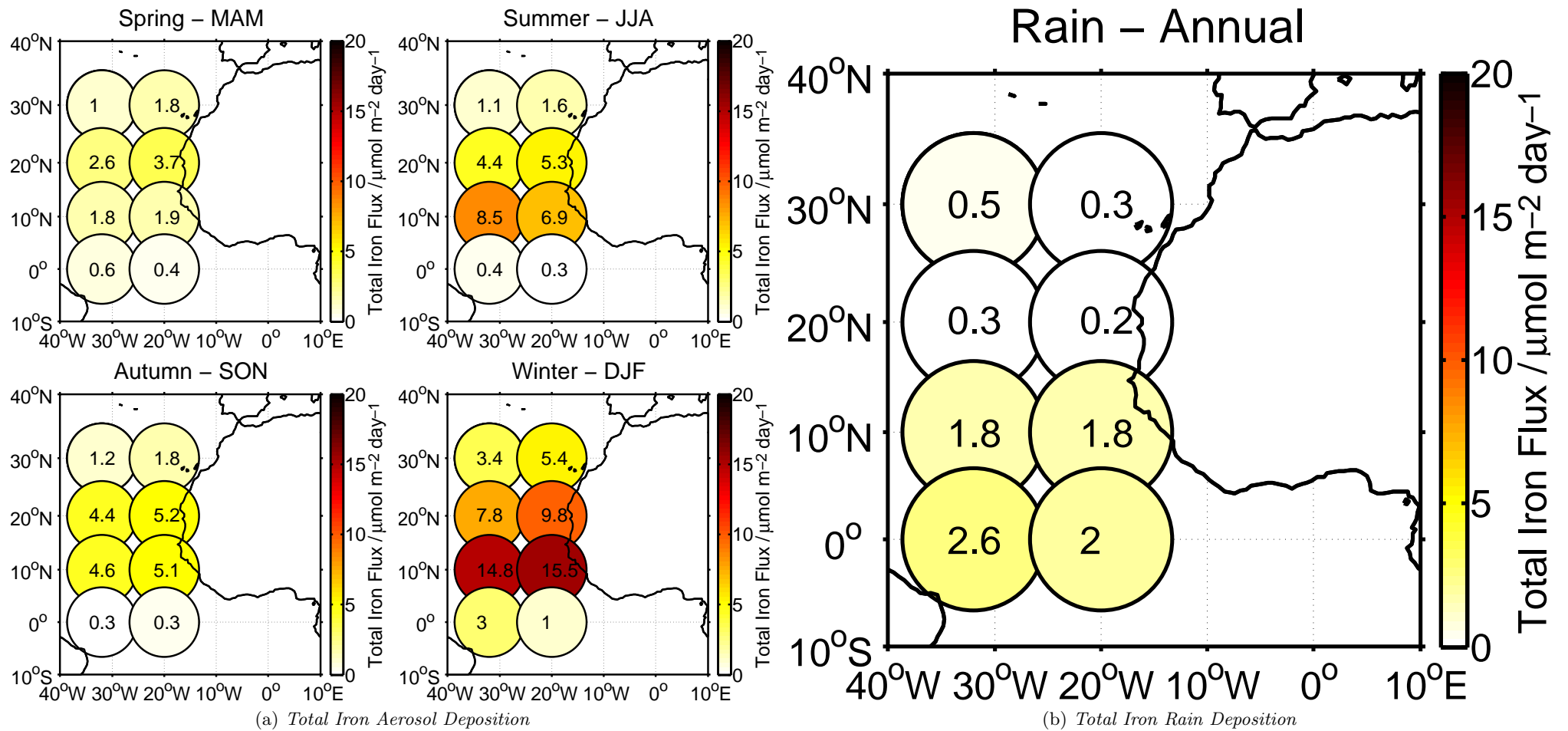


Figure 5.14: The climatologies for deposition of total iron to the ETNA shown as (a) total iron aerosol deposition and (b) total iron in rain

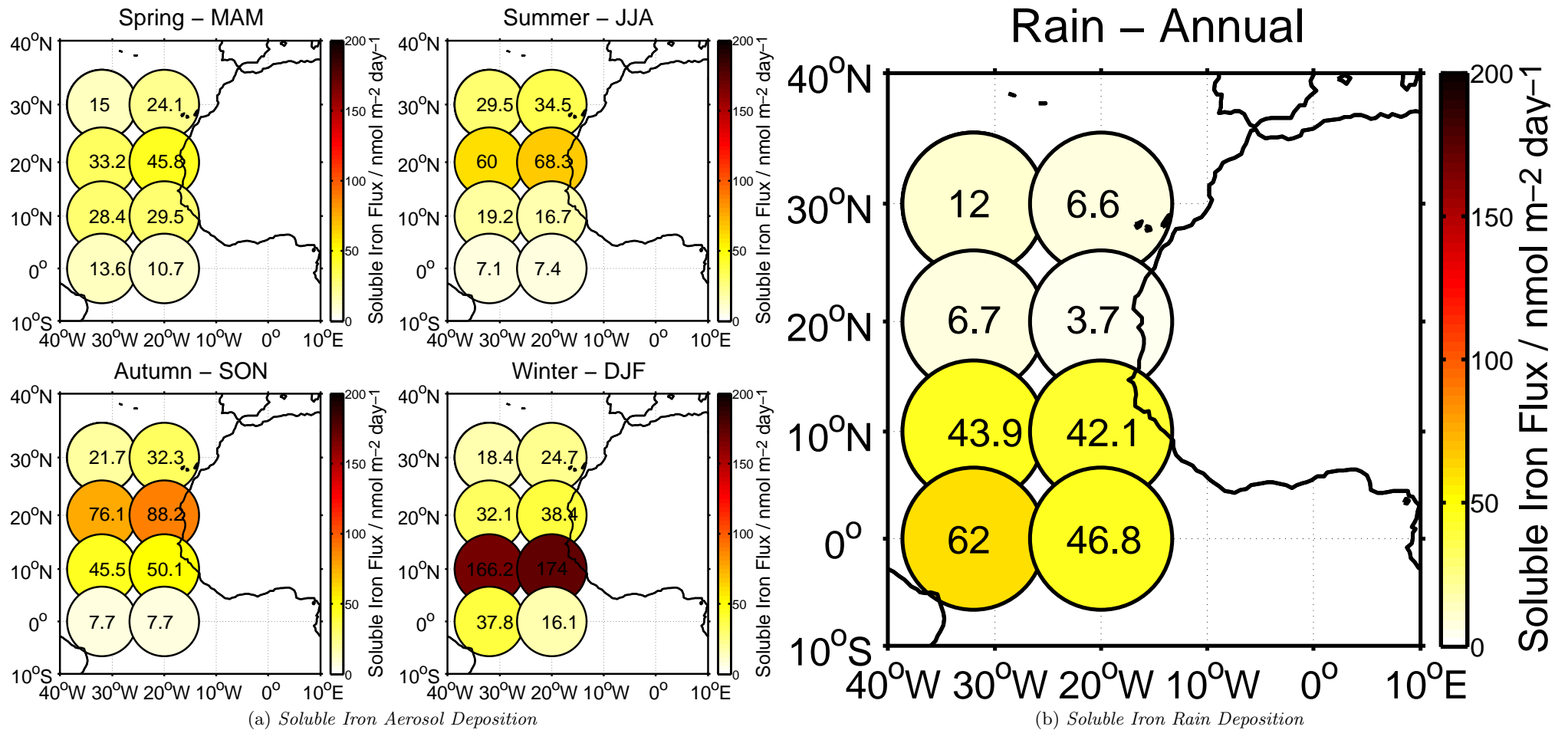


Figure 5.15: The climatologies for deposition of soluble iron to the ETNA shown as (a) soluble iron aerosol deposition and (b) soluble iron in rain. N.B. the difference in colour scales between these plots and figure 5.14

Region	Aerosol Deposition					Rain	R/A
	MAM	JJA	SON	DJF	Annual	Annual	Annual
Total Iron ($\mu\text{mol m}^{-2}\text{day}^{-1}$)							
ETNAA	1.0	1.1	1.2	3.4	1.7	0.5	0.29
ETNAB	1.8	1.6	1.8	5.4	2.6	0.3	0.12
ETNAC	2.6	4.4	4.4	7.8	4.8	0.3	0.06
ETNAD	3.7	5.3	5.2	9.8	6.0	0.2	0.33
ETNAE	1.8	8.5	4.6	14.8	7.4	1.8	0.24
ETNAF	1.9	6.9	5.1	15.5	7.3	1.8	0.25
ETNAG	0.6	0.4	0.3	3.0	1.1	2.6	2.36
ETNAH	0.4	0.3	0.3	1.0	0.5	2.0	4.00
ETNA	1.7	3.6	2.9	7.6	3.9	1.2	0.31
Soluble Iron ($\text{nmol m}^{-2}\text{day}^{-1}$)							
ETNAA	15.0	29.5	21.7	18.4	21.2	12.0	0.57
ETNAB	24.1	34.5	32.3	24.7	28.9	6.6	0.23
ETNAC	33.2	60.0	76.1	32.1	50.4	6.7	0.13
ETNAD	45.8	68.3	88.2	38.4	60.2	3.7	0.06
ETNAE	28.4	19.2	45.5	166.2	64.4	43.9	0.68
ETNAF	29.5	16.7	50.1	174.0	67.1	42.1	0.63
ETNAG	13.6	7.1	7.7	37.8	16.5	62.0	3.76
ETNAH	10.7	7.4	7.7	16.1	10.5	46.8	4.46
ETNA	25.0	30.3	41.2	63.5	39.9	27.9	0.67

Table 5.9: Total iron deposition flux in aerosol and rain, units in $\mu\text{mol m}^{-2} \text{day}^{-1}$ and soluble iron deposition flux, units in $\text{nmol m}^{-2} \text{day}^{-1}$; R/A is the rain flux divided by aerosol flux

The variation in the dry deposition of iron across the region and throughout the year shown in figures 5.14 and 5.15 show how the centre four boxes of the ETNA (ETNAC-F) experience most of the atmospheric flux of iron, and that the highest fluxes occur in the winter, due to the low level transport due to the trade winds. This is in agreement with *Chiapello et al. (1995)*, who report maximum dust concentrations transported to the Cape Verde during winter, although they do not quantify the flux to the region. The summer is also a peak season for the deposition of iron, although fluxes remain relatively large throughout the year. It is interesting to note that the proportion of wet to dry deposition is higher for soluble iron than for total iron, as shown in table 5.9, suggesting that the iron may be made more soluble by cloud processing (*Spokes et al., 1994*), although the leaching process used to analyse the soluble trace metal samples in dry deposition (section 2.1.3.5) is at a pH of 4.7 to reproduce the leaching conditions for trace metals in rainwater (*Baker et al., 2006c*), so it is strange that rainwater would increase the solubility of the iron relative to this leaching process. One possibility is that at higher dust loadings, precipitation is suppressed, an occurrence that has been observed in high resolution satellite data for the coast off west Africa by *Huang et al. (2009a)*. Aerosol iron solubility is much lower at high dust loadings (*Baker and Jickells, 2006*) and it is possible that if precipitation is more likely at slightly lower dust loadings, it would therefore scavenge particles containing more

soluble iron. It is also likely that the difference in the way total iron in aerosol is measured, compared to the total iron in rain water is measured could account for at least some of this difference. In general, rainfall fluxes are lower throughout the climatology region than dry deposition fluxes, except for boxes ETNAG and ETNAH, where rainfall dominates the flux of iron due to the migration of the ITCZ to the region during the winter months.

5.6.2 Inorganic nitrogen species, and total nitrogen estimate

Due to the uncertainties produced in the measurement the total soluble nitrogen (TSN) and how this uncertainty then propagates when calculating the organic nitrogen (SON) concentration (see section 3.4.1), total nitrogen has not been measured for rain samples and there are too few aerosol samples for which the TSN measurement is not subject to large standard errors. However, fluxes for the inorganic nitrogen species nitrate and ammonium have been estimated and are shown figures 5.16 and 5.17 respectively.

Recent estimates of the atmospheric flux of reactive nitrogen to the global ocean have found that at around 30%, organic nitrogen represents a significant proportion (*Duce et al.*, 2008). For this reason, in addition to the nitrate and ammonium fluxes, table 5.10 also lists the estimated TSN flux. This has been calculated by assuming that the total inorganic nitrogen (TIN) flux (the sum of the nitrate and ammonium fluxes) represents 70% of the total soluble nitrogen flux.

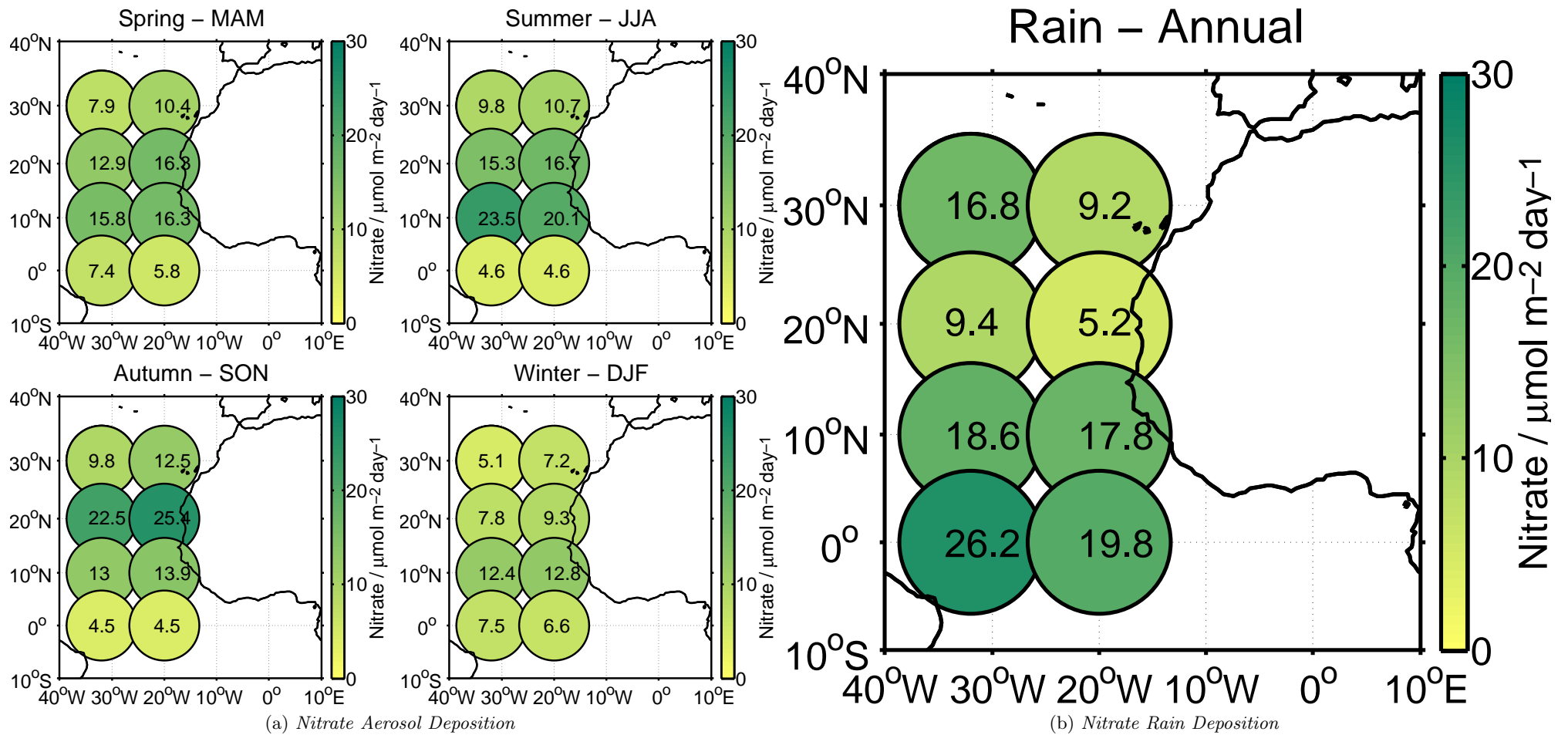


Figure 5.16: The climatologies for deposition of nitrogen to the ETNA shown as (a) nitrogen aerosol deposition and (b) nitrogen in rain

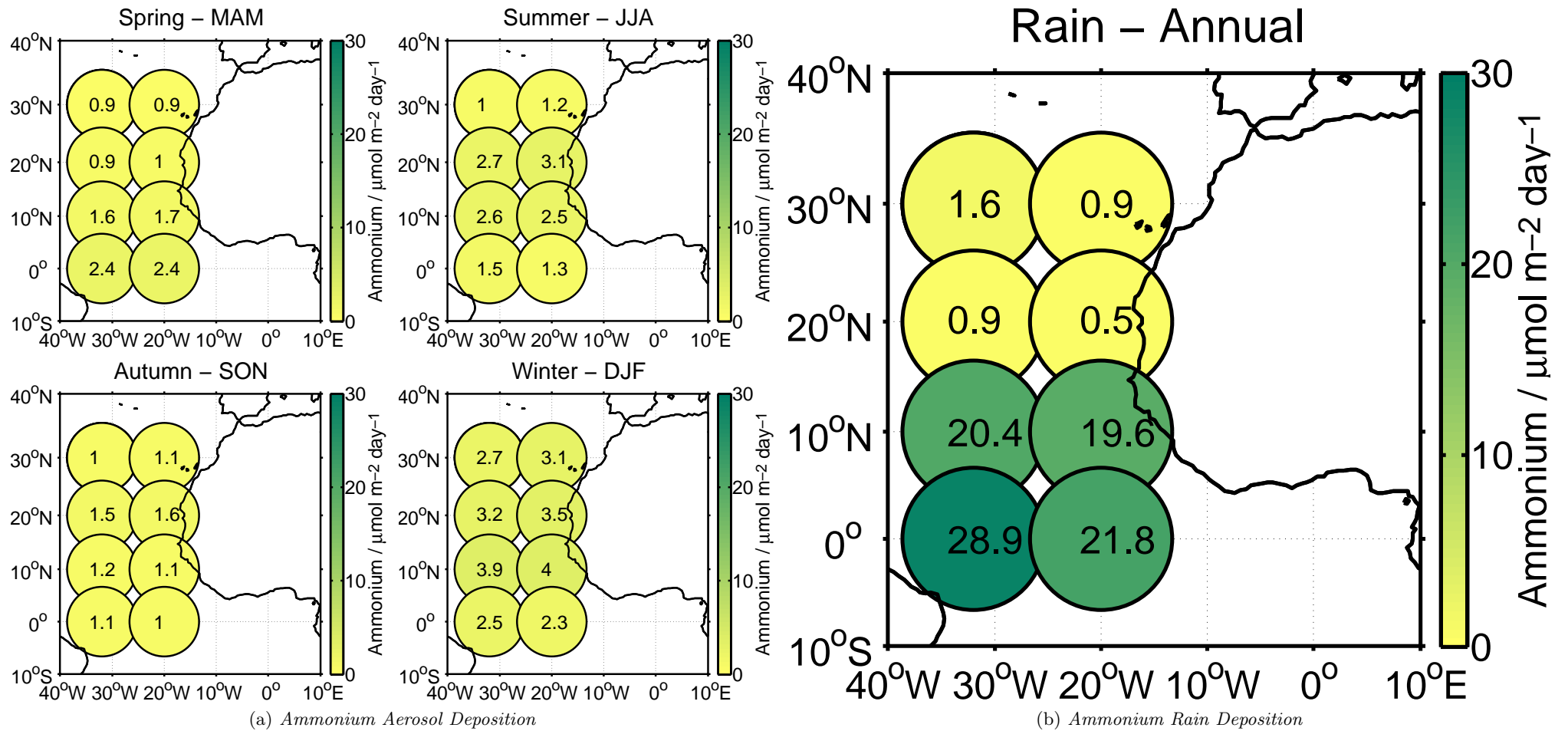


Figure 5.17: The climatologies for deposition of ammonium to the ETNA shown as (a) ammonium aerosol deposition and (b) ammonium in rain

Region	Aerosol Deposition					Rain	R/A
	MAM	JJA	SON	DJF	Annual	Annual	Annual
Nitrate ($\mu\text{mol m}^{-2}\text{day}^{-1}$)							
ETNAA	7.9	9.8	9.8	5.1	8.2	16.8	2.05
ETNAB	10.4	10.7	12.5	7.2	10.2	9.2	0.90
ETNAC	12.9	15.3	22.5	7.8	14.6	9.4	0.64
ETNAD	16.8	16.7	25.4	9.3	17.1	5.2	0.30
ETNAE	15.8	23.5	13.0	12.4	16.2	18.6	1.15
ETNAF	16.3	20.1	13.9	12.8	15.8	17.8	1.13
ETNAG	7.4	4.6	4.5	7.5	6.0	26.2	4.37
ETNAH	5.8	4.6	4.5	6.6	5.4	19.8	3.67
ETNA	11.7	13.2	13.3	8.6	11.7	15.4	1.32
Ammonium ($\mu\text{mol m}^{-2}\text{day}^{-1}$)							
ETNAA	0.9	1.0	1.0	2.7	1.4	1.6	1.14
ETNAB	0.9	1.2	1.1	3.1	1.6	0.9	0.56
ETNAC	0.9	2.7	1.5	3.2	2.1	0.9	0.43
ETNAD	1.0	3.1	1.6	3.5	2.3	0.5	0.21
ETNAE	1.6	2.6	1.2	3.9	2.3	20.4	8.87
ETNAF	1.7	2.5	1.1	4.0	2.3	19.6	8.52
ETNAG	2.4	1.5	1.1	2.5	1.9	28.9	15.21
ETNAH	2.4	1.3	1.0	2.3	1.7	21.8	12.82
ETNA	1.5	2.0	1.2	3.2	1.9	11.8	6.21
TSN - Total Soluble Nitrogen ($\mu\text{mol m}^{-2}\text{day}^{-1}$)							
ETNAA	12.6	15.4	15.5	11.1	13.6	26.3	4.6
ETNAB	16.2	17.0	19.4	14.7	16.8	14.4	2.1
ETNAC	19.7	25.6	34.3	15.7	23.8	14.7	1.5
ETNAD	24.7	28.4	38.5	18.3	27.5	8.1	0.7
ETNAE	24.9	37.2	20.3	23.3	26.5	55.7	14.3
ETNAF	25.7	32.4	21.5	24.0	25.9	53.4	13.7
ETNAG	14.0	8.7	8.0	14.3	11.2	78.7	28.2
ETNAH	11.8	8.4	7.9	12.7	10.2	59.5	23.0
ETNA	18.9	21.7	20.7	16.9	19.4	38.9	10.8

Table 5.10: Nitrate and ammonium deposition flux in aerosol and rain, units in $\mu\text{mol m}^{-2}\text{day}^{-1}$; TIN is the sum of ammonium and nitrate fluxes and TSN has been calculated from the TIN flux by assuming that soluble organic nitrogen represents 30% of the total soluble nitrogen flux (Duce et al., 2008). R/A is the rain flux divided by aerosol flux

In stark contrast to the deposition of iron, the dry deposition of nitrate and ammonium

do not show such a marked seasonal cycle, although nitrate fluxes are slightly higher in summer and autumn, and slightly lower in the winter, whereas ammonium fluxes are slightly higher in the winter (figures 5.16 and 5.17). The low values of dry deposition for ammonium throughout the year reflect the fact that the majority of NH_4^+ occurs in the fine mode, and although the atmospheric concentrations of ammonium are similar to nitrate, the deposition velocities for smaller particles are much less than for the coarse mode particles (*Duce and Tindale, 1991*). On the other hand, the wet deposition for ammonium, relative to the dry deposition flux (R/A in table 5.10), is quite high and the difference between the ammonium rain flux to the high rainfall region affected by the ITCZ and the northern four boxes of the climatology region is also very striking. The ratio between wet and dry flux for nitrate is not quite so marked, which might be surprising, since larger particles tend to be scavenged into rain more efficiently (*Kane et al., 1994*). However, the wet to dry flux ratio R/A calculated in table 5.10 is not the same as a scavenging ratio, which would be calculated by dividing the concentration of a chemical species in rain, in units of $\text{mol kg}^{-1}_{\text{water}}$ by its atmospheric concentration in aerosol, in units of $\text{mols kg}^{-1}_{\text{air}}$ (*Galloway et al., 1993*). A simple comparison of the concentrations of nitrate and ammonium in aerosol (table C.5) with their concentration in rain (table C.7), it is nitrate with the higher rain to aerosol concentration ratio.

5.6.3 Soluble reactive phosphate

Unfortunately, soluble reactive phosphate has not been measured for the rain samples, so only the dry deposition flux has been plotted here (figure 5.18, and table 5.11). It would be interesting to compare the deposition patterns of the SRP to those of iron and nitrogen, as SRP is known to exist in the coarse mode when derived from soil dusts, and fine mode when produced by biomass burning. Given the effect the change in particle size has on deposition velocity, and therefore flux, we would expect the differences in the rain fluxes and the dry deposition fluxes to reflect this.

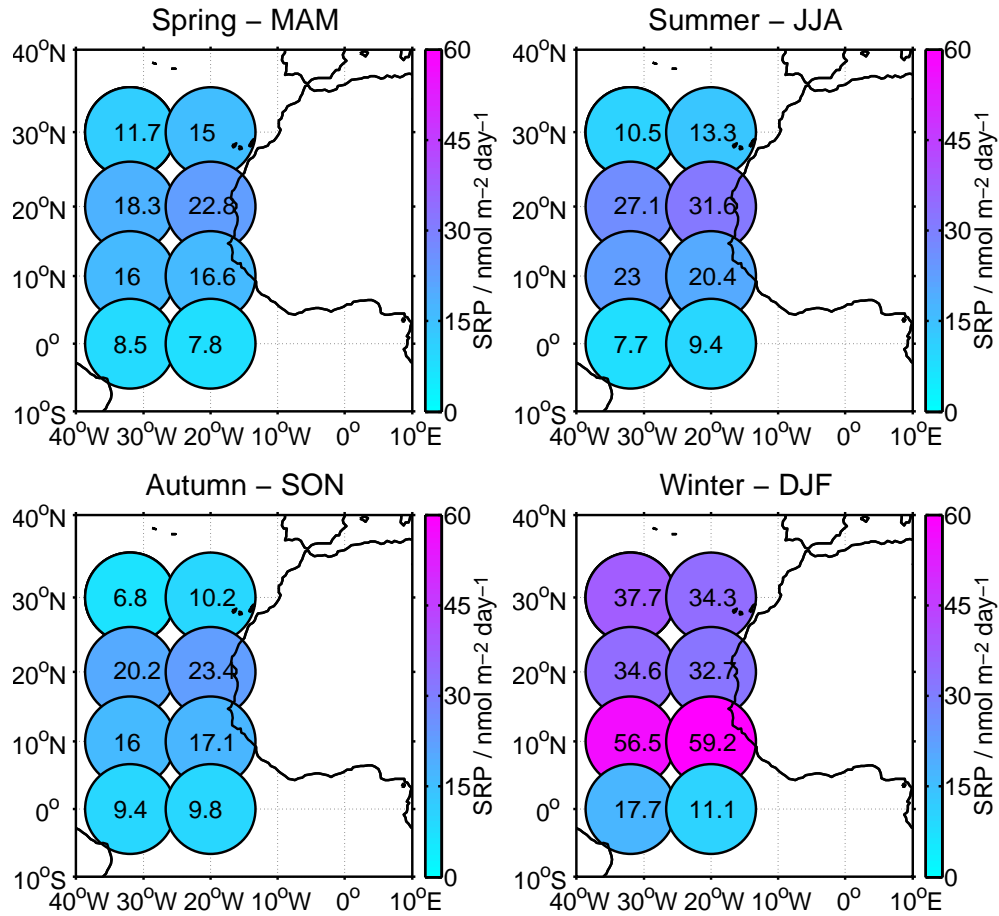


Figure 5.18: The climatology for the aerosol deposition of soluble reactive phosphate to the ETNA

Region	Aerosol Deposition / $\text{nmol m}^{-2} \text{ day}^{-1}$				
	MAM	JJA	SON	DJF	Annual
ETNAA	11.7	10.5	6.8	37.7	16.6
ETNAB	15.0	13.3	10.2	34.3	18.1
ETNAC	18.3	27.1	20.2	34.6	25.0
ETNAD	22.8	31.6	23.4	32.7	27.6
ETNAE	16.0	23.0	16.0	56.5	27.8
ETNAF	16.6	20.4	17.1	59.2	28.2
ETNAG	8.5	7.7	9.4	17.7	10.8
ETNAH	7.8	9.4	9.8	11.1	9.5
ETNA	14.6	17.9	14.1	35.5	20.5

Table 5.11: Soluble reactive phosphate deposition flux in aerosol, units in $\text{nmol m}^{-2} \text{ day}^{-1}$, N.B. rain samples were not analysed for SRP

It is interesting to note that the seasonal flux of SRP is strongly affected by a large input during the winter, coincident with the strong inputs of iron, so presumably this is due to the strong Saharan dust inputs in this season. The flux also increases, but to a lesser extent, during the summer, coincident with the summer high dust transport. Figure 5.19

shows the SRP to total aluminium flux ratio over each season for each climatology box. As total aluminium is used as a tracer for mineral dust (*Baker and Jickells, 2006*), where the SRP/Al ratio is higher, there are additional inputs to the flux of SRP than just mineral dust alone. The highest ratios are in areas G and H, those climatology regions that are most affected by Southern African biomass burning (*Cooke et al., 1996*), in addition the seasons most affected are summer (JJA) and autumn (SON).

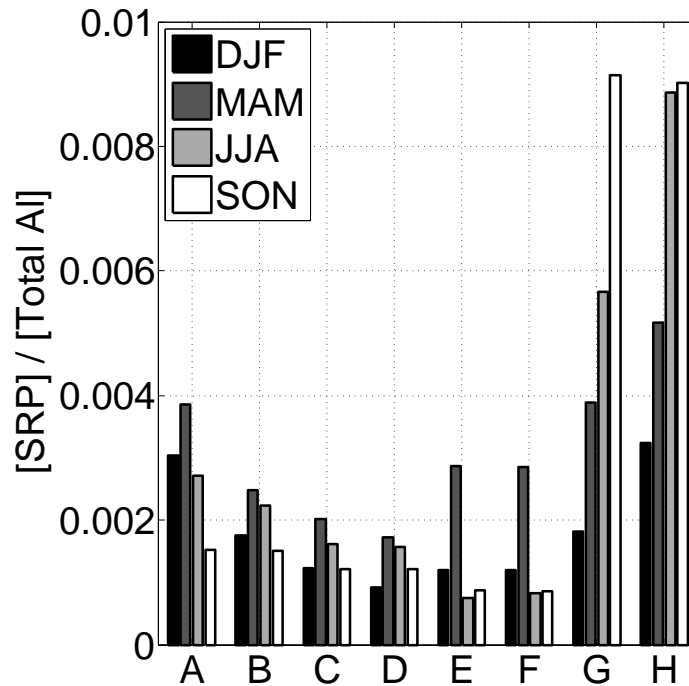


Figure 5.19: *The seasonal variation in the ratio of SRP flux / total aluminium flux for each climatology box*

5.6.4 The annual atmospheric flux and its impacts

The calculated atmospheric fluxes for the whole ETNA region for iron, ammonium, nitrate and SRP are summarised in table 5.12. These estimated fluxes can be compared to other estimates listed in table 5.1. The value of $1.18 \text{ Tg Fe yr}^{-1}$ seems a bit low compared to the values for the whole North Atlantic of 7.7 Tg yr^{-1} (*Duce and Tindale, 1991*) or 6 Tg yr^{-1} (*Prospero et al., 1996*), especially considering that the ETNA is adjacent, i.e. next, to the major source of iron to the Atlantic, but this is because the climatology region is a relatively small area compared to the Atlantic ocean as a whole. However, the estimated flux by unit area ($285.0 \mu\text{gFe m}^{-2} \text{ d}^{-1}$) is much greater than the long time-series estimate at Bermuda of $172.0 \mu\text{gFe m}^{-2} \text{ d}^{-1}$ (*Tian et al., 2008*), which reflects the heavy input of dust to the region throughout the year.

The flux to the ETNA of nitrate (1.56 Tg yr^{-1}) and ammonium (0.82 Tg yr^{-1}) also seem a little low considering the 4.48 Tg yr^{-1} and 2.28 Tg yr^{-1} estimated by *Baker et al. (2010)*

for the whole north Atlantic, but again the ETNA is only a small area of the Atlantic and in any case the major sources of nitrate and ammonium aerosol are combustion of fossil fuels and heavy agriculture (*NEG-TAP*, 2001), activities more associated with North America and Europe, so it is unlikely that the ETNA would experience a large proportion of this flux.

Finally the estimate of $0.615 \mu\text{g P m}^{-2} \text{d}^{-1}$ is very similar to the flux of $0.2 \mu\text{g P m}^{-2} \text{d}^{-1}$ derived for the North Atlantic by *Mahowald et al.* (2005b), yet a lot less than the mean flux of $110 \mu\text{g m}^{-2} \text{d}^{-1}$ from *Bergametti et al.* (1992). However measurements in the latter study were made for periods of high dust deposition using XRF and thus represent a total phosphate flux during dust outbreaks, rather than the annually averaged soluble phosphate measured here. (*Baker et al.*, 2006c) report solubilities of around 10% for the phosphorus in Saharan dust, which would change the *Bergametti et al.* (1992) flux to $11 \mu\text{g m}^{-2} \text{d}^{-1}$, which is still an order of magnitude higher than the estimate here, although it may represent peak P deposition, rather than the average. In contrast the figure of 0.081Tg yr^{-1} is rather higher than the 0.004Tg yr^{-1} estimated in (*Baker et al.*, 2010), although as this work does take into account seasonal changes in the deposition, the difference in fluxes is probably due to the bias towards spring and autumn sampling in the latter estimate, when the phosphate deposition is low.

	Dry Deposition		Wet Deposition		Total Deposition	
	$\mu\text{g m}^{-2} \text{d}^{-1}$	Tg yr^{-1}	$\mu\text{g m}^{-2} \text{d}^{-1}$	Tg yr^{-1}	$\mu\text{g m}^{-2} \text{d}^{-1}$	Tg yr^{-1}
Sol. Fe	2.23	0.0092	1.56	0.0068	3.79	0.016
Tot. Fe	217.8	0.90	67.0	0.28	285.0	1.18
NH_4^+	26.6	0.11	165.2	0.71	191.8	0.82
NO_3^-	163.8	0.67	215.6	0.89	379.4	1.56
TIN	190.4	0.78	380.8	1.60	571.2	2.38
TSN	272.0	1.11	544.0	2.29	816.0	3.40
SRP	0.615	0.081	–	–	0.615	0.081

Table 5.12: Annual deposition fluxes to the ETNA, in $\mu\text{g}(\text{Fe}, \text{N}, \text{P})\text{m}^{-2}\text{d}^{-1}$ and $\text{Tg}(\text{Fe}, \text{N}, \text{P})\text{year}^{-1}$, % are percentage of the total (dry + wet) flux; N.B. rain samples were not analysed for SRP

In order to assess the likely impact of the fluxes in table 5.12 on the marine biota in the ETNA the relative demand for the nutrients supplied must be taken into account. A similar thought experiment to the one used by *Baker et al.* (2003) has been used to consider the possible outcomes. The Fe:N and N:P ratios for the calculated atmospheric fluxes are compared to the Redfield ratio, and the estimated iron cellular quota for primary producers in iron replete waters (*Sunda*, 1997) in table 5.13.

	Fe:N	N:P	N:C
	$\mu\text{mol mol}^{-1}$	mol mol^{-1}	mol mol^{-1}
Atmospheric Flux (using TSN and Sol. Fe and dry TSN and SRP)	1168.7	29333	–
Primary Producers	13 – 86 ^a	16	6.625
Nitrogen Fixers	1896 (276–5760) ^b	–	12 (8.9–16) ^b

Table 5.13: *N:P, Fe:N and N:C ratios for primary producers and the calculated aerosol fluxes*

^a - from Sunda (1997)

^b - from Berman-Frank et al. (2001)

The amount of new production that could attributed to the estimated atmospheric input alone depends on the flux of SRP, as the N:P ratio for aerosol is far greater than the Redfield ratio, thus P will be depleted far sooner than N. Thus the amount of new production due to the aerosol input, and the amount of nitrogen used by this can be calculated as follows:

$$X_A = P_I * X : P_{Pr} \quad (5.4)$$

Where X_A is the amount of X taken up due to aerosol input, P_I is the aerosol input of phosphate, and $X:P_{Pr}$ is the X to phosphate Redfield ratio for primary production, from table 5.13. Thus the amount of new production due to aerosol inputs takes up $\approx 290 \text{ Mmol C yr}^{-1}$ and utilises $\approx 40 \text{ Mmol N yr}^{-1}$.

However, since much of the climatology region lies in the oligotrophic subtropical gyre where nitrogen has been shown to be the limiting nutrient on primary productivity (Mills et al., 2004), it seems reasonable to assume that there must be some reservoir of phosphate in the water column (possibly due to fast remineralisation of phosphate in the surface waters (Benitez-Nelson, 2000), or to the utilization of dissolved organic phosphorus via the activity of the phosphorus-specific enzyme alkaline phosphatase (Mather et al., 2008)). Assuming this PO_4^{3-} -reservoir is large enough, the new production from the remaining nitrogen input, and the amount of iron utilised can be calculated from:

$$X_N = (N_I - N_A) * X : N_{Pr} \quad (5.5)$$

Where X_N amount of X taken up due to the N input, N_I is the aerosol nitrogen input and $X:N_{Pr}$ is the X to nitrate ratio for primary producers (table 5.13). Thus the new production potentially stimulated by aerosol nitrogen input is $\approx 1600 \text{ Gmol C yr}^{-1}$, which compares to and utilises between 3–20 Mmol Fe yr^{-1} . Assuming that primary production takes up the maximum amount of iron, this still leaves an excess of $\approx 0.3 \text{ Gmol Fe yr}^{-1}$. This also assumes that the soluble iron calculated here is analogous to bioavailable iron.

However, it should be borne in mind that the analyses undertaken were leaches at pH 4, and therefore represent a maximum possible amount of iron that might dissolve from the aerosol as it falls through the entire water column, and thus is likely to be an overestimate.

Although high Trichodesmium abundance has been found to be correlated with shallow mixed layer depth and high iron deposition, rather than temperature or nitrate concentration (Tyrrell *et al.*, 2003), high excess iron input and nitrate limitation is thought to stimulate nitrogen fixation (Mahaffey *et al.*, 2005). In order to estimate the amount of nitrogen fixation that would potentially be stimulated by the excess atmospheric iron flux, the Trichodesmium sp. cellular ratios of iron to carbon and carbon to nitrogen reported by Berman-Frank *et al.* (2001) are used. The equation below was used:

$$X_F = (Fe_I - Fe_A - Fe_N) * N : Fe_F \quad (5.6)$$

Where X_F amount of X taken up due to the Fe input, Fe_I is the aerosol iron input and $X:Fe_F$ is the X to iron ratio for nitrogen fixation. Thus the nitrogen fixed as a result of the excess atmospheric iron is $\approx 140 \text{ Gmol N yr}^{-1}$, which is slightly lower than the estimated aerosol reactive nitrogen flux.

It should be noted that the cellular ratios above are variable between different organisms (Bertilsson *et al.*, 2003) and under different conditions (Berman-Frank *et al.*, 2001; Sunda, 1997). However, the exercise above does show that despite a high atmospheric input of SRP, the input of iron and fixed nitrogen is far greater with respect to phytoplankton requirements, and thus atmospheric input of SRP is unlikely to alleviate phosphate limitation in the region. Further, the excess of iron supplied is likely to stimulate nitrogen fixation, thus further consuming the phosphate available in the water column.

This would be consistent with observations of much lower phosphate concentrations and more abundant nitrogen fixers in the oligotrophic north Atlantic, where there is a strong input of iron from the Sahara, compared with the oligotrophic south Atlantic, where there is very little iron input (Mather *et al.*, 2008).

5.7 Summary

In order to assess how well the climatologies presented here represent the actual deposition of iron, inorganic nitrogen and phosphate to the ETNA, it is necessary to consider the uncertainties produced in all the calculations performed.

The main sources of uncertainty in the calculation of the dry deposition climatology arise from: the number and uneven spatial and temporal distribution of data; the uneven distribution of samples over air mass type; and the calculation of flux using dry deposition

velocities and assumed mass size distributions. These factors are all examined in the following discussion.

The issue of the distribution of dry deposition data was first addressed in section 5.4.3. The climatology area was chosen in order to maximise the amount of data available, and the decision was made to average the data by season, airmass type and for a north/south split of the climatology region. This decision was a compromise between the number of data and the need to take both the changes in atmospheric deposition between seasons and between air mass types into account, whilst elucidating any difference between samples taken in the northern half of the climatology region, which is dominated by dry deposition, and the southern half, which is strongly affected by the ITCZ and should therefore be dominated by the deposition of aerosol by rainfall. However, there were still some averages made that only included one or two data points. As outlined in section 5.4.2, there is some uncertainty associated with whether or not one or two data points can be representative of a whole population, and in order to account for this an uncertainty value was added to each average made. These uncertainty values are summarised in table 5.5 and give a greater uncertainty to averages made with fewer data. However, on weighting the average concentrations by the air mass type probabilities, it was found that most of the averages associated with high uncertainty values were from air mass types with very low probabilities and thus considerably downweighted, so the overall uncertainty for the final calculated concentrations were much improved, as can be seen in table C.5 on page 167.

The second major area of uncertainty arises from the calculation of flux from atmospheric concentrations of aerosol. Again, the uncertainties arising from this calculation were briefly discussed in sections 5.4.3 and 2.4. The use of a modelled dry deposition velocity is a major source of uncertainty in the flux calculation (*Baker et al.*, 2010; *Arimoto et al.*, 2003). It seems that the dry deposition velocity is most sensitive to the mass median diameter used, especially in particle sizes below 5 μm . Ideally, the mass median diameter would be calculated for each sample, unfortunately, this cannot be done with the hivol samples collected. Therefore, estimates have been made from other data and from values reported in the literature. The values used, along with upper and lower bounds are listed in table 2.4 on page 31. The mass median diameters chosen do agree with other values described in the literature, which are also listed in table 2.4. However, it is not possible with fixed mass median diameters to account for the growth of more hygroscopic particles at high humidity, although this effect is likely small as the newly formed larger particles are subject a faster rate of gravitational settling (*Zhang and Iwasaka*, 2004). The uncertainty caused by assuming these mass median diameters was calculated by determining the dry deposition velocity, and also the flux, using the upper and lower bounds of the mass median diameter. These upper and lower bound flux estimates were then used to derive a relative uncertainty in the flux estimate, and are the values quoted in table C.6 on page 169. Other uncertainties associated with the modelled dry deposition velocity include wind speed, and

the enhanced removal of particles due to whitecapping, although both effects are small compared to the mass median diameter effect, for the larger particles that dominate the dry deposition flux (*Ganzeveld et al.*, 1998).

The sources of uncertainty for rain sampling are slightly different in that no calculation of deposition velocity is necessary, so it is the distribution of data and the average amount of precipitation to the region that are the main sources of uncertainty in this case. The precipitation field used here (*Xie and Arkin*, 1997) has been shown to agree relatively well to those of others (*Baker et al.*, 2010), so is not likely to be a great source of uncertainty. Uncertainties arising from making averages from a small number of samples were accounted for in the same way as with dry deposition. However, the distribution of data is a much greater source of uncertainty as there were not enough samples to be able to average the data by season, so the average flux is biased to the precipitation in spring and autumn, when most of the rain samples were gathered. Therefore, the rain flux may underestimate the total flux of species related to dust deposition as dust events during summer and winter are known to be more intense.

In short, the atmospheric deposition climatologies in this chapter illustrate the flux of iron, inorganic nitrogen, and SRP to the ETNA. The number of samples in the ETNA dry deposition dataset is quite comprehensive, although there are far fewer rain samples. Creating atmospheric deposition climatologies in the way outlined attempts to solve the problem of whether the aerosol samples collected are truly representative of the deposition to the region as a whole. The dry deposition climatology also takes into account any changes in the seasonal signal and ensures that the seasonal sampling bias towards autumn and winter is also accounted for, although this is not the case for the wet deposition climatology. The largest uncertainties were associated with the calculation of dry deposition velocities, and the small number of rain samples.

Chapter 6

Conclusions

As stated in chapter 1, the aim of this thesis is to quantify and characterise the input of iron, reactive nitrogen and phosphate to the ETNA by completing the following three objectives:

- Characterisation of aerosols collected during dust storms in the ETNA
- Investigation into the solubility of iron aerosol transported to the region
- Quantification of the atmospheric fluxes of iron, nitrogen and phosphate to the ETNA

In order to *characterise the aerosols collected during dust storms in the ETNA*, aerosol concentrations for a variety of chemical species were analysed for 3 cruises in the ETNA region - D326, M68 and P332. Unfortunately there were not enough rain samples to be included in this analysis, but this reflects the low amounts of precipitation to the region.

The atmospheric concentration of total iron was very closely correlated to dust mass loading, which was calculated from the atmospheric concentration of total aluminium, indicating that most of the iron in aerosol collected on these cruises is derived from Saharan and Sahelian soils, and that the input of iron from anthropogenic sources is minor. No evidence could be found for a change in the ratio of total iron to total aluminium, or a change in the ratio of total iron to non-seasalt calcium, indicating that if variation in the composition of these soils exists it cannot be detected after transport to the ETNA with the sampling methods that we use here.

The atmospheric concentration of phosphate was a little more difficult to characterise. Although the concentration of phosphate in the coarse mode seemed to be coincident with total aluminium, the fine mode phosphate appeared to vary with non-seasalt potassium and non-seasalt sulphate, both species indicative of African biomass burning. Thus the source of aerosol phosphate to the ETNA is complex and need careful evaluation.

The atmospheric concentration of nitrogen species is probably dominated by nitrate and ammonium, although due to the uncertainties in analysing the total soluble nitrogen, it is difficult to quantify the amount of organic nitrogen present in samples. This highlights the need for a better system for measuring organic nitrogen. Aerosol nitrate appeared predominantly in the coarse mode, indicating that the acid displacement reaction of nitric acid and seasalt has taken place. This is in contrast to aerosol ammonium, which occurs for the most part in the fine mode and appears associated with non-seasalt sulphate. In both cases the atmospheric concentrations increase when dust mass loading is high, yet also have high concentrations at other times, suggesting that they transported with, if not on, Saharan dust, although Saharan dust is not the source of either nitrate or ammonium.

Overall, the data from D326, M68 and P332 can be used to asses the nature of the atmospheric input of iron, phosphate and inorganic nitrogen to the tropical North Atlantic.

By looking at other chemical species also present in the aerosol, it is possible to determine whether the iron, phosphate and nitrogen in each sample has been transported in the Saharan dust plume, or associated with biomass burning, or other sources. The analysis gives an indication of where the aerosols are coming from and the kind of concentrations present over a wide area of the eastern tropical North Atlantic.

As each sample only represents a snapshot in time of the aerosol deposition to the area, and as there are only a few samples, the temporal resolution is not very good. Any mean aerosol concentrations are unlikely to represent a true picture of the atmospheric concentrations in the region. However, this does not mean that the data from these cruises is not valuable as they provide insight into the aerosol concentrations and changes in the chemical composition of the aerosols across the ETNA region during winter and summer, the seasons when most of the Saharan dust transport occurs.

In order to *investigate the solubility of iron aerosol transported to the region*, a much larger dataset was used consisting of samples collected over a period of ten years, and although there is a bias towards the autumn, when most of the samples were collected, the temporal coverage is much better than for the data used in chapter 3 and the spatial coverage is much better than a single island based long-term aerosol observation station. This data was used in chapters 4 and 5. The amount of data makes the observed relationship in iron aerosol solubility with decrease in dust mass loading convincing.

It seems unlikely that more soluble, anthropogenically produced, iron aerosol is having an effect on the overall iron solubility, as the iron solubility does not change significantly with a change in source region for data collected in the ETNA. This leads to the conclusion that iron deposition in the ETNA region is dominated by mineral dust transport from the Sahara, in contrast with Bermuda (*Sedwick et al.*, 2007) and the Caribbean (*Trapp et al.*, 2010), where anthropogenically produced aerosol iron from North America become important in determining aerosol iron solubility at low dust loadings.

There is also no evidence that the dust produced from different point sources across the Sahara have a significantly different aerosol iron solubility, once the aerosol is transported out to the ETNA region. However, it is possible that these differences do exist closer to the location of dust uplift and that atmospheric transport itself has the effect of homogenising dust from the different sources.

The argument that aerosol iron solubility is increased by atmospheric chemical processing cannot be totally dismissed by these data, but it seems unlikely that acid processing could account for the order of magnitude change in iron solubility observed. It is possible that acid processing had some effect, in conjunction with some other effect. The observed increase in aerosol iron solubility could, in theory, be explained by the particle size-sorting during transport, the data used here does not contain sufficient size segregation either to confirm this hypothesis or to rule it out altogether. Collecting samples for the measurement

of the ratio of iron II to iron III may go some way to confirming the amount of redox chemistry that occurs, as would identifying the chemical environment in which the iron in the aerosol is contained.

In short, although the ETNA dry deposition data set has both good spatial and temporal coverage, the data contained within it do not contain the right information to fully investigate the controls on iron solubility in this region. Although the relationship between dust mass loading and iron solubility is more compelling given the amount of data supporting it, it is unclear whether this relationship is a result of a particle size sorting effect and smaller particles being more soluble and being suspended in the atmosphere for longer, or even how much photochemical processing and source region may enhance and/or be interlinked with this effect. Clearly more data is needed, but careful consideration needs to be given to the way in which this extra data is gathered. For example, it would be relatively easy to collect size segregated samples using all six stages of a cascade impactor on a transect of the Atlantic within the Saharan plume, which would go some way to examining the surface area to volume ratio and iron solubility. However, thought should be given to how to account for the particle growth of dust particles within the marine boundary layer and how this may change any possible relationship between particle size and iron solubility, perhaps by the careful investigation of the other species present with the iron aerosol.

Finally, the *quantification of the atmospheric fluxes of iron, nitrogen and phosphate to the ETNA* was addressed in this region where deposition is episodic and under sampled with few sampling time series longer than two or three years, using dry deposition and rain climatologies, calculated from the data set used in chapter 4 in addition to a total of 39 rain samples collected over the same period.

For the dry deposition climatology, potential biases in the distribution of data were overcome by averaging the data by season, and averaging the data by air mass type, then weighting the averages by an air mass type probability, derived from air mass back trajectories. Once the data had been categorised by air mass type, climatology region and season, there were some categories which contained only one or two samples to average, so in order to take into account the uncertainty associated with how representative of a whole population a small number of samples can be, uncertainty values were assigned to each average made according to how many samples in that category. However, the largest uncertainty in the dry deposition fluxes was the in the calculation of dry deposition velocities.

In contrast, in the wet deposition climatology, averages were weighted by the average rainfall fields generated by *Xie and Arkin (1997)*, which would appear to be less uncertain than the calculation of dry deposition velocities. However, the main uncertainty lies in the fact that there were not enough data to be able to average the data by season. This

meant that the averages are biased to the deposition during the spring and autumn, when most of the samples were collected.

It is difficult to directly compare the fluxes from the climatology with others in the literature, as there are relatively few flux estimates for the ETNA region. However, the values do agree relatively well with some of the global fluxes reported in table 5.1 on page 92, and although there are uncertainties associated with both the dry and the wet deposition climatologies, it would appear that both give reasonable flux estimates. The seasonal variation in the deposition of iron is reproduced in the climatology, and shows that for the ETNA the most intense period of dust deposition is during the winter, in agreement with other studies in and near the Cape Verde (*Chiapello et al.*, 1995). The deposition of inorganic nitrogen is shown to have less seasonal variation, which is consistent with observations by *Prospero et al.* (1996) who show that although there is some seasonal variations in reduced and oxidised nitrogen emission around the Atlantic are small compared to the total nitrogen emission. The dry deposition flux of phosphate is rather high compared with other estimates. In particular *Baker et al.* (2010) estimate SRP deposition to be much less for the entire North Atlantic than is estimated here for just the ETNA, however this may be due to the fact that seasonal variation in the deposition of SRP is taken into account in this study.

Considering the inputs of soluble iron, nitrogen and phosphate relative to average phytoplankton requirements shows that although the ETNA has a relatively high atmospheric input of phosphate, it is unlikely to alleviate any phosphate limitation, due to the much higher amount of iron and nitrogen deposited with it. Additionally, the excess iron is likely to stimulate nitrogen fixation, further exacerbating the low phosphate concentrations measured in the region.

Overall, the fluxes calculated here represent a sensible average for the atmospheric deposition to the eastern tropical North Atlantic, by attempting to take into account the distribution of sample data over season and air mass type, and is more likely to be representative of the atmospheric flux to the ETNA than a simple average of all the data. However, there are some major uncertainties associated with dry deposition velocities and the lack of data in some parts of the climatology region, particularly rain data. Uncertainties associated with sample distribution and lack of data might be relatively easy to solve in theory, as it is a matter of looking at which seasons and which air mass types are under sampled and going out and measuring them. However, bearing in mind that it has taken 10 years to collect 39 rain samples for the ETNA region, and that some air mass types are under sampled precisely because they do not occur in the ETNA very frequently, gathering specific types of samples may not be so easy in practice. One solution may be to compare data with the deposition data that is emerging from the SOLAS observatory at Cape Verde, although the data may not have the same spatial resolution. With reference to uncertainties associated with the dry deposition velocity, perhaps a system of reporting

atmospheric concentrations in addition to fluxes, would introduce fewer uncertainties when characterising the atmospheric deposition to the open ocean, however, this would not necessarily be of use to marine chemists wishing to quantify the budgets of nutrients in the surface ocean. Whilst *Tian et al.* (2008) have shown that it is possible to derive dry deposition iron fluxes from the difference between total iron deposition and wet iron deposition fluxes, the approach is unsuitable for ship based sampling due to the difficulties in rain sampling on board a ship. Another approach might be the use of an instrument which measures the particle size distribution coupled with a sonic anemometer to measure the atmospheric flux of particles by eddy covariance, although it would be difficult on a ship to discern aerosol being deposited from seasalt production. Perhaps a more simple strategy, that could be applied would be to take fully size segregated samples using all six stages of the cascade impactor, if not for all samples, then at least at regular intervals. This would at least reduce some of the uncertainty associated with calculating the dry deposition velocity from assumed mass median diameters. Additionally it would be useful if wind speed could be recorded for each sample, rather than using a climatological mean.

Précis

In addition to the quantification of the atmospheric deposition of iron, nitrogen and phosphate to the ETNA, a great deal of information has been inferred from the data used in chapter 3 in terms of chemical composition of aerosols across the ETNA during dust events. Although the data used in chapter 4 cannot fully elucidate reasons for gradients in the solubility of the iron aerosol, it can be used to suggest areas for future work, namely the need for more size segregated data in the Saharan plume region.

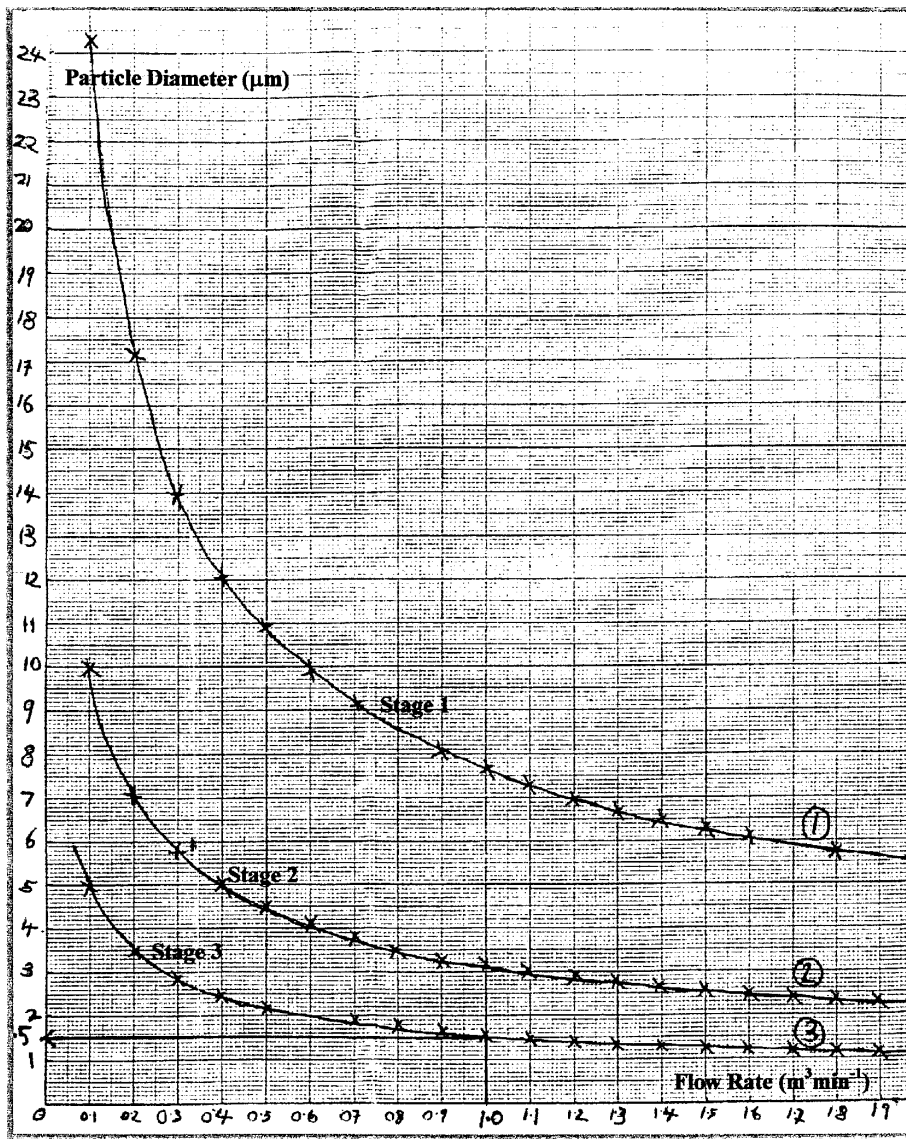
Finally, fluxes derived in chapter 5 have quantified the atmospheric deposition of iron, inorganic nitrogen and soluble reactive phosphate, within the limits of the data available. There are uncertainties associated with the data, which have been discussed above, and the climatology could be improved with more data. However, the fact that the fluxes derived are in some agreement with other estimated fluxes (see table 5.1 on page 92) seems to indicate that they offer a fair representation of the atmospheric deposition of aerosols to the ETNA.

Appendices

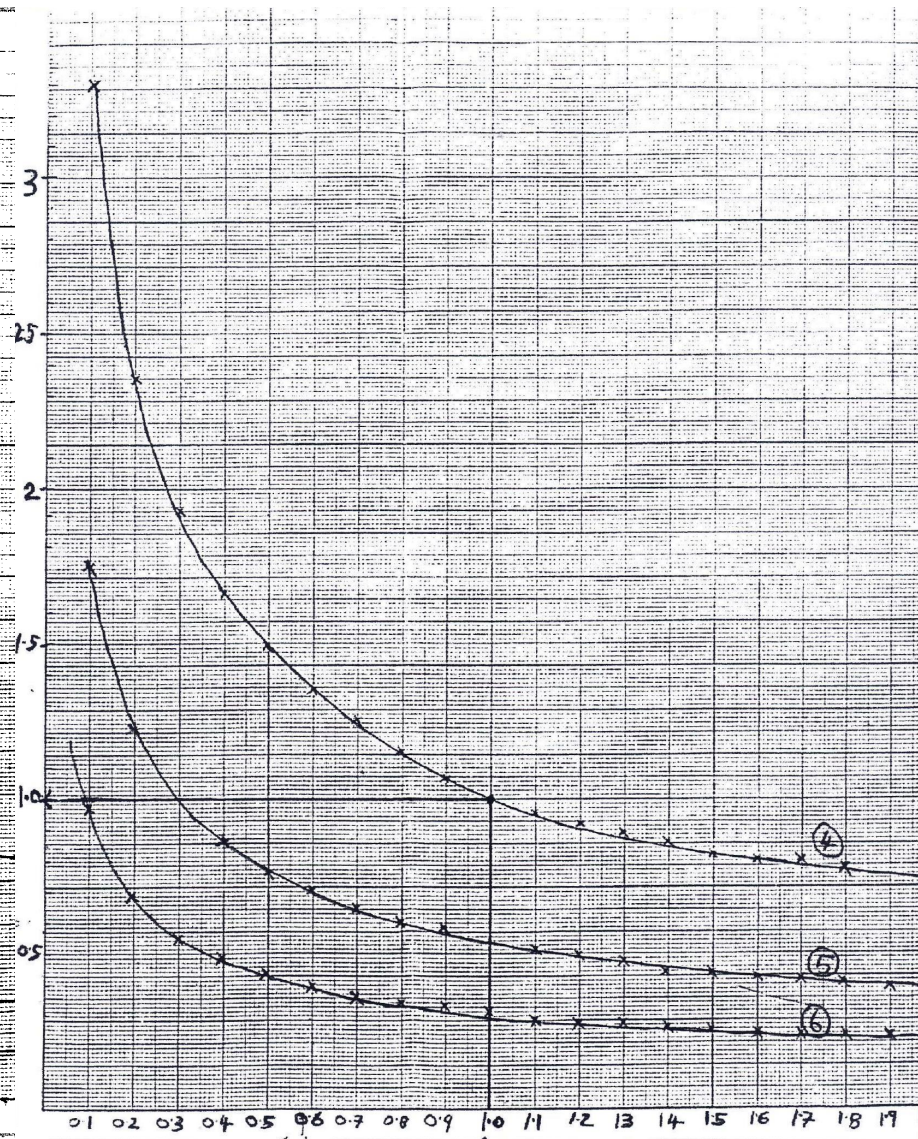
Appendix A

Appendix to Chapter 2





(a) Stages 1, 2, and 3



(b) Stages 4, 5, and 6

Figure A.1: Calibration curves for the six stage impactor from Yeatman (2000) - (a) stages 1, 2, and 3; (b) stages 4, 5, and 6. Particle diameter in μm is plotted on the vertical axes and flow rate in $\text{m}^3 \text{min}^{-1}$ on the horizontal axes. N.B only stages 3 and 4 were used for most of the aerosol samples, with a flow rate of $1 \text{m}^3 \text{min}^{-1}$

Ion	Chemical	Concentration (μM)					
		Standard 6	Standard 5	Standard 4	Standard 3	Standard 2	Standard 1
Coarse							
Chloride	NaCl	600	480	360	240	120	0
Nitrate	NaNO ₃	60	48	36	24	12	0
Sulphate	K ₂ SO ₄	60	48	36	24	12	0
Sodium	NaCl	600	480	360	240	120	0
Calcium	CaCl ₂ .2H ₂ O	60	48	36	24	12	0
Magnesium	MgCl ₂ .6H ₂ O	60	48	36	24	12	0
Potassium	K ₂ SO ₄	15	12	9	6	3	0
Ammonium	NH ₄ Cl	6	4.8	3.6	2.4	1.2	0
Fine							
Chloride	NaCl	400	320	240	160	80	0
Nitrate	NaNO ₃	75	60	45	30	15	0
Sulphate	K ₂ SO ₄	300	240	180	120	60	0
Sodium	NaCl	300	240	180	120	60	0
Calcium	CaCl ₂ .2H ₂ O	50	40	30	20	10	0
Magnesium	MgCl ₂ .6H ₂ O	60	48	36	24	12	0
Potassium	K ₂ SO ₄	75	60	45	30	15	0
Ammonium	NH ₄ Cl	400	320	240	160	80	0
Blank							
Chloride	NaCl	200	160	120	80	40	0
Nitrate	NaNO ₃	10	8	6	4	2	0
Sulphate	K ₂ SO ₄	15	12	9	6	3	0
Sodium	NaCl	150	120	90	60	30	0
Calcium	CaCl ₂ .2H ₂ O	15	12	9	6	3	0
Magnesium	MgCl ₂ .6H ₂ O	10	8	6	4	2	0
Potassium	K ₂ SO ₄	5	4	3	2	1	0
Ammonium	NH ₄ Cl	50	40	30	20	10	0

Table A.1: *Ideal standard concentrations used in ion chromatography analysis*

Samples	Concentration KNO ₃ (µM)					
	Standard 6	Standard 5	Standard 4	Standard 3	Standard 2	Standard 1
Coarse	800	600	400	200	100	0
Fine	400	200	150	100	50	0
Blank	150	120	90	60	30	0

Table A.2: *Ideal standard concentrations used in TN analysis*

Metal	Concentration (µM)					
	Standard 6	Standard 5	Standard 4	Standard 3	Standard 2	Standard 1
Coarse						
Aluminium	50	40	30	20	10	0
Iron	10	8	6	4	2	0
Manganese	2	1.6	1.2	0.8	0.4	0
Vanadium	1.5	1.2	0.9	0.6	0.3	0
Zinc	1.5	1.2	0.9	0.6	0.3	0
Fine						
Aluminium	50	40	30	20	10	0
Iron	2	1.6	1.2	0.8	0.4	0
Manganese	1	0.8	0.6	0.4	0.2	0
Vanadium	1.5	1.2	0.9	0.6	0.3	0
Zinc	1.5	1.2	0.9	0.6	0.3	0
Blank						
Aluminium	1	0.8	0.6	0.4	0.2	0
Iron	1	0.8	0.6	0.4	0.2	0
Manganese	0.5	0.4	0.3	0.2	0.1	0
Vanadium	0.5	0.4	0.3	0.2	0.1	0
Zinc	0.5	0.4	0.3	0.2	0.1	0

Table A.3: *Ideal standard concentrations used in soluble trace metal analysis by ICP OES*

Concentration K_2PO_4 (nM)					
Standard 6	Standard 5	Standard 4	Standard 3	Standard 2	Standard 1
800	600	400	200	100	0

Table A.4: *Ideal standard concentrations used in SRP analysis*

Appendix B

Appendix to Chapter 3

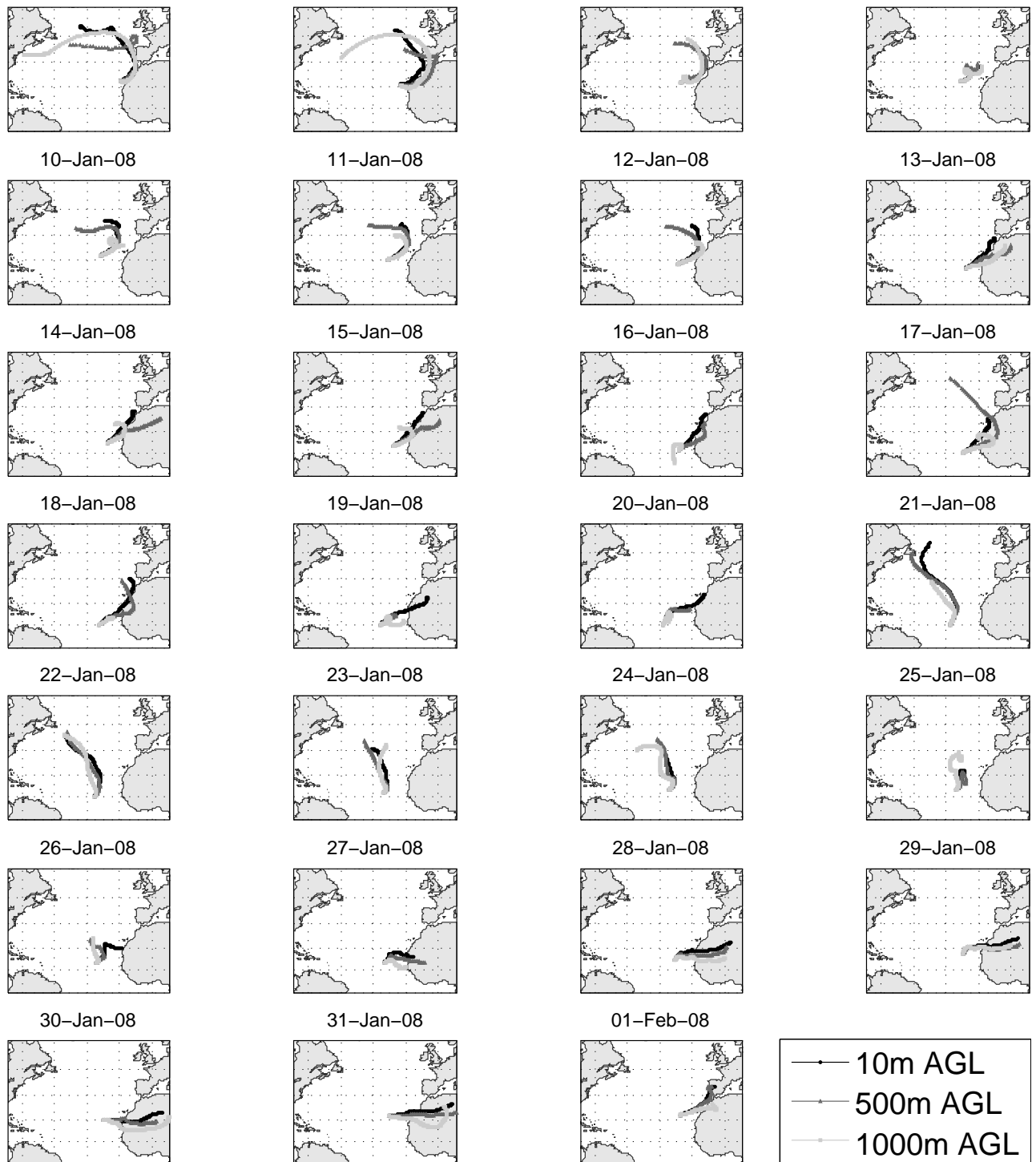


Figure B.1: Air mass back trajectory plots for each sampling date on D326. Dates are shown above each plot

Sample	Start	Airmass Type	Description of Filters		
			Stage 3	Stage 4	Backup
D326TM007	07-Jan-08	SAH	Light Orange	v.Light Orange	White
D326TM008	08-Jan-08	NRM	Light Orange	v.Light Orange	White
D326TM009	09-Jan-08	SAH	White	White	White
D326TM010	10-Jan-08	SAH	White	White	White
D326TM011	11-Jan-08	SAH	White	White	White
D326TM012	12-Jan-08	SAH	Light Orange	v.Light Orange	White
D326TM013	13-Jan-08	SAH	Orange	Light Orange	Pale Grey
D326TM014	14-Jan-08	SAH	Orange	Light Orange	Pale Grey
D326TM015	15-Jan-08	SAH	Light Orange	v.Light Orange	White
D326TM016	16-Jan-08	SAH	Light Orange	v.Light Orange	White
D326TM017	17-Jan-08	SAH	Orange Brown	Orange Brown	Grey Orange Brown
D326TM018	18-Jan-08	SAH	Orange Brown	Orange Brown	Grey Orange Brown
D326TM019	19-Jan-08	SAH	Orange Brown	Orange Brown	Grey Orange Brown
D326TM020	20-Jan-08	SAH	Orange	Light Orange	Pale Grey
D326TM021	21-Jan-08	NRM	White	White	White
D326TM022	22-Jan-08	NRM	White	White	White
D326TM023	23-Jan-08	NRM	White	White	White
D326TM024	24-Jan-08	NRM	Orange	Light Orange	Pale Grey
D326TM025	25-Jan-08	SAH	Orange Brown	Orange Brown	Grey Orange Brown
D326TM026A	26-Jan-08	SAH	Orange	Light Orange	Pale Grey
D326TM026B	26-Jan-08	SAH	Orange Brown	Orange Brown	Grey Orange Brown
D326TM027	27-Jan-08	SAH	Orange Brown	Orange Brown	Grey Orange Brown
D326TM028	28-Jan-08	SAH	Orange Brown	Orange Brown	Grey Orange Brown
D326TM029	29-Jan-08	SAH	Orange Brown	Orange Brown	Grey Orange Brown
D326TM030	30-Jan-08	SAH	Orange	Light Orange	Pale Grey
D326TM031	31-Jan-08	SAH	Orange	Light Orange	Pale Grey
D326TM032	01-Feb-08	SAH	Orange	Light Orange	Pale Grey

Table B.1: Air mass assignments and descriptions of the collected filters for each sampling date on D326

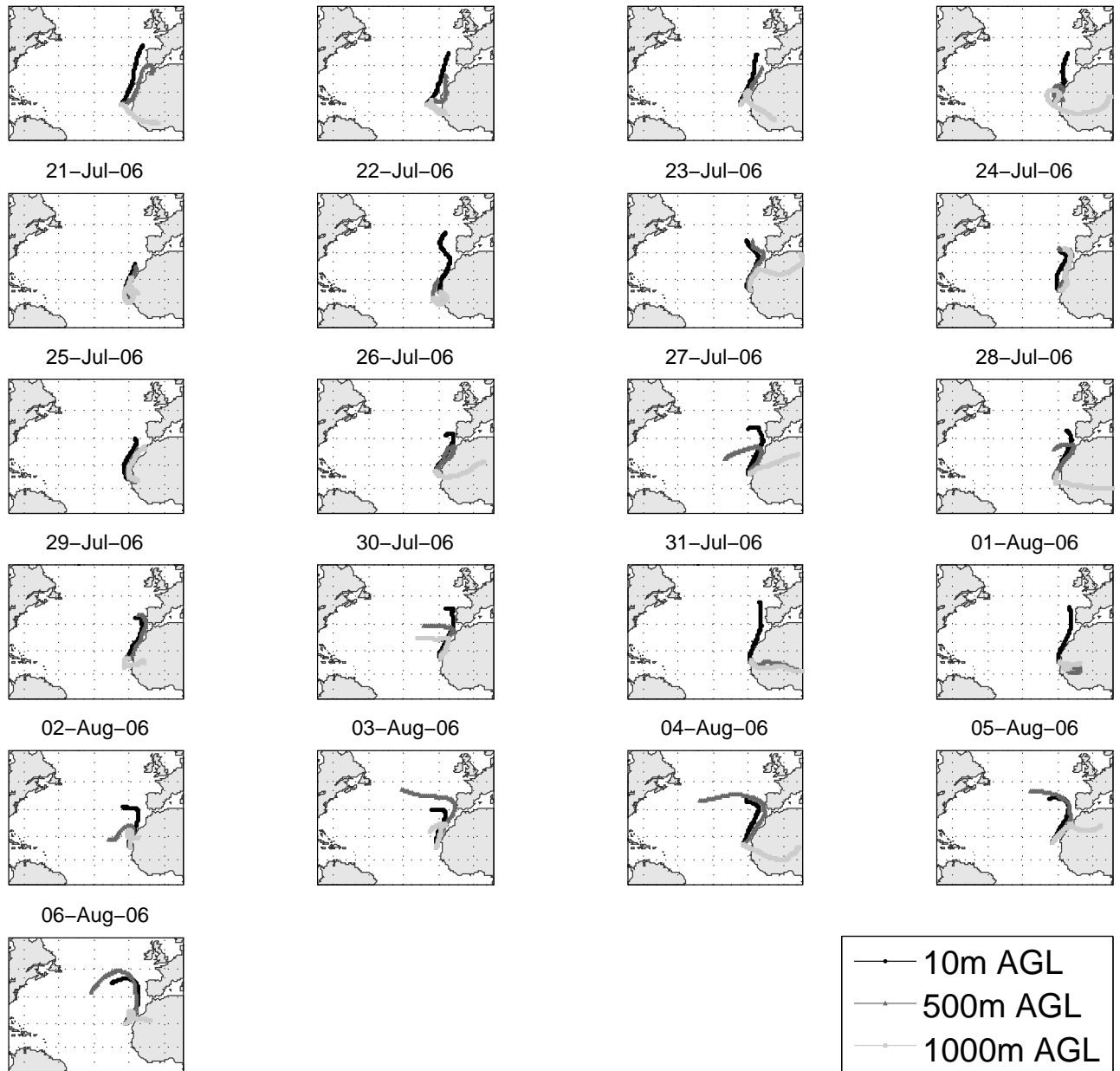


Figure B.2: Air mass back trajectory plots for each sampling date on M68. Dates are shown above each plot

Sample	Start	Airmass Type	Description of Filters		
			Stage 3	Stage 4	Backup
M68M197	16-Jul-06	SAH	Light Orange	v.Light Orange	White
M68M198	17-Jul-06	SAH	Light Orange	v.Light Orange	White
M68M199	18-Jul-06	SAH	Orange	Light Orange	Pale Grey
M68M200	19-Jul-06	SAH	Orange Brown	Orange Brown	Grey Orange Brown
M68M201	20-Jul-06	SAH	Orange Brown	Orange Brown	Grey Orange Brown
M68M202	21-Jul-06	SAH	Orange Brown	Orange Brown	Grey Orange Brown
M68M203	22-Jul-06	SAH	Orange Brown	Orange Brown	Grey Orange Brown
M68M204	23-Jul-06	SAH	Orange Brown	Orange Brown	Grey Orange Brown
M68M205	24-Jul-06	SAH	Orange Brown	Orange Brown	Grey Orange Brown
M68M206	25-Jul-06	SAH	Orange Brown	Orange Brown	Grey Orange Brown
M68M207	26-Jul-06	SAH	Orange Brown	Orange Brown	Grey Orange Brown
M68M208	27-Jul-06	SAH	Orange Brown	Orange Brown	Grey Orange Brown
M68M209	28-Jul-06	SAH	Orange Brown	Orange Brown	Grey Orange Brown
M68M210	29-Jul-06	SAH	Orange Brown	Orange Brown	Grey Orange Brown
M68M211	30-Jul-06	SAH	Orange Brown	Orange Brown	Grey Orange Brown
M68M212	31-Jul-06	SAH	Orange Brown	Orange Brown	Grey Orange Brown
M68M213	01-Aug-06	SAH	Orange Brown	Orange Brown	Grey Orange Brown
M68M214	02-Aug-06	SAH	Light Orange	v.Light Orange	White
M68M215	03-Aug-06	SAH	Light Orange	v.Light Orange	White
M68M216	04-Aug-06	SAH	Light Orange	v.light grey	light grey
M68M217	05-Aug-06	SAH	Light Orange	v.light grey	light grey

Table B.2: *Air mass assignments and descriptions of the collected filters for each sampling date on M68*

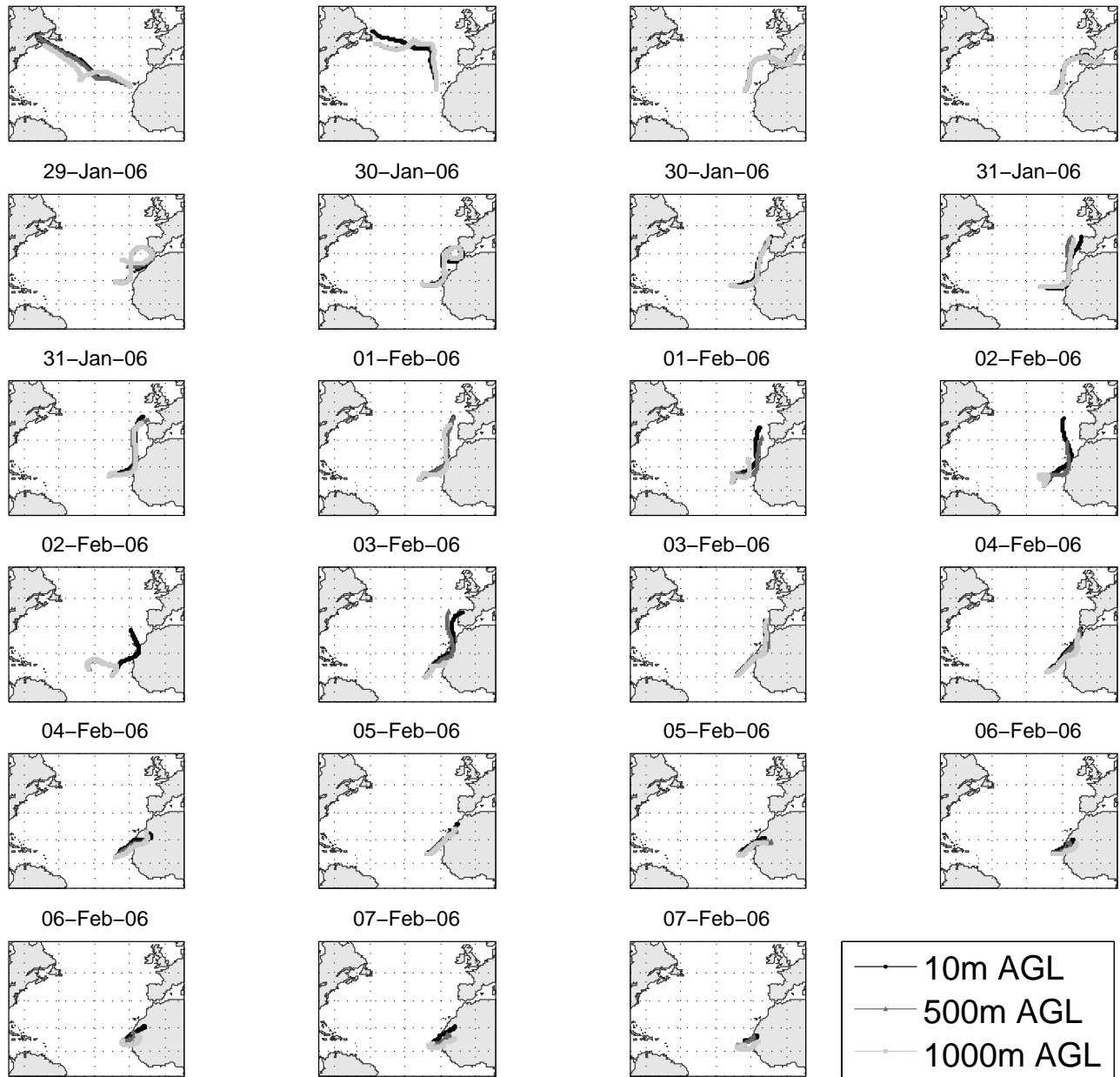


Figure B.3: Air mass back trajectory plots for each sampling date on P332. Dates are shown above each plot

Sample	Start	Airmass Type	Description of Filters		
			Stage 3	Stage 4	Backup
POS06M029	29-Jan-06	EUR	Grey Lines	Grey Lines	Grey
POS06M030	30-Jan-06	SAH	dark grey	dark grey	almost black
POS06M031	31-Jan-06	NRM	Light grey	v.light grey	light grey
POS06M032	01-Feb-06	SAH	Light Orange	v.light grey	light grey
POS06M033	02-Feb-06	SAH	ORANGE BROWN	light orange grey	v light grey
POS06M034A	03-Feb-06	SAH	orange brown	light orange	v light grey
POS06M034B	03-Feb-06	SAH	orange brown	light orange	v light grey
POS06M035A	04-Feb-06	SAH	orange brown	light orange	v light grey
POS06M035B	04-Feb-06	SAH	orange brown	light orange	v light grey
POS06M036	05-Feb-06	SAH	orange stripes	v light orange	vlight orange grey
POS06M037	06-Feb-06	SAH	orange stripes	v light orange	vlight orange grey
POS06M038	07-Feb-06	SAH	filters were a bit mangled		
POS06M039	08-Feb-06	NRM	faint grey	faint grey	white
POS06M040	09-Feb-06	NRM	faint grey	faint grey	white
POS06M041	10-Feb-06	NRM	faint grey	faint grey	white
POS06M043	12-Feb-06	SAH	brown/orange lines	faint grey orange	light grey
POS06M045	14-Feb-06	SAH	Light Orange	v.light grey	light grey
POS06M046	15-Feb-06	SAH	Light Orange	v.light grey	light grey
POS06M047	16-Feb-06	NRM	Light Orange	v.light grey	light grey
POS06M048	17-Feb-06	NRM	faint grey	faint grey	white
POS06M049	18-Feb-06	NRM	faint grey	faint grey	white
POS06M050	19-Feb-06	NRM	v light grey	v light grey	light grey
POS06M052	21-Feb-06	NRM	white	white	white

Table B.3: *Air mass assignments and descriptions of the collected filters for each sampling date on P332*

Appendix C

Appendix to Chapter 5

Cruise	Dates		Ports		No. Samples		
			From	To	Dry	Rain	
ANT18/1	Sep-00	Oct-00	Bremerhaven, Germany	Cape Town, South Africa	4	b	1
JCR	Sep-01	Oct-01	Grimsby, UK	Port Stanley, Falkland Islands	8	ss	1
PEL	Oct-02	Oct-02	Punta Delgada, Azores	Funchal, Madeira	12	b	-
M55	Oct-02	Nov-02	Curacao, Caribbean	Douala, Cameroon	20	ss	8
AMT12	May-03	Jun-03	Port Stanley, Falkland Islands	Grimsby, UK	12	ss	5
AMT13	Sep-03	Oct-03	Immingham, UK	Port Stanley, Falkland Islands	10	ss	5
24N	Apr-04	May-04	Freeport, Bahamas	Tenerife, Canary Islands	10	b	-
AMT14	Apr-04	Jun-04	Port Stanley, Falkland Islands	Grimsby, UK	12	ss	5
FEEP	Apr-04	May-04	Santa Cruz, Tenerife	Santa Cruz, Tenerife	8	b	-
AMT15	Sep-04	Oct-04	Southampton, UK	Cape Town, South Africa	11	ss	6
AIM	Mar-05	Apr-05	Las Palmas, Canaries	Mindelo, Cape Verde	11	b	-
AMT16	May-05	Jun-05	Cape Town, South Africa	Falmouth, UK	5	b	-
AMT17	Oct-05	Nov-05	Glasgow, UK	Port Elizabeth, South Africa	11	ss	6
ANT23/1	Oct-05	Nov-05	Bremerhaven, Germany	Cape Town, South Africa	8	b	-
P332	Jan-06	Feb-06	Las Palmas, Gran Canaria	Las Palmas, Gran Canaria	23	ss	2
M68/3	Jul-06	Aug-06	Santa Cruz, Tenerife	Santa Cruz, Tenerife	20	ss	-
P348	Jan-07	Feb-07	Las Palmas, Canaries	Las Palmas, Canaries	11	b	-
RMB	May-07	May-07	Lisbon, Portugal	Falmouth, UK	14	ss	-
INSPIRE	Nov-07	Dec-07	Santa Cruz, Tenerife	Santa Cruz, Tenerife	18	b	-
D326	Jan-08	Feb-08	Santa Cruz, Tenerife	Santa Cruz, Tenerife	27	ss	1
ANT24-4	Apr-08	May-08	Punta Arenas, Chile	Bremerhaven, Germany	9	b	-
AMT18	Oct-08	Nov-08	Immingham, UK	Port Stanley, Falkland Islands	9	ss	-

Table C.1: *Details of the cruises crossing the ETNA between 2000 and 2009, including the number of rain and dry deposition samples collected in the region and whether they were collected in size segregated (ss) or bulk (b) mode*

Airmass		MAM	JJA	SON	DJF	Annual	Airmass		MAM	JJA	SON	DJF	Annual
ABCD	NAM	0	0	0	0	0	EFGH	NAM	0	0	0	0	0
	NRM	35	12	28	19	94		NRM	0	1	0	5	6
	EUR	1	1	0	1	3		EUR	0	0	0	0	0
	SAH	12	21	25	37	95		SAH	9	2	25	8	44
	SAF	0	0	0	0	0		SAF	1	2	14	0	17
	SAB	0	0	0	0	0		SAB	0	0	8	0	8
	SRM	0	0	0	0	0		SRM	4	0	2	0	6
Total		48	34	53	57	192	Total		14	5	49	13	81

Table C.2: *Distribution of dry deposition data throughout the climatology region (numbers are number of samples)*

Table C.3: Unweighted average dry deposition atmospheric concentration for northern (ABCD) and southern (EFGH) regions listed by component and source region. Error given is the standard deviation of the calculated average

Species	Source	MAM		JJA		SON		DJF		Average	
ABCD											
NH ₄ ⁺ (nmol m ⁻³)	NAM	10.34		16.11		4.53		5.73		9.18	
	NRM	10.34	±6.4	16.11	±7.26	4.53	±2.89	5.73	±1.8	8.46	±5.72
	EUR	25.64		28.09		13.19		10.14		24.63	±4.6
	SAH	15.08	±11.64	31.75	±18	18.63	±18.97	6.83	±6.35	16.48	±15.66
NO ₃ ⁻ (nmol m ⁻³)	NAM	15.37		13.32		11.06		6.01		11.44	
	NRM	15.37	±7.43	13.32	±8.52	11.06	±5.14	6.01	±3.55	11.48	±6.16
	EUR	41.96		13.91		25.76		24.37		26.75	±16.08
	SAH	33.18	±8.31	25.51	±8.65	32.62	±18.75	19.02	±10.46	25.54	±13.03
PO ₄ ³⁻ (pmol m ⁻³)	NAM	26.1		30.35		11.12		52.63		30.05	
	NRM	26.1	±19.77	30.35	±18.17	11.12	±6.86	52.63	±48.51	26.62	±21.63
	EUR	26.33		76.68		18.7		39.42		44.76	±24.5
	SAH	70.95	±23.67	98.23	±31.92	69.01	±33.14	58.55	±25.18	73.14	±36.65
NSS K (nmol m ⁻³)	NAM	0.11		0.44		-0.25		0.43		0.18	
	NRM	0.11	±1.04	0.44	±0.15	-0.25	±0.43	0.43	±0.04	0.17	±0.84
	EUR	0.6		0.77		-1.41		1.19		0.98	
	SAH	1.19	±0.69	1.01	±0.57	1.88	±2.04	0.32	±1.43	1.02	±1.01
NSS Ca (nmol m ⁻³)	NAM	1.86		2.02		1.51		1.03		1.6	
	NRM	1.86	±1.3	2.02	±0.72	1.51	±0.78	1.03	±1.93	1.67	±1.12
	EUR	0.85		3.54		0.69		-2		0.77	
	SAH	26.53	±16.5	11.14	±6.06	12.8	±7.44	16.22	±13.86	15.2	±10.83

Continued on next page

Table C.3 – continued from previous page

Species	Source	MAM		JJA		SON		DJF		Average	
NSSSO ₄ ²⁻ (nmol m ⁻³)	NAM	10.28		13.17		6.08		2.59		8.03	
	NRM	10.28	±5.41	13.17	±6.85	6.08	±3.28	2.59	±1.65	7.57	±4.89
	EUR	19.52		21.49		15.31		16.2		19.07	±3.03
	SAH	21.05	±5.58	31.68	±16.64	23.54	±16.16	13.11	±6.21	19.8	±11.27
Sol. Fe (pmol m ⁻³)	NAM	53.27		66.31		10.28		32.18		40.51	
	NRM	53.27	±24.67	66.31	±24.5	10.28	±5.22	32.18	±26.64	32.43	±26.99
	EUR	154.36		120.4		29.78		67.53		93.96	
	SAH	159.08	±87.09	212.26	±131.81	257.35	±190.2	294.57	±243.63	240.46	±177.19
Sol. Al (pmol m ⁻³)	NAM	254.61		661.65		79.33		188.84		296.11	
	NRM	254.61	±193.38	661.65	±130.08	79.33	±49.32	188.84	±149.74	153.67	±113.87
	EUR	560.81		596.42		174.72		80.53		338.47	
	SAH	1270.44	±788.42	1388.82	±727.12	2178.02	±1834.37	1911.94	±1728.46	1629.16	±1209.4
Total Fe (pmol m ⁻³)	NAM	1360.21		2226.1		285.63		877.78		1187.43	
	NRM	1360.21	±770.76	2226.1	±1872.74	285.63	±196.13	877.78	±819.56	800.55	±682.92
	EUR	5199.57		6085.87		1091.86		34.52		3060.19	
	SAH	11431.4	±9289.87	14905.05	±10988.21	13698.38	±11800.87	28718.03	±26650.74	16827.48	±13995.11
Total Al (pmol m ⁻³)	NAM	2583.07		6836.67		586.49		2277.79		3071.01	
	NRM	2583.07	±1523.58	6836.67	±5824.64	586.49	±430.97	2277.79	±2048.41	1728.24	±1477.64
	EUR	15200.56		20146.1		3451.32		194.2		10170.15	
	SAH	39906.48	±38872.59	54399.1	±43133.41	46342.2	±39985.31	101499.01	±98559.76	62090.47	±56335.38
EFGH											
NH ₄ ⁺ (nmol m ⁻³)	NRM	3.35		22.4		1.47		0.36	±0.2	2.74	±3.43
	SAH	17.96	±3.82	37.19		13.53	±7.04	13.48	±1.82	14.23	±7.35
	SAF	29.48		8.95		12	±5.89	20.74		12.01	±6.23
	SAB	9.93		9.93		9.93	±2.46			9.93	±2.46
	SRM	12.82		12.82		12.82		12.82		12.82	
Continued on next page											

Table C.3 – continued from previous page

Species	Source	MAM		JJA		SON		DJF		Average	
NO ₃ ⁻ (nmol m ⁻³)	NRM	7.36		9.23		5.3		2.63	±0.4	5.5	±4.06
	SAH	20.07	±3.9	29.38		21.42	±13.11	22.21	±10.85	22.4	±13.67
	SAF	8.68		13.94		9.55	±5.71	9.12		10.13	±5.48
	SAB	10.01		10.01		10.01	±3.02			10.01	±3.02
	SRM	10.08		10.08		10.08		10.08		10.08	
NSS K (nmol m ⁻³)	NRM	-0.05		-0.2		0.11		-0.08	±0.2	-0.08	±0.2
	SAH	0.86	±0.37	1.31		2.37	±2.06	1.31		1.74	±1.31
	SAF	1.87		3.92		1.86	±1.58	1.86		2.31	±1.92
	SAB	2.28		2.28		2.28	±0.99			2.28	±0.99
	SRM	-0.05		-0.2		0.11		-0.08			
NSS Ca (nmol m ⁻³)	NRM	1.98		2.66		1.6		0.9		1.78	
	SAH	10.97	±6.34	25.74		13.74	±8.67	22.99	±20.84	15.64	±10.85
	SAF	2.01		1.98		2.18	±0.67	2.09		2.19	±0.82
	SAB	2.15		2.15		2.15	±0.58			2.15	±0.58
	SRM	3.91		3.91		3.91		3.91		3.91	
NSSSO ₄ ²⁻ (nmol m ⁻³)	NRM	4.98		9.74		2.95		1.5	±0.44	3.67	±3.32
	SAH	13.29	±2.09	27.27		14.07	±8.32	16.26	±6.94	15.45	±8.81
	SAF	11.99		14.31		8.38	±4.23	10.18		9.41	±4.52
	SAB	9.04		9.04		9.04	±1.98			9.04	±1.98
	SRM	5.51		5.51		5.51		5.51		5.51	
Sol. Fe (pmol m ⁻³)	NRM	45.04		56.05		8.69		27.41	±1.06	27.41	±1.06
	SAH	85.8	±38.51	65.35		192.45	±126.61	404.68	±236.92	192.49	±134.82
	SAF	33.35		8.79		41.53	±21.96	16.98		38.24	±26.51
	SAB	38.19		38.19		38.19	±15.9			38.19	±15.9
	SRM	34.55		34.55		34.55		34.55		34.55	

Continued on next page

Table C.3 – continued from previous page

Species	Source	MAM		JJA	SON		DJF		Average	
Sol. Al (pmol m^{-3})	NRM	306.23		795.79	95.41		184.82	± 62.47	184.82	± 62.47
	SAH	630.52	± 303.08	551.6	1711.01	± 1038.69	3238.6	± 2201.93	1570.33	± 1049.93
	SAF	278.37		58.45	351.68	± 225.17	131.76		289.58	± 201.8
	SAB	346.68		346.68	346.68	± 229.08			346.68	± 229.08
	SRM	228.88		228.88	228.88		228.88		228.88	
Total Fe (pmol m^{-3})	NRM	1278.58		2092.51	268.49		752.5	± 28.95	752.5	± 28.95
	SAH	3999.23	± 1729.44	26315.73	13687.71	± 10702.75	38097.39	± 41804.28	12149.97	± 9579.72
	SAF	1145.94		1702.13	960.55	± 511.42	1516.73		1062.31	± 693.03
	SAB	1386.35		1386.35	1386.35	± 1119.93			1386.35	± 1119.93
	SRM	1464.21		1464.21	1464.21		1464.21		1464.21	
Total Al (pmol m^{-3})	NRM	3738.12		9893.75	848.75		2501.04	± 537.39	2501.04	± 537.39
	SAH	12204.89	± 4916.45	92061.51	52997.82	± 41151.59	118898.72	± 129399.28	48580.75	± 41186.29
	SAF	4279.44		6351.12	3588.88	± 2253.55	5660.56		3686.75	± 2435.22
	SAB	3745.74		3745.74	3745.74	± 2846.97			3745.74	± 2846.97
	SRM	4217.08		4217.08	4217.08		4217.08		4217.08	

Table C.4: *Unweighted average dry deposition flux for northern (ABCD) and southern (EFGH) regions listed by component and source region. Ranges given were calculated using the dry deposition velocity correlating to the upper and lower MMD bounds*

Species	Source	MAM		JJA		SON		DJF	
ABCD									
NH ₄ ⁺ (mmol m ⁻² d ⁻¹)	NAM	0.82	(0.23 - 1.31)	0.63	(0.31 - 0.97)	0.6	(0.21 - 0.97)	2.34	(0.37 - 3.78)
	NRM	0.85	(0.23 - 1.34)	0.72	(0.31 - 1.06)	0.6	(0.21 - 0.97)	2.24	(0.36 - 3.67)
	EUR	3.08	(0.64 - 4.78)	2.82	(0.74 - 4.18)	2.17	(0.53 - 3.43)	4.58	(0.68 - 7.04)
	SAH	1.06	(0.39 - 1.47)	3.79	(0.92 - 5.65)	1.8	(0.58 - 2.64)	3.77	(0.59 - 5.78)
NO ₃ ⁻ (mmol m ⁻² d ⁻¹)	NAM	5.8	(0.9 - 9.8)	7.1	(1.3 - 13.2)	5.3	(0.9 - 9.4)	2.9	(0.4 - 4.6)
	NRM	6.1	(0.9 - 10)	9	(1.4 - 14.9)	5.3	(0.9 - 9.4)	2.7	(0.4 - 4.5)
	EUR	14.1	(2 - 22.3)	9.7	(1.3 - 15)	12.9	(2 - 21.2)	17	(2.3 - 26.3)
	SAH	22.7	(2.9 - 34)	18.5	(2.5 - 28.6)	28.1	(3.9 - 43.8)	10.8	(1.5 - 16.6)
PO ₄ ³⁻ (μmol m ⁻² d ⁻¹)	NAM	8.9	(1.7 - 14.7)	6.5	(1.4 - 11.8)	2	(0.4 - 3.4)	42.2	(7 - 68)
	NRM	9.3	(1.7 - 15)	8.2	(1.5 - 13.2)	2	(0.4 - 3.4)	40.5	(6.9 - 66)
	EUR	20.3	(3.4 - 31.9)	34.2	(5.1 - 52.6)	4.6	(0.9 - 7.4)	10.5	(1.8 - 16)
	SAH	30.2	(4.4 - 45)	36.1	(5.6 - 55.5)	24.7	(3.9 - 38.3)	31.2	(4.6 - 48)
NSS K (mmol m ⁻² d ⁻¹)	NAM	-0.016	(-0.001 - -0.027)	0.248	(0.051 - 0.454)	0.378	(0.065 - 0.665)	-0.036	(0.005 - -0.065)
	NRM	-0.016	(-0.001 - -0.028)	0.313	(0.053 - 0.51)	0.378	(0.065 - 0.665)	-0.034	(0.005 - -0.063)
	EUR	-0.009	(0.001 - -0.015)	0.148	(0.028 - 0.225)	0.272	(0.043 - 0.445)	-0.026	(0.004 - -0.044)
	SAH	0.439	(0.059 - 0.657)	0.254	(0.045 - 0.387)	1.427	(0.206 - 2.223)	-0.028	(0 - -0.046)
NSS Ca (mmol m ⁻² d ⁻¹)	NAM	1.23	(0.2 - 2.06)	0.88	(0.17 - 1.61)	0.63	(0.11 - 1.11)	-0.25	(-0.01 - -0.42)
	NRM	1.28	(0.2 - 2.1)	1.11	(0.18 - 1.82)	0.63	(0.11 - 1.11)	-0.24	(-0.01 - -0.41)
	EUR	-1.17	(-0.15 - -1.87)	1.85	(0.27 - 2.85)	-0.6	(-0.08 - -1)	-3.4	(-0.42 - -5.27)
	SAH	16.29	(2.13 - 24.41)	7.41	(1.04 - 11.43)	8.64	(1.22 - 13.47)	3.2	(0.46 - 4.93)

Continued on next page

Table C.4 – continued from previous page

Species	Source	MAM		JJA		SON		DJF	
NSS SO ₄ ²⁻ (mmol m ⁻² d ⁻¹)	NAM	1.01	(0.26 - 1.63)	1.78	(0.46 - 3.16)	1.26	(0.28 - 2.16)	-0.02	(0.03 - -0.06)
	NRM	1.05	(0.26 - 1.66)	2.21	(0.48 - 3.53)	1.26	(0.28 - 2.16)	-0.02	(0.03 - -0.05)
	EUR	1.23	(0.43 - 1.81)	1.7	(0.51 - 2.48)	1.42	(0.39 - 2.22)	1.12	(0.36 - 1.62)
	SAH	3.67	(0.68 - 5.41)	5.03	(1.06 - 7.57)	9.52	(1.55 - 14.73)	0.87	(0.26 - 1.26)
Sol. Fe (μmol m ⁻² d ⁻¹)	NAM	7.6	(4.3 - 11.3)	18.1	(11.3 - 29.7)	2.5	(1.5 - 3.9)	8.7	(4.6 - 12.2)
	NRM	8.2	(4.5 - 11.8)	25.4	(13.4 - 36.8)	2.5	(1.5 - 3.9)	8.1	(4.3 - 11.7)
	EUR	22	(12.3 - 29.9)	37.7	(22 - 49.4)	7.1	(3.9 - 10.2)	10.5	(6.3 - 13.6)
	SAH	63.8	(40.8 - 81.1)	78.6	(45.6 - 103)	93.7	(52.1 - 125.5)	46.3	(27 - 60.6)
Sol. Al (μmol m ⁻² d ⁻¹)	NAM	41	(23 - 61)	137	(86 - 224)	14	(8 - 22)	49	(26 - 69)
	NRM	44	(24 - 64)	191	(102 - 278)	14	(8 - 22)	46	(25 - 66)
	EUR	103	(56 - 141)	207	(121 - 272)	35	(19 - 51)	21	(13 - 28)
	SAH	583	(372 - 742)	641	(370 - 842)	826	(458 - 1106)	275	(160 - 360)
Total Fe (μmol m ⁻² d ⁻¹)	NAM	350	(190 - 530)	450	(280 - 730)	60	(40 - 100)	260	(140 - 370)
	NRM	380	(200 - 550)	620	(330 - 900)	60	(40 - 100)	250	(130 - 350)
	EUR	2180	(1260 - 2850)	2180	(1260 - 2850)	2180	(1260 - 2850)	10	(10 - 20)
	SAH	5410	(3450 - 6880)	6360	(3680 - 8350)	5530	(3070 - 7400)	12260	(7090 - 16080)
Total Al (μmol m ⁻² d ⁻¹)	NAM	740	(400 - 1100)	1500	(940 - 2440)	150	(80 - 230)	750	(400 - 1050)
	NRM	790	(420 - 1140)	2090	(1120 - 3030)	150	(80 - 230)	700	(370 - 1010)
	EUR	7890	(4570 - 10350)	7890	(4570 - 10350)	7890	(4570 - 10350)	80	(40 - 100)
	SAH	19420	(12390 - 24710)	23880	(13800 - 31340)	19230	(10660 - 25770)	44560	(25750 - 58480)
EFGH									
NH ₄ ⁺ (mmol m ⁻² d ⁻¹)	NRM	1.22	(0.34 - 1.91)	0.83	(0.41 - 1.18)	0.86	(0.3 - 1.39)	1.87	(0.3 - 3.06)
	SAH	1.69	(0.46 - 2.43)	2.79	(1.39 - 3.78)	1.05	(0.31 - 1.55)	5.98	(0.87 - 9.2)
	SAF	3	(0.78 - 4.49)	1.48	(0.51 - 2.63)	0.99	(0.29 - 1.72)	2.34	(0.56 - 3.43)
	SAB	0.88	(0.28 - 1.6)	0.85	(0.28 - 1.56)	0.75	(0.27 - 1.44)		
	SRM	1.52	(0.44 - 2.92)	2.16	(0.46 - 3.54)	2.35	(0.48 - 3.72)	1.81	(0.45 - 3.23)
Continued on next page									

Table C.4 – continued from previous page

Species	Source	MAM		JJA		SON		DJF	
NO_3^- ($\text{mmol m}^{-2} \text{d}^{-1}$)	NRM	6.2	(0.9 - 10.2)	6.2	(0.9 - 10.1)	5.4	(0.9 - 9.5)	4.8	(0.7 - 7.8)
	SAH	16.5	(2.1 - 24.8)	29.2	(3.9 - 45.1)	14.6	(2 - 22.7)	17.9	(2.4 - 27.7)
	SAF	6.3	(0.9 - 9.8)	3.9	(0.8 - 7.6)	4.3	(0.8 - 8)	6.7	(0.9 - 10.2)
	SAB	4.7	(0.9 - 9.2)	4.5	(0.9 - 8.9)	3.8	(0.9 - 8.1)		
	SRM	4.4	(0.9 - 8.8)	6.5	(1 - 10.8)	7.1	(1 - 11.4)	5.3	(1 - 9.8)
PO_4^{3-} ($\mu\text{mol m}^{-2} \text{d}^{-1}$)	NRM	1.6	(0.4 - 2.6)	6.9	(1.2 - 11.3)	0.4	(0.1 - 0.6)	1.4	(0.3 - 2.2)
	SAH	16.9	(2.6 - 25.1)	27.5	(4.5 - 42.1)	17.9	(2.8 - 27.7)	63.9	(9.1 - 98.5)
	SAF	7	(1.2 - 10.7)	6.2	(1.4 - 11.9)	8.8	(1.8 - 16.1)	10.5	(1.6 - 15.8)
	SAB	12.8	(2.7 - 24.8)	12.3	(2.7 - 24.1)	10.4	(2.5 - 21.9)		
	SRM	6.7	(1.5 - 13.4)	9.8	(1.6 - 16.4)	10.7	(1.7 - 17.3)	8.1	(1.6 - 14.9)
NSS K ($\text{mmol m}^{-2} \text{d}^{-1}$)	NRM	-0.029	(-0.003 - -0.049)	0.545	(0.087 - 0.892)	0.668	(0.115 - 1.174)	0.355	(0.07 - 0.572)
	SAH	1.059	(0.142 - 1.585)	0.391	(0.067 - 0.597)	0.479	(0.086 - 0.738)	0.401	(0.068 - 0.613)
	SAF	0.311	(0.064 - 0.474)	0.208	(0.057 - 0.386)	0.232	(0.057 - 0.414)	0.341	(0.064 - 0.51)
	SAB	0.438	(0.103 - 0.834)	0.419	(0.102 - 0.813)	0.358	(0.097 - 0.739)		
	SRM	-0.018	(-0.002 - -0.038)	0.521	(0.086 - 0.872)	0.801	(0.119 - 1.297)	0.284	(0.067 - 0.51)
NSS Ca ($\text{mmol m}^{-2} \text{d}^{-1}$)	NRM	0.11	(0.03 - 0.18)	1.19	(0.19 - 1.95)	0.06	(0.02 - 0.09)	-1.03	(-0.14 - -1.7)
	SAH	8.43	(1.08 - 12.63)	12.72	(1.77 - 19.62)	8.9	(1.26 - 13.88)	10.83	(1.69 - 16.62)
	SAF	0.92	(0.14 - 1.42)	0.71	(0.15 - 1.37)	0.92	(0.17 - 1.7)	1.21	(0.17 - 1.83)
	SAB	0.89	(0.18 - 1.73)	0.85	(0.18 - 1.68)	0.72	(0.17 - 1.52)		
	SRM	1.62	(0.34 - 3.28)	2.39	(0.38 - 4.02)	2.61	(0.39 - 4.23)	1.97	(0.36 - 3.65)
NSS SO_4^{2-} ($\text{mmol m}^{-2} \text{d}^{-1}$)	NRM	0.87	(0.22 - 1.37)	1.08	(0.27 - 1.7)	1.04	(0.23 - 1.78)	0.84	(0.18 - 1.35)
	SAH	2.46	(0.47 - 3.62)	6.13	(1.18 - 9.29)	2.68	(0.5 - 4.11)	4.83	(0.84 - 7.37)
	SAF	2.04	(0.41 - 3.11)	1.1	(0.32 - 2.04)	0.95	(0.25 - 1.68)	1.8	(0.35 - 2.69)
	SAB	1.22	(0.32 - 2.28)	1.17	(0.32 - 2.22)	1.01	(0.31 - 2.03)		
	SRM	0.5	(0.16 - 0.94)	0.7	(0.17 - 1.14)	0.76	(0.17 - 1.19)	0.59	(0.16 - 1.04)

Continued on next page

Table C.4 – continued from previous page

Species	Source	MAM		JJA		SON		DJF	
Sol. Fe ($\mu\text{mol m}^{-2} \text{d}^{-1}$)	NRM	7.9	(4.3 - 11.4)	24.9	(13.2 - 36.1)	2.4	(1.4 - 3.8)	7.9	(4.2 - 11.4)
	SAH	29.8	(19.2 - 37.9)	22.7	(13.2 - 29.7)	54.3	(30.5 - 72.6)	184.1	(106.3 - 241.5)
	SAF	12.7	(7.1 - 17)	6.9	(4.5 - 11.2)	7.5	(4.8 - 12.3)	14.2	(8.6 - 18.2)
	SAB	8.2	(5.4 - 13.3)	7.9	(5.2 - 12.7)	6.8	(4.6 - 10.8)		
	SRM	4.8	(3.2 - 7.6)	7.3	(4 - 10.8)	8.3	(4.5 - 11.6)	5.6	(3.6 - 9.1)
Sol. Al ($\mu\text{mol m}^{-2} \text{d}^{-1}$)	NRM	38	(20 - 54)	162	(86 - 235)	12	(7 - 19)	37	(20 - 54)
	SAH	265	(169 - 337)	200	(117 - 262)	558	(312 - 746)	1552	(895 - 2037)
	SAF	124	(69 - 166)	66	(43 - 108)	73	(46 - 119)	138	(84 - 178)
	SAB	70	(46 - 115)	68	(45 - 109)	58	(40 - 93)		
	SRM	38	(26 - 61)	58	(32 - 87)	67	(36 - 94)	45	(28 - 73)
Total Fe ($\mu\text{mol m}^{-2} \text{d}^{-1}$)	NRM	210	(110 - 300)	210	(110 - 300)	210	(110 - 300)	210	(110 - 300)
	SAH	1890	(1210 - 2410)	11230	(6490 - 14740)	5520	(3060 - 7400)	16260	(9400 - 21340)
	SAF	510	(280 - 690)	410	(270 - 670)	250	(160 - 410)	760	(460 - 970)
	SAB	130	(80 - 210)	120	(80 - 200)	270	(190 - 440)		
	SRM	250	(170 - 400)	380	(210 - 570)	440	(230 - 610)	290	(190 - 480)
Total Al ($\mu\text{mol m}^{-2} \text{d}^{-1}$)	NRM	760	(410 - 1110)	760	(410 - 1110)	760	(410 - 1110)	760	(410 - 1110)
	SAH	5940	(3790 - 7560)	40420	(23350 - 53040)	21990	(12200 - 29470)	52200	(30160 - 68500)
	SAF	1850	(1020 - 2480)	1470	(960 - 2410)	910	(570 - 1500)	2730	(1650 - 3520)
	SAB	510	(340 - 840)	490	(330 - 800)	730	(490 - 1170)		
	SRM	780	(520 - 1260)	1200	(650 - 1790)	1380	(730 - 1940)	920	(580 - 1510)

Table C.5: *Weighted dry deposition atmospheric concentrations for each climatology box (A-H)*

Species	Box	MAM		JJA		SON		DJF	
NH_4^+ (nmol m ⁻³)	A	11.0	±2.07	17.4	±2.64	7.4	±1.25	6.1	±1.40
	B	12.3	±2.93	18.9	±3.03	9.3	±2.10	6.5	±1.73
	C	12.3	±1.86	26.4	±3.97	15.1	±2.29	6.4	±0.98
	D	13.5	±2.46	28.8	±4.35	17.0	±2.70	6.7	±1.14
	E	17.0	±5.25	31.5	±31.52	12.7	±3.34	12.8	±3.84
	F	17.7	±5.35	27.7	±27.65	13.4	±2.88	13.4	±4.02
	G	23.0	±21.12	9.9	±9.90	11.6	±3.22	18.5	±17.07
	H	23.5	±23.42	10.0	±9.96	11.2	±3.60	19.0	±18.77
NO_3^- (nmol m ⁻³)	A	17.5	±3.28	14.3	±2.16	15.4	±2.62	9.7	±2.12
	B	21.2	±4.94	15.4	±2.42	18.5	±4.15	13.0	±3.59
	C	22.7	±3.43	21.3	±3.20	27.3	±4.13	14.2	±2.15
	D	26.8	±4.72	23.2	±3.50	30.1	±4.81	16.6	±2.83
	E	19.2	±6.11	24.5	±24.53	19.0	±4.19	21.2	±6.37
	F	19.8	±6.05	21.7	±21.70	20.3	±3.78	22.1	±6.62
	G	10.7	±8.53	12.7	±12.70	9.8	±2.71	11.2	±8.79
	H	9.2	±9.10	11.7	±11.69	9.9	±3.14	9.6	±9.25
PO_4^{3-} (pmol m ⁻³)	A	31.1	±6.71	35.8	±9.62	22.6	±3.65	54.0	±17.03
	B	37.7	±9.70	42.3	±10.60	29.1	±5.38	54.2	±15.37
	C	44.4	±11.04	74.9	±12.84	54.6	±8.22	56.3	±11.46
	D	53.6	±15.01	85.5	±13.76	61.8	±9.49	57.1	±10.65
	E	50.8	±15.67	45.8	±45.83	43.5	±8.95	118.2	±35.56
	F	53.1	±16.04	40.9	±40.92	47.0	±8.51	123.6	±37.09
	G	30.1	±24.35	36.7	±36.74	30.5	±7.99	41.2	±27.82
	H	28.6	±28.20	39.1	±39.12	33.6	±9.95	28.1	±26.17
NSS K (nmol m ⁻³)	A	0.2	±0.10	0.5	±0.13	0.2	±0.01	0.4	±0.20
	B	0.4	±0.21	0.5	±0.14	0.3	±0.02	0.4	±0.22
	C	0.6	±0.26	0.8	±0.15	1.3	±0.20	0.4	±0.11
	D	0.8	±0.39	0.9	±0.15	1.6	±0.22	0.4	±0.10
	E	0.8	±0.40	0.9	±0.93	2.0	±0.31	1.2	±1.24
	F	0.8	±0.42	0.7	±0.71	2.2	±0.33	1.3	±1.30
	G	1.3	±1.24	2.9	±2.88	1.8	±0.36	1.5	±1.53
	H	1.5	±1.54	2.6	±2.62	1.8	±0.43	1.5	±1.46
NSS Ca (nmol m ⁻³)	A	4.6	±0.74	2.7	±0.42	3.7	±0.58	5.0	±0.80
	B	8.2	±1.28	3.6	±0.56	4.9	±0.77	7.3	±0.99
	C	11.9	±1.79	8.0	±1.20	10.0	±1.50	10.6	±1.59
	D	17.0	±2.56	9.4	±1.42	11.4	±1.71	13.0	±1.93
	E	10.4	±3.20	20.2	±20.24	11.8	±2.27	21.8	±6.58
	F	10.8	±3.27	17.0	±17.04	12.8	±2.20	22.8	±6.85
	G	3.7	±2.55	2.4	±2.44	2.4	±0.78	5.5	±3.04
	H	2.5	±2.40	2.4	±2.36	2.5	±0.90	2.9	±2.57

Continued on next page

Table C.5 – weighted dry concentrations – continued from previous page

Species	Source	MAM	JJA	SON	DJF
NSS SO ₄ ²⁻ (nmol m ⁻³)	A	11.5 ±2.12	14.6 ±2.22	9.6 ±1.62	5.6 ±1.19
	B	13.5 ±2.88	16.4 ±2.61	11.9 ±2.61	8.1 ±2.28
	C	14.7 ±2.22	25.3 ±3.81	19.2 ±2.91	9.2 ±1.40
	D	17.1 ±2.88	28.2 ±4.25	21.5 ±3.40	11.1 ±1.89
	E	12.7 ±4.05	22.0 ±22.03	12.3 ±2.59	15.5 ±4.66
	F	13.1 ±4.00	18.7 ±18.69	13.3 ±2.39	16.2 ±4.85
	G	10.6 ±9.23	11.9 ±11.90	8.3 ±2.05	10.5 ±8.74
	H	10.4 ±10.28	10.8 ±10.78	8.4 ±2.39	9.4 ±9.13
Sol. Fe (pmol m ⁻³)	A	65.6 ±14.81	77.9 ±33.15	59.1 ±9.20	102.7 ±18.24
	B	85.3 ±25.44	91.6 ±33.63	86.2 ±14.52	147.6 ±27.00
	C	96.5 ±24.33	162.0 ±32.34	195.8 ±29.42	197.4 ±29.69
	D	120.1 ±35.20	184.9 ±32.19	226.4 ±34.30	240.8 ±37.06
	E	83.0 ±43.05	58.6 ±58.60	161.9 ±28.38	384.4 ±115.62
	F	85.1 ±42.94	53.5 ±53.46	178.0 ±29.11	402.0 ±120.63
	G	42.1 ±35.63	17.7 ±17.71	40.8 ±10.52	78.7 ±35.07
	H	34.8 ±34.34	25.5 ±25.48	40.7 ±12.00	29.2 ±22.84
Sol. Al (pmol m ⁻³)	A	368.9 ±86.58	719.2 ±321.73	493.9 ±76.21	647.1 ±110.14
	B	531.8 ±153.31	785.5 ±312.46	720.2 ±117.42	921.4 ±146.98
	C	669.7 ±178.69	1138.2 ±250.69	1654.9 ±248.54	1273.4 ±191.36
	D	883.4 ±258.69	1252.2 ±231.65	1913.8 ±289.12	1553.5 ±234.29
	E	608.4 ±314.65	495.6 ±495.56	1430.3 ±243.63	3074.7 ±924.38
	F	624.7 ±315.10	432.5 ±432.53	1576.5 ±252.76	3216.6 ±965.24
	G	326.1 ±278.41	129.0 ±129.03	345.3 ±84.26	620.7 ±271.93
	H	281.7 ±278.67	210.6 ±210.60	347.7 ±97.27	221.1 ±170.10
Total Fe (pmol m ⁻³)	A	2498.0 ±630.57	3232.7 ±1206.67	2936.5 ±451.23	8294.4 ±1301.06
	B	4144.6 ±1279.44	4421.4 ±1343.12	4393.3 ±716.56	12780.7 ±1936.55
	C	5475.7 ±1524.98	10539.0 ±1851.93	10355.8 ±1555.23	18401.8 ±2761.69
	D	7610.1 ±2278.88	12528.6 ±2030.92	12012.7 ±1814.66	22940.8 ±3442.43
	E	3813.4 ±1950.37	20143.0 ±20143.05	11366.8 ±1873.85	36092.6 ±10835.85
	F	3950.7 ±1986.75	16447.5 ±16447.46	12577.3 ±1987.73	37828.1 ±11349.52
	G	1648.5 ±1346.24	1655.9 ±1655.91	1184.4 ±355.45	7120.6 ±3023.44
	H	1265.9 ±1246.73	1569.5 ±1569.46	1320.1 ±433.25	2329.2 ±1729.22
Total Al (pmol m ⁻³)	A	6789.6 ±1834.84	10611.8 ±3809.23	9630.3 ±1474.76	28722.8 ±4457.26
	B	12829.6 ±4084.94	15063.3 ±4356.57	14606.1 ±2371.17	44767.0 ±6772.09
	C	17834.1 ±5128.85	38020.0 ±6536.27	34939.6 ±5246.82	64733.0 ±9713.69
	D	25714.0 ±7778.20	45482.9 ±7289.60	40593.3 ±6129.30	80923.8 ±12143.39
	E	11626.6 ±5940.97	70391.6 ±70391.63	43819.0 ±7062.90	112650.1 ±33821.88
	F	12053.9 ±6060.27	57235.6 ±57235.60	48581.0 ±7579.11	118059.5 ±35421.45
	G	5426.4 ±4504.13	5741.2 ±5741.19	3962.7 ±1097.58	22849.3 ±10061.84
	H	4270.5 ±4212.05	5041.3 ±5041.29	4189.7 ±1290.20	7919.1 ±6046.66

Table C.6: *Weighted dry deposition flux for each climatology box (A-H)*

Species	Box	MAM	JJA	SON	DJF
NH ₄ ⁺ (mmol m ⁻² d ⁻¹)	A	0.9 ±0.07	1.0 ±0.04	0.9 ±0.01	2.7 ±0.18
	B	1.0 ±0.18	1.3 ±0.04	1.1 ±0.04	3.1 ±0.06
	C	0.9 ±0.14	2.7 ±0.13	1.5 ±0.05	3.2 ±0.31
	D	1.0 ±0.24	3.2 ±0.16	1.7 ±0.05	3.5 ±0.25
	E	1.7 ±0.23	2.6 ±1.89	1.2 ±0.14	5.8 ±0.27
	F	1.7 ±0.20	2.5 ±1.73	1.2 ±0.06	5.9 ±0.24
	G	2.4 ±1.31	1.5 ±0.72	1.1 ±0.00	2.8 ±1.26
	H	2.4 ±1.44	1.3 ±0.60	1.0 ±0.06	2.3 ±1.37
NO ₃ ⁻ (mmol m ⁻² d ⁻¹)	A	8.0 ±0.44	9.8 ±1.47	9.9 ±1.01	5.1 ±0.28
	B	10.8 ±1.53	10.7 ±1.43	12.7 ±0.92	7.2 ±0.18
	C	12.9 ±2.00	15.3 ±1.52	22.4 ±2.30	7.8 ±0.72
	D	16.4 ±3.30	16.7 ±1.53	25.3 ±2.50	9.3 ±0.64
	E	15.8 ±1.29	23.5 ±13.65	13.1 ±0.67	17.2 ±0.72
	F	16.4 ±1.20	20.1 ±11.48	13.9 ±1.06	17.8 ±0.65
	G	7.4 ±2.71	4.6 ±1.60	4.5 ±0.46	8.3 ±3.32
	H	5.8 ±2.86	4.6 ±1.58	4.5 ±0.28	6.7 ±3.59
PO ₄ ³⁻ (μmol m ⁻² d ⁻¹)	A	11.6 ±2.09	10.4 ±0.50	6.5 ±0.58	37.7 ±0.16
	B	15.2 ±5.44	13.1 ±0.59	9.0 ±0.69	34.3 ±0.98
	C	17.8 ±7.89	26.5 ±1.94	19.1 ±1.80	34.6 ±2.21
	D	22.3 ±12.23	30.9 ±2.31	21.9 ±2.04	32.7 ±2.20
	E	15.8 ±1.30	23.0 ±13.56	15.9 ±0.71	60.6 ±2.31
	F	16.6 ±1.32	20.4 ±11.71	17.1 ±1.12	63.5 ±2.42
	G	8.4 ±3.22	7.7 ±2.85	9.4 ±1.10	18.3 ±5.44
	H	7.8 ±3.74	9.4 ±3.39	9.8 ±0.80	11.2 ±5.71
NSS K (mmol m ⁻² d ⁻¹)	A	0.0 ±0.03	0.3 ±0.02	0.6 ±0.01	0.0 ±0.01
	B	0.1 ±0.07	0.3 ±0.01	0.7 ±0.02	0.0 ±0.00
	C	0.2 ±0.12	0.3 ±0.02	1.2 ±0.02	0.0 ±0.00
	D	0.3 ±0.17	0.3 ±0.02	1.3 ±0.02	0.0 ±0.00
	E	1.0 ±0.23	0.4 ±0.24	0.5 ±0.03	0.4 ±0.10
	F	1.0 ±0.25	0.4 ±0.23	0.5 ±0.00	0.4 ±0.09
	G	0.4 ±0.15	0.3 ±0.12	0.3 ±0.01	0.3 ±0.19
	H	0.3 ±0.15	0.3 ±0.13	0.4 ±0.02	0.3 ±0.19
NSS Ca (mmol m ⁻² d ⁻¹)	A	2.9 ±0.38	1.6 ±0.21	2.2 ±0.23	0.6 ±0.06
	B	5.1 ±0.93	2.2 ±0.24	3.0 ±0.33	1.0 ±0.23
	C	7.4 ±1.54	5.2 ±0.46	6.6 ±0.68	1.9 ±0.14
	D	10.4 ±2.33	6.2 ±0.53	7.6 ±0.78	2.4 ±0.22
	E	7.9 ±0.56	10.1 ±5.91	7.6 ±0.57	10.2 ±0.48
	F	8.3 ±0.59	8.6 ±4.95	8.3 ±0.72	10.7 ±0.52
	G	2.1 ±0.51	1.1 ±0.41	1.1 ±0.04	2.8 ±0.69
	H	1.1 ±0.50	1.0 ±0.37	1.1 ±0.01	1.6 ±0.72

Continued on next page

Table C.6 – weighted dry flux – continued from previous page

Species	Source	MAM		JJA		SON		DJF	
NSS SO ₄ ²⁻ (mmol m ⁻² d ⁻¹)	A	1.3	±0.12	2.4	±0.30	2.9	±0.13	0.2	±0.03
	B	1.7	±0.28	2.7	±0.29	3.8	±0.20	0.4	±0.07
	C	2.1	±0.38	4.1	±0.30	7.5	±0.66	0.5	±0.01
	D	2.7	±0.59	4.5	±0.30	8.5	±0.76	0.7	±0.02
	E	2.4	±0.24	4.8	±2.97	2.3	±0.11	4.6	±0.30
	F	2.4	±0.23	4.0	±2.45	2.5	±0.17	4.8	±0.29
	G	1.7	±0.84	1.0	±0.44	1.0	±0.10	2.1	±0.92
	H	1.6	±0.92	1.1	±0.45	1.0	±0.07	1.6	±0.97
Sol. Fe (µmol m ⁻² d ⁻¹)	A	14.4	±9.53	29.6	±12.64	20.5	±3.44	18.4	±3.43
	B	23.2	±19.30	34.5	±12.72	30.3	±5.16	24.7	±4.53
	C	30.9	±27.51	60.3	±12.11	70.9	±10.75	32.1	±4.84
	D	42.5	±40.43	68.6	±11.99	82.2	±12.46	38.4	±5.91
	E	28.3	±14.45	19.6	±19.57	45.5	±7.82	174.6	±52.46
	F	29.5	±14.80	16.8	±16.82	50.1	±8.10	182.8	±54.85
	G	13.5	±11.25	7.1	±7.10	7.7	±2.12	39.2	±19.36
	H	10.7	±10.60	7.4	±7.39	7.7	±2.43	16.3	±13.37
Sol. Al (µmol m ⁻² d ⁻¹)	A	104.1	±77.80	226.9	±95.82	174.2	±28.19	106.8	±19.42
	B	186.6	±165.48	268.2	±96.64	260.9	±42.36	142.5	±23.68
	C	264.5	±246.17	486.3	±96.07	623.3	±94.08	190.0	±28.58
	D	376.0	±364.59	556.8	±96.23	723.2	±109.14	227.0	±34.39
	E	249.1	±125.86	169.1	±169.06	464.1	±77.30	1470.5	±441.54
	F	260.6	±130.63	145.3	±145.28	513.0	±81.57	1540.8	±462.31
	G	124.2	±104.16	65.0	±65.04	71.4	±18.63	343.1	±176.23
	H	101.4	±100.16	66.0	±65.97	70.4	±20.97	151.1	±126.66
Total Fe (µmol m ⁻² d ⁻¹)	A	932.7	±932.65	1077.1	±1077.06	1141.1	±1141.05	3448.6	±3448.56
	B	1666.7	±1666.73	1613.9	±1613.88	1713.6	±1713.64	5391.4	±5391.41
	C	2433.7	±2433.66	4385.4	±4385.39	4164.5	±4164.49	7807.0	±7807.04
	D	3456.6	±3456.59	5286.1	±5286.10	4834.6	±4834.58	9767.7	±9767.66
	E	1763.1	±1763.12	8509.3	±8509.35	4560.2	±4560.20	15400.4	±15400.43
	F	1858.6	±1858.61	6913.2	±6913.24	5060.8	±5060.78	16146.4	±16146.42
	G	639.6	±639.62	385.2	±385.15	305.6	±305.58	3077.9	±3077.87
	H	422.8	±422.79	295.3	±295.27	332.6	±332.61	1012.8	±1012.79
Total Al (µmol m ⁻² d ⁻¹)	A	2843.3	±2843.30	3819.3	±3819.28	3906.8	±3906.77	12395.8	±12395.83
	B	5586.2	±5586.16	5856.7	±5856.65	5911.7	±5911.72	19504.7	±19504.70
	C	8399.8	±8399.84	16378.8	±16378.76	14470.6	±14470.60	28308.8	±28308.85
	D	12201.5	±12201.46	19798.1	±19798.11	16812.9	±16812.93	35471.5	±35471.53
	E	5534.8	±5534.85	30583.9	±30583.91	18115.0	±18115.01	49441.2	±49441.20
	F	5834.6	±5834.62	24810.9	±24810.92	20125.0	±20124.96	51831.7	±51831.69
	G	2155.9	±2155.91	1361.8	±1361.79	1031.8	±1031.83	10096.6	±10096.62
	H	1503.7	±1503.74	1064.3	±1064.35	1084.4	±1084.36	3482.8	±3482.75

Species	ABCD		EFGH	
	Conc	% u	Conc	% u
NH_4^+ ($\mu\text{ mol dm}^{-3}$)	0.96	50	5.40	15
NO_3^- ($\mu\text{ mol dm}^{-3}$)	9.95	50	4.91	15
NSS K ($\mu\text{ mol dm}^{-3}$)	0.54	50	0.98	15
NSS Ca ($\mu\text{ mol dm}^{-3}$)	4.93	50	2.61	15
NSS SO_4 ($\mu\text{ mol dm}^{-3}$)	16.37	50	5.41	15
Dissolved Fe (nmol dm^{-3})	7.14	100	11.60	30
Dissolved Al (nmol dm^{-3})	16.25	100	29.91	100
Total Fe (nmol dm^{-3})	297.87	100	484.12	15
Total Al (nmol dm^{-3})	677.91	100	1247.98	15

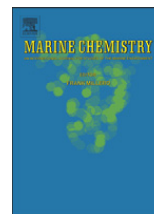
Table C.7: Volume weighted mean rainwater concentrations (conc), with % uncertainties (%u), for northern (ABCD) and southern (EFGH) climatology regions

Species	Flux	% u						
	ETNAA		ETNAB		ETNAC		ETNAD	
NH_4^+ ($\mu\text{ mol m}^{-2}\text{ d}^{-1}$)	1.61	50	0.89	50	0.9	50	0.5	50
NO_3^- ($\mu\text{ mol m}^{-2}\text{ d}^{-1}$)	16.78	50	9.21	50	9.39	50	5.16	50
NSS K ($\mu\text{ mol m}^{-2}\text{ d}^{-1}$)	0.91	50	0.5	50	0.51	50	0.28	50
NSS Ca ($\mu\text{ mol m}^{-2}\text{ d}^{-1}$)	8.31	50	4.56	50	4.65	50	2.56	50
NSS SO_4 ($\mu\text{ mol m}^{-2}\text{ d}^{-1}$)	27.6	50	15.15	50	15.46	50	8.49	50
Dissolved Fe ($\text{nmol m}^{-2}\text{ d}^{-1}$)	12.04	100	6.61	100	6.74	100	3.7	100
Dissolved Al ($\text{nmol m}^{-2}\text{ d}^{-1}$)	27.4	100	15.04	100	15.34	100	8.43	100
Total Fe ($\text{nmol m}^{-2}\text{ d}^{-1}$)	502.38	100	275.74	100	281.28	100	154.56	100
Total Al ($\text{nmol m}^{-2}\text{ d}^{-1}$)	1143.34	100	627.54	100	640.14	100	351.75	100
	ETNAE		ETNAF		ETNAG		ETNAH	
NH_4^+ ($\mu\text{ mol m}^{-2}\text{ d}^{-1}$)	20.44	15	19.6	15	28.87	15	21.81	15
NO_3^- ($\mu\text{ mol m}^{-2}\text{ d}^{-1}$)	18.56	15	17.8	15	26.21	15	19.81	15
NSS K ($\mu\text{ mol m}^{-2}\text{ d}^{-1}$)	3.7	15	3.55	15	5.23	15	3.95	15
NSS Ca ($\mu\text{ mol m}^{-2}\text{ d}^{-1}$)	9.89	15	9.48	15	13.96	15	10.55	15
NSS SO_4 ($\mu\text{ mol m}^{-2}\text{ d}^{-1}$)	20.46	15	19.62	15	28.89	15	21.83	15
Dissolved Fe ($\text{nmol m}^{-2}\text{ d}^{-1}$)	43.9	30	42.11	30	62	30	46.85	30
Dissolved Al ($\text{nmol m}^{-2}\text{ d}^{-1}$)	113.17	100	108.55	100	159.83	100	120.76	100
Total Fe ($\text{nmol m}^{-2}\text{ d}^{-1}$)	1831.9	15	1757.04	15	2587.24	15	1954.8	15
Total Al ($\text{nmol m}^{-2}\text{ d}^{-1}$)	4722.29	15	4529.32	15	6669.41	15	5039.11	15

Table C.8: The calculated rain flux for each climatology region and % uncertainty (%u), based on the volume weighted mean and the average annual rainfall to each climatology region

Appendix D

Papers published using data from this thesis



Changes in iron speciation following a Saharan dust event in the tropical North Atlantic Ocean

Micha J.A. Rijkenberg^a, Claire F. Powell^b, Manuel Dall'Osto^c, Maria C. Nielsdottir^a, Matthew D. Patey^a, Polly G. Hill^a, Alex R. Baker^b, Tim D. Jickells^b, Roy M. Harrison^c, Eric P. Achterberg^{a,*}

^a University of Southampton, National Oceanography Centre Southampton, School of Ocean and Earth Science, Southampton SO14 3ZH, UK

^b Laboratory for Global Marine and Atmospheric Chemistry, University of East Anglia, School of Environmental Sciences, Norwich NR4 7TJ, UK

^c University of Birmingham, Division of Environmental Health and Risk Management, Birmingham B15 2TT, UK

ARTICLE INFO

Article history:

Received 8 August 2007

Received in revised form 14 February 2008

Available online 25 February 2008

Keywords:

Atmospheric input

Aerosols

Saharan dust

Dry deposition

Dissolved iron

Organic iron complexation

Equatorial Atlantic Ocean

ABSTRACT

Concentrations of dissolved iron (DFe) and Fe-binding ligands were determined in the tropical Northeast Atlantic Ocean (12–30°N, 21–29°W) as part of the UK-SOLAS (Surface Ocean Lower Atmosphere Study) cruise Poseidon 332 (P332) in January–February 2006. The surface water DFe concentrations varied between 0.1 and 0.4 nM with an average of 0.22 ± 0.05 nM ($n=159$). The surface water concentrations of total Fe-binding ligands varied between 0.82 and 1.46 nM with an average of 1.11 ± 0.14 nM ($n=33$). The concentration of uncomplexed Fe-binding ligands varied between 0.64 and 1.35 nM with an average of 0.90 ± 0.14 nM ($n=33$). Thus, on average 81% of the total Fe-binding ligand concentration was uncomplexed. The average logarithmic conditional stability constant of the pool of Fe-binding ligands was 22.85 ± 0.38 with respect to Fe^{3+} ($n=33$). A transect (12°N, 26°W to 16°N, 25.3°W) was sailed during a small Saharan dust event and repeated a week later. Following the dust event, the concentration of DFe increased from 0.20 ± 0.026 nM ($n=125$) to 0.25 ± 0.028 nM ($n=17$) and the concentration of free Fe-binding ligands decreased from 1.15 ± 0.15 nM ($n=4$) to 0.89 ± 0.10 nM ($n=4$). Furthermore, the logarithmic stability constants of the Fe-binding ligands south of the Cape Verde islands were distinctively lower than north of the islands. The absence of a change in the logarithmic stability constant after the dust event south of the Cape Verde islands suggests that there was no significant atmospheric input of new Fe-binding ligands during this dust event.

© 2008 Elsevier B.V. All rights reserved.

1. Introduction

Iron (Fe) is a key element in biological processes including photosynthesis (Cherestkin and Castelfranco, 1982; Geider et al., 1993), nitrate uptake (Timmermans et al., 2004; van Leeuwe et al., 1997), N_2 fixation (Berman-Frank et al., 2001), and detoxification of reactive oxygen species (Sunda and Huntsman, 1995). The low Fe inputs and its low solubility in oxygenated waters limits primary production in open ocean environments including the “High Nutrient Low Chlorophyll” regions (de Baar et al., 1990; Martin and Fitzwater, 1988), the North Atlantic (Blain et al., 2004; Moore et al., 2006) and

coastal areas (Bruland et al., 2001; Hutchins and Bruland, 1998). Low Fe concentrations also influence diazotrophs, which have high iron demands, in tropical and subtropical ocean regions (Falkowski, 1997; Karl et al., 1997; Michaels et al., 1996; Mills et al., 2004).

It has become evident that atmospheric transport of dust and its deposition into the ocean forms an important supply route of Fe to the euphotic zone of open ocean regions (Baker et al., 2003; Bonnet et al., 2005; Martin and Fitzwater, 1988; Sarthou et al., 2003). The North Atlantic Ocean receives about a third of the global oceanic dust inputs, which are estimated to range between 400 and 1000×10^{12} g y^{-1} (Jickells and Spokes, 2001). Most dust inputs into the North Atlantic originate from the Saharan desert and Sahel region (Duce and Tindale, 1991; Stuut et al., 2005). Deposition of dust occurs via

* Corresponding author.

E-mail address: eric@noc.soton.ac.uk (E.P. Achterberg).

dry and wet deposition, and is strongly seasonal and episodic in nature (Gao et al., 2001; Prospero and Carlson, 1972). The latitude of highest dust transport from the Saharan region to the North Atlantic Ocean changes between winter and summer, and is determined by the seasonal migration of the Inter Tropical Convergence Zone (ITCZ) (Prospero et al., 1981). At the Cape Verde islands in the tropical North East Atlantic, the maximum dust deposition occurs in winter and is the result of dust transport in the lower air masses of the trade winds (Chiapello et al., 1995). In summer, Saharan dust reaches the American continent (Prospero and Carlson, 1972; Prospero et al., 1981), as it is transported at higher altitude within the Saharan Air Layer (1.5–6 km).

The processes in the ocean surface that influence the dissolution of the atmospheric dust associated Fe play a key role in ocean productivity. Upon entering the ocean, the physico-chemical environment of atmospheric Fe changes drastically. The inorganic speciation of Fe(III) in seawater is dominated by its hydrolysis behaviour (Waite, 2001), so that Fe tends to form particulate Fe oxyhydroxides (Moffett, 2001). However, more than 99% of the DFe in the ocean is reported to be organically complexed (Gledhill and van den Berg, 1994; van den Berg, 1995). The organic complexation of Fe enhances its solubility in seawater (Boyé et al., 2005; Gerringa et al., 2007; Johnson et al., 1997; Kuma et al., 1996) and plays an important role in the dissolution of Fe from Fe minerals (Borer et al., 2005; Kraemer, 2004; Kraemer et al., 2005). The identity, origin, and chemical characteristics of these Fe-binding ligands are largely unknown. Nevertheless, evidence exists that siderophores, small high affinity organic Fe(III) binding molecules excreted by prokaryotes to chelate and take up Fe (Gledhill et al., 2004; Macrellis et al., 2001), and organic molecules resulting from the lysis of cells (Gerringa et al., 2006; Witter et al., 2000a) may form part of the organic Fe-binding capacity. Additionally, part of the Fe-binding capacity in the dissolved phase may be provided by a mixed organic–inorganic fraction (Boyé et al., 2005). In many ocean regions, the observed Fe-binding capacity in the dissolved phase is in excess of the DFe concentration (Boyé et al., 2001) and conditional stability constants have been reported to range between 10^{18} and 10^{23} (Nolting et al., 1998; Rijkenberg et al., 2006; Rue and Bruland, 1995; Wu and Luther, 1995).

To elucidate the role of aeolian dust inputs on the Fe supply to the ocean, it is important to unravel mechanisms which play a role in the dissolution and solubilisation of dust-derived Fe. In this study we investigated the influence of a Saharan dust event on the concentrations of DFe, the free Fe-binding capacity and the conditional stability constants of the Fe-binding ligands in the tropical Northeast Atlantic Ocean.

2. Materials and methods

2.1. Sampling

During a cruise in the vicinity of the Cape Verde islands (26 January to 26 February 2006) on board the research vessel *FS Poseidon*, surface seawater was pumped into a trace metal clean laboratory container using a Teflon diaphragm pump (Almatec A-15, Germany) connected by an acid-washed braided PVC tubing to a towed fish positioned at approximately 3 m depth alongside the ship. The seawater was filtered

in-line using a Sartobran 300 filter capsule (Sartorius) with a 0.2 μm cut-off. All low density polyethylene bottles (Nalgene) were cleaned according to a standard protocol (Achterberg et al., 2001). Samples for DFe were acidified to pH 2 (a final concentration of 0.011 M) using ultra clean HCl (Romil UHP grade). Samples for Fe-binding ligand analysis were immediately frozen at $-20\text{ }^\circ\text{C}$ for subsequent land-based analysis.

Underway temperature and salinity were determined using a thermosalinograph (Meerestechnik Elektronik, Germany).

2.2. Dissolved aluminium and iron

Dissolved aluminium (DAL) ($<0.2\text{ }\mu\text{m}$) was determined using the fluorimetric lumogallion method (Hydes and Liss, 1976) with a spectrofluorometer (model Aminco, American Instruments Co.). The detection limit, $3\times$ the standard deviation of the lowest standard addition, was 3 nM DAL.

DFe was determined using an automated flow injection method employing a luminol-based chemiluminescence detection for total reduced dissolved Fe following preconcentration on a column of 8-hydroxyquinoline (8-HQ) immobilized on Toyopearl gel (Bowie et al., 1998; Landing et al., 1986). All solutions were prepared using $18.2\text{ M}\Omega\text{ cm}^{-1}$ de-ionised water (MQ-water, Millipore). A 0.02 M Fe(II) stock solution was prepared by dissolving 1.9607 g of ferrous ammonium sulphate hexahydrate ($\text{Fe}^{\text{II}}(\text{NH}_4)_2(\text{SO}_4)_2\cdot 6\text{H}_2\text{O}$) in 250 ml of 0.1 M HCl (Romil SpA) and 1 μM cleaned sodium sulfite (Sigma–Aldrich) was added to this stock to prevent oxidation of the Fe(II). This stock solution was used during the cruise (made up monthly). Other standards were prepared daily in 0.01 M HCl (Romil SpA) by serial dilution.

A 0.01 M luminol (5-amino-2,3-dihydro-1,4-phthalazine-dione, Sigma–Aldrich, used as received) stock solution was prepared in 0.1 M Na_2CO_3 (Sigma–Ultra, minimum 90%, Sigma–Aldrich). A 10 μM luminol reagent working solution was prepared in 0.1 M Na_2CO_3 (Sigma–Ultra, minimum 90%, Sigma–Aldrich), 0.01 M NaOH (99.99% semiconductor grade, Sigma–Aldrich) and 10 μM dimethyl glyoxime (Sigma–Aldrich). To remove Fe impurities this reagent was passed over a Chelex-100 chelating resin (Sigma–Aldrich) column. The FIA manifold eluent consisted of 0.06 M HCl (Romil SpA). A 2 M ammonium acetate stock solution was prepared using acetic acid of SpA grade (Romil) and ammonia of UHP grade (Romil). The pH of the 0.4 M ammonium-acetate buffer was 5.5. The buffer was cleaned in-line using an 8-HQ column. A 0.04 M stock solution of sodium sulfite (Sigma–Ultra $\geq 98\%$, Sigma–Aldrich) was made up in 0.4 M ammonium acetate buffer (final pH 5.4). The sodium sulfite solution was cleaned by passing through three sequential 8-HQ columns. After addition of the sulfite solution (final concentration 100 μM), the acidified seawater samples were allowed to stand for 3 days to reduce all Fe(III) to Fe(II).

The analytical blank was on average 0.015 ± 0.003 nM DFe ($n=8$). The detection limit, $3\times$ the standard deviation of the lowest standard addition, was on average 0.05 ± 0.03 nM Fe. An average concentration of 0.56 ± 0.05 nM DFe ($n=8$) was obtained for an Fe reference material from the Ironages inter-comparison exercise (bottle 93), while the reported inter-comparison value was 0.59 ± 0.21 nM DFe (Bowie et al., 2006). A recent inter-comparison study on the Ironages samples showed an excellent agreement in the concentration of DFe (0.54 ± 0.03 nM) as determined by two different methods, co-

precipitation followed by isotope dilution inductively coupled plasma mass spectrometry and chemical reduction to Fe(II) followed by flow injection analysis (Bowie et al., 2007).

All uncertainties are given as standard deviation unless noted otherwise.

2.3. Dissolved Fe-binding ligands

Determination of the Fe-binding capacity in seawater was performed using competitive ligand exchange-adsorptive cathodic stripping voltammetry (CLE-ACSV). 2-(2-Thiazolylazo)-*p*-cresol (TAC) reagent (Aldrich, used as received) was used as competing ligand (Croot and Johansson, 2000). All solutions were prepared using MQ water. The equipment consisted of a μ Autolab potentiostat (Ecochemie, Netherlands), a static mercury drop electrode (Metrohm Model VA663), a double-junction Ag/saturated AgCl reference electrode with a salt bridge containing 3 M KCl, and a counter electrode of glassy carbon. The titrations were performed using a 0.01 M stock solution of TAC in triple quartz distilled (QD) methanol and a 1 M boric acid (Suprapur, Merck) solution in 0.3 M ammonia (Suprapur, Merck) (further cleaned by the addition of TAC with subsequent removal of TAC and Fe(TAC)₂ using a C18 SepPak column (Whatman)) to buffer the samples to a pH of 8.05. A 10⁻⁶ M Fe(III) stock solution, acidified with 0.012 M HCl (Romil UHP), was used for Fe additions. Seawater aliquots of 15 ml were spiked with Fe(III) to concentrations between 0 and 8 nM and allowed to equilibrate overnight (>15 h) with 5 mM borate buffer and 10 μ M TAC (all final concentrations). The concentration of Fe(TAC)₂ in the samples was determined using the following procedure: i) removal of oxygen from the samples for 200 s with nitrogen gas, after which a fresh Hg drop was formed, ii) a deposition potential of -0.40 V was applied for 30–60 s according to the Fe concentration in the sample, the solution was stirred to facilitate the adsorption of the Fe(TAC)₂ to the Hg drop, iii) at the end of the adsorption period, the stirrer was stopped and the potential was scanned from -0.40 to -0.90 V using the differential pulse method at 19.5 mV s⁻¹ and the stripping current from the reduction of the adsorbed Fe(TAC)₂ was recorded.

Determination of natural ligand binding characteristics with Fe has been described in detail by Gledhill and van den Berg (1994) and Croot and Johansson (2000). A sufficiently high concentration of a known organic ligand, in this case TAC, is added to a sample, and competes with the natural Fe-binding ligands for reversibly bound Fe. The equilibrium expression is (1):

$$K'_{\text{TAC}} * [\text{TAC}]^2 / K'_{\text{ligands}} * [\text{L}] = [\text{Fe}(\text{TAC})_2] / [\text{FeL}] \quad (1)$$

where K' is the conditional stability constant of Fe with a ligand, and [L] and [TAC] are the concentrations of free Fe-binding ligands. The [Fe(TAC)₂] and [FeL] represent the concentrations of Fe complexes with TAC and L.

The concentration of Fe(TAC)₂ is determined by CSV. Since the added concentration of TAC and its binding strength with Fe are known, it is possible to determine L and K' of the natural Fe-binding ligands from the curved response (van den Berg, 1982) using non-linear regression of the Langmuir isotherm (Gerringa et al., 1995). There was no evidence for the presence of two classes of ligands (Rue and Bruland, 1995), so

all data presented in the present work have been calculated assuming that only one class of Fe-binding ligand was present. Although we assumed the presence of one class of ligands, it is clear that there is a whole spectrum of molecules able to bind Fe. Witter et al. (2000a) showed for example that it was not possible to distinguish between different model Fe-binding molecules using CSV because the resulting conditional stability constants were very similar.

The validity of the reported conditional stability constants of natural Fe-binding ligands is currently under debate (Hunter, 2005; Town and van Leeuwen, 2005; van den Berg, 2005). Metal complexation proceeds according to the Eigen mechanism and depends on the rate constant for water substitution, k_{-w} , and the stability constant for the intermediate outer-sphere complex, K_{os} (Town and van Leeuwen, 2005). Using an average value for k_{-w} of 10³ s⁻¹ Town and van Leeuwen (2005) showed that the conditional stability constant is overestimated due to non-equilibrium conditions after overnight equilibration. In reply, van den Berg (2006) reported a reaction time of 50 min for natural FeL indicating that overnight equilibration would be sufficient. In support of van den Berg (2006), Nagai et al. (2007) argued that the seawater system may be more complex than considered by Town and van Leeuwen (2005). Seawater contains a complex mixture of organic material including organic ligands but also inorganic ligands and other trace metals. Various ligand and metal exchange reactions, and the catalytic influence of other trace metals and amino acids result in kinetics that allow overnight equilibration (Nagai et al., 2007). Furthermore, Gerringa et al. (2007) showed that the formation and dissociation kinetics of Fe-binding ligands in the Scheldt estuary allowed overnight equilibration. Also Hudson et al. (1992) reported formation rate constants for Fe'-siderophore complexation that were higher than the average value for k_{-w} of 10³ s⁻¹. Based on the arguments brought forward by Nagai et al. (2007) and the results of van den Berg (2006), Gerringa et al. (2007) and Hudson et al. (1992) we assume that overnight equilibration was sufficient to equilibrate our titration experiments.

All uncertainties are reported as standard deviation unless noted otherwise.

2.4. Aerosol sampling and analysis

Aerosols were collected on the *FS Poseidon* using a high-volume aerosol sampler equipped with a cascade impactor for separation of particles into coarse (>1 μ m diameter) and fine (<1 μ m diameter) fractions. The soluble Fe and Al fraction of these samples was determined in a land based laboratory by an ammonium-acetate leach (pH 4.7, 1–2 h). The sampling and analysis methods employed have been described in detail previously (Baker et al., 2006; Sarthou et al., 2003). A soluble Fe and Al flux was calculated using deposition velocities of 0.001 m s⁻¹ for the fine aerosol mode and 0.02 m s⁻¹ for the coarse aerosol mode (Baker et al., 2003; Duce et al., 1991). Deposition velocities are poorly constrained and uncertainties can be as much as a factor 2–3 (Duce et al., 1991).

Direct on-board elemental dust analysis was performed using aerosol time-of-flight mass spectrometry (ATOFMS, TSI, model 3800) as described in Dall'Osto et al. (2006). ATOFMS provides real time information on individual aerosols. The

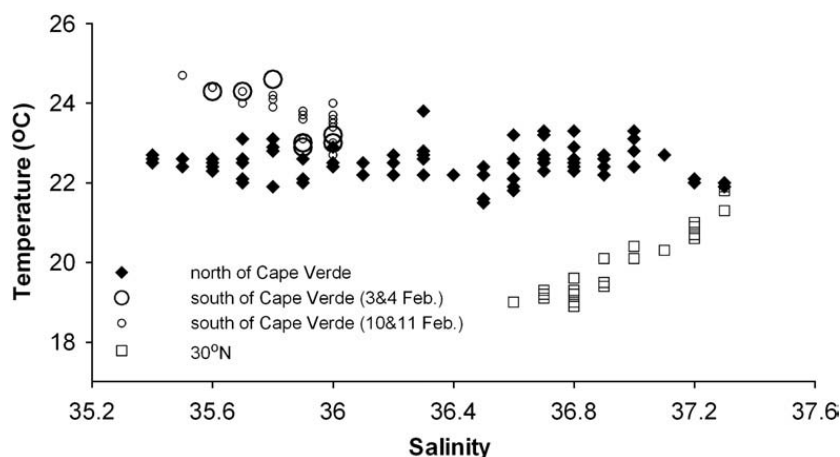


Fig. 1. Temperature–salinity diagram for surface waters between 12°N and 30°N in the region of the Cape Verde islands.

measurement of the aerodynamic diameter ($\pm 1\%$) within a range of 0.3 to 3 μm is based on the time-of-flight between two points. The positive and negative mass spectral data of individual particles are acquired after particle ionisation using laser desorption/ionization (LDI) (Gard et al., 1997).

Air mass back trajectories were calculated by the HYSPLIT transport and dispersion model (NOAA Air Resources Laboratory).

3. Results and discussion

3.1. Study area

The Canary Current flows southward along the African coast between 30°N (north of Canary islands) and 10°N (south of Cape Verde islands) (Fedoseev, 1970) at 10–30 cm s^{-1} , and is about 1000 km wide and ~500 m deep (Batteen et al., 2000; Wooster et al., 1976; Zhou et al., 2000). The Canary Current

system contains coastal upwelling, filaments and eddies (Johnson and Stevens, 2000). In the region of 15°N, the current deviates westward under the influence of the Equatorial Countercurrent (Peterson et al., 1996). During the P332 cruise we sampled three different surface water masses, as distinguished from a temperature–salinity plot (T–S plot) (Fig. 1). One water mass was situated in the latitudinal region of 30°N, the second water mass north of the Cape Verde islands up to ca. 30°N and the third water mass south of the Cape Verde islands.

Samples were taken along 465 km transect sailed south of the Cape Verde islands between 12°N, 26°W and 16.1°N, 25.3°W during a Saharan dust event on 3–4 February. We revisited this transect a week later on 10–11 February and sampled the same surface ocean water mass with similar T–S characteristics (Fig. 1). Distinctive Chl *a* features observed on MODIS chlorophyll ocean colour satellite images were near stationary during the period 3–10 February, confirming that the same surface water mass was sampled during both

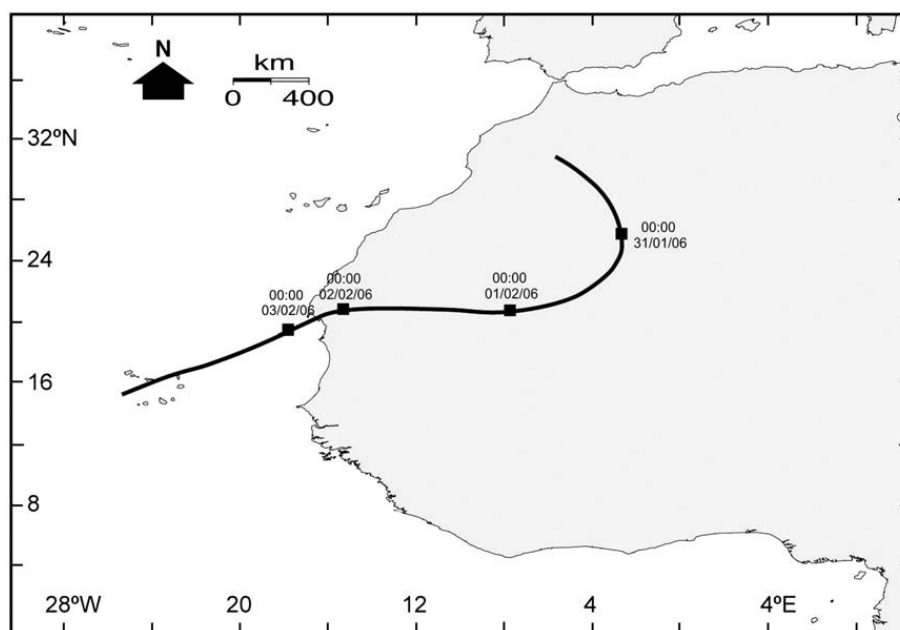


Fig. 2. Example of a 5-day air mass back trajectory for an air mass arriving at mid-day at 500 m above the position of the ship during the dust event on 4 Feb 2006 (NOAA Hysplit Model).

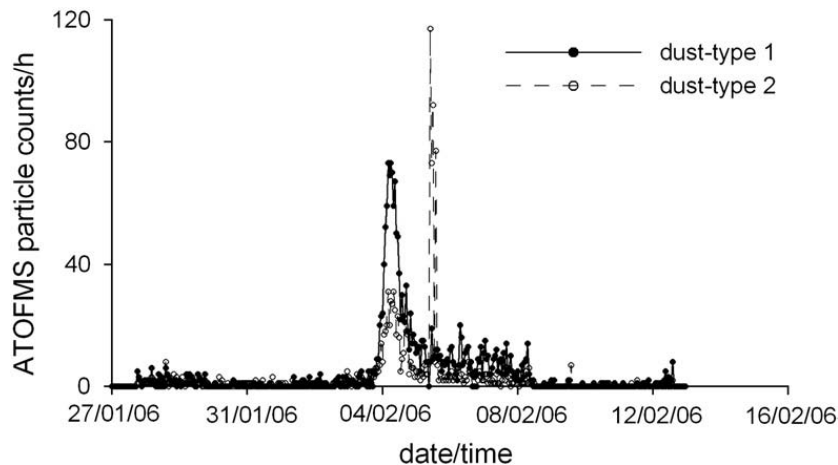


Fig. 3. Aerosol time-of-flight mass spectrometry (ATOFMS) results indicating two dust types. Dust-type 1, a coarse Saharan dust-type ($>1 \mu\text{m}$) rich in Na, Al, K, Ca, Fe, Cl, and nitrate, and dust-type 2, a finer dust type ($<1 \mu\text{m}$) rich in K and silicate sampled close to the Cape Verde islands.

transects (water mass had travelled $< 3\text{km}$ between 3–10 February according to current estimates). Furthermore, sea surface temperature satellite images (AVHRR, $11 \mu\text{m}$) did not show any changes in the patterns and absolute values of sea surface temperature along the repeat transect over the period 3–11 February 2006. The constant sea surface temperature distribution observed during this period makes it unlikely that important upwelling/mixing events occurred along the 465 km transect. In addition, the uniform concentrations of DFe observed during the individual first and second transects ($0.20 \pm 0.03 \text{ nM}$ and $0.25 \pm 0.03 \text{ nM}$ DFe respectively, see below) indicated that the DFe was not influenced by upwelling and/or mixing events.

3.2. Dust

The MODIS and SEAWIFS aerosol optical depth satellite data showed low dust transport over our research area during the winter season of 2005/2006. This low dust transport was associated with a negative North Atlantic Oscillation (NAO) index of -1.09 (as defined by Hurrell) (Hurrell, 1995). A negative NAO index predicts that precipitation is likely to be enhanced over the Mediterranean region and large areas of North Africa, thus limiting the intensity of both dust uplift and transport (Moulin et al., 1997).

Dissolved Al is used as a tracer for dust input into surface waters and has an estimated residence time of 3–4 years in

Table 1

The estimated increase in soluble Fe concentrations as a result of dust inputs into the ocean south of the Cape Verde islands for the period 03/02/06 (9:10 h) to 11/02/06 (09:00 h)

Start date	Start time (UTC)	Start decimal lat	Start decimal long	End decimal lat	End decimal long	F_{Fe}^{a} ($\text{nmol m}^{-2} \text{d}^{-1}$)	Sample period ^b (h)	D_{Fe} (nmol m^{-2})	Mixing layer depth ^c (m)	Mixing layer depth ^c (m)
03/02/06	09:23	12.00	-26.00	13.08	-25.80	764 ± 10	12.67	403 ± 5	65	65
03/02/06	22:00	13.13	-25.80	14.68	-25.52	465 ± 10	11.48	223 ± 5	65	65
04/02/06	09:39	14.78	-25.33	15.66	-25.33	243 ± 8	11.41	115 ± 4	65	65
04/02/06	20:30	15.68	-25.3	16.90	-25.04	194 ± 7	16.58	134 ± 5	65	65
05/02/06	17:42	16.98	-24.65	17.36	-22.38	97 ± 7	20.28	82 ± 6	65	20
06/02/06	09:23	17.36	-22.39	16.48	-21.51	58 ± 5	23.89	58 ± 5	65	20
07/02/06	09:20	16.48	-21.51	16.77	-22.57	77 ± 22	26.17	84 ± 24	65	20
08/02/06	11:40	16.81	-22.63	17.05	-24.10	$^{\text{d}} < 10$	24.2	–	65	20
09/02/06	11:12	17.05	-24.10	14.83	-25.51	36 ± 4	23.89	36 ± 4	45	45
10/02/06	11:29	14.67	-25.53	16.99	-24.79	54 ± 2	46.5	104 ± 5	18	18
Total increase in soluble Fe concentration ^e (nmol L^{-1})									0.024 ± 0.001	0.031 ± 0.002

Note that we used our aerosol data for the period 3–11 February, although between 4 February and 10 February the ship was north of the Cape Verde islands. Shown are the time and location for the start and finish of each sampling period. F_{Fe} is the dry deposition flux of soluble Fe calculated from measured atmospheric concentrations, D_{Fe} is the deposition amount per unit area of soluble Fe during each sample period. The calculation of the increase in soluble Fe assumes no loss term for the atmospheric input of soluble Fe.

^a The reported soluble Fe flux is the combined soluble Fe from the fine dust as well as the coarse dust fraction.

^b The time used to change the filter is included in the sample period. Half of the time necessary to exchange a filter is included with the previous sample period and half is included with the next sample period.

^c The mixed layer depths for 3–4 and 10–11 February are known. We used a 20 and a 65 m mixed layer depth in our calculations for the period 4–10 February. Mixed layer depths shown in italics were assumed for periods when the ship was north of the Cape Verde islands.

^d Soluble Fe concentration for this sample was below the limit of detection. It has been excluded from the soluble Fe increase calculation. Note that its maximum potential contribution to this calculation is $< 0.5 \text{ pmol L}^{-1}$.

^e The soluble Fe concentration (nmol L^{-1}) during each sample period was calculated (soluble Fe flux during sample period/(mixed layer depth \times 1000)) and summed to get the total increase in the soluble Fe concentration in nmol L^{-1} for the period 3–11 February.

surface waters as reported for the oligotrophic waters of the central north Pacific gyre (Measures et al., 1984; Orrians and Bruland, 1986). Low concentrations of DAI, ranging between 8 and 25 nM, were observed during our cruise with an average of 14.7 ± 4.3 nM ($n=147$), which confirmed the low dust input in the winter of 2005/2006. Measures (1995) also observed low DAI concentrations in our study region: 7.5 nM at 14°N to 16–19 nM at $26\text{--}31^\circ\text{N}$, during a period of southerly winds and limited aeolian dust inputs. In contrast, surface DAI concentrations ranging between 40 and 60 nM have been reported in the equatorial Atlantic corresponding with dust deposition events in the ITCZ in the equatorial Atlantic (Bowie et al., 2002).

During our cruise, we encountered a dust event in the period 3–8 February. Air-mass back trajectories (Fig. 2) showed that the air-mass originated from the Saharan region. Direct on-board elemental dust analysis using ATOFMS indicated the presence of both a coarse Saharan dust type ($>1 \mu\text{m}$) rich in Na, Al, K, Ca, Fe, Cl, and nitrate, and a second finer dust type ($<1 \mu\text{m}$) rich in K and silicate sampled close to the Cape Verde islands (Fig. 3). The second dust type contained very low Ca and Al concentrations suggesting a possible anthropogenic contribution, in the form of fly ash, for this particle type. Most of the dust crossed the cruise trajectory of the *FS Poseidon* in the period 3 to 4 February (Fig. 3), and this is

confirmed by aerosol optical depth MODIS satellite images. However, due to cloud cover, there is no aerosol optical depth data available for the period 4–11 February.

An expected increase in surface water DFe and DAI was calculated using a mixed layer of 65 m for the period 3–4 February, and 45 m and 18 m on 10 and 11 February, respectively (Table 1). The mixed layer depth was unknown for our transect during for the period 4–10 February, and therefore we used 65 and 20 m mixed-layer depth estimates in our calculations for this period. Furthermore, a range is given (between brackets) for DFe input based on the uncertainty of the deposition velocity of a factor 2.5 (Duce et al., 1991). Using the soluble Fe fraction of the dust collected in the period between 3 and 11 February with the high-volume aerosol collectors, we calculated an expected increase of about 0.024 ± 0.001 nM Fe (ranging between 0.009 and 0.059 nM DFe) assuming a 65 m mixed layer, and an increase of about 0.031 ± 0.002 nM Fe (ranging between 0.013 and 0.079 nM DFe) for a 20 m mixed layer depth for the period 4–10 February. The expected increase in the concentration of Al for the period 4–10 February was 0.17 ± 0.002 nM (ranging between 0.07 and 0.43 nM DAI) assuming a 65 m mixed layer, and 0.21 ± 0.004 nM (ranging between 0.08 and 0.53 nM DAI) assuming a 20 m mixed layer depth (data not shown). This expected increase in the concentration of Al was too low for

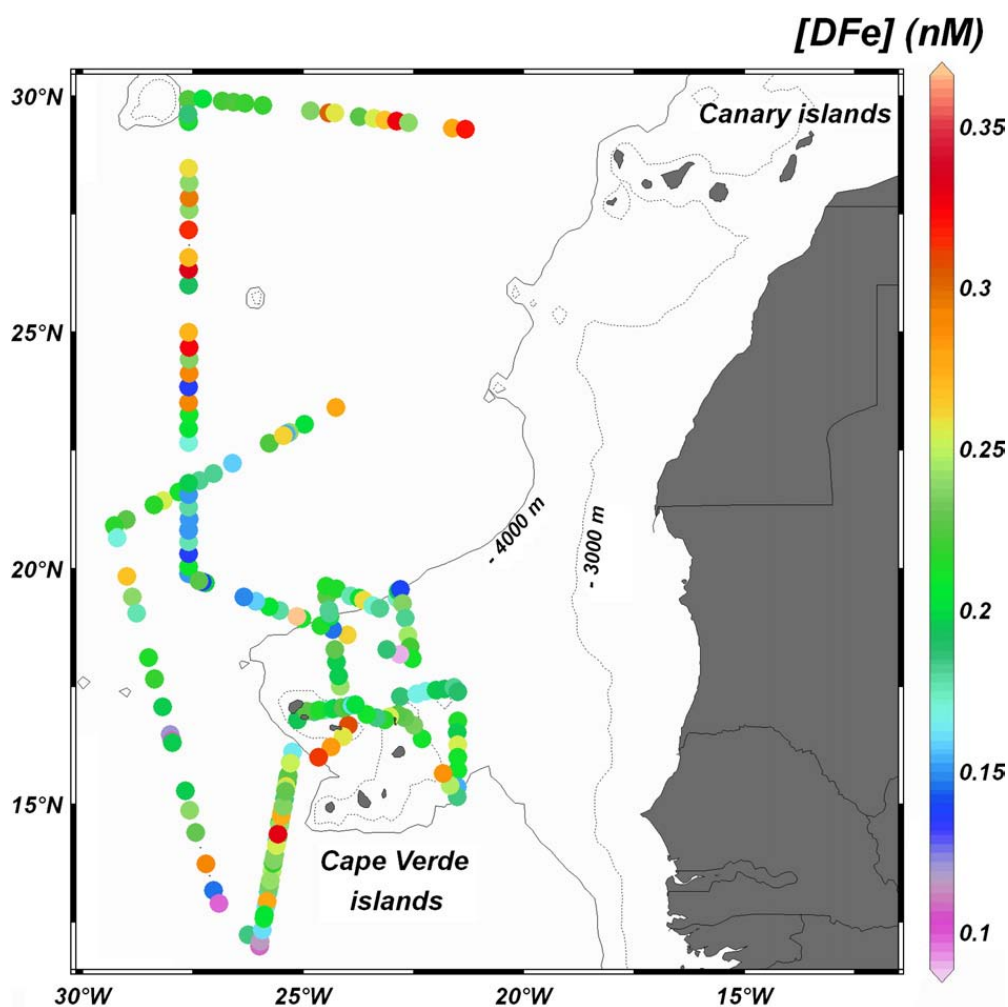


Fig. 4. Contour map showing near surface water DFe concentrations for the period 26 January–26 February 2006.

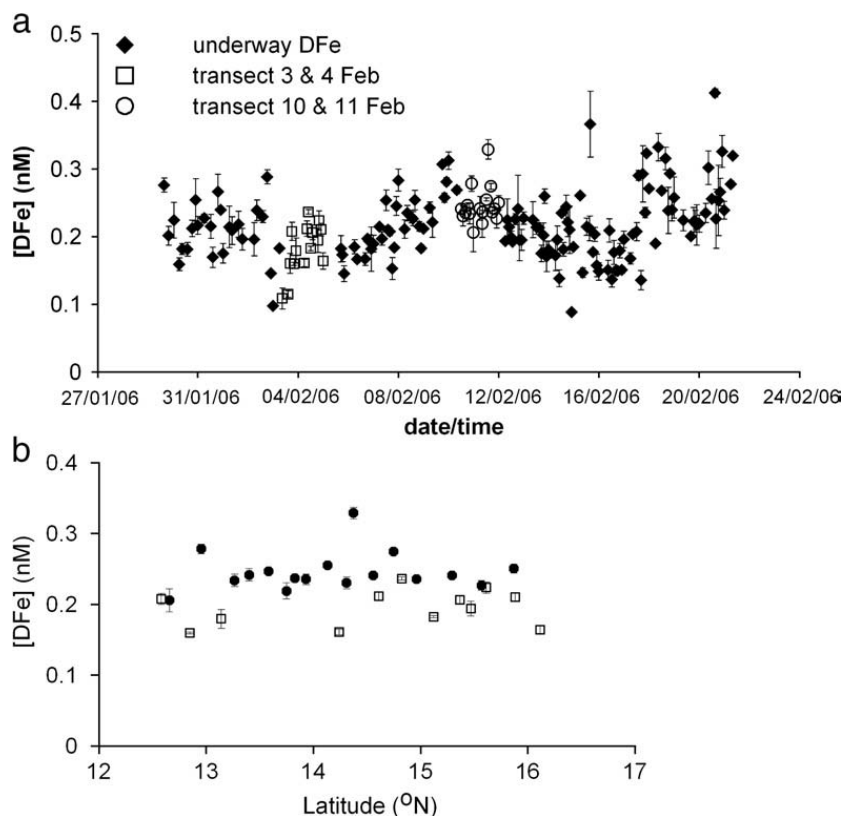


Fig. 5. a) The concentration of surface DFe (nM) versus date/time. The surface DFe concentrations of samples taken during the Saharan dust event at 3–4 Feb 2006 on a transect south of the Cape Verde islands are shown as open squares and the surface DFe concentrations of samples taken at the same transect a week later, 10–11 Feb, are shown as open circles. All other surface DFe concentrations are shown as filled diamonds. b) A close up of the DFe concentrations along a 465 km transect south of the Cape Verde islands between 12°N, 26°W and 16.1°N, 25.3°W during a Saharan dust event at 3–4 February (open squares) and during a repeat transect at 10–11 February (closed circles).

detection by our analytical system. The absence of a measurable change in the concentration of DAI during the repeated transect implied that this dust event was of a low magnitude.

3.3. Surface water DFe concentrations

The surface DFe concentrations varied between 0.1 and 0.4 nM (Fig. 4), with an average of 0.22 ± 0.05 nM ($n=159$) for all samples. Although reported surface concentrations of DFe from this region are scarce, our values agree with DFe concentrations published by Sarthou et al. (2003) which ranged from ~0.2 to 0.55 nM along a meridional transect at ~19°W.

DFe concentrations were determined during the Saharan dust event in the period 3–4 February, and a week later in the period 10–11 February on a transect south of the Cape Verde islands (Fig. 5 a). The concentration of DFe in the surface waters increased significantly from a near constant 0.20 ± 0.03 nM ($n=12$) during 3–4 February to a near constant 0.25 ± 0.03 nM ($n=17$) during 10–11 February (one-way Anova $P < 0.001$) (Fig. 5 b).

It has been reported that Saharan dust contains the highest concentrations of soluble Fe of various aerosol types collected over the Atlantic Ocean (Baker et al., 2006). Based on Fe dissolution experiments, Bonnet and Guieu (2004) predicted that an extremely low magnitude Saharan dust event (yielding an increase of 0.001 mg dust per liter of seawater) would increase the concentration of DFe by 0.07 nM in a 10 m mixed layer. Using the soluble Fe fraction of the aerosols collected by the high-volume aerosol collector in the period 3–11 February we calculated an

increase between 0.024 and 0.031 nM Fe for a 65 and a 20 m mixed layer, respectively, south of the Cape Verde islands. This value corresponds well with the increase in the concentration of DFe that we observed a week after the Saharan dust event. However, as the solubility of Fe is strongly related to pH, Fe is more soluble in an ammonium-acetate leach at a pH of 4.7 compared with seawater (pH ca. 8.1). We would hence expect the calculated increase in the Fe concentration to be higher than the observed increase in the DFe concentration for the transect sailed on 10–11 February. It may be that the higher ionic strength of seawater (Liu and Millero, 2002) or more probably the presence of free Fe-binding ligands increases the solubility of aerosol Fe upon prolonged exposure. Furthermore, there are large uncertainties in deposition velocity estimates (Duce et al., 1991) resulting in an increase in DFe ranging between 0.009 and 0.059 nM DFe for a 65 m mixed layer and ranging between 0.013 and 0.079 nM DFe for a 20 m mixed layer. Dust deposition is also quite variable in space and time and the quantity and identity of the dust collected when the *Poseidon* sailed north of the Cape Verde islands in the period 4–10 February may not have been representative of the dust deposited south of the Cape Verde islands. Due to cloud cover there was no MODIS aerosol optical depth data for this period to verify atmospheric dust concentrations.

3.4. Fe-binding ligands

A total of 33 samples were collected to investigate the effect of the dust event on the Fe-binding ligand concentrations in the

Table 2

The concentration of dissolved Fe ($[DFe]$) (nM), the total concentration of Fe-binding ligands (nM) (total $[L]=[FeL]+[L^-]$), the concentration of free Fe-binding ligands (nM) ($[L^-]$), and the logarithmic conditional stability constant of the Fe-binding ligands ($\log K'_{FeL}$) expressed with respect to Fe^{3+}

Sample no.	Date	Time	Latitude ($^{\circ}N$)	Longitude ($^{\circ}W$)	$[DFe]$ (nM)	Total $[L]$ (nM)	$[L^-]$ (nM)	$\log K'_{FeL}$
28	03/02/2006	08:55	12.0003	-25.9987	0.109±0.016	1.463±0.121	1.355	21.94±0.18
33	03/02/2006	22:05	13.1426	-25.7948	0.179±0.019	1.336±0.066	1.157	22.39±0.10
37	04/02/2006	10:00	14.8269	-25.4867	0.237±0.003	1.321±0.050	1.084	22.25±0.09
42	04/02/2006	22:00	15.8829	-25.2932	0.211±0.009	1.210±0.075	0.999	22.61±0.15
46	05/02/2006	20:00	17.0404	-24.3084	0.145±0.012	0.859±0.041	0.643	22.87±0.25
48	06/02/2006	08:30	17.3472	-22.4371	0.167±0.005	1.015±0.066	0.849	22.43±0.16
52	06/02/2006	22:00	17.4861	-21.5900	0.182±0.033	1.000±0.058	0.818	23.16±0.17
55	07/02/2006	08:20	16.5359	-21.5078	0.197±0.010	1.140±0.050	0.943	22.90±0.15
61	07/02/2006	22:00	15.4113	-21.6756	0.245±0.014	1.000±0.048	0.755	23.21±0.26
64	08/02/2006	08:30	16.6753	-22.4997	0.235±0.012	1.128±0.049	0.894	23.05±0.19
69	08/02/2006	21:55	16.8458	-23.3465	0.183±0.005	1.186±0.042	0.957	23.15±0.11
72	09/02/2006	08:30	17.0376	-24.0863	0.221±0.022	0.993±0.041	0.772	22.98±0.11
75	09/02/2006	22:00	16.2220	-24.3736	0.281±0.006	1.162±0.054	0.881	23.12±0.16
77	10/02/2006	08:00	14.9596	-25.4654	0.269±0.006	1.234±0.070	0.965	22.50±0.12
84	10/02/2006	23:45	12.6578	-25.8821	0.206±0.028	1.035±0.076	0.829	22.57±0.15
87	11/02/2006	08:45	13.8273	-25.6711	0.237±0.009	1.023±0.064	0.786	22.47±0.09
93	11/02/2006	22:00	15.5691	-25.3546	0.227±0.014	1.219±0.071	0.993	22.02±0.16
97	12/02/2006	10:00	17.0006	-24.6454	0.214±0.004	1.090±0.058	0.876	23.41±0.25
104	12/02/2006	23:55	18.2831	-24.2870	0.228±0.009	1.215±0.052	0.988	23.21±0.20
106	13/02/2006	08:50	19.4124	-24.4658	0.225±0.027	1.143±0.065	0.918	22.76±0.24
112	13/02/2006	22:00	19.2152	-23.4305	0.171±0.023	1.070±0.049	0.900	23.38±0.22
115	14/02/2006	08:10	19.5292	-22.8454	0.196±0.020	1.100±0.045	0.905	23.04±0.16
122	14/02/2006	22:00	18.1853	-22.8157	0.088±0.002	1.226±0.045	1.138	22.84±0.13
124	15/02/2006	08:30	18.7083	-24.3349	0.147±0.007	0.822±0.037	0.675	22.97±0.14
130	15/02/2006	22:00	19.3091	-26.0782	0.157±0.018	0.966±0.028	0.809	23.04±0.14
132	16/02/2006	08:45	19.8935	-27.5986	0.151±0.014	0.893±0.034	0.743	23.36±0.21
139	16/02/2006	22:00	21.5532	-27.5988	0.151±0.005	1.071±0.035	0.921	23.26±0.15
142	17/02/2006	08:30	22.9586	-27.5969	0.204±0.004	0.950±0.046	0.746	23.00±0.24
151	18/02/2006	08:50	26.3341	-27.5988	0.332±0.020	1.262±0.045	0.930	22.65±0.19
157	18/02/2006	21:55	28.1643	-27.5885	0.239±0.016	1.143±0.059	0.904	22.97±0.23
159	19/02/2006	08:40	29.9361	-27.6130	0.224±0.015	1.061±0.045	0.837	22.86±0.13
163	19/02/2006	21:40	29.8509	-26.3231	0.217±0.030	1.015±0.053	0.798	23.06±0.23
166	20/02/2006	08:40	29.6473	-24.4205	0.302±0.025	1.154±0.059	0.852	22.64±0.17

The inorganic side reaction coefficient for Fe was taken as $\alpha_{Fe^{3+}}=1.3 \cdot 10^{10}$ (Sunda and Huntsman, 2003). Uncertainties are given as standard deviation.

dissolved phase (Table 2). A representative titration of the Fe-binding ligands is presented in Fig. 6. The CSV titrations showed clear Fe-binding in all samples at low Fe additions, indicating the presence of free Fe-binding ligands (Fig. 6a). In this study the uncomplexed Fe-binding ligand concentration is defined by the detection window of the competing ligand (TAC) (centred by $\alpha_{Fe(TAC)2} (= \beta_{Fe(TAC)2}[TAC]^2)$) and is within one order of magnitude on either side of $\alpha_{Fe(TAC)2}$ (Apte et al., 1988). Uncomplexed Fe-binding ligands with an $\alpha_{FeL} < 10^{11.4}$ or $\alpha_{FeL} > 10^{13.4}$ may not have been detected by our titration technique (Gerringa et al., 2007). The strong ligands with a $\alpha_{FeL} > 10^{13.4}$ will be occupied by Fe, but in the uncomplexed Fe-binding ligand pool our approach may miss a fraction of the weak ligands with an $\alpha_{FeL} < 10^{11.4}$.

The total Fe-binding ligand concentration in Cape Verde surface waters varied between 0.82 and 1.46 nM with an average of 1.11 ± 0.14 nM ($n=33$), and the uncomplexed Fe-binding ligand concentration varied between 0.64 and 1.35 nM with an average of 0.90 ± 0.14 nM ($n=33$) (Fig. 7 a). The average logarithmic conditional stability constant of the Fe-binding ligands was 22.85 ± 0.38 ($n=33$) for all samples. The values from this study fall within the range of concentrations of Fe-binding ligands and their conditional stability constants as determined using different protocols for surface waters of the North Atlantic Ocean (Boyé et al., 2006; Boyé et al., 2003;

Gerringa et al., 2006; Powell and Donat, 2001; Witter and Luther, 1998), Southern Ocean (Boyé et al., 2001; Croot et al., 2004; Tian et al., 2006), Arabian Sea (Witter et al., 2000b) and the Gulf of Mexico (Powell and Wilson-Finelli, 2003). Furthermore, our values for uncomplexed Fe-binding ligand concentrations compare well with values reported for the equatorial North Atlantic: 1.29 ± 0.48 nM (Boyé et al., 2006), 2.38 ± 1.55 nM (Gerringa et al., 2006) and 0.39 ± 0.38 nM (Powell and Donat, 2001).

During the dust event (3–4 February) we observed a gradual decrease in the uncomplexed Fe-binding ligand concentrations. Subsequently, on the repeat transect (10–11 February) the concentrations of uncomplexed Fe-binding ligands were lower still (Fig. 7b). The concentration of uncomplexed Fe-binding ligands decreased significantly from an average of 1.15 ± 0.15 nM ($n=4$, 86% of total L) during the dust event to an average of 0.89 ± 0.10 nM ($n=4$, 79% of total L) in the following week (one-way Anova, $P < 0.05$). The logarithmic stability constants of the Fe-binding ligands were not significantly different during the dust event (average 22.30 ± 0.28 , $n=4$) and in the week following the dust event (average 22.39 ± 0.25 , $n=4$). The concentration of uncomplexed Fe-binding ligands following the dust event in the period of 3–4 February remained constant at 0.86 ± 0.10 nM ($n=29$) north of the Cape Verde islands.

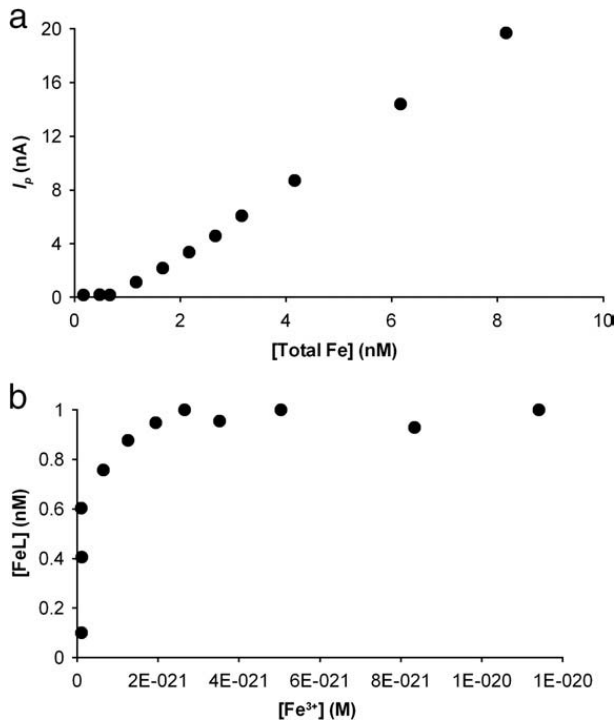


Fig. 6. Representative titration curve for surface seawater sample number 48 (Table 1). a) The current (nA) plotted versus the total amount of Fe (nM). b) The non-linear least-squares fit using the Gerringa method (Gerringa et al., 1995).

Interestingly, a dust event would need to add $\sim 37.4 \mu\text{mol}$ soluble Fe $\text{m}^{-2} \text{d}^{-1}$ to a 65 m mixed layer depth over a period of 2 days to exhaust the original uncomplexed Fe-binding ligand concentration of 1.15 nM on 3 and 4 February. That is 70 times more input of soluble Fe as observed during our study for 3–4 February and roughly 40 times higher than the highest soluble Fe fluxes we have observed previously using these methods (Baker et al., 2003).

When we compare the average concentration of uncomplexed Fe-binding ligands during the dust event (3–4 February) with the average concentration during the repeat transect (10–11 February) we observe a significant decrease of about 0.26 nM (one-way Anova, $P < 0.05$). An increased total DFe concentration in concert with binding of Fe by the uncomplexed ligands [L^-] suggests an increase in organically complexed Fe ([FeL]) after the dust event.

The discrepancy between the increase of DFe of 0.05 nM and the decrease of L^- of 0.26 nM was possibly due to an analytical artefact and/or a biological process. A possibility is that part of [FeL] may not have been detected by the FI-CL method resulting in an underestimation of the observed DFe concentration (Ussher et al., 2005). Another possibility involves the uptake of FeL by the microbial community.

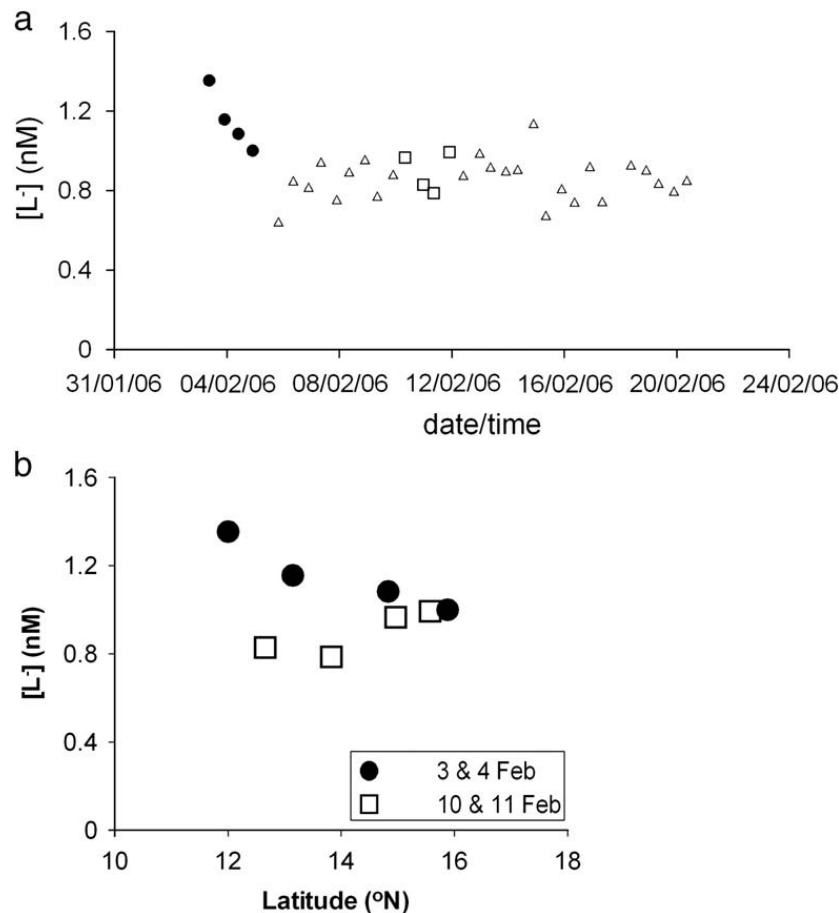


Fig. 7. a) The surface concentrations of uncomplexed Fe-binding ligands versus time during a Saharan dust event on 3–4 February (closed circles) and a week later, 10–11 February (open squares), on the transect south of the Cape Verde islands. The open triangles represent the surface concentrations of uncomplexed Fe-binding ligands north of the Cape Verde islands. b) The surface concentration of uncomplexed Fe-binding ligands for 3–4 February (closed circles) during the Saharan dust event and a week later, 10–11 February (open squares), on the transect south of the Cape Verde islands.

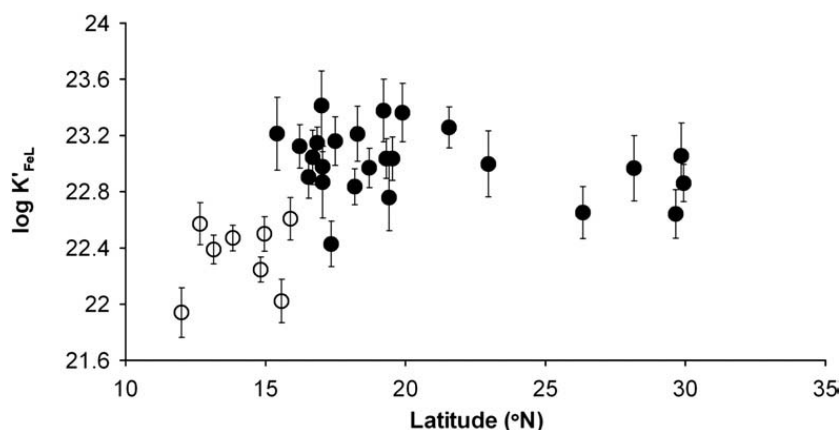
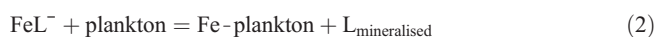


Fig. 8. The conditional stability constants of the Fe-binding ligands in surface water samples from the Cape Verde region versus latitude. The conditional stability constants for samples of the transect south of the Cape Verde islands are given as open circles and north and east of the Cape Verde islands as closed circles. Uncertainties are given as standard deviation.

Upon the deposition of aerosol Fe to the ocean, the Fe is complexed by ligands (1):



The FeL may subsequently be taken up by microorganisms (Maldonado and Price, 1999), and the ligands are broken down in this process (2):



We hypothesise that when 5 equivalents of dissolved FeL are formed from Fe' (denotes inorganic Fe) and L⁻, and subsequently 4 equivalents of FeL are taken up, then the decrease in L⁻ would constitute 5 equivalents, while DFe increases by only 1 equivalent (as FeL), i.e. (3):



This process would therefore lead to a decrease of 5 units of L⁻ and a decrease of 4 units of the total ligand pool due to the microbial break down of the ingested ligands. Consistent with the uptake of FeL, the uncomplexed ligand concentration decreased by 0.22 nM L⁻ and the total ligand pool decreased by 0.15 nM total L during the Saharan dust event on 3–4 February. As a consequence, the net increase in the DFe concentration due to the dust event is somewhere between the 0.05 nM Fe as determined with FI-CL and 0.26 nM Fe as determined using CSV.

The conditional stability constant of the Fe-binding ligands in the water mass north of the Cape Verde islands was relatively constant ($\log K'_{\text{FeL}} = 23.01 \pm 0.24$, $n=25$) and significantly higher than the conditional stability constant in the waters south of the Cape Verde islands ($\log K'_{\text{FeL}} = 22.34 \pm 0.25$, $n=8$, one-way Anova, $P < 0.001$, Fig. 8). The different conditional stability constants suggest differences between the Fe-binding ligands north and south of the Cape Verde islands. This could be an effect of differences in biological sources for Fe-binding ligands. Another possibility is that different fractions of the Fe-binding ligand pool are taken up by the microbial community (Hutchins et al., 1999). However, no clear difference in Chl *a* concentrations, *Prochlorococcus*, *Synechococcus*, picoeukaryotes, and heterotrophic bacteria cell numbers were observed between the areas. In the waters

south of the Cape Verde islands the surface phosphate concentrations were 28 ± 14 nM and about 50% lower than to the north of the islands. Upwelling of nutrients north of the islands could be responsible for the increased surface phosphate concentrations, and upwelling of strong Fe-binding ligands could also form an explanation for the difference in the conditional stability constants of Fe-binding ligands found.

During the dust event (3–4 February), the conditional stability constants of the Fe-binding ligands ($\log K'_{\text{FeL}} = 22.30 \pm 0.28$, $n=4$) did not change as a result of the inputs of dust. Furthermore, no enhanced concentrations of TAC-labile Fe (Fe bound by 10 μM TAC after >12 h equilibration), which would indicate the deposition of Fe bound by weak Fe-binding ligands ($\alpha_{\text{FeL}} < 10^{11.4}$) (Gerringa et al., 2007; Rijkenberg et al., 2006), were observed in our titrations of samples collected during and following the dust event. Therefore, there was no detectable input of aeolian Fe-binding ligands with binding strengths within or below our applied detection window.

4. Conclusions

An increase of the DFe concentration in concert with a decrease in the uncomplexed Fe-binding ligand concentration was observed following a minor Saharan dust event in the Cape Verde region. No input of aeolian Fe-binding ligands was observed.

The Fe-binding ligands present in seawater in our study region therefore play a key role in keeping Fe, which is released from dust particles, in solution. By prevention of formation of insoluble inorganic Fe complexes, the ligands provide resident microorganisms with a source of dissolved Fe. However, the availability to the microorganisms of the Fe that is complexed by the ligands is still largely a mystery.

Acknowledgements

Mark Stinchcombe, James Cooper, and Jane Heywood are thanked for all their help on board of the ship. We further want to thank Sarah Bennet and Turki Al-Said for their help with the voltammetric measurements and Tanya Compton for improving the manuscript. We want to thank the reviewers

for their very useful comments. The authors thank the NERC Earth Observation Data Acquisition and Analysis Service (NEODAAS) for supplying data for this study. Satellite data were also provided by the Department of Meteorology (E. Highwood) of the University of Reading. We used the NAO index according to Hurrell as found on: www.cgd.ucar.edu/cas/jhurrell/nao.stat.winter.html. The authors gratefully acknowledge the NOAA Air Resources Laboratory (ARL) for the provision of the HYSPLIT transport and dispersion model and/or READY website (www.arl.noaa.gov/ready.html) used in this publication. We further want to express our gratitude to the Master and crew of *FS Poseidon* for support during the cruise. This research is funded by NERC as part of the UK-SOLAS programme, project grant number NE/C001931/1.

Appendix A. Supplementary data

Supplementary data associated with this article can be found, in the online version, at [doi:10.1016/j.marchem.2008.02.006](https://doi.org/10.1016/j.marchem.2008.02.006).

References

- Achterberg, E.P., Holland, T.W., Bowie, A.R., Mantoura, R.F.C., Worsfold, P.J., 2001. Determination of iron in seawater. *Anal. Chim. Acta* 442 (1), 1–14.
- Apte, S.C., Gardner, M.J., Ravenscroft, J.E., 1988. An evaluation of voltammetric titration procedures for the determination of trace-metal complexation in natural-waters by use of computer-simulation. *Anal. Chim. Acta* 212 (1–2), 1–21.
- Baker, A.R., Kelly, S.D., Biswas, K.F., Witt, M., Jickells, T.D., 2003. Atmospheric deposition of nutrients to the Atlantic Ocean. *Geophys. Res. Lett.* 30 (24).
- Baker, A.R., Jickells, T.D., Biswas, K.F., Weston, K., French, M., 2006. Nutrients in atmospheric aerosol particles along the Atlantic Meridional Transect. *Deep-Sea Res. II* 53 (14–16), 1706–1719.
- Batteen, M.L., Martinez, J.R., Bryan, D.W., Buch, E.J., 2000. A modeling study of the coastal eastern boundary current system off Iberia and Morocco. *J. Geophys. Res., Oceans* 105 (C6), 14173–14195.
- Berman-Frank, I., Cullen, J.T., Shaked, Y., Sherrell, R.M., Falkowski, P.G., 2001. Iron availability, cellular iron quotas, and nitrogen fixation in *Trichodesmium*. *Limnol. Oceanogr.* 46 (6), 1249–1260.
- Blain, S., Guieu, U., Claustre, H., Leblanc, K., Moutin, T., Queguiner, B., Ras, J., Sarthou, G., 2004. Availability of iron and major nutrients for phytoplankton in the northeast Atlantic Ocean. *Limnol. Oceanogr.* 49 (6), 2095–2104.
- Bonnet, S., Guieu, C., 2004. Dissolution of atmospheric iron in seawater. *Geophys. Res. Lett.* 31 (3).
- Bonnet, S., Guieu, C., Chiaverini, J., Ras, J., Stock, A., 2005. Effect of atmospheric nutrients on the autothrophic communities in a low nutrient low chlorophyll system. *Limnol. Oceanogr.* 50 (6), 1810–1819.
- Borer, P.M., Sulzberger, B., Reichard, P., Kraemer, S.M., 2005. Effect of siderophores on the light-induced dissolution of colloidal iron(III) (hydr)oxides. *Mar. Chem.* 93 (2–4), 179–193.
- Bowie, A.R., Achterberg, E.P., Mantoura, R.F.C., Worsfold, P.J., 1998. Determination of sub-nanomolar levels of iron in seawater using flow injection with chemiluminescence detection. *Anal. Chim. Acta* 361 (3), 189–200.
- Bowie, A.R., Whitworth, D.J., Achterberg, E.P., Mantoura, R.F.C., Worsfold, P.J., 2002. Biogeochemistry of Fe and other trace elements (Al, Co, Ni) in the upper Atlantic Ocean. *Deep-Sea Res. I* 49 (4), 605–636.
- Bowie, A.R., Achterberg, E.P., Croot, P.L., de Baar, H.J.W., Laan, P., Moffett, J.W., Ussher, S., Worsfold, P.J., 2006. A community-wide intercomparison exercise for the determination of dissolved iron in seawater. *Mar. Chem.* 98 (1), 81–99.
- Bowie, A.R., Ussher, S.J., Landing, W.M., Worsfold, P.J., 2007. Intercomparison between FI-CL and ICP-MS for the determination of dissolved iron in Atlantic seawater. *Environ. Chem.* 4 (1), 1–4.
- Boyé, M., van den Berg, C.M.G., de Jong, J.T.M., Leach, H., Croot, P.L., de Baar, H.J.W., 2001. Organic complexation of iron in the Southern Ocean. *Deep-Sea Res. I* 48 (6), 1477–1497.
- Boyé, M., Aldrich, A.P., van den Berg, C.M.G., de Jong, J.T.M., Veldhuis, M., de Baar, H.J.W., 2003. Horizontal gradient of the chemical speciation of iron in surface waters of the northeast Atlantic Ocean. *Mar. Chem.* 80 (2–3), 129–143.
- Boyé, M., Nishioka, J., Croot, P.L., Laan, P., Timmermans, K.R., de Baar, H.J.W., 2005. Major deviations of iron complexation during 22 days of a mesoscale iron enrichment in the open Southern Ocean. *Mar. Chem.* 96, 257–271.
- Boyé, M., Aldrich, A., van den Berg, C.M.G., de Jong, J.T.M., Nirmaier, H., Veldhuis, M., Timmermans, K.R., de Baar, H.J.W., 2006. The chemical speciation of iron in the north–east Atlantic Ocean. *Deep-Sea Res. I* 53 (4), 667–683.
- Brundland, K.W., Rue, E.L., Smith, G.J., 2001. Iron and macronutrients in California coastal upwelling regimes: implications for diatom blooms. *Limnol. Oceanogr.* 46 (7), 1661–1674.
- Chereskin, B.M., Castelfranco, P.A., 1982. Effects of iron and oxygen on chlorophyll biosynthesis. 2. Observations on the biosynthetic-pathway in isolated etioclroplasts. *Plant Physiol.* 69 (1), 112–116.
- Chiappello, I., Bergametti, G., Gomes, L., Chatenet, B., Dulac, F., Pimenta, J., Soares, E.S., 1995. An additional low layer transport of Sahelian and Saharan dust over the North-Eastern Tropical Atlantic. *Geophys. Res. Lett.* 22 (23), 3191–3194.
- Croot, P.L., Johansson, M., 2000. Determination of iron speciation by cathodic stripping voltammetry in seawater using the competing ligand 2-(2-thiazolylazo)-*p*-cresol (TAC). *Electroanalysis* 12 (8), 565–576.
- Croot, P.L., Andersson, K., Ozturk, M., Turner, D.R., 2004. The distribution and speciation of iron along 6 degrees E in the Southern Ocean. *Deep-Sea Res. II* 51 (22–24), 2857–2879.
- Dall'Osto, M., Harrison, R.M., Beddows, D.C.S., Freney, E.J., Heal, M.R., Donovan, R.J., 2006. Single-particle detection efficiencies of aerosol time-of-flight mass spectrometry during the North Atlantic marine boundary layer experiment. *Environ. Sci. Technol.* 40 (16), 5029–5035.
- de Baar, H.J.W., Buma, A.G.J., Nolting, R.F., Cadee, G.C., Jacques, G., Treguer, P.J., 1990. On iron limitation of the Southern Ocean—experimental observations in the Weddell and Scotia seas. *Mar. Ecol. Progr. Ser.* 65 (2), 105–122.
- Duce, R.A., Tindale, N.W., 1991. Atmospheric transport of iron and its deposition in the ocean. *Limnol. Oceanogr.* 36, 1715–1726.
- Duce, R.A., Liss, P.S., Merrill, J.T., Atlas, E.L., Buat-Menard, P., Hicks, B.B., Miller, J. M., Prospero, J.M., Arimoto, R., Church, T.M., Ellis, W., Galloway, J.N., Hansen, L., Jickells, T.D., Knap, A.H., Reinhardt, K.H., Schneider, B., Soudine, A., Tokos, J.J., Tsunogai, S., Wollast, R., Zhou, M., 1991. The atmospheric input of trace species to the world ocean. *Glob. Biogeochem. Cycles* 5 (3), 193–259.
- Falkowski, P.G., 1997. Evolution of the nitrogen cycle and its influence on the biological sequestration of CO₂ in the ocean. *Nature* 387 (6630), 272–275.
- Fedoseev, A., 1970. Geostrophic circulation of surface waters on the shelf of north–west Africa. *Rapp. P.-V. Reun. Cons. Int. Explor. Mer.* 159, 32–37.
- Gao, Y., Kaufman, Y.J., Tanre, D., Kolber, D., Falkowski, P.G., 2001. Seasonal distributions of aeolian iron fluxes to the global ocean. *Geophys. Res. Lett.* 28 (1), 29–32.
- Gard, E., Mayer, J.E., Morrical, B.D., Dienes, T., Fergenson, D.P., Prather, K.A., 1997. Real-time analysis of individual atmospheric aerosol particles: design and performance of a portable ATOMFS. *Anal. Chem.* 69 (20), 4083–4091.
- Geider, R.J., la Roche, J., Greene, R.M., Olaizola, M., 1993. Response of the photosynthetic apparatus of *Phaeodactylum tricoratum* (Bacillariophyceae) to nitrate, phosphate, or iron starvation. *J. Phycol.* 29 (6), 755–766.
- Gerringa, L.J.A., Herman, P.M.J., Poortvliet, T.C.W., 1995. Comparison of the linear van den Berg Ruzic transformation and a nonlinear fit of the Langmuir isotherm applied to Cu speciation data in the estuarine environment. *Mar. Chem.* 48 (2), 131–142.
- Gerringa, L.J.A., Veldhuis, M.J.W., Timmermans, K.R., Sarthou, G., de Baar, H.J.W., 2006. Co-variance of dissolved Fe-binding ligands with phytoplankton characteristics in the Canary Basin. *Mar. Chem.* 102 (3–4), 276–290.
- Gerringa, L.J.A., Rijkenberg, M.J.A., Wolterbeek, H.T., Verburg, T.G., Boye, M., de Baar, H.J.W., 2007. Kinetic study reveals weak Fe-binding ligand, which affects the solubility of Fe in the Scheldt estuary. *Mar. Chem.* 103, 30–45.
- Gledhill, M., van den Berg, C.M.G., 1994. Determination of complexation of iron(III) with natural organic complexing ligands in seawater using cathodic stripping voltammetry. *Mar. Chem.* 47 (1), 41–54.
- Gledhill, M., McCormack, P., Ussher, S., Achterberg, E.P., Mantoura, R.F.C., Worsfold, P.J., 2004. Production of siderophore type chelates by mixed bacterioplankton populations in nutrient enriched seawater incubations. *Mar. Chem.* 88 (1–2), 75–83.
- Hudson, R.J.M., Covault, D.T., Morel, F.M.M., 1992. Investigations of iron coordination and redox reactions in seawater using Fe-59 radiometry and ion-pair solvent-extraction of amphiphilic iron complexes. *Mar. Chem.* 38 (3–4), 209–235.
- Hunter, K.A., 2005. Comment on 'Measuring marine iron(III) complexes by CLE-AdSV'. *Environ. Chem.* 2 (2), 85–87.
- Hurrell, J.W., 1995. Decadal trend in the North Atlantic oscillation: regional temperatures and precipitations. *Science* 269, 676–679.
- Hutchins, D.A., Brundland, K.W., 1998. Iron-limited diatom growth and Si: N uptake ratios in a coastal upwelling regime. *Nature* 393 (6685), 561–564.
- Hutchins, D.A., Witter, A.E., Butler, A., Luther, G.W., 1999. Competition among marine phytoplankton for different chelated iron species. *Nature* 400 (6747), 858–861.
- Hydes, D.J., Liss, P.S., 1976. Fluorimetric method for determination of low concentrations of dissolved aluminum in natural-waters. *Analyst* 101 (1209), 922–931.

- Jickells, T.D., Spokes, L.J., 2001. Atmospheric iron inputs to the oceans. In: Turner, D.R., Hunter, K.A. (Eds.), *The Biogeochemistry of Iron in Seawater*. IUPAC Series on Analytical and Physical Chemistry of Environmental Systems. John Wiley & Sons, LTD, New York, pp. 85–122.
- Johnson, J., Stevens, I., 2000. A fine resolution model of the eastern North Atlantic between the Azores, the Canary Islands and the Gibraltar Strait. *Deep-Sea Res. I, Oceanogr. Res. Papers* 47 (5), 875–899.
- Johnson, K.S., Gordon, R.M., Coale, K.H., 1997. What controls dissolved iron concentrations in the world ocean? *Mar. Chem.* 57 (3–4), 137–161.
- Karl, D., Letelier, R., Tupas, L., Dore, J., Christian, J., Hebel, D., 1997. The role of nitrogen fixation in biogeochemical cycling in the subtropical North Pacific Ocean. *Nature* 388 (6642), 533–538.
- Kraemer, S.M., 2004. Iron oxide dissolution and solubility in the presence of siderophores. *Aquat. Sci.* 66 (1), 3–18.
- Kraemer, S.M., Butler, A., Borer, P., Cervini-Silva, J., 2005. Siderophores and the dissolution of iron-bearing minerals in marine systems. *Mol. Geomicrobiol. Rev. Mineral. Geochem.* 53–84.
- Kuma, K., Nishioka, J., Matsunaga, K., 1996. Controls on iron(III) hydroxide solubility in seawater: the influence of pH and natural organic chelators. *Limnol. Oceanogr.* 41 (3), 396–407.
- Landing, W.M., Haraldsson, C., Paxeus, N., 1986. Vinyl polymer agglomerate based transition-metal cation chelating ion-exchange resin containing the 8-hydroxyquinoline functional-group. *Anal. Chem.* 58 (14), 3031–3035.
- Liu, X.W., Millero, F.J., 2002. The solubility of iron in seawater. *Mar. Chem.* 77 (1), 43–54.
- Macrellis, H.M., Trick, C.G., Rue, E.L., Smith, G., Bruland, K.W., 2001. Collection and detection of natural iron-binding ligands from seawater. *Mar. Chem.* 76 (3), 175–187.
- Maldonado, M.T., Price, N.M., 1999. Utilization of iron bound to strong organic ligands by plankton communities in the subarctic Pacific Ocean. *Deep Sea Res. II* 46, 2447–2473.
- Martin, J.H., Fitzwater, S.E., 1988. Iron-deficiency limits phytoplankton growth in the northeast Pacific subarctic. *Nature* 331 (6154), 341–343.
- Measures, C.I., 1995. The distribution of Al in the IOC stations of the eastern Atlantic between 30-degrees-S and 34-degrees-N. *Mar. Chem.* 49 (4), 267–281.
- Measures, C.I., Grant, B., Khadem, M., Lee, D.S., Edmond, J.M., 1984. Distribution of Be, Al, Se and Bi in the surface waters of the western North-Atlantic and Caribbean. *Earth. Planet. Sci. Lett.* 71 (1), 1–12.
- Michaels, A.F., Olson, D., Sarmiento, J.L., Ammerman, J.W., Fanning, K., Jahnke, R., Knap, A.H., Lipschultz, F., Prospero, J.M., 1996. Inputs, losses and transformations of nitrogen and phosphorus in the pelagic North Atlantic Ocean. *Biogeochemistry* 35 (1), 181–226.
- Mills, M.M., Ridame, C., Davey, M., La Roche, J., Geider, R.J., 2004. Iron and phosphorus co-limit nitrogen fixation in the eastern tropical North Atlantic. *Nature* 429 (6989), 292–294.
- Moffett, J.W., 2001. Transformations among different forms of iron in the ocean. In: Turner, D.R., Hunter, K.A. (Eds.), *The Biogeochemistry of Iron in Seawater*. IUPAC Series on Analytical and Physical Chemistry of Environmental Systems. John Wiley & Sons, LTD, New York, pp. 343–372.
- Moore, C.M., Mills, M.M., Milne, A., Langlois, R., Achterberg, E.P., Lochte, K., Geider, R.J., La Roche, J., 2006. Iron limits primary productivity during spring bloom development in the central North Atlantic. *Glob. Change Biol.* 12 (4), 626–634.
- Moulin, C., Lambert, C.E., Dulac, F., Dayan, U., 1997. Control of atmospheric export of dust from North Africa by the North Atlantic oscillation. *Nature* 387 (6634), 691–694.
- Nagai, T., Imai, A., Matsushige, K., Yokoi, K., Fukushima, T., 2007. Dissolved iron and its speciation in a shallow eutrophic lake and its inflowing rivers. *Water Res.* 41 (4), 775–784.
- Nolting, R.F., Gerringa, L.J.A., Swagerman, M.J.W., Timmermans, K.R., de Baar, H.J.W., 1998. Fe(III) speciation in the high nutrient, low chlorophyll Pacific region of the Southern Ocean. *Mar. Chem.* 62 (3–4), 335–352.
- Orians, K.J., Bruland, K.W., 1986. The biogeochemistry of aluminum in the Pacific-Ocean. *Earth Planet. Sci. Lett.* 78 (4), 397–410.
- Peterson, R.G., Stramma, L., Kortum, G., 1996. Early concepts and chart of ocean circulation. *Progr. Oceanogr.* 37 (1), 1–115.
- Powell, R.T., Donat, J.R., 2001. Organic complexation and speciation of iron in the South and Equatorial Atlantic. *Deep-Sea Res. II* 48 (13), 2877–2893.
- Powell, R.T., Wilson-Finelli, A., 2003. Photochemical degradation of organic iron complexing ligands in seawater. *Aquat. Sci.* 65 (4), 367–374.
- Prospero, J.M., Carlson, T.N., 1972. Vertical and areal distribution of Saharan dust over the western equatorial North Atlantic Ocean. *J. Geophys. Res.* 77 (27), 5255–5265.
- Prospero, J.M., Glaccum, R.A., Nees, R.T., 1981. Atmospheric transport of soil dust from Africa to South-America. *Nature* 289 (5798), 570–572.
- Rijkenberg, M.J.A., Gerringa, L.J.A., Velzeboer, I., Timmermans, K.R., Buma, A.G.J., de Baar, H.J.W., 2006. Iron-binding ligands in Dutch estuaries are not affected by UV induced photochemical degradation. *Mar. Chem.* 100 (1–2), 11–23.
- Rue, E.L., Bruland, K.W., 1995. Complexation of iron(III) by natural organic-ligands in the central north Pacific as determined by a new competitive ligand equilibration adsorptive cathodic stripping voltammetric method. *Mar. Chem.* 50 (1–4), 117–138.
- Sarthou, G., Baker, A.R., Blain, S., Achterberg, E.P., Boye, M., Bowie, A.R., Croot, P., Laan, P., de Baar, H.J.W., Jickells, T.D., Worsfold, P.J., 2003. Atmospheric iron deposition and sea-surface dissolved iron concentrations in the eastern Atlantic Ocean. *Deep-Sea Res. I* 50 (10–11), 1339–1352.
- Stuut, J.B., Zabel, M., Ratmeyer, V., Helmke, P., Schefuss, E., Lavik, G., Schneider, R., 2005. Provenance of present-day eolian dust collected off NW Africa. *J. Geophys. Res.-Atmos.* 110 (D4).
- Sunda, W.G., Huntsman, S.A., 1995. Iron uptake and growth limitation in oceanic and coastal phytoplankton. *Mar. Chem.* 50 (1–4), 189–206.
- Sunda, W., Huntsman, S., 2003. Effect of pH, light, and temperature on Fe-EDTA chelation and Fe hydrolysis in seawater. *Marine Chemistry* 84 (1–2), 35–47.
- Tian, F., Frew, R.D., Sander, S., Hunter, K.A., Ellwood, M.J., 2006. Organic iron (III) speciation in surface transects across a frontal zone: the Chatham Rise, New Zealand. *Mar. Freshwater Res.* 57 (5), 533–544.
- Timmermans, K.R., van der Wagt, B., de Baar, H.J.W., 2004. Growth rates, half-saturation constants, and silicate, nitrate, and phosphate depletion in relation to iron availability of four large, open-ocean diatoms from the Southern Ocean. *Limnol. Oceanogr.* 49 (6), 2141–2152.
- Town, R.M., van Leeuwen, H.P., 2005. Measuring marine iron(III) complexes by CLE-AdSV. *Environmental Chemistry* 2 (2), 80–84.
- Ussher, S.J., Yaqoob, M., Achterberg, E.P., Nabi, A., Worsfold, P.J., 2005. Effect of model ligands on iron redox speciation in natural waters using flow injection with luminol chemiluminescence detection. *Anal. Chem.* 77 (7), 1971–1978.
- van den Berg, C.M.G., 1982. Determination of copper complexation with natural organic-ligands in sea-water by equilibration with $M_nO_{2.1}$. *Theory. Mar. Chem.* 11 (4), 307–322.
- van den Berg, C.M.G., 1995. Evidence for organic complexation of iron in seawater. *Mar. Chem.* 50 (1–4), 139–157.
- van den Berg, C.M.G., 2005. Organic iron complexation is real, the theory is used incorrectly. Comment on 'Measuring marine iron(III) complexes by CLE-AdSV'. *Environ. Chem.* 2 (2), 88–89.
- van den Berg, C.M.G., 2006. Chemical speciation of iron in seawater by cathodic stripping voltammetry with dihydroxynaphthalene. *Anal. Chem.* 78 (1), 156–163.
- van Leeuwe, M.A., Scharek, R., de Baar, H.J.W., de Jong, J.T.M., Goeyens, L., 1997. Iron enrichment experiments in the Southern Ocean: physiological responses of plankton communities. *Deep Sea Res. II* 44, 189–207.
- Waite, T.D., 2001. Thermodynamics of the iron system in seawater. In: Turner, D.R., Hunter, K.A. (Eds.), *The Biogeochemistry of Iron in Seawater*. IUPAC series on Analytical and Physical Chemistry of Environmental Systems. John Wiley & Sons, LTD, pp. 291–342.
- Witter, A.E., Luther, G.W., 1998. Variation in Fe-organic complexation with depth in the northwestern Atlantic Ocean as determined using a kinetic approach. *Mar. Chem.* 62 (3–4), 241–258.
- Witter, A.E., Hutchins, D.A., Butler, A., Luther, G.W., 2000a. Determination of conditional stability constants and kinetic constants for strong model Fe-binding ligands in seawater. *Mar. Chem.* 69 (1–2), 1–17.
- Witter, A.E., Lewis, B.L., Luther, G.W., 2000b. Iron speciation in the Arabian Sea. *Deep Sea Res. II* 47 (7–8), 1517–1539.
- Wooster, W.S., Bakun, A., McLain, D.R., 1976. Seasonal upwelling cycle along eastern boundary of North-Atlantic. *J. Mar. Res.* 34 (2), 131–141.
- Wu, J.F., Luther, G.W., 1995. Complexation of Fe(III) by natural organic-ligands in the northwest Atlantic Ocean by a competitive ligand equilibration method and a kinetic approach. *Mar. Chem.* 50 (1–4), 159–177.
- Zhou, M., Paduan, J.D., Niiler, P.P., 2000. Surface currents in the Canary Basin from drifter observations. *J. Geophys. Res., Oceans* 105 (C9), 21893–21911.

Appendix E

Appendix - Matlab Code

This appendix includes all the Matlab code I used to calibrate; find sample concentrations; correct for instrument drift; find the molar amount on filter; correct for blanks; and calculate atmospheric concentrations for each sample, once all the analyses were done. It should be possible for any user to copy these pages and use them to arrive at the same data set as I have.

E.1 Cal.m

Calibrations were done using a GUI in Matlab. The interactive interface is shown in figure E.1.

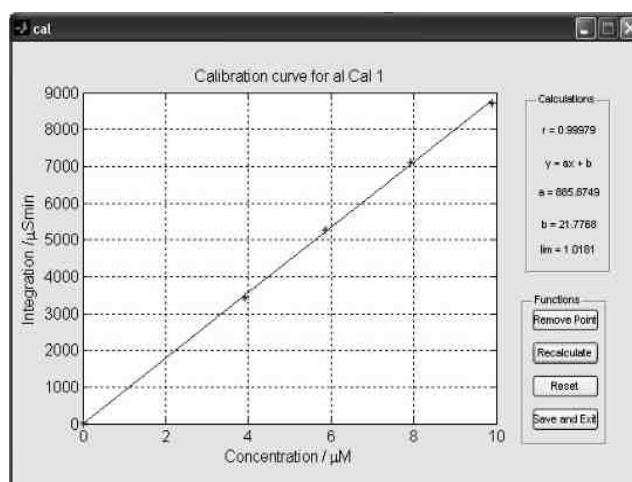


Figure E.1: Screen shot of the *cal* GUI

The script is adapted from matlab's GUI-creation wizard.

```
function varargout = cal(varargin)
% CAL M-file for cal.fig
% cal is for calibrating linear data cfp 30 oct 06, modified 06 JUN 08
% [array] = cal(measured, conc, 'ion');
%
% EQUATIONS USED...
% xbar = mean(conc(indx));
% ybar = mean(sam(indx));
%
% sumxsq = 0; sumysq = 0; sumprod = 0;
% for i = 1 : length(indx)
%     sumprod = sumprod + ((conc(indx(i))-xbar)*(sam(indx(i))-ybar));
%     sumxsq = sumxsq + ((conc(indx(i))-xbar)^2);
%     sumysq = sumysq + ((sam(indx(i))-ybar)^2);
% end
%
% r = sumprod / sqrt(sumxsq*sumysq);
%
% slope = sumprod / sumxsq;
% intercept = ybar - slope*xbar;
```

```

%
% calcd = conc(indx)*slope + intercept;
% yres = sam(indx)-calcd;
% degfreedom = length(indx)-2;
% syonx = sqrt(sum(yres.^2) / degfreedom);
% stdslope = syonx / sqrt(sumxsq);
% stdintercept = syonx * sqrt((sum(conc(indx).^2))/(length(indx)*sumxsq));
%
% if intercept >= 0
%     lim = (3*syonx) / slope;
% else
%     lim = (3*syonx - intercept) / slope;
% end
%
%     CAL, by itself, creates a new CAL or raises the existing
%     singleton*.
%
%     H = CAL returns the handle to a new CAL or the handle to
%     the existing singleton*.
%
%     CAL('CALLBACK',hObject,eventData,handles,...) calls the local
%     function named CALLBACK in CAL.M with the given input arguments.
%
%     CAL('Property','Value',...) creates a new CAL or raises the
%     existing singleton*. Starting from the left, property value pairs are
%     applied to the GUI before cal_OpeningFunction gets called. An
%     unrecognized property name or invalid value makes property application
%     stop. All inputs are passed to cal_OpeningFcn via varargin.
%
%     *See GUI Options on GUIDE's Tools menu. Choose "GUI allows only one
%     instance to run (singleton)".
%
% See also: GUIDE, GUIDATA, GUIHANDLES

% Edit the above calculationtext to modify the response to help cal

% Last Modified by GUIDE v2.5 30-Oct-2006 15:40:57

% Begin initialization code - DO NOT EDIT
gui_Singleton = 1;
gui_State = struct('gui_Name',       mfilename, ...
                  'gui_Singleton',  gui_Singleton, ...
                  'gui_OpeningFcn', @cal_OpeningFcn, ...
                  'gui_OutputFcn',  @cal_OutputFcn, ...
                  'gui_LayoutFcn',  [], ...
                  'gui_Callback',    []);
if nargin && ischar(varargin{1})
    gui_State.gui_Callback = str2func(varargin{1});
end

if nargout
    [varargout{1:nargout}] = gui_mainfcn(gui_State, varargin{:});
else
    gui_mainfcn(gui_State, varargin{:});
end
% End initialization code - DO NOT EDIT

% --- Executes just before cal is made visible.
function cal_OpeningFcn(hObject, eventdata, handles, varargin)
% This function has no output args, see OutputFcn.

```

```

% hObject    handle to figure
% eventdata reserved - to be defined in a future version of MATLAB
% handles    structure with handles and user data (see GUIDATA)
% varargin   command line arguments to cal (see VARARGIN)

% first plot calibration
handles.sam = varargin{1};
handles.conc = varargin{2};
handles.ion = varargin{3};
handles.bad = [];
handles.indx = [1:length(handles.conc)];
handles.indx = handles.indx(find(~isnan(handles.sam)));
% handles.table = [12.71,4.30,3.18,2.78,2.57,2.45,2.36,2.31,2.26,2.23,2.23,2.18,2.18,2.14];
plot(handles.conc(handles.indx),handles.sam(handles.indx),'r*');
set(gca, 'fontsize', 12);
xlabel('Concentration / \muM'); ylabel('Integration / \muSmin'); hold on; grid on;
title(['Calibration curve for ',handles.ion]);

% Now plot line of best fit
% first find moment correlation coefficient, r. goodness of fit.
xbar = mean(handles.conc(handles.indx));
ybar = mean(handles.sam(handles.indx));
sumxsq = 0; sumysq = 0; sumprod = 0;
for i = 1 : length(handles.indx)
    sumprod = sumprod + ((handles.conc(handles.indx(i))-xbar)*(handles.sam(handles.indx(i))-ybar));
    sumxsq = sumxsq + ((handles.conc(handles.indx(i))-xbar)^2);
    sumysq = sumysq + ((handles.sam(handles.indx(i))-ybar)^2);
end
handles.r = sumprod / sqrt(sumxsq*sumysq);
handles.sumxsq = sumxsq; handles.sumysq = sumysq; handles.ybar = ybar;
handles.xbar = xbar; handles.sumprod = sumprod;

% Use miller & miller: least squares fit to find slope and intercept
handles.slope = sumprod / sumxsq;
handles.intercept = ybar - handles.slope*xbar;

% Display this
plot(handles.conc,(handles.conc*handles.slope + handles.intercept));
set(handles.calculationtext,'string',['r = ',num2str(handles.r)]);
set(handles.atext,'string',['a = ',num2str(handles.slope)]);
set(handles.btext,'string',['b = ',num2str(handles.intercept)]);

% Use miller and miller to find limit of detection (error is in Y!!!)
calcd = handles.conc(handles.indx)*handles.slope + handles.intercept;
handles.yres = handles.sam(handles.indx)-calcd;
handles.degfreedom = length(handles.indx)-2;
handles.syonx = sqrt(sum(handles.yres.^2) / handles.degfreedom);
handles.stdslope = handles.syonx / sqrt(sumxsq);
handles.stdintercept = handles.syonx * sqrt((sum(handles.conc(handles.indx).^2))/...
    (length(handles.indx)*sumxsq));
% N.B. limit in y = intercept + syonx; BUT in x =((limy)-intercept)/slope
if handles.intercept >= 0
    handles.lim = (3*handles.syonx) / handles.slope;
else
    handles.lim = (3*handles.syonx - handles.intercept) / handles.slope;
end
set(handles.detlim,'string',['lim = ',num2str(handles.lim)]);

% Choose default command line output for cal
handles.output = hObject;

```

```

% Update handles structure
guidata(hObject, handles);

% UIWAIT makes cal wait for user response (see UIRESUME)
uiwait %(handles.figure1);

% --- Outputs from this function are returned to the command line.
function varargout = cal_OutputFcn(hObject, eventdata, handles)
% varargout cell array for returning output args (see VARARGOUT);
% hObject handle to figure
% eventdata reserved - to be defined in a future version of MATLAB
% handles structure with handles and user data (see GUIDATA)

% Get default command line output from handles structure
handles.array.indx = handles.output;
handles.array.slope = handles.slope;
handles.array.intercept = handles.intercept;
handles.array.r = handles.r;
handles.array.lim = handles.lim;
handles.array.xbar = handles.xbar;
handles.array.ybar = handles.ybar;
handles.array.sumxsq = handles.sumxsq;
handles.array.sumysq = handles.sumysq;
handles.array.sumprod = handles.sumprod;
handles.array.yres = handles.yres;
handles.array.degfreedom = handles.degfreedom;
handles.array.syonx = handles.syonx;
handles.array.stdslope = handles.stdslope;
handles.array.stdintercept = handles.stdintercept;
handles.array.n = length(handles.indx);

varargout{1} = handles.array;
% varargout{2} = handles.calib;
% varargout{3} = handles.r;
% varargout{4} = handles.lim;
% varargout{5} = handles.conf;
close

% --- Executes on button press in saveandexit.
function saveandexit_Callback(hObject, eventdata, handles)
% hObject handle to saveandexit (see GCBO)
% eventdata reserved - to be defined in a future version of MATLAB
% handles structure with handles and user data (see GUIDATA)

% saveas(gcf, 'cal.png', 'png')
handles.indx(handles.bad) = [];
handles.output = handles.indx;
guidata(hObject, handles);
uiresume;
% handles.output = handles.indx;
% close

% --- Executes on button press in recalculate.
function recalculate_Callback(hObject, eventdata, handles)
% hObject handle to recalculate (see GCBO)
% eventdata reserved - to be defined in a future version of MATLAB
% handles structure with handles and user data (see GUIDATA)
indx = handles.indx; indx(handles.bad) = [];
hold off;
plot(handles.conc(indx),handles.sam(indx),'r*'); set(gca, 'fontsize', 12);

```

```

xlabel('Concentration / \muM'); ylabel('Integration / \muSmin'); hold on; grid on;
title(['Calibration curve for ',handles.ion]);

% first find moment correlation coefficient, r. goodness of fit.
xbar = mean(handles.conc(indx));
ybar = mean(handles.sam(indx));
sumxsq = 0; sumysq = 0; sumprod = 0;
for i = 1 : length(indx)
    sumprod = sumprod + ((handles.conc(indx(i))-xbar)*(handles.sam(indx(i))-ybar));
    sumxsq = sumxsq + ((handles.conc(indx(i))-xbar)^2);
    sumysq = sumysq + ((handles.sam(indx(i))-ybar)^2);
end
handles.r = sumprod / sqrt(sumxsq*sumysq);
handles.sumxsq = sumxsq; handles.sumysq = sumysq; handles.ybar = ybar;
handles.xbar = xbar; handles.sumprod = sumprod;

% Use miller & miller: least squares fit to find slope and intercept
handles.slope = sumprod / sumxsq;
handles.intercept = ybar - handles.slope*xbar;

% Display this
plot(handles.conc,(handles.conc*handles.slope + handles.intercept));
set(handles.calculationtext,'string',['r = ',num2str(handles.r)]);
set(handles.atext,'string',['a = ',num2str(handles.slope)]);
set(handles.btext,'string',['b = ',num2str(handles.intercept)]);

% Use miller and miller to find limit of detection (error is in Y!!!)
calcd = handles.conc(handles.indx)*handles.slope + handles.intercept;
handles.yres = handles.sam(handles.indx)-calcd;
handles.degfreedom = length(handles.indx)-2;
handles.syonx = sqrt(sum(handles.yres.^2) / handles.degfreedom);
handles.stdslope = handles.syonx / sqrt(sumxsq);
handles.stdintercept = handles.syonx * sqrt((sum(handles.conc(handles.indx).^2))/...
    (length(handles.indx)*sumxsq));
if handles.intercept >= 0
    handles.lim = (3*handles.syonx) / handles.slope;
else
    handles.lim = (3*handles.syonx - handles.intercept) / handles.slope;
end
set(handles.detlim,'string',['lim = ',num2str(handles.lim)]);

guidata(hObject, handles);

% --- Executes on button press in removepoint.
function removepoint_Callback(hObject, eventdata, handles)
% hObject    handle to removepoint (see GCBO)
% eventdata  reserved - to be defined in a future version of MATLAB
% handles    structure with handles and user data (see GUIDATA)

dcm_obj = datacursormode(gcf);
set(dcm_obj,'enable','on','snaptovertex','off'); %
infostruct = [];
while isempty(infostruct)
    pause(0.5)
    infostruct=getCursorInfo(dcm_obj);
end
% while isempty(get(gcf,'CurrentCharacter'))
%     infostruct = getCursorInfo(dcm_obj);
%     handles.bad = [handles.bad infostruct.DataIndex];
% end
set(dcm_obj,'enable','off')

```

```

delete(findall(gca,'type','hgggroup','marker','square'))
handles.bad = [handles.bad infostruct.DataIndex];
plot(handles.conc(handles.indx(handles.bad)),handles.sam(handles.indx(handles.bad)), 'g*');

guidata(hObject, handles);

% --- Executes on button press in Reset.
function Reset_Callback(hObject, eventdata, handles)
% hObject    handle to Reset (see GCBO)
% eventdata  reserved - to be defined in a future version of MATLAB
% handles    structure with handles and user data (see GUIDATA)

handles.indx = [1:length(handles.conc)]; handles.bad = [];
handles.indx = handles.indx(find(~isnan(handles.sam)));
hold off; plot(handles.conc(handles.indx),handles.sam(handles.indx),'r*'); set(gca, 'fontsize', 12);
xlabel('Concentration / \muM'); ylabel('Integration / \muSmin'); hold on; grid on;
title(['Calibration curve for ',handles.ion]);

% then calculate as before...
xbar = mean(handles.conc(handles.indx));
ybar = mean(handles.sam(handles.indx));
sumxsq = 0; sumysq = 0; sumprod = 0;
for i = 1 : length(handles.indx)
    sumprod = sumprod + ((handles.conc(handles.indx(i))-xbar)*(handles.sam(handles.indx(i))-ybar));
    sumxsq = sumxsq + ((handles.conc(handles.indx(i))-xbar)^2);
    sumysq = sumysq + ((handles.sam(handles.indx(i))-ybar)^2);
end
handles.r = sumprod / sqrt(sumxsq*sumysq);
handles.sumxsq = sumxsq; handles.sumysq = sumysq; handles.ybar = ybar;
handles.xbar = xbar; handles.sumprod = sumprod;
handles.slope = sumprod / sumxsq;
handles.intercept = ybar - handles.slope*xbar;
plot(handles.conc,(handles.conc*handles.slope + handles.intercept));
set(handles.calculationtext,'string',['r = ',num2str(handles.r)]);
set(handles.atext,'string',['a = ',num2str(handles.slope)]);
set(handles.btext,'string',['b = ',num2str(handles.intercept)]);
calcd = handles.conc(handles.indx)*handles.slope + handles.intercept;
handles.yres = handles.sam(handles.indx)-calcd;
handles.degfreedom = length(handles.indx)-2;
handles.syonx = sqrt(sum(handles.yres.^2) / handles.degfreedom);
handles.stdslope = handles.syonx / sqrt(sumxsq);
handles.stdintercept = handles.syonx * sqrt((sum(handles.conc(handles.indx).^2)/...
    (length(handles.indx)*sumxsq)));
if handles.intercept >= 0
    handles.lim = (3*handles.syonx) / handles.slope;
else
    handles.lim = (3*handles.syonx - handles.intercept) / handles.slope;
end
set(handles.detlim,'string',['lim = ',num2str(handles.lim)]);
guidata(hObject, handles);

```

E.2 Conc.m

Used to find sample concentrations once cal.m has been used.

```

function [c err flag] = conc(signal, cal)
% [c err flag] = conc(signal, calibration)

```

```
%
% calculate the concentration and standard error of some signal data given
% the calibration data from cal.m and flag all values below detection limit
%
% these are calculated by:
% Concentration = (measured signal - intercept) / slope)
% Standard error = (syonx/slope) * sqrt(1 + (1/n) + ...
%                 ((meas-ybar)^2 / (slope^2 * sumxsq^2)))
% for more info see Miller & Miller
%
% N.B. The calibration array MUST contain the following structure:
%   calibration.slope
%   calibration.intercept
%   calibration.ybar
%   calibration.n
%   calibration.lim
%   calibration.syonx
%   calibration.sumxsq
%
% cfp 19 Sep 07 N.B. changed 06 Jun 08

% concentration
c = (signal - cal.intercept)./ cal.slope;

% standard error
err = (cal.syonx/cal.slope) * sqrt(1 + (1/cal.n) + ...
    ((signal-cal.ybar).^2 ./ (cal.slope^2*cal.sumxsq^2)));

% flag all values below the detection limit.
flag = cell(length(c),1);
flag(c<=cal.lim) = {'d'};

% change these values to 75% of the detection limit...
c(c<=cal.lim) = 0.75*cal.lim;

% therefore the std error also changes...
err(c<=cal.lim) = nan;

return
```

E.3 Driftconc.m

Corrects sample concentrations for instrumental drift by interpolating between calibrations.

```
function [conc err f dl] = driftcorrection(conc1,conc2,err1,err2,d1,d2,l1,l2);
%[conc err flag detlim] = ...
%   driftcorrection(conc1,conc2,err1,err2,dist1,dist2,lim1,lim2);
%
% conc1 - concentrations from calibration 1
% conc2 - concentrations from calibration 2
% err1 - standard errors from calibration 1
% err2 - standard errors from calibration 2
% dist1 - distance of first conc from last point of 1st calibration
% dist2 - distance of last conc from first point of 2nd calibration
% lim1 - detection limit for 1st calibration
% lim2 - detection limit for 2nd calibration
%
```

```

% cfp 9 Jun 08
%
% first check all the vectors are equal
if length(conc1)~=length(conc2) | length(err1)~=length(err2)
    error('The length of conc1 and err1 MUST equal that of conc2 and err1');
end

% make up an index
total = d1 + length(conc1) - 1 + d2;
i1 = (total - [d1 : 1 : d1 + length(conc1) - 1]) ./ total;
i2 = (total - [d2 + length(conc2) - 1 : -1 : d2]) ./ total;

% find drift corrected concentration
conc = i1 .* conc1 + i2 .* conc2;

% find stderr
err = sqrt( (i1.*err1).^2 + (i2.*err2).^2 );

% set up flags
f = cell(length(conc),1);

% concentrations below detection limit in cal1 only...
conc((conc1<l1)&(conc2>l2)) = conc2((conc1<l1)&(conc2>l2));
err((conc1<l1)&(conc2>l2)) = err2((conc1<l1)&(conc2>l2));
f((conc1<l1)&(conc2>l2)) = {'c'};

% concentrations below detection limit in cal2 only...
conc((conc1>l1)&(conc2<l2)) = conc1((conc1>l1)&(conc2<l2));
err((conc1>l1)&(conc2<l2)) = err1((conc1>l1)&(conc2<l2));
f((conc1>l1)&(conc2<l2)) = {'c'};

% concentrations below detection limit (already changed to 0.75*d1)
f((conc1<l1)&(conc2<l2)) = {'d'};

% find detection limit function
dl = i1*l1 + i2*l2;
dl((conc1<l1)&(conc2>l2)) = l2;
dl((conc1>l1)&(conc2<l2)) = l1;

return

```

E.4 Molar.m

Used to find sample molar concentrations from the sample concentration an extract volume.

```

function [molconc molerr] = molar(conc, err, extvol)
% [molarconc molarerr] = molar(conc,err,extractvolume);
%
% find the molar concentration on each filter from the concentration of
% extract and the volume of extract. Also finds the propagated standard
% error from the standard error in the concentration.
%
% N.B. Extract Volume MUST be in ml
%
% Uses:
%     Molarconcentration = Concentration * 4 * ExtractVolume

```

```
%  
% cfp 20 September 2007  
%  
  
% change units of extvol from ml to l  
extvol = extvol/1000;  
  
% first find the molar concentration:  
molconc = conc * 4 * extvol;  
  
% now find the propagated error:  
molerr = err * 4 * extvol;
```

E.5 Dblanks.m

Used to establish which procedural blanks are significant and then subtract this from the sample molar amounts.

```
function varargout = dblanks(varargin)  
% [blankcorr, correrr] = dblanks(blankconc,blankerr,blanklabel,ionlabel,lim)  
%  
% a function to plot dblanks for an instrument and calculate the blank  
% correction number from  
%  
% INPUT    blankconc  array of molar concentrations of blanks  
%          blankerr   array with corresponding std. errors  
%          blanklabel array containing the labels for each blank  
%          ion label  names of the ions in array - e.g. [fe,zn,al,mn,v]  
%          lim        molar concentration detection limit for each ion  
%  
% OUTPUT   blankcorr  a value for the blank correction for each ion type  
%          correrr    corresponding error in this calculation  
%  
% What happens is that the blanks are plotted on a bar chart, grouped by  
% ion type. Detection limit should also be plotted. User must decide if  
% there are any outliers for each ion and if so these can be selected and  
% deleted. The blank correction is the worked out by averaging the blank  
% values. If all blanks are below the detection limit blank correction = 0,  
% or if only some of the blanks are below the detection limit the blank  
% correction is calculated as the average value, taking those value below  
% the detection limit as 0.75*detection limit, rather than the detected  
% value...  
%  
% cfp 29 Apr 2007  
  
% initialize data array  
[a b] = size(varargin{1});  
array = zeros(a,b);  
  
for i = 1 : b  
array(:,i) = [varargin{1}(:,i)];  
end  
  
% do the same for the error array and limit array  
[c d] = size(varargin{2});  
[e f] = size(varargin{5});  
if (a==c & b==d & a==e & b==f)==0
```

```

        error('ERROR: data array and error array are not the same size!');
    end
    errors = zeros(a,b);
    limit = zeros(a,b);
    for i = 1 : b
        errors(:,i) = [varargin{2}(:,i)];
        limit(:,i) = [varargin{5}(:,i)];
    end
    %plot up all the data...
    fig = figure;
    bar(array','grouped'); hold on;
    legend(varargin{3});
    set(gca,'XTickLabel',varargin{4});
    title('blank concentrations');ylabel('Molar Concentrations');xlabel('Ion');

    % put in limits
    for i = 1 : b
        eval(['plot',num2str(i),' = plot([0:(b+1)/(a-1):b+1],[limit(:,i)],'k');']);
        text(i,varargin{5}(1,i),varargin{4}(i))
    end

    % now the analysis starts...
    % set up an 'index array'
    arr = (zeros(a,b));
    for i = 1 : b
        next = 'y';
        while next == 'y'
            next = input(['Are there any (more) outliers in the ',...
                varargin{4}{i},' blanks? (y/n)'], 's');
        % select outliers for each ion...
        if next == 'y'
            dcm_obj = datacursormode(gcf);
            set(dcm_obj,'enable','on','snaptodatavertex','on'); %
            infostruct = [];
            while isempty(infostruct)
                pause(0.5)
                infostruct=getCursorInfo(dcm_obj);
            end
            set(dcm_obj,'enable','off');
            ind = find(strcmp(varargin{3},get(infostruct.Target,...
                'DisplayName')));
            arr(ind,i) = 1;
            delete(findall(gca,'type','hgroup','marker','square'))
        % make sure bad point is marked on the plot...
            text(infostruct.Position(1),infostruct.Position(2),'OUTLIER')
        end
    end
end

% save figure
saveas(fig,'blanks.png','png');

% take out outliers from main array
array(find(arr==1))=NaN;
% do not include zero blanks...
array(find(array==0))=NaN;
% make error array the same...
errors(find(isnan(array))) = NaN;
% make sure that all underlimit blanks are made 0.75 * dl
array(array<limit) = 0.75 * limit(array<limit);
errors(array<limit) = nan;

```

```
% now work out correction and error
for i = 1 : b
    if isempty(find(array(:,i)>=limit(:,i)))
        varargout{1}(i) = 0;
        varargout{2}(i) = 0;
    else
        varargout{1}(i) = nanmean(array(:,i));
        stderr = nanstd(array(:,i));
        properr = sqrt(nansum(errors(:,i).^2));
        if stderr>=properr
            varargout{2}(i) = stderr;
        else
            varargout{2}(i) = properr;
            warning(['propagated error used for ',varargin{4}{i}]);
        end
    end
end
end
```

E.6 Atmospheric.m

Used to find sample atmospheric concentrations.

```
function[atmconc atmerr] = atmospheric(amnt,amnterr,airvol)
% [atmconc atmerr] = atmospheric(amnt,amnterr,airvol)
%
% calculate the atmospheric concentration (atmconc) and standard error
% (atmerr) from the molar amount an filter (amnt) its error (amnterr) and
% the air volume drawn through the filter (airvol)
%
% uses atmconc = amnt ./ airvol * 1000
%
% Assumes that there is no error in the airvolume therefore the atmerr is
% scaled up from the amnterr
%
% cfp 24 Sep 2007

atmconc = amnt ./ airvol .* 1000;
atmerr = amnterr ./airvol .* 1000;
```

E.7 Climatology.m

Used for all calcaultions made for the climatology

```
function[atmconc atmerr] = atmospheric(amnt,amnterr,airvol)
% [atmconc atmerr] = atmospheric(amnt,amnterr,airvol)
%
% calculate the atmospheric concentration (atmconc) and standard error
% (atmerr) from the molar amount an filter (amnt) its error (amnterr) and
% the air volume drawn through the filter (airvol)
%
% uses atmconc = amnt ./ airvol * 1000
%
% Assumes that there is no error in the airvolume therefore the atmerr is
```

```
% scaled up from the amnterr
%
% cfp 24 Sep 2007

atmconc = amnt ./ airvol .* 1000;
atmerr = amnterr ./airvol .* 1000;
```

Bibliography

- Aguilar-Islas, A. M., J. Wu, R. Rember, A. M. Johansen, and L. M. Shank (2010), Dissolution of aerosol-derived iron in seawater: Leach solution chemistry, aerosol type, and colloidal iron fraction, *Marine Chemistry, In Press, Corrected Proof*, doi:10.1016/j.marchem.2009.01.011.
- Alastuey, A., X. Querol, S. Castillo, M. Escudero, A. Avila, E. Cuevas, C. Torres, P. Romero, F. Exposito, O. García, J. P. Diaz, R. V. Dingenen, and J. P. Putaud (2005), Characterisation of TSP and PM_{2.5} at izaña and sta. cruz de tenerife (Canary islands, spain) during a saharan dust episode (July 2002), *Atmospheric Environment*, 39(26), 4715–4728, doi:10.1016/j.atmosenv.2005.04.018.
- Albarède, F. (2003), *Geochemistry: an introduction*, Cambridge University Press.
- Anderson, L., K. Faul, and A. Paytan (2010), Phosphorus associations in aerosols: What can they tell us about p bioavailability?, *Marine Chemistry*, 120(1-4), 44–56, doi:10.1016/j.marchem.2009.04.008.
- Andreae, M. O. (1983), Soot carbon and excess fine potassium: Long-Range transport of Combustion-Derived aerosols, *Science*, 220(4602), 1148–1151, doi:10.1126/science.220.4602.1148.
- Andreae, M. O., and P. J. Crutzen (1997), Atmospheric aerosols: Biogeochemical sources and role in atmospheric chemistry, *Science*, 276(5315), 1052–1058, doi:10.1126/science.276.5315.1052.
- Andrews, J. E., P. Brimblecombe, T. D. Jickells, P. S. Liss, and B. Reid (2003), *An Introduction to Environmental Chemistry*, 2nd edition ed., Wiley-Blackwell.
- Arimoto, R., and R. A. Duce (1986), Dry deposition models and the Air/Sea exchange of trace elements, *Journal of Geophysical Research*, 91(D2), 2787–2792.
- Arimoto, R., R. A. Duce, B. J. Ray, W. G. E. Jr, J. D. Cullen, and J. T. Merrill (1995), Trace elements in the atmosphere over the north atlantic, *Journal of Geophysical Research*, 100(D1), PAGES 1199–1213.

- Arimoto, R., R. A. Duce, B. J. Ray, and U. Tomza (2003), Dry deposition of trace elements to the western north atlantic, *Global Biogeochemical Cycles*, 17(1), 1010, doi:10.1029/2001GB001406.
- Artaxo, P., H. Storms, F. Bruynseels, R. Van Grieken, and W. Maenhaut (1988), Composition and sources of aerosols from the amazon basin, *Journal of Geophysical Research*, 93(D2), PAGES 1605–1615.
- Baker, A., and P. Croot (2010), Atmospheric and marine controls on aerosol iron solubility in seawater, *Marine Chemistry*, 120(1-4), 4–13, doi:10.1016/j.marchem.2008.09.003.
- Baker, A., M. French, and K. Linge (2006a), Trends in aerosol nutrient solubility along a west-east transect of the saharan dust plume, *Geophysical Research Letters*, 33(7).
- Baker, A., T. Jickells, K. Biswas, K. Weston, and M. French (2006b), Nutrients in atmospheric aerosol particles along the atlantic meridional transect, *Deep Sea Research Part II: Topical Studies in Oceanography*, 53(14-16), 1706–1719, doi:10.1016/j.dsr2.2006.05.012.
- Baker, A., T. Jickells, M. Witt, and K. Linge (2006c), Trends in the solubility of iron, aluminium, manganese and phosphorus in aerosol collected over the atlantic ocean, *Marine Chemistry*, 98(1), 43–58, doi:10.1016/j.marchem.2005.06.004.
- Baker, A., K. Weston, S. Kelly, M. Voss, P. Streu, and J. Cape (2007), Dry and wet deposition of nutrients from the tropical atlantic atmosphere: Links to primary productivity and nitrogen fixation, *Deep Sea Research Part I: Oceanographic Research Papers*, 54(10), 1704–1720, doi:10.1016/j.dsr.2007.07.001.
- Baker, A. R., and T. D. Jickells (2006), Mineral particle size as a control on aerosol iron solubility, *Geophysical Research Letters*.
- Baker, A. R., S. D. Kelly, K. F. Biswas, M. Witt, and T. D. Jickells (2003), Atmospheric deposition of nutrients to the atlantic ocean, *Geophysical Research Letters*, 30, 4 PP., doi:200310.1029/2003GL018518.
- Baker, A. R., T. Lesworth, C. Adams, T. D. Jickells, and L. Ganzeveld (2010), Estimation of atmospheric nutrient inputs to the atlantic ocean from 50°N to 50°S based on large-scale field sampling: Fixed nitrogen and dry deposition of phosphorus, *Global Biogeochemical Cycles*, 24, 16 PP., doi:201010.1029/2009GB003634.
- Bao, H., S. Yu, and D. Q. Tong (2010), Massive volcanic SO₂ oxidation and sulphate aerosol deposition in cenozoic north america, *Nature*, 465(7300), 909–912, doi:10.1038/nature09100.
- Bell, T., G. Malin, C. McKee, and P. Liss (2006), A comparison of dimethylsulphide (DMS) data from the atlantic meridional transect (AMT) programme with proposed

- algorithms for global surface DMS concentrations, *Deep Sea Research Part II: Topical Studies in Oceanography*, 53(14-16), 1720–1735, doi:10.1016/j.dsr2.2006.05.013.
- Benitez-Nelson, C. (2000), The biogeochemical cycling of phosphorus in marine systems, *Earth Science Reviews*, 51(1-4), 109–135.
- Bennett, S., E. Achterberg, D. Connelly, P. Statham, G. Fones, and C. German (2008), The distribution and stabilisation of dissolved Fe in deep-sea hydrothermal plumes, *Earth and Planetary Science Letters*, 270(3-4), 157–167.
- Bergametti, G., L. Gomes, G. Coude-Gaussen, P. Rognon, and M. L. Coustumer (1989), African dust observed over canary islands: Source-Regions identification and transport pattern for some summer situations, *Journal of Geophysical Research*, 94(D12), 864.
- Bergametti, G., E. Remoudaki, R. Losno, E. Steiner, B. Chatenet, and P. Buat-Menard (1992), Source, transport and deposition of atmospheric phosphorus over the northwestern mediterranean, *Journal of Atmospheric Chemistry*, 14(1), 501–513, doi:10.1007/BF00115254.
- Berman-Frank, I., J. T. Cullen, Y. Shaked, R. M. Sherrell, and P. G. Falkowski (2001), Iron availability, cellular iron quotas, and nitrogen fixation in trichodesmium, *Limnology and Oceanography*, 46(6), 1249–1260, doi:10.4319/lo.2001.46.6.1249.
- Bertilsson, S., O. Berglund, D. M. Karl, and S. W. Chisholm (2003), Elemental composition of marine prochlorococcus and synechococcus: Implications for the ecological stoichiometry of the sea, *Limnology and Oceanography*, 48(5), 1721–1731, doi:10.4319/lo.2003.48.5.1721.
- Boyd, P. W., T. Jickells, C. S. Law, S. Blain, E. A. Boyle, K. O. Buesseler, K. H. Coale, J. J. Cullen, H. J. W. de Baar, M. Follows, M. Harvey, C. Lancelot, M. Levasseur, N. P. J. Owens, R. Pollard, R. B. Rivkin, J. Sarmiento, V. Schoemann, V. Smetacek, S. Takeda, A. Tsuda, S. Turner, and A. J. Watson (2007), Mesoscale iron enrichment experiments 1993-2005: Synthesis and future directions, *Science*, 315(5812), 612–617, doi:10.1126/science.1131669.
- Broecker, W. S., and T. Peng (1982), *Tracers in the sea*, Eldigo Press.
- Buck, C. S., W. M. Landing, and J. A. Resing (2010), Particle size and aerosol iron solubility: A high-resolution analysis of atlantic aerosols, *Marine Chemistry*, 120(1-4), 14–24, doi:doi:10.1016/j.marchem.2008.11.002.
- Cape, J., A. Kirika, A. Rowland, D. Wilson, T. Jickells, and S. Cornell (2001), Organic nitrogen in precipitation: Real problem or sampling artefact?, *TheScientificWorld*, 1(s2), 230–237, doi:10.1100/tsw.2001.278.

- Castillo, S., T. Moreno, X. Querol, A. Alastuey, E. Cuevas, L. Herrmann, M. Mounkaila, and W. Gibbons (2008), Trace element variation in size-fractionated african desert dusts, *Journal of Arid Environments*, *72*(6), 1034–1045, doi:10.1016/j.jaridenv.2007.12.007.
- Chiapello, I., G. Bergametti, L. Gomes, B. Chatenet, F. Dulac, J. Pimenta, and E. S. Soares (1995), An additional low layer transport of sahelian and saharan dust over the north-eastern tropical atlantic, *Geophysical Research Letters*, *22*(23), PAGES 3191–3194.
- Chiapello, I., G. Bergametti, B. Chatenet, P. Bousquet, F. Dulac, and E. S. Soares (1997), Origins of african dust transported over the northeastern tropical atlantic, *Journal of Geophysical Research*, *102*(D12), 13,701–13,709, doi:10.1029/97JD00259.
- Chiapello, I., G. Bergametti, B. Chatenet, F. Dulac, I. Jankowiak, C. Liousse, E. S. Soares, and C. Liousse (1999), Contribution of the different aerosol species to the aerosol mass load and optical depth over the northeastern tropical atlantic, *Journal of Geophysical Research*, *104*(D4), PAGES 4025–4035.
- Chiapello, I., C. Moulin, and J. M. Prospero (2005), Understanding the long-term variability of african dust transport across the atlantic as recorded in both barbados surface concentrations and large-scale total ozone mapping spectrometer (TOMS) optical thickness, *Journal of Geophysical Research*, *110*, 9 PP., doi:200510.1029/2004JD005132.
- Cooke, W. F., B. Koffi, and J. Grégoire (1996), Seasonality of vegetation fires in africa from remote sensing data and application to a global chemistry model, *Journal of Geophysical Research*, *101*(D15), 065.
- Cornell, S., T. D. Jickells, J. Cape, A. Rowland, and R. A. Duce (2003), Organic nitrogen deposition on land and coastal environments: a review of methods and data, *Atmospheric Environment*, *37*(16), 2173–2191, doi:10.1016/S1352-2310(03)00133-X.
- Croot, P. L., P. Streu, and A. R. Baker (2004), Short residence time for iron in surface seawater impacted by atmospheric dry deposition from saharan dust events, *Geophysical Research Letters*, *31*, 4 PP., doi:200410.1029/2004GL020153.
- Crutzen, P. J., and M. O. Andreae (1990), Biomass burning in the tropics: Impact on atmospheric chemistry and biogeochemical cycles, *Science*, *250*(4988), 1669–1678, doi:10.1126/science.250.4988.1669.
- Delon, C., C. Galy-Lacaux, A. Boone, C. Liousse, D. Serça, M. Adon, B. Diop, A. Akpo, F. Lavenu, E. Mougouin, and F. Timouk (2010), Atmospheric nitrogen budget in sahelian dry savannas, *Atmospheric Chemistry and Physics*, *10*(6), 2691–2708.

- DeMott, P. J., K. Sassen, M. R. Poellot, D. Baumgardner, D. C. Rogers, A. J. P. Sarah D. Brooks, and S. M. Kreidenweis (2003), African dust aerosols as atmospheric ice nuclei, *Geophysical Research Letters*, *30*(14), 1732, doi:10.1029/2003GL017410.
- Desboeufs, K. V., R. Losno, F. Vimeux, and S. Cholbi (1999), The pH-dependent dissolution of wind-transported saharan dust, *Journal of Geophysical Research*, *104*(D17), PP. 21,287–21,299, doi:199910.1029/1999JD900236.
- Desboeufs, K. V., A. Sofikitis, R. Losno, J. L. Colin, and P. Ausset (2005), Dissolution and solubility of trace metals from natural and anthropogenic aerosol particulate matter, *Chemosphere*, *58*(2), 195–203, doi:10.1016/j.chemosphere.2004.02.025.
- Deutsch, C., J. L. Sarmiento, D. M. Sigman, N. Gruber, and J. P. Dunne (2007), Spatial coupling of nitrogen inputs and losses in the ocean, *Nature*, *445*(7124), 163–167, doi:10.1038/nature05392.
- Draxler, R. R., and G. D. Rolph (2003), HYSPLIT (Hybrid Single-Particle lagrangian integrated trajectory) model, <http://www.arl.noaa.gov/ready/hysplit4.html>.
- Duce, R., and N. Tindale (1991), Atmospheric transport of iron and its deposition in the ocean, *Limnology & Oceanography*, *36*(8), 1715–1726.
- Duce, R. A., J. LaRoche, K. Altieri, K. R. Arrigo, A. R. Baker, D. G. Capone, S. Cornell, F. Dentener, J. Galloway, R. S. Ganeshram, R. J. Geider, T. Jickells, M. M. Kuypers, R. Langlois, P. S. Liss, S. M. Liu, J. J. Middelburg, C. M. Moore, S. Nickovic, A. Oschlies, T. Pedersen, J. Prospero, R. Schlitzer, S. Seitzinger, L. L. Sorensen, M. Uematsu, O. Ulloa, M. Voss, B. Ward, and L. Zamora (2008), Impacts of atmospheric anthropogenic nitrogen on the open ocean, *Science*, *320*(5878), 893–897, doi:10.1126/science.1150369.
- Dulac, F., P. Buat-Menard, U. Ezat, S. Melki, and G. Bergametti (1989), Atmospheric input of trace metals to the western mediterranean: uncertainties in modelling dry deposition from cascade impactor data, *Tellus, Series B*, *41 B*(3), 362–378.
- ECMWF (2006), European centre for Medium-Range weather forecasts. operational analysis data, [Internet], available from <http://badc.nerc.ac.uk/data/ecmwf-op/>, *British Atmospheric Data Centre*.
- ECMWF (2010), ERA interim data, http://data-portal.ecmwf.int/data/d/interim_daily/.
- Falkowski, P. G. (1997), Evolution of the nitrogen cycle and its influence on the biological sequestration of CO₂ in the ocean, *Nature*, *387*(6630), 272–275, doi:10.1038/387272a0.
- Falkowski, P. G., R. T. Barber, and V. Smetacek (1998), Biogeochemical controls and feedbacks on ocean primary production, *Science*, *281*(5374), 200–206, doi:10.1126/science.281.5374.200.

- Farhana, B. K. (2005), Study on inorganic halogens and other related ions in the lower atmospheric aerosols, Ph.D., Univeristy of East Anglia, Norwich, UK.
- Formenti, P., J. Rajot, K. Desboeufs, S. Caquineau, S. Chevaillier, S. Nava, A. Gaudichet, E. Journet, S. Triquet, S. Alfaro, M. Chiari, J. Haywood, H. Coe, and E. Highwood (2008), Regional variability of the composition of mineral dust from western africa: Results from the AMMA SOP0/DABEX and DODO field campaigns, *Journal of Geophysical Research D: Atmospheres*, 113(23).
- Galloway, J., D. Savoie, W. Keene, and J. Prospero (1993), The temporal and spatial variability of scavenging ratios for NSS sulfate, nitrate, methanesulfonate and sodium in the atmosphere over the north atlantic ocean, *Atmospheric Environment - Part A General Topics*, 27 A(2), 235–250.
- Galloway, J. N., A. R. Townsend, J. W. Erisman, M. Bekunda, Z. Cai, J. R. Freney, L. A. Martinelli, S. P. Seitzinger, and M. A. Sutton (2008), Transformation of the nitrogen cycle: Recent trends, questions, and potential solutions, *Science*, 320(5878), 889–892, doi:10.1126/science.1136674.
- Ganzeveld, L., J. Lelieveld, and G. Roelofs (1998), A dry deposition parameterization for sulfur oxides in a chemistry and general circulation model, *Journal of Geophysical Research*, 103(D5), PP. 5679–5694, doi:199810.1029/97JD03077.
- Graham, W., and R. Duce (1979), Atmospheric pathways of the phosphorus cycle, *Geochimica et Cosmochimica Acta*, 43(8), 1195–1208.
- Greenwood, N., and A. Earnshaw (1997), *Chemistry of the Elements*, 2 ed., A Butterworth-Heinemann Title.
- Guieu, C., S. Bonnet, T. Wagener, and M. Loÿe-Pilot (2005), Biomass burning as a source of dissolved iron to the open ocean?, *Geophysical Research Letters*, 32(19), 1–5.
- Guieu, C., M. Loÿe-Pilot, L. Benyahya, and A. Dufour (2010), Spatial variability of atmospheric fluxes of metals (Al, fe, cd, zn and pb) and phosphorus over the whole mediterranean from a one-year monitoring experiment: Biogeochemical implications, *Marine Chemistry*, 120(1-4), 164–178, doi:10.1016/j.marchem.2009.02.004.
- Helsel, D. R., and R. M. Hirsch (2005), *Statistical Methods in Water Resources*, vol. Book 4, U.S. Geological Survey.
- Hopkinson, C., L. Cifuentes, D. Burdige, S. Fitzwater, D. Hansell, S. Henrichs, P. Kähler, I. Koike, T. Walsh, and B. Bergamaschi (1993), DON subgroup report, *Marine Chemistry*, 41(1-3), 23–36, doi:10.1016/0304-4203(93)90103-U.
- Huang, J., C. Zhang, and J. M. Prospero (2009a), African aerosol and large-scale precipitation variability over west africa, *Environmental Research Letters*, 4(1), 015,006, doi:10.1088/1748-9326/4/1/015006.

- Huang, J., C. Zhang, and J. M. Prospero (2009b), Large-scale effect of aerosols on precipitation in the west african monsoon region, *Quarterly Journal of the Royal Meteorological Society*, *135*(640), 581–594, doi:10.1002/qj.391.
- Hummelshøj, P., N. O. Jensen, and S. E. Larsen (1992), Particle dry deposition to a sea surface, in *Precipitation Scavenging and Atmosphere-Surface Exchange*, edited by S. E. Schwartz and W. Slinn, pp. 547–550, Hemisphere Publ. Corp., Washington, USA.
- Jickells, T., S. Kelly, A. Baker, K. Biswas, P. Dennis, L. Spokes, M. Witt, and S. Yeatman (2003), Isotopic evidence for a marine ammonia source, *Geophysical Research Letters*, *30*(7), 27–1.
- Jickells, T. D., and L. J. Spokes (2001), Atmospheric iron inputs to the oceans, in *The Biogeochemistry of Iron in Seawater*, edited by D. R. Turner and K. A. Hunter, IUPAC Series on Analytical and Physical Chemistry of Environmental Systems, pp. 85–122, WileyBlackwell.
- Jickells, T. D., Z. S. An, K. K. Andersen, A. R. Baker, G. Bergametti, N. Brooks, J. J. Cao, P. W. Boyd, R. A. Duce, K. A. Hunter, H. Kawahata, N. Kubilay, J. laRoche, P. S. Liss, N. Mahowald, J. M. Prospero, A. J. Ridgwell, I. Tegen, and R. Torres (2005), Global iron connections between desert dust, ocean biogeochemistry, and climate, *Science*, *308*(5718), 67–71, doi:10.1126/science.1105959.
- Johnson, M. T., P. S. Liss, T. G. Bell, T. J. Lesworth, A. R. Baker, A. J. Hind, T. D. Jickells, K. F. Biswas, E. M. S. Woodward, and S. W. Gibb (2008), Field observations of the ocean-atmosphere exchange of ammonia: Fundamental importance of temperature as revealed by a comparison of high and low latitudes, *Global Biogeochemical Cycles*, *22*, 15 PP., doi:200810.1029/2007GB003039.
- Journet, E., K. V. Desboeufs, S. Caquineau, and J. Colin (2008), Mineralogy as a critical factor of dust iron solubility, *Geophysical Research Letters*, *35*, L07,805, doi:10.1029/2007GL031589.
- Kane, M., A. Rendell, and T. Jickells (1994), Atmospheric scavenging processes over the north sea, *Atmospheric Environment*, *28*(15), 2523–2530.
- Kaufman, Y. J., I. Koren, L. A. Remer, D. Tanré, P. Ginoux, and S. Fan (2005), Dust transport and deposition observed from the Terra-Moderate resolution imaging spectroradiometer (MODIS) spacecraft over the atlantic ocean, *Journal of Geophysical Research*, *110*, D10S12, doi:10.1029/2003JD004436.
- Kebbekus, B., and S. Mitra (1997), *Environmental Chemical Analysis*, 1 ed., CRC Press.
- Keene, W. C., A. A. P. Pszenny, J. N. Galloway, and M. E. Hawley (1986), Sea-Salt corrections and interpretation of constituent ratios in marine precipitation, *Journal of Geophysical Research*, *91*(D6), PAGES 6647–6658.

- Keene, W. C., A. A. P. Pszenny, D. J. Jacob, R. A. Duce, J. N. Galloway, J. J. Schultz-Tokos, H. Sievering, and J. F. Boatman (1990), The geochemical cycling of reactive chlorine through the marine troposphere, *Global Biogeochemical Cycles*, 4(4), PP. 407–430, doi:199010.1029/GB004i004p00407.
- Keene, W. C., R. Sander, A. A. P. Pszenny, R. Vogt, P. J. Crutzen, and J. N. Galloway (1998), Aerosol pH in the marine boundary layer: a review and model evaluation, *Journal of Aerosol Science*, 29(3), 339–356, doi:10.1016/S0021-8502(97)10011-8.
- Keene, W. C., M. S. Long, A. A. P. Pszenny, R. Sander, J. R. Maben, A. J. Wall, T. L. O'Halloran, A. Kerkweg, E. V. Fischer, and O. Schrems (2009), Latitudinal variation in the multiphase chemical processing of inorganic halogens and related species over the eastern north and south atlantic oceans, *Atmos. Chem. Phys.*, 9(19), 7361–7385.
- Krishnamurthy, A., J. K. Moore, N. Mahowald, C. Luo, and C. S. Zender (2010), Impacts of atmospheric nutrient inputs on marine biogeochemistry, *Journal of Geophysical Research*, 115, 13 PP., doi:201010.1029/2009JG001115.
- Kump, L. R., J. F. Kasting, and R. G. Crane (2004), *The earth system*, Pearson Prentice Hall.
- Langmann, B., B. Duncan, C. Textor, J. Trentmann, and G. R. van der Werf (2009), Vegetation fire emissions and their impact on air pollution and climate, *Atmospheric Environment*, 43(1), 107–116, doi:10.1016/j.atmosenv.2008.09.047.
- Lenton, T. M., and A. J. Watson (2000), Redfield revisited: 2. what regulates the oxygen content of the atmosphere?, *Global Biogeochemical Cycles*, 14(1), PP. 249–268, doi:200010.1029/1999GB900076.
- Lewis, E. R., and S. E. Schwartz (2004), *Sea salt aerosol production: mechanisms, methods, measurements and models : a critical review*, American Geophysical Union.
- Libes, S. M. (1992), *An Introduction to Marine Biogeochemistry*, 1 ed., Wiley.
- Liu, X., and F. Millero (2002), The solubility of iron in seawater, *Marine Chemistry*, 77(1), 43–54.
- Longhurst, A., S. Sathyendranath, T. Platt, and C. Caverhill (1995), An estimate of global primary production in the ocean from satellite radiometer data, *Journal of Plankton Research*, 17(6), 1245–1271.
- Luo, C., N. Mahowald, N. Meskhidze, Y. Chen, R. Siefert, A. Baker, and A. Johansen (2005), Estimation of iron solubility from observations and a global aerosol model, *Journal of Geophysical Research D: Atmospheres*, 110(23), 1–23.

- Luo, C., N. Mahowald, T. Bond, P. Y. Chuang, P. Artaxo, R. Siefert, Y. Chen, and J. Schauer (2008), Combustion iron distribution and deposition, *Global Biogeochemical Cycles*, *22*, GB1012, doi:10.1029/2007GB002964.
- Mahaffey, C., A. F. Michaels, and D. G. Capone (2005), The conundrum of marine n₂ fixation, *Am J Sci*, *305*(6-8), 546–595, doi:10.2475/ajs.305.6-8.546.
- Maher, B., J. Prospero, D. Mackie, D. Gaiero, P. Hesse, and Y. Balkanski (2010), Global connections between aeolian dust, climate and ocean biogeochemistry at the present day and at the last glacial maximum, *Earth-Science Reviews*, *99*(1-2), 61–97.
- Mahowald, N., T. D. Jickells, A. R. Baker, P. Artaxo, C. R. Benitez-Nelson, G. Bergametti, T. C. Bond, Y. Chen, D. D. Cohen, B. Herut, N. Kubilay, R. Losno, C. Luo, W. Maenhaut, K. A. McGee, G. S. Okin, R. L. Siefert, and S. Tsukuda (2008), Global distribution of atmospheric phosphorus sources, concentrations and deposition rates, and anthropogenic impacts, *Global Biogeochemical Cycles*, *22*, 19 PP., doi:200810.1029/2008GB003240.
- Mahowald, N. M., P. Artaxo, A. R. Baker, T. D. Jickells, G. S. Okin, J. T. Randerson, and A. R. Townsend (2005a), Impacts of biomass burning emissions and land use change on amazonian atmospheric phosphorus cycling and deposition, *Global Biogeochemical Cycles*, *19*, GB4030, doi:10.1029/2005GB002541.
- Mahowald, N. M., A. R. Baker, G. Bergametti, N. Brooks, R. A. Duce, T. D. Jickells, N. Kubilay, J. M. Prospero, and I. Tegen (2005b), Atmospheric global dust cycle and iron inputs to the ocean, *Global Biogeochemical Cycles*, *19*, GB4025, doi:10.1029/2004GB002402.
- Mahowald, N. M., J. Lamarque, X. X. Tie, and E. Wolff (2006), Sea-salt aerosol response to climate change: Last glacial maximum, preindustrial, and doubled carbon dioxide climates, *Journal of Geophysical Research*, *111*, 11 PP., doi:200610.1029/2005JD006459.
- Martcorena, B., G. Bergametti, B. Aumont, Y. Callot, C. N'Doumé, and M. Legrand (1997), Modeling the atmospheric dust cycle 2. simulation of saharan dust sources, *Journal of Geophysical Research*, *102*(D4), PAGES 4387–4404.
- Martin, J. H., and S. E. Fitzwater (1988), Iron deficiency limits phytoplankton growth in the north-east pacific subarctic, *Nature*, *331*(6154), 341–343, doi:10.1038/331341a0.
- Mather, R. L., S. E. Reynolds, G. A. Wolff, R. G. Williams, S. Torres-Valdes, E. M. S. Woodward, A. Landolfi, X. Pan, R. Sanders, and E. P. Achterberg (2008), Phosphorus cycling in the north and south atlantic ocean subtropical gyres, *Nature Geosci*, *1*(7), 439–443, doi:10.1038/ngeo232.
- McConnell, C. L., E. J. Highwood, H. Coe, P. Formenti, B. Anderson, S. Osborne, S. Nava, K. Desboeufs, G. Chen, and M. A. J. Harrison (2008), Seasonal variations of the physical

- and optical characteristics of saharan dust: Results from the dust outflow and deposition to the ocean (DODO) experiment, *Journal of Geophysical Research*, *113*(D14), doi:10.1029/2007JD009606.
- McConnell, C. L., P. Formenti, E. J. Highwood, and M. A. J. Harrison (2010), Using aircraft measurements to determine the refractive index of saharan dust during the DODO experiments, *Atmos. Chem. Phys.*, *10*(6), 3081–3098.
- Mendez, J., C. Guieu, and J. Adkins (2010), Atmospheric input of manganese and iron to the ocean: Seawater dissolution experiments with saharan and north american dusts, *Marine Chemistry*, *120*(1-4), 34–43, doi:10.1016/j.marchem.2008.08.006.
- Middleton, N. J., and A. S. Goudie (2001), Saharan dust: sources and trajectories, *Transactions of the Institute of British Geographers*, *26*(2), 165–181, doi:10.1111/1475-5661.00013.
- Miller, J., and J. C. Miller (2005), *Statistics and Chemometrics for Analytical Chemistry*, 5 ed., Prentice Hall.
- Mills, M. M., C. Ridame, M. Davey, J. L. Roche, and R. J. Geider (2004), Iron and phosphorus co-limit nitrogen fixation in the eastern tropical north atlantic, *Nature*, *429*(6989), 292–294, doi:10.1038/nature02550.
- Murphy, J., and J. Riley (1962), A modified single solution method for the determination of phosphate in natural waters, *Analytica Chimica Acta*, *27*, 31–36, doi:10.1016/S0003-2670(00)88444-5.
- NEGTA (2001), *National Expert Group on Transboundary Air Pollution: Acidification, eutrophication and ground-level ozone in the UK*, DEFRA.
- Ooki, A., J. Nishioka, T. Ono, and S. Noriki (2009), Size dependence of iron solubility of asian mineral dust particles, *Journal of Geophysical Research*, *114*, 8 PP., doi:200910.1029/2008JD010804.
- Osborne, S. R., B. T. Johnson, J. M. Haywood, A. J. Baran, M. A. J. Harrison, and C. L. McConnell (2008), Physical and optical properties of mineral dust aerosol during the dust and biomass-burning experiment, *Journal of Geophysical Research*, *113*, 14 PP., doi:200810.1029/2007JD009551.
- Painter, S., R. Sanders, H. Waldron, M. Lucas, E. Woodward, and K. Chamberlain (2008), Nitrate uptake along repeat meridional transects of the atlantic ocean, *Journal of Marine Systems*, *74*(1-2), 227–240.
- Paiva, R. P., C. S. Munita, I. I. L. Cunha, C. D. Alonso, J. Romano, and M. H. R. Martins (1993), A contribution to the characterization of the aerosol sources in são paulo, *Journal of Radioanalytical and Nuclear Chemistry Articles*, *167*(2), 295–307, doi:10.1007/BF02037188.

- Parsons, T. R., Y. Maita, and C. M. Lalli (1984), *A Manual of Chemical and Biological Methods for Seawater Analysis*, Pergamon Press.
- Patey, M. D., M. J. Rijkenberg, P. J. Statham, M. C. Stinchcombe, E. P. Achterberg, and M. Mowlem (2008), Determination of nitrate and phosphate in seawater at nanomolar concentrations, *TrAC Trends in Analytical Chemistry*, *27*(2), 169–182, doi:10.1016/j.trac.2007.12.006.
- Poulton, A., P. Holligan, A. Hickman, Y. Kim, T. Adey, M. Stinchcombe, C. Holeton, S. Root, and E. Woodward (2006), Phytoplankton carbon fixation, chlorophyll-biomass and diagnostic pigments in the atlantic ocean, *Deep-Sea Research Part II: Topical Studies in Oceanography*, *53*(14-16), 1593–1610.
- Prospero, J., K. Barrett, T. Church, F. Dentener, R. Duce, J. Galloway, H. Levy, J. Moody, and P. Quinn (1996), Atmospheric deposition of nutrients to the north atlantic basin, *Biogeochemistry*, *35*(1), 27–73, doi:10.1007/BF02179824.
- Prospero, J. M. (1989), The use of whatman 41 filters for high volume aerosol sampling: Comments, *Atmospheric Environment (1967)*, *23*(12), 2861, doi:10.1016/0004-6981(89)90568-4.
- Prospero, J. M., and P. J. Lamb (2003), African droughts and dust transport to the caribbean: Climate change implications, *Science*, *302*(5647), 1024–1027, doi:10.1126/science.1089915.
- Pryor, S. C., and L. L. Sørensen (2002), Dry deposition of reactive nitrogen to marine environments: recent advances and remaining uncertainties, *Marine Pollution Bulletin*, *44*(12), 1336–1340, doi:10.1016/S0025-326X(02)00234-5.
- Pszenny, A., C. Fischer, A. Mendez, and M. Zetwo (1993), Direct comparison of cellulose and quartz fiber filters for sampling submicrometer aerosols in the marine boundary layer, *Atmospheric Environment. Part A. General Topics*, *27*(2), 281–284, doi:10.1016/0960-1686(93)90359-7.
- Pye, K. (1987), *Aeolian Dust and Dust Deposits*, Academic Press Inc.
- Rädlein, N., and K. G. Heumann (1995), Size fractionated impactor sampling of aerosol particles over the atlantic ocean from europe to antarctica as a methodology for source identification of cd, pb, tl, ni, cr, and fe, *Fresenius' Journal of Analytical Chemistry*, *352*(7), 748–755, doi:10.1007/BF00323059.
- Raes, F., R. Van Dingenen, E. Vignati, J. Wilson, J. Putaud, J. H. Seinfeld, and P. Adams (2000), Formation and cycling of aerosols in the global troposphere, *Atmospheric Environment*, *34*(25), 4215–4240, doi:10.1016/S1352-2310(00)00239-9.

- Real, E., E. Orlandi, K. Law, F. Fierli, D. Josset, F. Cairo, H. Schlager, S. Borrmann, D. Kunkel, C. Volk, J. McQuaid, D. Stewart, J. Lee, A. Lewis, J. Hopkins, F. Ravegnani, A. Ulanovski, and C. Liousse (2010), Cross-hemispheric transport of central african biomass burning pollutants: Implications for downwind ozone production, *Atmospheric Chemistry and Physics*, 10(6), 3027–3046.
- Ridgwell, A. J. (2009), The global dust cycle: Sources, sinks, and relationship with climate change, in *Surface ocean-lower atmosphere processes*, edited by C. L. Quéré and E. S. Saltzman, American Geophysical Union.
- Rijkenberg, M. J., C. F. Powell, M. Dall’Osto, M. C. Nielsdottir, M. D. Patey, P. G. Hill, A. R. Baker, T. D. Jickells, R. M. Harrison, and E. P. Achterberg (2008), Changes in iron speciation following a saharan dust event in the tropical north atlantic ocean, *Marine Chemistry*, 110(1-2), 56–67, doi:10.1016/j.marchem.2008.02.006.
- Rogora, M., M. Minella, A. Orrù, and G. Tartari (2006), A comparison between high-temperature catalytic oxidation and persulphate oxidation for the determination of total nitrogen in freshwater, *International Journal of Environmental Analytical Chemistry*, 86(14), 1065–1078.
- Rue, E. L., and K. W. Bruland (1995), Complexation of iron(III) by natural organic ligands in the central north pacific as determined by a new competitive ligand equilibration/adsorptive cathodic stripping voltammetric method, *Marine Chemistry*, 50(1-4), 117–138, doi:10.1016/0304-4203(95)00031-L.
- Sarthou, G., A. R. Baker, S. Blain, E. P. Achterberg, M. Boye, A. R. Bowie, P. Croot, P. Laan, H. J. W. de Baar, T. D. Jickells, and P. J. Worsfold (2003), Atmospheric iron deposition and sea-surface dissolved iron concentrations in the eastern atlantic ocean, *Deep Sea Research Part I: Oceanographic Research Papers*, 50(10-11), 1339–1352, doi:10.1016/S0967-0637(03)00126-2.
- Savoie, D. L., and J. M. Prospero (1982), Particle size distribution of nitrate and sulfate in the marine atmosphere, *Geophysical Research Letters*, pp. 1207–1210.
- Savoie, D. L., R. Arimoto, W. C. Keene, J. M. Prospero, R. A. Duce, and J. N. Galloway (2002), Marine biogenic and anthropogenic contributions to non-sea-salt sulfate in the marine boundary layer over the north atlantic ocean, *Journal of Geophysical Research*, 107, 21 PP., doi:200210.1029/2001JD000970.
- Schlosser, C., and P. L. Croot (2009), Controls on seawater Fe(III) solubility in the mauritanian upwelling zone, *Geophysical Research Letters*, 36, 5 PP., doi:200910.1029/2009GL038963.
- Schroth, A., J. Crusius, E. Sholkovitz, and B. Bostick (2009), Iron solubility driven by speciation in dust sources to the ocean, *Nature Geoscience*, 2(5), 337–340.

- Sedwick, P. N., E. R. Sholkovitz, and T. M. Church (2007), Impact of anthropogenic combustion emissions on the fractional solubility of aerosol iron: Evidence from the sargasso sea, *Geochemistry Geophysics Geosystems*, 8, Q10Q06, doi:10.1029/2007GC001586.
- Seinfeld, J. H., and S. N. Pandis (2006), *Atmospheric Chemistry and Physics: From Air Pollution to Climate Change*, 2nd edition ed., WileyBlackwell.
- Sholkovitz, E., P. Sedwick, and T. Church (2009), Influence of anthropogenic combustion emissions on the deposition of soluble aerosol iron to the ocean: Empirical estimates for island sites in the north atlantic, *Geochimica et Cosmochimica Acta*, 73(14), 3981–4003.
- Siefert, R. L., A. M. Johansen, and M. R. Hoffmann (1999), Chemical characterization of ambient aerosol collected during the southwest monsoon and intermonsoon seasons over the arabian sea: Labile-Fe(II) and other trace metals, *Journal of Geophysical Research*, 104(D3), PAGES 3511–3526.
- Slinn, S., and W. Slinn (1980), Predictions for particle deposition on natural waters, *Atmospheric Environment (1967)*, 14(9), 1013–1016, doi:10.1016/0004-6981(80)90032-3.
- Spokes, L., and T. Jickells (1995), Factors controlling the solubility of aerosol trace metals in the atmosphere and on mixing into seawater, *Aquatic Geochemistry*, 1(4), 355–374.
- Spokes, L. J., T. D. Jickells, and B. Lim (1994), Solubilisation of aerosol trace metals by cloud processing: A laboratory study, *Geochimica et Cosmochimica Acta*, 58(15), 3281–3287, doi:10.1016/0016-7037(94)90056-6.
- Spokes, L. J., S. G. Yeatman, S. Cornell, and T. D. Jickells (2000), Nitrogen deposition to the eastern atlantic ocean. the importance of southeasterly flow, *Tellus B*, 52(1), 37–49, doi:10.1034/j.1600-0889.2000.00062.x.
- Stuut, J., M. Zabel, V. Ratmeyer, P. Helmke, E. Schefuß, G. Lavik, and R. Schneider (2005), Provenance of present-day eolian dust collected off NW africa, *Journal of Geophysical Research*, 110, 14 PP., doi:200510.1029/2004JD005161.
- Stuut, J., I. Smalley, and K. O’Hara-Dhand (2009), Aeolian dust in europe: African sources and european deposits, *Quaternary International*, 198(1-2), 234–245, doi:10.1016/j.quaint.2008.10.007.
- Sunda, W. (1997), Control of dissolved iron concentrations in the world ocean: A comment, *Marine Chemistry*, 57(3-4), 169–172.
- Suratman, S. (2007), The seasonal distribution and cycling of nitrogen and organic carbon-based nutrients in the north sea., Ph.D., University of East Anglia.

- Suratman, S., T. Jickells, K. Weston, and L. Fernand (2008), Seasonal variability of inorganic and organic nitrogen in the north sea, *Hydrobiologia*, *610*(1), 83–98, doi:10.1007/s10750-008-9424-y.
- Tagliabue, A., and K. R. Arrigo (2006), Processes governing the supply of iron to phytoplankton in stratified seas, *Journal of Geophysical Research*, *111*, 14 PP., doi:200610.1029/2005JC003363.
- Tang, M., J. Thieser, G. Schuster, and J. Crowley (2010), Uptake of NO₃ and N₂O₅ to saharan dust, ambient urban aerosol and soot: A relative rate study, *Atmospheric Chemistry and Physics*, *10*(6), 2965–2974.
- Taylor, S. R., and S. M. McLennan (1985), *The Continental Crust: Its Composition and Evolution*, illustrated edition ed., Wiley-Blackwell.
- Tian, Z., P. Ollivier, A. Véron, and T. M. Church (2008), Atmospheric fe deposition modes at bermuda and the adjacent sargasso sea, *Geochemistry Geophysics Geosystems*, *9*, 14 PP., doi:200810.1029/2007GC001868[Citation].
- Trapp, J. M., F. J. Millero, and J. M. Prospero (2010), Trends in the solubility of iron in dust-dominated aerosols in the equatorial atlantic trade winds: Importance of iron speciation and sources, *Geochemistry Geophysics Geosystems*, *11*(3), doi:10.1029/2009GC002651.
- Twohy, C. H., S. M. Kreidenweis, T. Eidhammer, E. V. Browell, A. J. Heymsfield, A. R. Bansemer, B. E. Anderson, G. Chen, S. Ismail, P. J. DeMott, and S. C. V. D. Heever (2009), Saharan dust particles nucleate droplets in eastern atlantic clouds, *Geophysical Research Letters*, *36*, 6 PP., doi:200910.1029/2008GL035846.
- Tyrrell, T. (1999), The relative influences of nitrogen and phosphorus on oceanic primary production, *Nature*, *400*(6744), 525–531, doi:10.1038/22941.
- Tyrrell, T., E. M. nón, A. J. Poulton, A. R. Bowie, D. S. Harbour, and E. M. S. Woodward (2003), Large-scale latitudinal distribution of trichodesmium spp. in the atlantic ocean, *Journal of Plankton Research*, *25*(4), 405–416, doi:10.1093/plankt/25.4.405.
- Wagener, T., C. Guieu, R. Losno, S. Bonnet, and N. Mahowald (2008), Revisiting atmospheric dust export to the southern hemisphere ocean: Biogeochemical implications, *Global Biogeochemical Cycles*, *22*, GB2006, doi:10.1029/2007GB002984.
- Watts, S., R. Yaaqub, and T. Davies (1987), The use of whatman 41 filter papers for high volume aerosol sampling, *Atmospheric Environment*, *21*(12), 2731–2732, doi:10.1016/0004-6981(87)90207-1.
- Wedepohl, K. H. (1995), The composition of the continental crust, *Geochimica et Cosmochimica Acta*, *59*(7), 1217–1232, doi:10.1016/0016-7037(95)00038-2.

- Witt, M. L. I. (2003), Studies of trace metals in the atmosphere, Ph.D., Univeristy of East Anglia, Norwich, UK.
- Worsfold, P. J., P. Monbet, A. D. Tappin, M. F. Fitzsimons, D. A. Stiles, and I. D. McKelvie (2008), Characterisation and quantification of organic phosphorus and organic nitrogen components in aquatic systems: A review, *Analytica Chimica Acta*, 624(1), 37–58, doi:10.1016/j.aca.2008.06.016.
- Wright, K. (2009), Dionex DX600 specifications and use, personal communication.
- Wu, J., E. Boyle, W. Sunda, and L. Wen (2001), Soluble and colloidal iron in the oligotrophic north atlantic and north pacific, *Science*, 293(5531), 847–849, doi:10.1126/science.1059251.
- Xie, P., and P. A. Arkin (1997), Global precipitation: A 17-Year monthly analysis based on gauge observations, satellite estimates, and numerical model outputs, *Bulletin of the American Meteorological Society*, 78(11), 2539–2558.
- Yeatman, S. G. (2000), Major-ion and isotopic studies of aerosol nitrogen species in the marine atmosphere, Ph.D., University of East Anglia, Norwich, UK.
- Zhang, D., and Y. Iwasaka (2004), Size change of asian dust particles caused by sea salt interaction: Measurements in southwestern japan, *Geophysical Research Letters*, 31, 4 PP., doi:200410.1029/2004GL020087.
- Zhang, D., Y. Iwasaka, and G. Shi (2005), Sea salt shifts the range sizes of asian dust, *Eos*, 86(50), 523.

All we are is dust in the wind, dude

- Ted "Theodore" Logan